Multi-Layer Flows with Yield Stress Fluids

by

Sarah Hormozi

B.Sc. Mechanical Engineering, Shiraz University, 2003
M.Sc. Mechanical Engineering, Sharif University of Technology, 2006

A THESIS SUBMITTED IN PARTIAL FULFILLMENT OF
THE REQUIREMENTS FOR THE DEGREE OF

DOCTOR OF PHILOSOPHY

in

The Faculty of Graduate Studies

(Mechanical Engineering)

THE UNIVERSITY OF BRITISH COLUMBIA

(Vancouver)

July 2011

Abstract

Interfacial instabilities of multi-layer shear flows may be eliminated by astute positioning of yield stress fluid layers that remain unyielded at the interface(s). The contribution of this thesis comes in three parts. Firstly, we have performed a computational study of these flows in the setting of a Newtonian core fluid surrounded by a Bingham lubricating fluid, within pipe and channel configurations. The simulations include an inlet geometry in the computational model and study the multi-layer flows, both as the fluids are initially injected (start up) and later the established steady flows (development lengths). Nonlinear perturbations are also studied, showing in particular that during energy decay of stable perturbations the initial rapid decay of the perturbation kinetic energy relates to reforming/breaking of the unyielded plug and is followed by slower viscous decay. For axisymmetric perturbations these flows can be stable to order unity initial perturbation amplitudes and for $Re \lesssim 10^2$. The channel geometry allows for symmetry breaking and appears to be less stable. A number of interesting effects are explored using the channel geometry.
Secondly, we focus on demonstrating whether the stable core annular flow can be achieved when lubricating a visco-elastic core fluid with a yield stress fluid. We have performed over 100 experiments using Carbopol solutions as the lubricating yield stress fluid and Polyethylene Oxide solutions as the visco-elastic fluid. Thirdly, we have applied the energy stability method to study nonlinear stability of a core-annular flow of an Oldroyd-B fluid surrounded by a Bingham fluid. Together with the experimental study, this shows that visco-elasticity is not a barrier to use of this methodology.

Preface

In this section, we briefly explain the contents of the journal papers that are published or submitted for publication from this thesis and clarify the contributions of co-authors in the papers. We also include list of conference contributions.

Journal papers

- **[Hormozi, S.], Wielage-Burchard, K. & Frigaard, I.A. (2011) Entry and start up effects in visco-plastically lubricated viscous shear flow in pipe. J. Fluid Mech. 673, 432-467.**

  This publication has mostly focused at trying to understand better the stability and robustness of visco-plastically lubricated pipe flows. Chapter 2 includes the contents of this publication. The author of this thesis was the principal contributor to this publication. Dr. Kerstin Wielage-Burchard assisted with code development. Professor Ian Frigaard supervised the research and assisted with writing the paper.

- **[Hormozi, S.], Wielage-Burchard, K. & Frigaard, I.A. (2011) Multi-layer channel flows with yield stress fluids. J. Non-Newtonian Fluid Mech. 166, 262-278.**

  In this publication, we present results of a computational study of visco-plastically lubricated plane channel multi-layer flows, in which the yield stress fluid layers are unyielded at the interface. Chapter 3 includes the contents of this publication. The author of this thesis was the principal

contributor to this publication. Dr. Kerstin Wielage-Burchard assisted with code development. Professor Ian Frigaard supervised the research and assisted with writing the paper.

- **[Hormozi, S.], Martinez, D.M. & Frigaard, I.A. (2011) Stable core-annular flows of viscoelastic fluids using the visco-plastic lubrication technique. Submitted for publication, under review.**

  In this paper, we give an experimental demonstration that stable core-annular flows can be achieved when lubricating a viscoelastic core fluid with a yield stress fluid. Chapter 4 includes the contents of this publication. The author of this thesis was the principal contributor to this publication. Professor Ian Frigaard and professor Mark Martinez supervised the research and assisted with writing the paper.

- **[Hormozi, S.] & Frigaard, I.A. (2011) Nonlinear stability of a visco-plastically lubricated viscoelastic fluid flow. Submitted for publication, under review.**

  In this paper, a core-annular flow of an Oldroyd-B fluid surrounded by a lubricating Bingham fluid is studied using energy stability methods. Chapter 5 includes the contents of this publication. The author of this thesis was the principal contributor to this publication. Professor Ian Frigaard supervised the research and assisted with writing the paper.

Contributions to refereed conference proceedings

- Hormozi, S., Wielage-Burchard, K., Frigaard, I.A, Martinez, D.M. & Grecov, D. Entry and start-up flows in visco-plastic lubrication. CSME (2010), June 6-9, Victoria, Canada.

- Hormozi, S., Wielage-Burchard, K., Frigaard, I.A, Martinez, D.M. & Grecov, D. Numerical approach to nonlinear temporal stability of visco-plastic lubrication. ASME (2010), November 12-18, Vancouver, Canada.
- Hormozi, S., Martinez, D.M., Frigaard, I.A. & Grecov, D. Experimental studies of visco-elastic flow using visco-plastic lubricant. ASME (2010), November 12-18, Vancouver, Canada.
- Hormozi, S., Wielage-Burchard, K. & Frigaard, I.A. Visco-plastic lubrication flow in channel geometry. CANCAM (2011), June 5-9, Vancouver, Canada.

Conference presentations

- Hormozi, S., Frigaard, I.A, Martinez, D.M. & Grecov , D. Visco-plastic lubrication of visco-elastic fluid: Theory. 5th Annual European Rheology Conference (2009), April 15-17, Cardiff, United Kingdom.
- Hormozi, S, Martinez, D.M. & , Frigaard, I.A. (2009) .Visco-plastic lubrication of visco-elastic fluid: Experiment . 5th Annual European Rheology Conference (2009), April 15- 17, Cardiff, United Kingdom.
- Invited speaker for minisemester on evolution of interfaces at Hokkaido University (2010). July 25-31, Sapporo, Japan.
- Hormozi, S., Martinez, D.M. & Frigaard, I.A. Experimental Studies on Visco-plastic lubrication of visco-elastic fluid. 5th Pacific Rim Conference on Rheology (2010). August 1-6, Sapporo, Japan. (Recipient of the best poster presentation award)

Table of Contents

Appendices

List of Tables

List of Figures

Acknowledgments

I would like to convey my gratitude to all people who gave me the possibility to complete this dissertation.

In the first place, I would like to express my sincere gratitude to my supervisor, Professor Ian Frigaard for the continuous support of my Ph.D study and research, for his patience, motivation, enthusiasm, and immense knowledge. His wide knowledge and his logical way of thinking have been of great value to me.

I am deeply grateful to Professor Mark Martinez and Dr Dana Grecov for their supervision, advice, and guidance from the early stage of this research. Above all and the most needed, they provided me support and friendly help in various ways.

I gratefully acknowledge Dr Kerstin Wielage-Burchard for her crucial contribution. Kerstin, I am grateful in every possible way and hope to keep up our collaboration in the future.

I would like to thank Mr Leonid Sergueev, for assisting me with performing the experiments and Mr Markus Fengler who provided technical support.

Most importantly, I would like to thank my entire family. My immediate family to whom this dissertation is dedicated, has been a constant source of love, concern, support and strength all these years. I would like to express my heart-felt gratitude to my mother and brother in law who have supported and encouraged me throughout this endeavor.

Finally, financial support of the Natural Sciences and Engineering Research Council of Canada (NSERC) is gratefully acknowledged.

Dedication

To my wonderful parents, who stood by me and supported all my ideas and dreams. I love you dearly.

To my beloved husband, best friend in all aspects of my life, the one person who has been by my side throughout this entire journey. Your constant support and encouragement continue to help me reach my goals. I am forever thankful to have you in my life.

Chapter 1

Introduction

Multi-layer flows occur industrially in

- Co-extrusion processes, where a product is made of more than one layer simultaneously.
- Film coating processes, where a layer is applied to a fluid substrate.
- Lubricated transport processes, where a lubricating fluid lies in a layer between the wall of a duct and the transported fluid.

In all 3 processes the flow rate (or production rate) is frequently limited by the growth of interfacial instabilities. Methodologies to suppress or eliminate interfacial instabilities and further stabilise multi-layer flows are therefore of considerable practical interest. In this thesis we study one such method that uses a visco-plastic fluid as the lubricating fluid.

1.1 The visco-plastic lubrication flow paradigm

The unique feature of a visco-plastic fluid is that it possesses a yield stress. The yield stress is a stress value that separates the flow behavior into two distinctly different qualitative regimes. If the shear stresses in the fluid lie below the yield stress then the fluid has a solid-like structure and moves as a rigid body. For stresses above the yield stress, the fluid deforms and flows (see §1.2).

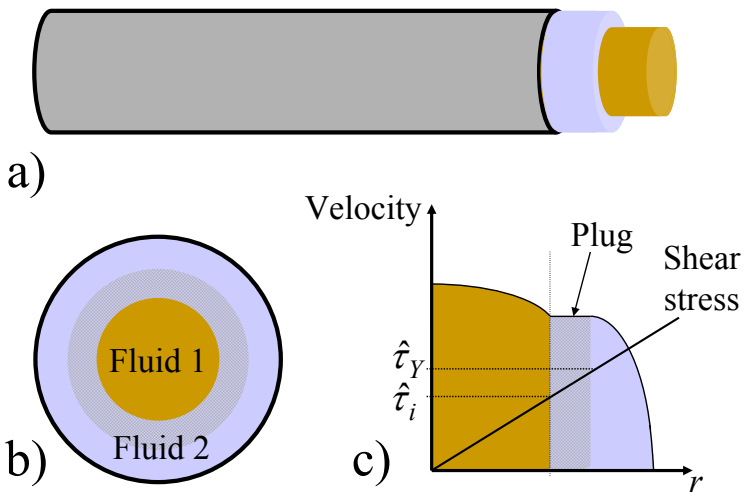

Figure 1.1: Schematic of the flow geometry: a) axisymmetric core-annular flow; b) cross-section of the pipe; c) velocity and stress profile across a radial section, showing unyielded plug configuration at the interface.

The key feature of our methodology is best illustrated by considering either a steady core annular flow (Fig. 1.1) or a symmetric 3-layer plane Poiseuille flow of iso-density fluids (Fig. 1.2). The shear stress increases linearly from the pipe or channel center to the outer walls. The main idea is to position the visco-plastic fluid in the outer lubricating layer and ensure that the yield stress ($\hat{\tau}_Y$) is larger than the interfacial shear stress ($\hat{\tau}_i$) by a finite amount. This has the effect of assuring that there is an unyielded solid-like ring of visco-plastic fluid surrounding the core fluid. Since the yield stress exceeds the interfacial stress by a finite amount, we would expect that finite perturbations are needed to yield the fluid at the interface. Therefore without finite perturbations we expect that there will be no growth of interfacial instabilities. The above idea is simplistic, but has been further developed by [26, 55, 85], and is studied for the remainder of this thesis.

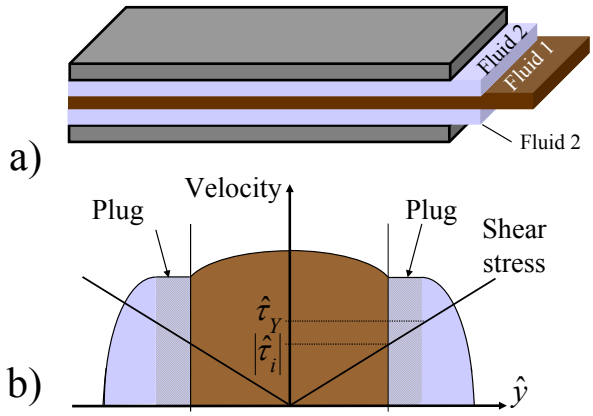

Figure 1.2: Schematic of the flow geometry: a) symmetric 3-layer flow; b) velocity and stress profile across a section, showing unyielded plug configuration at the interface.

1.1.1 Context of the thesis

Before giving a more general literature survey in §1.3, we review the 4 studies that have specifically considered VPL (Visco-Plastically Lubricated) flows. This helps to understand the context of the thesis, Then, in §1.1.2, we outline the objectives.

- Frigaard, [26] studied the linear stability of a configuration similar to that of Fig. 1.2, with the inner fluid also a Bingham fluid. Linear stability studies of Bingham fluids, e.g. [27], show that the unyielded regions of parallel shear flows are not perturbed by linear perturbations (since the perturbations are modal the stress perturbations average to zero longitudinally). The results show that the linear stability studies only consider decoupled yielded layers. In [26] the same analysis is applied as in [27], resulting in a decoupling of the stability problems for the 2 fluids. Via a mapping technique, each linear stability problem is then shown to be more stable than the linear stability problem of the same fluid flowing alone in the channel. The approach used by [26, 27] involves

considering the even extensions of linear eigenvalue problem, following a symmetry argument which has been questioned by [89]. The full domain eigenvalue problem has been extensively studied by [89] and no unstable modes have been found. The authors of [89] also present a convincing argument for the unconditional linear stability of this flow. In either case one can say that flows of the type illustrated in Fig. 1.1 & Fig. 1.2 will not become linearly unstable to interfacial modes.

- Very recently in [86] this linear stability approach was extended to two-layer flows of a Bingham fluid coupled with either a Carreau fluid or a modified FENE-CR fluid. Configurations were identified in which the two-layer flows were linearly stable even as $Re \to \infty$. This was achieved by combining the VPL technique with selection of base flows that have a strong enough Couette component in the non-Bingham fluid layer.

- Moyers-Gonzalez [84] and Moyers-Gonzalez et al. [85] explore the non-linear stability of these flows. The configuration chosen consists of a Bingham lubricating fluid and a Newtonian core (Fig. 1.1). The main method used by [85] is the energy stability method, but there are various complications due to the 2 fluids and possibilities of interfacial motion. For general two-fluid flows energy stability methods are not particularly useful as the interface topology is unknown and may vary significantly. The authors of [85] consider only perturbations for which the fluid at the interface remains unyielded in a layer about the core fluid, but do not restrict the interface motion. The unyielded cylinder may also translate in the axial direction and may translate and rotate within the plane of the cross-section. These restrictions allow the interface motion to be described in terms of the bulk fluid motion and in this way energy decay is established. Although in [85] the authors prove energy decay, they in fact show that the perturbed flow decays only to a base flow that has a Newtonian core encapsulated within the Bingham fluid surrounded by

an unyielded ring of fluid, but not necessarily to the concentric base flow. The results of [85] are not weakly nonlinear results, although conditional on the perturbation amplitude. This dependency is not easy to resolve quantitatively (except if the core fluid domain remains concentrically positioned) and this makes the results unwieldy. Thus, the main contribution of [85] is in establishing that the flows are nonlinearly stable and hence in some sense robust, without quantifying this robustness.

- Huen [54] and Huen et al. [55] demonstrate that these flows can be achieved experimentally. They use aqueous Carbopol and Xanthan solutions as the base fluids (Carbopol has a yield stress, Xanthan is shear thinning). Four sequences of experiments are conducted using different concentration solutions with slightly different rheologies. In each case stable multi-layer flows are found, where they are predicted to be by the existence of base flows of the type illustrated schematically in Fig. 1.1. Unstable flows are found where these base flow solutions do not exist. In addition, where stable multi-layer flows are found they appeared to be both stable and concentrically positioned.

Therefore, although VPL flows have been studied, we can easily identify unanswered questions and limitations. Firstly, the stability studies have either been linear stability, which is not always practical, or nonlinear energy stability. The energy stability method tells us little about the structure of the flow and is usually conservative. Clearly, computational studies can tell us much about these aspects. Secondly, due to practical restrictions on the possible fluid types, on the pump flow rates, as well as costs of performing the experiments, the study in [55] was necessarily not a broad systematic study, but rather a proof of concept. There is clear scope for further experimental work. Thirdly, in using the VPL technique for more industrial application, we are likely to encounter different fluid types than those studied so far.

1.1.2 Objectives of the thesis

This thesis concerns flows such as in Fig. 1.1 & Fig. 1.2. Overall our programme of study seeks to establish the practicality of the VPL method, at least in the fluid mechanic context. Different objectives of this study include the following.

1. We want to explore aspects of flow development and start-up in geometries such as pipes and channels. The plane channel geometry is a generic geometry for laminated products and eventually also coating applications. The pipe geometry is used in co-extrusion and transport processes.

2. Understanding the stability of these flows in greater detail, e.g. what role does the unyielded plug play, do perturbations remain concentric or develop asymmetries, how large an amplitude of perturbation can be withstood and at what Re, etc.

3. In working with a geometry that allows for asymmetry (i.e. plane channel) we want to look at new types of flow, where interesting and exotic effects could be introduced, but in a controlled manner, exploiting still the underlying method of retaining unyielded fluid at the interface.

4. Extension of the VPL concept to different flow scenarios (e.g. new fluid types, different flow geometries) while retaining the basic method of eliminating interfacial instabilities. Many industrial multi-layer flows involve fluids with visco-elastic properties. Therefore, the feasibility of establishing visco-plastic lubrication flows with visco-elastic core fluids is inherently of interest from experimental and theoretical perspectives.

1.2 Non-Newtonian fluids

For Newtonian fluids, shear stress $\tau_{ij}(\boldsymbol{u})$ and shear rate $\dot{\gamma}_{ij}(\boldsymbol{u})$ are proportional

$$\tau_{ij}(\boldsymbol{u}) = \mu\dot{\gamma}_{ij}(\boldsymbol{u}), \tag{1.1}$$

where μ is the viscosity of the material. However, daily life teems with examples of fluids with macro-molecular structures and as a consequence, a rich variety of behavior which can not be explained by the constitutive laws of a Newtonian fluid, (1.1). Such fluids are called non-Newtonian. This category includes visco-plastic fluids and visco-elastic fluids, on both of which this thesis will concentrate.

1.2.1 Visco-plastic fluids

In classical models of visco-plastic fluids, these materials do not deform when subjected to a shear stress smaller than a certain value, which is called the yield stress, (τ_Y). In this range of applied shear stress, these materials behave as ideal rigid solids. If the shear stress in the fluid exceeds the yield stress then the fluid deforms as a (nonlinearly) viscous fluid and is typically shear-thinning since the fluid structure breaks down progressively with shear.

Although it is doubtful that any real material actually behaves precisely in this manner, the behavior of many materials can be adequately approximated in this fashion. Examples of visco-plastic fluids are pastes, suspensions, slurries, paints, etc (see Fig. 1.3). The most common rheological models of this form are the Bingham, Casson and Herschel-Bulkley fluid models, Fig. 1.4.

- **Bingham plastic model**

  The Bingham model is one of the simplest visco-plastic models. It describes the characteristics of a fluid with yield stress and with a viscosity that is independent of shear rate. The constitutive equations are

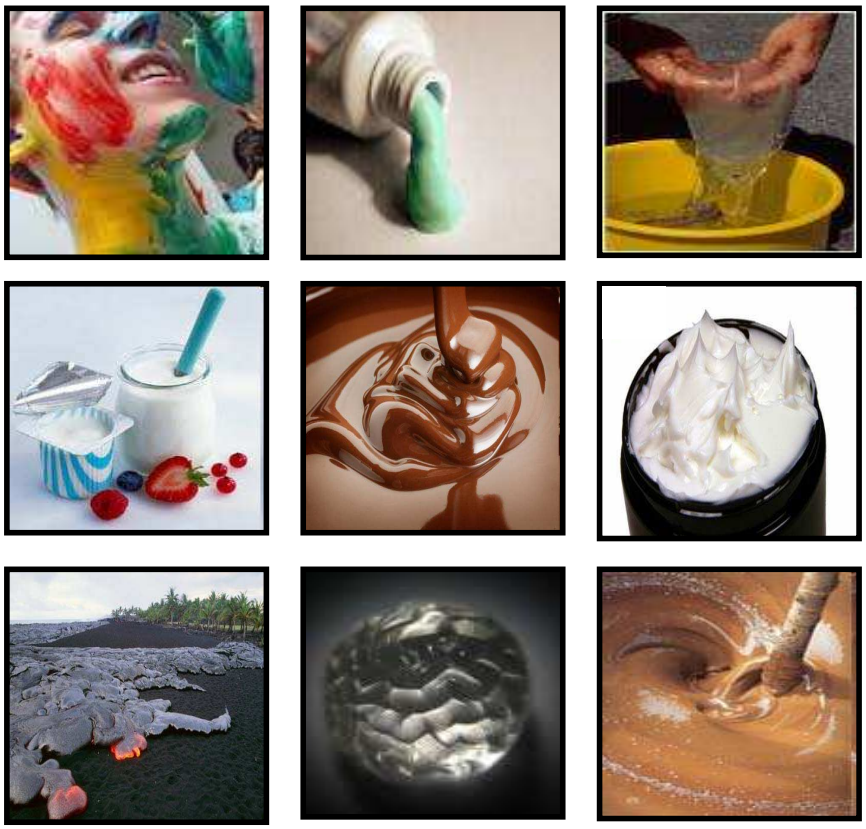

Figure 1.3: Examples of visco-plastic fluids. Top row (left to right); paint, toothpaste, hagfish mucus, Middle row (left to right); dairy products, liquid chocolate, diaper cream, Bottom row (left to right); basaltic lavas, polymer gels, drilling Fluids

$$\dot{\gamma}(\boldsymbol{u}) = 0 \iff \tau(\boldsymbol{u}) \leq \tau_Y, \tag{1.2}$$

$$\tau_{ij}(\boldsymbol{u}) = \left(\frac{\tau_Y}{\dot{\gamma}(\boldsymbol{u})} + \mu\right)\dot{\gamma}_{ij}(\boldsymbol{u}) \iff \tau(\boldsymbol{u}) > \tau_Y. \tag{1.3}$$

- **Casson model**

  The Casson model is based on a structural model of the interactive be-

havior of solid and liquid phases of a two-phase suspension. The model has both a yield stress and a shear-thinning non-Newtonian viscosity. The constitutive equations are

$$\dot{\gamma}(\boldsymbol{u}) = 0 \iff \tau(\boldsymbol{u}) \leq \tau_Y, \tag{1.4}$$

$$\tau_{ij}(\boldsymbol{u}) = \left(\sqrt{\frac{\tau_Y}{\dot{\gamma}(\boldsymbol{u})}} + \sqrt{\mu} \right)^2 \dot{\gamma}_{ij}(\boldsymbol{u}) \iff \tau(\boldsymbol{u}) > \tau_Y. \tag{1.5}$$

- **Herschel-Bulkley model**

  The Herschel-Bulkley model extends the simple power-law model to include a yield stress as follows

$$\dot{\gamma}(\boldsymbol{u}) = 0 \iff \tau(\boldsymbol{u}) \leq \tau_Y, \tag{1.6}$$

$$\tau_{ij}(\boldsymbol{u}) = \left(\frac{\tau_Y}{\dot{\gamma}(\boldsymbol{u})} + \mu \dot{\gamma}(\boldsymbol{u})^{n-1} \right) \dot{\gamma}_{ij}(\boldsymbol{u}) \iff \tau(\boldsymbol{u}) > \tau_Y. \tag{1.7}$$

In all of the mentioned models, $\dot{\gamma}(\boldsymbol{u})$ and $\tau(\boldsymbol{u})$ denote the second invariants of the strain rate and stress tensors, respectively and we have

$$\dot{\gamma}_{ij} = \frac{\partial u_i}{\partial x_j} + \frac{\partial u_j}{\partial x_i},$$

$$\dot{\gamma}(\boldsymbol{u}) = \left[\frac{1}{2} \sum_{i,j=1}^{3} [\dot{\gamma}_{ij}(\boldsymbol{u})]^2 \right]^{1/2} \qquad \tau(\boldsymbol{u}) = \left[\frac{1}{2} \sum_{i,j=1}^{3} [\tau_{ij}(\boldsymbol{u})]^2 \right]^{1/2}. \tag{1.8}$$

1.2.2 Visco-elastic fluids

As implied by the name, visco-elastic fluids exhibit the properties of both viscous and elastic materials. Fig. 1.5 shows few examples of visco-elastic

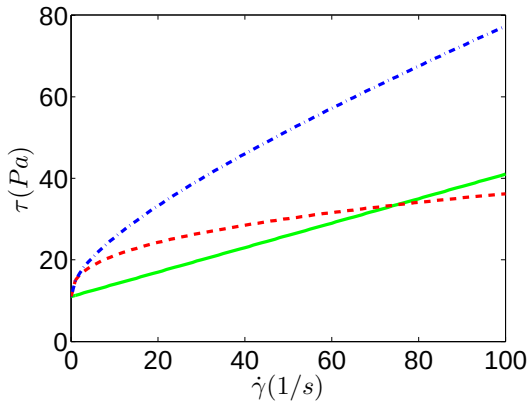

Figure 1.4: Relationship between shear rate $\dot{\gamma}$ and shear stress τ for; Bingham fluids(-); Casson fluids (-.) & Herschel-Bulkley fluids(- -).

fluids.

We have mentioned that for a purely viscous material, internal stresses are a function only of the instantaneous shear rate or strain rate. On the contrary, a purely elastic material develops stresses which are a function only of the instantaneous strain. For visco-elastic fluids, internal stresses are a function not only of the instantaneous deformation (e.g. strain, strain rate, etc.) but also depend upon the entire past history of the deformation. The influence of time upon the relation between stress and strain can be described either by a differential equation, which includes derivatives of the stress and strain tensors with respect to time, or by an integral equation with time as the independent variable. In the limit of small deformation, visco-elastic fluids have a linear relationship between their strain history and current value of stress. Linear visco-elastic models can be constructed by combination of linear mechanical or electrical elements which represent purely viscous and elastic properties. The conventional mechanical/electrical elements representing the linear viscous and elastic behavior are spring/circuit's capacitance and dashpot/circuit's resistance respectively. Figure (1.6) shows mechanical and electrical analogs used to construct the simplest linear visco-elastic model

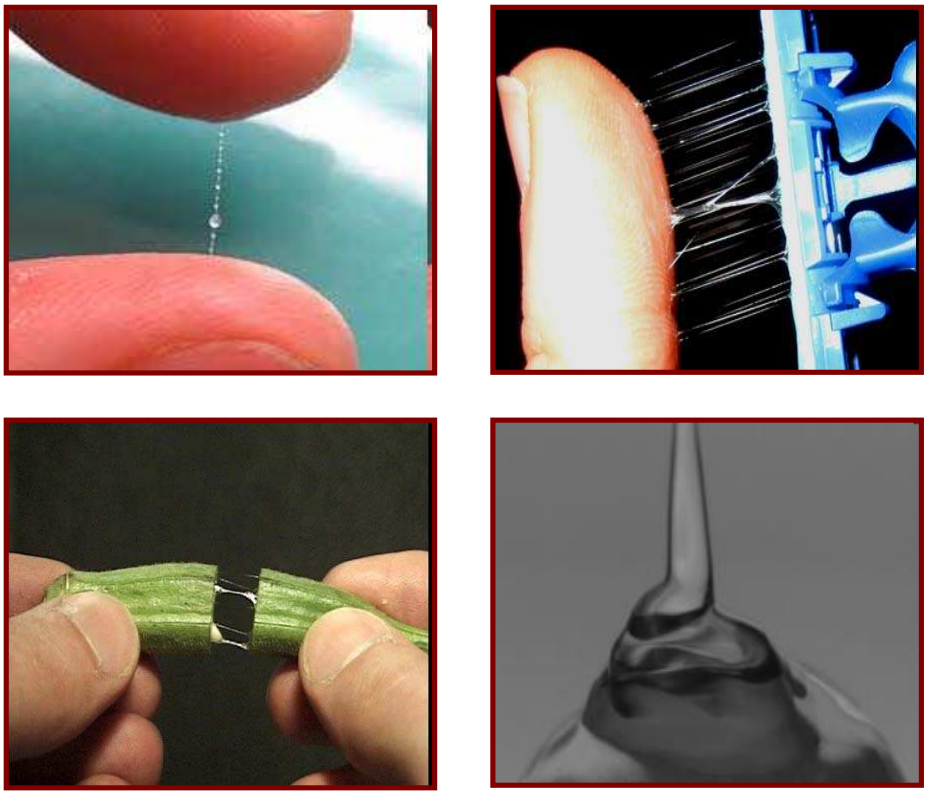

Figure 1.5: Examples of visco-elastic fluids (*http://web.mit.edu/nnf*). Top row (left to right); saliva , shaving gels, Bottom row (left to right); okra's juice, polymer solution.

called linear Maxwell model. In this model the total strain is the sum of the elastic strain (γ_s) of the spring and the fluid strain (γ_d) of the dashpot

$$\gamma = \gamma_s + \gamma_d,$$

Differentiating this with respect to time:

$$\dot{\gamma} = \dot{\gamma_s} + \dot{\gamma_d} = \frac{\dot{\tau}}{G} + \frac{\tau}{\mu},$$

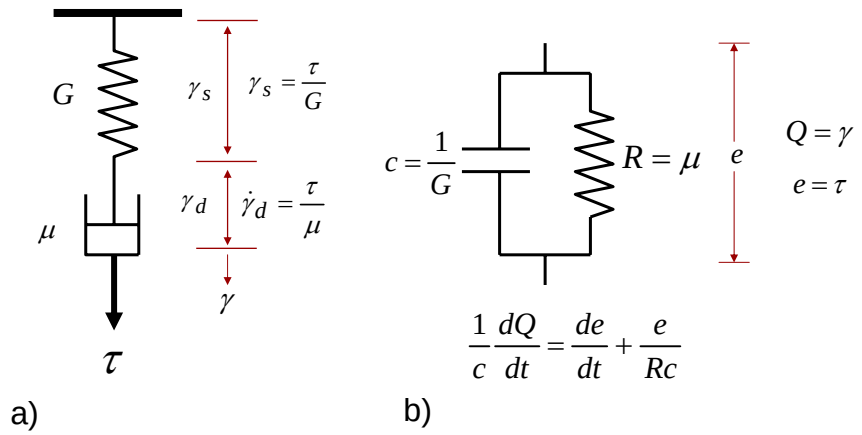

Figure 1.6: a) Mechanical ; b) Electrical, model of Maxwell Fluid.

or

$$\tau + \lambda\dot{\tau} = \mu\dot{\gamma}, \tag{1.9}$$

where $\lambda = \mu/G$.

Let us compare the behavior of an ideal viscous fluid (Newtonian fluid), an ideal elastic solid (Hookean solid) and a visco-elastic fluid (linear Maxwell fluid) subjected to a stress relaxation test where a shear strain of magnitude γ_0 is suddenly applied on the materials (see Fig. 1.7). We consider the following strain function

$$\gamma(t) = \gamma_0 U(t). \tag{1.10}$$

where $U(t)$ is the unit step function, defined as

$$U(t) = 0, \quad \texttt{for} \quad t \leq 0 \qquad \texttt{and} \qquad U(t) = 1, \quad \texttt{for} \quad t > 0. \tag{1.11}$$

We express the resulting stress as a function of time by solving (1.9) and (1.11). The following solution obtained by using the laplace transform method:

$$\tau(t) = G\gamma_0 e^{-t/\lambda} = \tau_0 e^{-t/\lambda}. \tag{1.12}$$

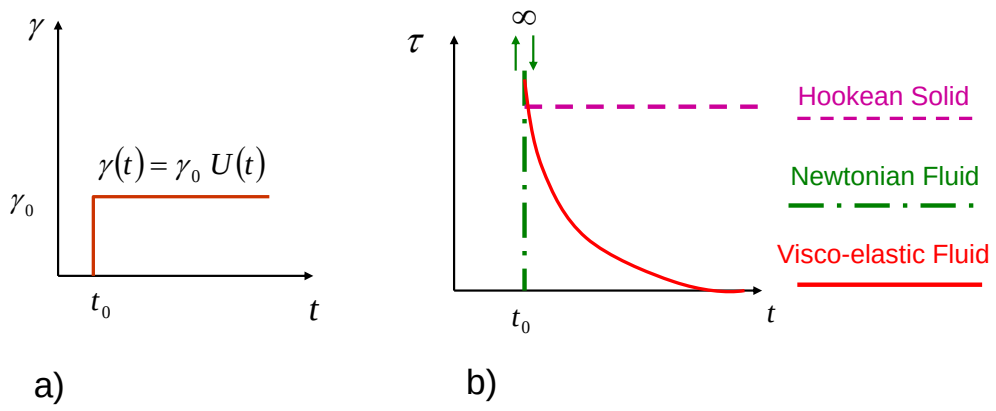

Figure 1.7: a) Applied strain for stress relaxation test, b)Response to stress relaxation test ($t_0 = 0$), (see [17]).

When the material is a purely viscous fluid (Newtonian fluid: $G \to \infty$ and $\lambda \to 0$), the stress would relax infinitely fast ($\tau \to 0$ as $\lambda \to 0$). Therefore the relaxation time of stress is zero for Newtonian fluid. On the other hand, when the material is purely elastic (Hookean solid: $\mu \to \infty$ and $\lambda \to \infty$) the stress would not relax at all and the relaxation time is infinity ($\tau \to \tau_0$ as $\lambda \to \infty$). Lastly, for a Maxwell fluid, the initial stress response is purely elastic ($\tau \to G\gamma_0$ as $t \to 0^+$). It then decays exponentially with time, reaching 37% of its initial value at a time equal to λ. Thus, the material property λ is a characteristic time constant, representative the time scale of the material for stress relaxation, and is called the stress relaxation time [17].

Linear visco-elastic models are not valid when the applied deformation is not small. As previously noted, for visco-elastic materials, it is not only the instantaneous strain or rate of strain, but the entire past history of strain that determines the measure of deformation. Moreover, the constitutive equation (rheological equation) has meaning only when associated with a specific element of material (material point). Hence, an embedded coordinate axes should be established which always passes through the same material elements as they

move through the system. An objective deformation [1] is measured relative to this system and a constitutive equation of state is formulated for a given material in terms of stress and strain variables relative to these convected coordinates. The constitutive equation must then be transformed from convected coordinates to a fixed coordinate frame to where all physical observations are made relative [17]. The nonlinear modification of Maxwell's linear law (1.9) considering convected coordinates is

$$\dot{\tau} + (\boldsymbol{u}.\bigtriangledown)\tau - (\bigtriangledown\boldsymbol{u})\tau - \tau(\bigtriangledown\boldsymbol{u})^T + \lambda\tau = \mu\dot{\gamma}, \tag{1.13}$$

This model is called the upper convected Maxwell model (UCM) which is the nonlinear extension of Maxwell's idea (1.9) and takes account of frame-indifference [2] which is violated by linear models for large deformation. The reader is referred to [56, 68, 117, 118] for more details.

The UCM model (1.13) can also be motivated by molecular theories [7, 98]. The Oldroyd B model has a stress that is the linear superposition of the UCM and a Newtonian contribution. Other popular differential models differ from the UCM by adding additional nonlinearities.

1.3 Literature review

In this thesis we study parallel multi-layer shear flow with a visco-plastic fluid in one of the layers. It is evident that the subject area, although quite specialized, touches on many related areas. In the first place, we give a survey on stability of single fluid flows with yield stress in §1.3.1 to elucidate the role of yield stress. Secondly, the start-up phase of the flow typically involves filling the pipe initially with the visco-plastic fluid then injecting both fluids simultaneously. This flow is similar to displacement flows, which have been studied

[1] Any measure of deformation defined to such a coordinate system should be independent of the local translation or rotation of the material

[2] The frame-indifference constitutive operator is the same for all observers in relative motion

in detail, both experimentally and numerically. Our fluids are miscible and we therefore mostly provide an overview of miscible displacement flow studies in §1.3.2.

Moving now to multi-layer flows, the main focus is on stability of the flow. There are a number of studies of multi-layer flows without a yield stress. These studies are in both planar and axisymmetric geometries, but since the usual instability is interfacial the base flow is less significant. We review these studies in §1.3.3. Moreover, we have validated our computational study on stability of the visco-plastic lubrication using the available results in the context of miscible Newtonian multi-fluid flows. The related literature is reviewed in §1.3.4.

Finally, there are numerous effects related to visco-elasticity. We try to summarise only those that appear to us most relevant in §1.3.5 - §1.3.7 .

1.3.1 Visco-plastic fluids and shear flow stability

The first study of linear stability of a visco-plastic fluid flow is given by [27], who studied the linear stability of Bingham fluid in plane channel Poiseuille flow. They considered odd and even perturbation separately, and found marginal stability curves that approached the Newtonian limit as the yield stress vanished. However, treatment of odd and even perturbation has been questioned by [89] who implemented the correct conditions at the yield surface and found no unstable modes. Three-dimensional linear instabilities have been studied in [88] and transient growth phenomena in [89]. A key feature of the linear stability studies is that the plug region remains unyielded for linear perturbations. This fact can lead to interesting mathematical anomalies. For example, [77] consider the distinguished asymptotic limit of linear stability with small yield stress (vanishing slower than the linear perturbation). This results in a rigid sheet in the center of a plane channel and is linearly stable. They suggest that the passage to the Newtonian limit of a yield stress fluid is ill-defined insofar as questions of stability are concerned, i.e. based on the linear theory the flow

is believed to be stable for all Re. However, the boundary conditions in the linear theory are derived based on the continued existence of the plug region.

Apart from the linear analysis, fully nonlinear (energy) stability results are derived in [87]. As with the Newtonian fluid energy stability results are very conservative. For yield stress fluids the nonlinearity of the problem is not simply in the inertial terms, but also in the shear stress and in the existence of unyielded plug regions, which are defined in a non-local fashion even for simple flows. This means that the gap between linear and nonlinear theories is much wider than with Newtonian fluids. In Newtonian fluids, this gap is partly filled by weakly nonlinear theories, but in the case of visco-plastic fluid flows, these methods are algebraically complicated. Only [78] have performed this type of analysis, for Rayleigh-Benard-Poiseuille flow and they found that the range of the validity of the amplitude equation was limited. Outside of the domain of shear flows there are only a small number of studies of stability, e.g. [134].

1.3.2 Displacement flow in pipes and channels

Miscible displacement flows have been studied in detail, both experimentally and numerically. In experimental studies large Péclet number (Pe) is common, e.g. [92] study displacements over a range of Péclet, Atwood (At) and Stokes-buoyancy numbers, using a glycerine-water system which only can give Pe in the range $Pe \gtrsim 400$. For the large Pe regime, depending on At, (or viscosity ratio m), quasi-steady viscous fingers may form and propagate with a *sharp* displacement front that is retained over $O(1)$ timescales, or longer. Chen & Meiburg [14] presented a computational investigation in conjunction with the experimental work in [92].

A mix of experimental, computational and asymptotic methods have been used to study this regime, e.g. [5, 66, 69, 70, 71, 72, 95, 105, 131]. Rakotomalala,et al. [95] applied the Lattice Gas Method (BGK) [3] with a viscos-

[3]Lattice Boltzmann methods is a class of computational fluid dynamics methods for fluid

ity mixing rule to study the miscible displacement of two fluids between two parallel plates over a range of Péclet number (Pe) and viscosity ratio. They showed that the interface becomes a well-defined finger at high Pe number and for large viscosity ratio. The fingering pattern is analogous to the Saffman-Taylor [103] finger in potential flows. Asymptotic methods are used in [131] to solve miscible displacements in geometries such as Hele-Shaw cells or long capillary tubes. Yang and Yortsos, [131] showed that the leading order term in the regular expansion satisfies a single integro-differential equation for the concentration of displacing fluid. This equation is solved numerically to investigate the flow behavior over a range of viscosity ratio and Pe number. The authors of [69, 70, 72, 105] studied experimentally the miscible displacements in a vertical planar Hele-Shaw cell in the high Pe regime. They obtained a threshold in both the flow velocity and viscosity ratio beyond which a 3D finger pattern develops. They showed that the experimental threshold is in agreement with analytical result based on a 2D argument similar to [131]. Further experimental studies of miscible displacement in pipe geometry are given in [5, 66, 105].

Considering generalised Newtonian fluids in tubes and between parallel plates, the formal high Pe limit has been considered in the lubrication limit by [1, 4, 113]. The propagation of fingers in fully two-dimensional displacement flows of yield stress fluids is considered both computationally and analytically in [1, 30]. Related experimental studies are those of [31, 32]. It is worth mentioning that of the above studies the vast majority are concerned with finger propagation, efficiency of displacements and residual layers, rather than stability of the flow; see e.g. [39, 40] and [104].

There is also an extensive literature on immiscible displacements, including Newtonian and non-Newtonian effects. The most important early works belong to [16] and [115], who discussed the fractional amount of viscous fluid left behind on the wall of a tube when it is displaced by an inviscid fluid (air),

simulation in which the discrete Boltzmann equation is solved to simulate the flow of fluid.

as a function of capillary number, Ca. These flows are investigated computationally by [97], who showed the results are in a very good agreement with experimental observations. Soares,et al. [109] extended this classical work to flows with finite viscosity ratios. Displacement of visco-plastic fluids by gas has also been studied by various authors. Dimakopoulos and Tsamopoulos, [20] studied computationally the transient displacement of Newtonian and visco-plastic liquids by highly pressurized air in cylindrical tubes of finite length with an expansion followed by a contraction in their cross section. The regularised method with Papanastasiou's formula was considered for Bingham model. They examined the evolution of the free surface, the distribution of the displaced material and velocity and pressure field for a range of the dimensionless parameters such as pressure, Reynolds and Bingham numbers and geometric characteristics. The problem of gas-liquid displacement in capillary tubes has been studied by [18, 110, 116].

1.3.3 Multi-layer viscous shear flow instability

For Newtonian fluids perhaps the earliest study of viscosity stratified shear flow is the classical study of [133]. Yih, [133] found that both plane Poiseulle flow and plane Couette flow can be unstable even at small Re number. Later work includes studies of multi-layer Couette, Poiseuille and Couette-Poiseuille flows of Newtonian fluids, e.g. [43, 49, 132]. A fairly extensive review of this literature is given in [61], which also includes the many contributions of the authors to the study of core annular flows; see also [59]. Broadly speaking, the linear stability of immiscible iso-density flows requires a sufficiently large surface tension and that the lubricating fluid is less viscous. Surface tension stabilises short wavelength interfacial modes and the viscosity ratio tends to stabilise long wavelength instabilities. More recent contributions to this field are [108, 114], who consider a plane channel core-annular flow.

Other than Newtonian fluids, a number of authors have considered the linear stability of multi-layer flows of inelastic non-Newtonian fluids, e.g. power-

law fluids are treated extensively in [63, 111, 121, 122]. Carreau-Yasuda and (regularised) Bingham-like fluids are treated in [93]. In brief, these results are qualitatively similar to those found for Newtonian fluids, i.e. linear interfacial instabilities arise at small-moderate Reynolds numbers. Importantly, these studies do not consider fluids with a yield stress and unyielded plug at the interface. Explanations of the physical mechanisms that govern this type of instability for Newtonian fluids have been offered by [12, 13, 45]. These explanations can be largely extended to purely viscous generalised Newtonian fluids. In simple terms, sufficiently close to the fluid-fluid interface, the non-Newtonian (nonlinear) character of any purely viscous generalised Newtonian fluid is simply not recognised, i.e. the dominant feature at the interface is a discontinuity in a finite constant viscosity between two fluids.

1.3.4 Miscible multi-fluid flows

In the context of miscible multi-fluid flows there is less work on shear instabilities. In the first place, the term *multi-layer* is ill-defined if the fluids can mix completely. Where linear stability studies have been performed the parallel base state is assumed quasi-steady. This assumption and the necessity to specify a closure law relating viscosity to fluid concentration lead to inherent difficulties in establishing the generality of results. Ranganathan and Govindarajan [96, 102] analysed the stability of miscible fluids of different viscosities flowing through a channel in a three-layer Poiseuille configuration. They obtained instabilities at high Schmidt numbers and low Reynolds numbers, resembling those of [133]. In Couette flow it appears that the stability characteristics of the miscible flow are predicted by those of the immiscible flow with zero surface tension; see [25]. However, for core annular flow this is not the case; see [106]. It does appear true that introduction of a diffuse layer of intermediate concentration and rheological properties does serve to stabilise the flow. On the other hand non-monotone variations in rheological properties can lead to shear-type instability, as in the reactive flows studied by [11].

More recently, interest has focused on convective instabilities in miscible multi-layer flows. d'Olce [22] and d'Olce et al. [23] studied experimentally a miscible core annular flow with more viscous fluid adjacent to the wall. On controlling the respective flow rates one can adjust the equilibrium radius of the the interface. As this interfacial position was increased a number of interesting secondary flows were observed, resembling pearls at smaller interfacial radii and mushrooms at larger radii. A similar transition was affected by increasing Re. This flow has been studied more deeply, both experimentally by [24] and computationally/analytically by [107] in an effort to understand the transition between convective instability and absolute instability. In a related vein, Sahu et al. [104] have recently considered the onset of convective instabilities in 3-layer plane channel flows.

1.3.5 Linear stability of shear flow of visco-elastic fluids

There are a number of theoretical studies on stability of single viscoelastic fluid in Couette or Poiseuille flow geometries. Accurate study of the linear stability for Upper Convected Maxwell (UCM) fluid in plane Poiseulle flow dates back to the work of [46], who show that the flow is linearly stable at low Reynolds number to sinuous or symmetric modes. This study was extended to antisymmetric or varicose modes by [74] who also obtained linear stability results for inertia-less plane Poiseuille flows. However, they reported that unlike the Newtonian fluid the most dangerous modes correspond to anti-symmetric modes. They also indicated that the Maxwell model is stable in plane Couette flow. The absence of unstable eigenvalues for plane Couette flow of Maxwell fluids at high Reynolds number has been verified in [100] using spectral methods.

Linear instability results for plane Poiseuille and Couette flows have been established for other viscoelastic models by several authors, e.g. [8, 9, 129, 130]. Grillet et al. [130] have used transient finite element calculations and

the Chebyshev-tau spectral method to investigate planar shear flows of PTT (Phan-Thien-Tanner) and Giesekus fluids. Their results show the existence of unstable modes for both plane Poiseuille and Couette flows of a PTT fluid. The Giesekus model was found to be stable for Couette flow but unstable in pressure driven flows. The mechanisms were investigated using the linearized energy equation in [35] and [57]. The results indicate that the instability mechanism is associated with coupling between the base state stresses and the perturbation velocity gradients.

1.3.6 Nonlinear stability of single visco-elastic fluid

There is less work in the context of nonlinear stability. Atalik and Keuninngs [2] have investigated the nonlinear stability of plane channel flows for Giesekus, Oldroyd-B and UCM models using a fully-spectral Galerkin method. The temporal evolution of 2D, finite amplitude perturbations at high and low Re is considered and the results show the development of finite amplitude waves for Poiseuille flow. In the case of Couette flow the finite amplitude disturbances decay in an oscillatory fashion over the considered parameter range. Sarloos and coworkers [79, 80, 83] studied the weakly nonlinear stability of Poiseuille flow of a UCM fluid in channel and pipe geometries. They derived an amplitude equation and obtained the critical amplitude beyond which the flow is nonlinearly unstable. Similar to [2], they have found subcritical instabilities.

Lozinski and Owen [90] obtained an energy estimate for the flow of Oldroyd B fluid in a bounded domain. They have integrated the trace of the stress tensor over the flow domain as a form of elastic energy. Two barriers to generalizing the energy stability method to Oldroyd B fluids in a self-consistent way have been raised in [21]. The first is due to the impossibility of defining a norm on the stress space, which is a space of symmetric positive-definite tensors. The second difficulty is related to non-normality of the operator describing the time evolution of infinitesimal disturbances of an Oldroyd-B fluid, which may cause the transient growth of disturbances at low Reynolds num-

ber. Further interesting studies in the context of transient growth phenomena are [67, 99, 112]. Recently, Kumar and coworkers [47, 48, 62] analysed the ensemble-averaged kinetic energy density of the linearized momentum equation for plane Couette and Poiseuille flows of Oldroyd-B fluids. They obtained monotonic decay of their energy density by controlling both Reynolds and Weissenberg numbers to be small.

1.3.7 Theoretical and experimental studies on multi-layer visco-elastic fluid

Moving now to multi-layer flows of visco-elastic fluids, the main focus is on the linear stability of the flow, see e.g. [15, 33, 34, 44, 101, 129]. Generally, the results indicate that elastic stratification (jump in the normal stresses) can produce linear interfacial instabilities even in the absence of any viscosity or density mismatch. In the long wave limit the perturbations affect the entire domain and the flow becomes stable when the more elastic fluid is the major component of the flow. However in the short wave limit, the disturbances decay exponentially fast away from the interface and the instability mechanism is local in nature. The physical mechanism of instability is explained in [33, 35, 44]. Recently, Miller & Rallison [81, 82] considered the relaxation length-scale which is a measure of the distance that a typical particle travels during a relaxation time. They explored linear stability in two parametric regimes. In the first regime, the wavelength is long compared to the channel width but short compare to the relaxation length scale [82]. In the second regime, the relaxation length scale is the longest length scale, but the interface is close to the center-line [81].

In terms of experimental studies there is less work for interfacial instability of viscoelastic flows. Wilson & Khomami [125, 126, 127] performed a comprehensive series of experiments on two-layer co-extrusion polymer melts in a channel configuration. They studied interfacial instabilities generated by introducing temporally regular disturbances of different amplitude and wave length

at the interface. In [125] the neutral stability was constructed experimentally for an incompatible polymer system of PP/HDPE, with a jump in both elastic and viscous properties along the interface. As with the theoretical results the most dangerous wave number is of order of unity. Qualitative agreement with theory was also found with measurements of the growth rate. Later theoretical studies based on a more realistic model were able to achieve a reasonable quantitative comparison, [34, 35]. In [126] experiments were performed with a similar two fluid system (PP/HDPE), but at temperatures for which the fluids have the same viscosity but different normal stress at the interface. In this way they verified experimentally the existence of purely elastic instabilities. In [127] a compatible polymer system of LLDPE/HDPE was used. A later study [128] used a modified apparatus with a converging-diverging channel instead of a parallel channel; similar experiments to [125] were performed. Their results showed stabilizing and destabilizing effects in converging and diverging sections, respectively. According to [127] this can be explained by an analysis similar to [44]. In the diverging channel, as it follows the converging section, the destabilizing mechanism was partly due to the release of elastic energy stored in converging part. In the context of experimental work, we should also mention the studies [119, 120] on stability of two layer co-extrusion flow. They find that long wave asymptotic analysis gives a good prediction of the occurrence of instabilities, but do find some instabilities in flows predicted to be stable. Finally, in [64] interfacial instability is investigated in three-layer symmetric and asymmetric pressure-driven channel flow of polymeric melts. Interfacial instability in multi-layer viscous flows often leads to encapsulation, which happens due to the tendency for the more viscous fluid to migrate into the less viscous one, irrespective of the stability of the interface. There have also been a limited number of experimental studies of encapsulation in the context of viscoelastic flows e.g. [41, 42, 64, 65, 73, 125].

1.4 Outline of the thesis

The axisymmetric core-annular geometry is studied computationally in Chapter 2 for the simplest rheological pair of fluids (a Bingham lubricating fluid and Newtonian core fluid). The simulations include an inlet geometry in the computational model and study the development of the multi-layer flow, both as the fluids are initially injected (start up) and later the established steady flows (development lengths). We have also studied the Nonlinear stability, considering temporal stability of a periodic cell of established parallel flow.

In chapter 3 visco-plastic lubrication flows are investigated computationally in a plane channel configuration. This geometry allows for symmetry breaking while retaining the advantages of 2D computation. In addition to start-up and stability of the flows, a number of different effects are explored using this geometry. These include the ability to control the downstream flow via changing the inlet positioning and flow rate with time, different ways of establishing the steady parallel flows, multi-layer flows with up to 7 layers.

Chapter 4 serves to extend the breadth of experimental observations of visco-plastic lubrication flows by considering viscoelastic core fluids. Our study has two principal objectives. Firstly, we demonstrate the experimental feasibility of this type of flow in a laboratory environment. Secondly, we study how viscoelasticity might affect design of the inlet geometry, e.g. the effects of downstream contraction and expansion.

In chapter 5 nonlinear stability via the Reynolds-Orr equation has been studied for visco-plastic lubrication of visco-elastic fluid along an infinite pipe. The core fluid is an Oldroyd-B fluid and the outer fluid is a Bingham fluid. We show that, when the maximal shear stress and elastic stress perturbations are bounded, a suitable energy functional will decay exponentially for sufficiently small Reynolds and Weissenberg numbers.

Chapter 6 of the thesis contains a summary of the results of the thesis and recommendations for future work.

Chapter 2

Visco-plastically lubricated pipe flows [1]

In this Chapter we study axisymmetric core-annular VPL flows computationally. The simulations include an inlet geometry in the computational model and we study the development of the multi-layer flow, both as the fluids are initially injected (start up) and later when steady flows are established (development lengths). As mentioned in chapter 1, previous studies considered the stability of the established flow both theoretically [26, 85] and experimentally [55]. However, the theoretical approach does not consider how to set the flows up and perhaps a criticism of [55] is that all experiments were in a single geometry with established core fluid radius similar to the inlet. Therefore, one of the motivations for this work is investigating two aspects of the initial part of the core annular flow. First, is it possible to establish the base multi-layer flows at all, i.e. from a practically realizable initial flow configuration. Secondly, having established a base flow, what factors affect the entry or development length of the flow. Whilst the latter problem could be studied via a steady flow computation, we have studied both questions via a transient flow computation.

The fact that the start-up flows become steady implies some kind of convective stability. Nonlinear temporal stability to axisymmetric perturbations is also studied . Our aim is to understand structural aspects of the flow stability,

[1] A version of Chapter 2 has been published. [S. Hormozi], K. Wielage-Burchard and I.A. Frigaard. (2011) Entry, start up and stability effects in visco-plastically lubricated pipe flows. Journal of Fluid Mechanics. **673**, 432-467, [52].

not easily extracted from the energy stability results of [85].

An outline of this chapter is as follows. Section 2.1 introduces the physical model of the flows that we study and also outlines the numerical method and various computational studies used to validate the code. Section 2.2 presents the results of our study of start-up flows and development lengths. Nonlinear temporal stability is studied in §2.3 and the chapter ends with a brief discussion (§2.4).

2.1 A multi-layer flow model

An axisymmetric pipe flow is considered throughout this chapter. The pipe has outer radius $\hat{R}$ and is initially filled with Bingham fluid (fluid 2). The pipe is vertically oriented and we use axisymmetric cylindrical coordinates with $\hat{z}$ pointing upwards along the pipe axis. For time $\hat{t} > 0$ a Newtonian fluid (fluid 1) is injected upwards through a concentrically positioned inner pipe of radius $\hat{R}_i < \hat{R}$, while at the same time the Bingham fluid is pumped through the annular space surrounding this pipe, (see Fig. 2.1a). The Bingham fluid thus acts as lubricating layer for the Newtonian core fluid. For the stability studies later (§2.3) we consider an axially periodic section of uniform pipe downstream of the inlet.

Although the setting described is general, we consider flow parameters that correspond approximately to those that we can achieve experimentally in our lab. As a guide, we consider radii $0.005\text{m} \lesssim \hat{R} \lesssim 0.1\text{m}$, mean velocities $0.001\text{m/s} \lesssim \hat{U}_0 \lesssim 1\text{m/s}$, and suppose that the fluids consist of miscible aqueous solutions of equal density, $\hat{\rho}$. The choice of a Bingham fluid as the lubricant is a simplification of a typical yield stress rheology (which is often shear-thinning) and the Newtonian core is also primarily for simplicity.

Fluid 1 has Newtonian viscosity $\hat{\mu}^{[1]}$ and fluid 2 is characterised by its yield stress $\hat{\tau}^{[2]}_{yield}$ and plastic viscosity $\hat{\mu}^{[2]}$. The total flow rate along the pipe is $\hat{Q}$, which defines the mean axial velocity: $\hat{U}_0 = \hat{Q}/\pi\hat{R}^2$. The pressure is

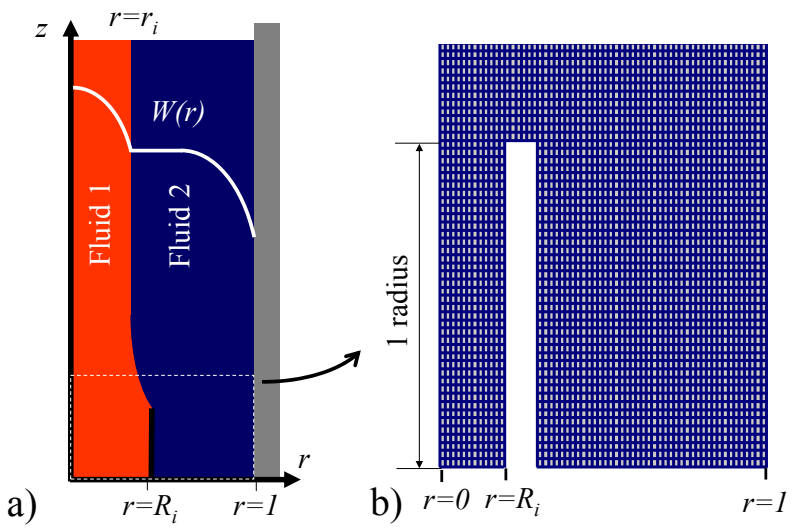

Figure 2.1: a) Schematic of the dimensionless flow geometry in an axisymmetric pipe; b) example computational mesh close to the inlet region for $R_i = 0.2$.

denoted by $\hat{p}(\hat{\boldsymbol{x}}, \hat{t})$, $\hat{\boldsymbol{u}}(\hat{\boldsymbol{x}}, \hat{t})$ is the velocity, $\hat{\tau_{ij}}^{[k]}$ denotes the deviatoric stress tensor in fluid k, and $\hat{g}$ is the gravitational acceleration. We model the change between (pure) fluids 1 and 2 via a scalar concentration C, representing the concentration of fluid 2. The Navier-Stokes equations are made dimensionless with the following scaling:

$$\boldsymbol{x} = \frac{\hat{\boldsymbol{x}}}{\hat{R}}, \quad t = \frac{\hat{t}\hat{U}_0}{\hat{R}}, \quad \boldsymbol{u} = \frac{\hat{\boldsymbol{u}}}{\hat{U}_0}, \quad p = \frac{\hat{p} + \hat{\rho}\hat{g}\hat{z}}{\hat{\rho}\hat{U}_0^2}, \quad \tau_{ij} = \frac{\hat{\tau}_{ij}\hat{R}}{\hat{\mu}^{[2]}\hat{U}_0}. \tag{2.1}$$

The dimensionless model considered is as follows:

$$\frac{\partial u_i}{\partial t} + u_j \frac{\partial u_i}{\partial x_j} = -\frac{\partial p}{\partial x_i} + \frac{1}{Re}\frac{\partial \tau_{ij}}{\partial x_j}, \tag{2.2}$$

$$\frac{\partial C}{\partial t} + u_j \frac{\partial C}{\partial x_j} = \frac{1}{Pe}\frac{\partial^2 C}{\partial x_j^2}, \tag{2.3}$$

$$0 = \frac{\partial u_i}{\partial x_i}. \tag{2.4}$$

Constitutive laws for the two pure fluids are:

$$\tau_{ij}^{[1]} = m\dot{\gamma}_{ij}, \tag{2.5}$$

$$\dot{\gamma}(\boldsymbol{u}) = 0 \iff \tau^{[2]}(\boldsymbol{u}) \leq B, \tag{2.6}$$

$$\tau_{ij}^{[2]}(\boldsymbol{u}) = \left[1 + \frac{B}{\dot{\gamma}(\boldsymbol{u})}\right] \dot{\gamma}_{ij}(\boldsymbol{u}) \iff \tau^{[2]}(\boldsymbol{u}) > B. \tag{2.7}$$

where

$$\dot{\gamma}_{ij} = \frac{\partial u_i}{\partial x_j} + \frac{\partial u_j}{\partial x_i},$$

$$\dot{\gamma}(\boldsymbol{u}) = \left[\frac{1}{2}\sum_{i,j=1}^{3} [\dot{\gamma}_{ij}(\boldsymbol{u})]^2\right]^{1/2} \qquad \tau^{[2]}(\boldsymbol{u}) = \left[\frac{1}{2}\sum_{i,j=1}^{3} [\tau_{ij}^{[2]}(\boldsymbol{u})]^2\right]^{1/2}. \tag{2.8}$$

Note that in dealing with mixtures, we will use constitutive laws that are interpolated from the pure fluid constitutive laws; see (2.15) and (2.16). The dimensionless model has 3 principal dimensionless groups, defined by:

$$m = \frac{\hat{\mu}^{[1]}}{\hat{\mu}^{[2]}}, \qquad Re = \frac{\hat{\rho}\hat{R}\hat{U}_0}{\hat{\mu}^{[2]}}, \qquad B = \frac{\hat{\tau}_{yield}^{[2]}\hat{R}}{\hat{U}_0\hat{\mu}^{[2]}}. \tag{2.9}$$

These are the viscosity ratio, Reynolds number and Bingham number, respectively. The Bingham number denotes the ratio of the yield stress of the fluid to a typical viscous stress of the flow. The Reynolds number has been based on fluid 2 properties. The relevant Reynolds number for fluid 1 is Re/m. Note that we also have 2 geometric groups: $R_i = \hat{R}_i/\hat{R}$, the inlet radius ratio, and r_i which is the radial position of the interface in a parallel multi-layer flow. This latter is governed by the relative distribution of the total flow rate between the two fluids, as we shall discuss below in §2.1.1. A final dimensionless group is the Péclet number, $Pe = \hat{R}\hat{U}_0/\hat{D}_m$, with $\hat{D}_m$ the molecular diffusivity. Typically we have $Pe \sim 10^6 - 10^{10}$, for which values the concentration is effectively advected with the flow. The Péclet number is discussed further in §2.1.3.

In considering a start-up flow (Fig. 2.1a) we impose uniform axial velocity

and concentrations (0 or 1) at the inlets at the base of the pipe. The mean axial velocity that we impose is determined by solving the problem for *base flow*, which is the parallel flow that we are trying to achieve in the downstream region; see §2.1.1 following. No slip conditions are imposed at the solid walls, with no flux for the concentration. Outflow conditions are imposed at the exit of the pipe.

2.1.1 Basic flows, $Pe \to \infty$

In the limit $Pe \to \infty$, we recover a model of 2 immiscible fluids without surface tension. Following [85], there are three distinct types of base velocity profile, $\boldsymbol{u} = (0, W(r))$, for which a Newtonian core fluid is surrounded by a Bingham fluid. The inner core fluid always assumes a characteristic parabolic velocity profile, but the velocity profile in fluid 2 depends on the fraction of the outer layer that is yielded. The case of primary interest here is that for which the inner core is surrounded by a ring of unyielded fluid. With interface at $r = r_i$ and yield surface position $r = r_y$, these flows have $r_i < r_y < 1$ and velocity profile

$$W(r) = \begin{cases} \dfrac{B}{2r_y}\left[\dfrac{1}{m}(r_i^2 - r^2) + (1 - r_y)^2\right] & 0 \le r \le r_i, \\ \dfrac{B}{2r_y}(1 - r_y)^2 & r_i < r \le r_y, \\ \dfrac{B}{2r_y}\left[(1 - r_y)^2 - (r - r_y)^2\right] & r_y < r \le 1. \end{cases} \tag{2.10}$$

The yield surface position r_y depends only on r_i, B and m. It is computed from the constraint that the mean velocity, averaged over both inner and outer fluid layers, is equal to 1. After some algebra, $r_y \in (r_i, 1)$ is found as the root of the following quartic equation:

$$0 = (r_y)^4 - 4r_y\left(1 + \frac{3}{B}\right) + 3\left(1 + \frac{r_i^4}{m}\right). \tag{2.11}$$

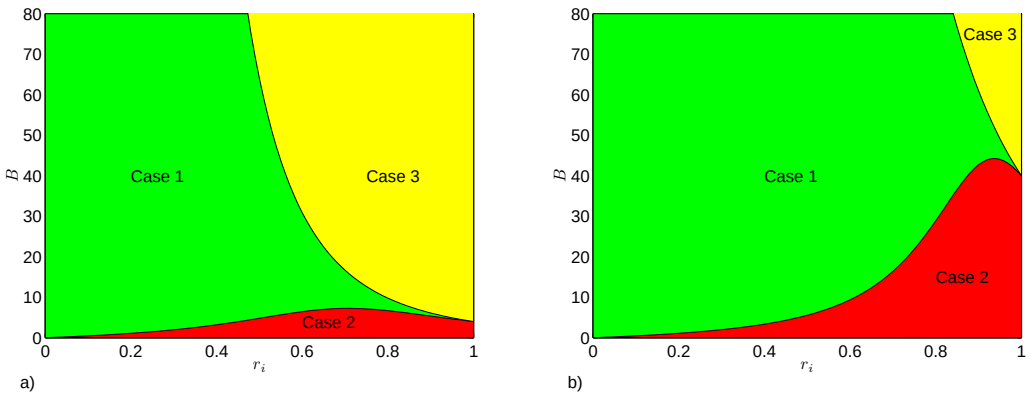

Figure 2.2: Parameter domains where the base solutions are found in (r_i, B, m)-space: a) $m = 1$; b) $m = 10$.

Following [85] this solution is denoted as *case 1* solution. As r_i, B and m are varied the other 2 solution types are found: a *case 2* solution, for which the outer fluid is entirely yielded, and a *case 3* solution for which the outer fluid is entirely unyielded and stationary. These solutions are described further in [85]. It is only the case 1 solutions that allow stable visco-plastically lubricated flows. In the 3-dimensional (r_i, B, m)-parameter space the boundary between case 2 and case 1 solutions is given by:

$$B < \frac{12 r_i}{r_i^4 \left(\frac{3}{m} + 1 \right) - 4 r_i + 3}, \tag{2.12}$$

(with case 1 solutions found when this inequality is not satisfied). The boundary between case 3 and case 1 solutions is given by:

$$B > \frac{4m}{r_i^4}. \tag{2.13}$$

(again case 1 solutions are found when this inequality is not satisfied). Figure 2.2 illustrates the domain in which case 1 solutions are found for 2 different viscosity ratios, m.

Returning to the dimensional parameters of the problem, we recall that for a typical hydraulic flow one can specify either the flow rate or the pressure drop, but not both. The analogy for the multi-layer flows studied is that if one specifies the flow rates of the individual fluid phases, then it can be shown that the pressure drop and the radial interface position are uniquely determined. Conversely (and perhaps more obviously) specifying the pressure drop and radial interface position uniquely determines (the velocity and) the flow rates in the individual fluid phases.

2.1.2 Computational solution

The model equations (2.2)-(2.8) have been discretised using a mixed finite element/finite volume method. The Navier-Stokes equations are solved using the Galerkin finite element method. The computations are carried out on a structured rectangular mesh, with linear elements (Q1) for the velocity and constant elements (P0) for the pressure discretisation. The divergence-free condition is enforced by an augmented Lagrangian technique; see [38]. Although we could use a higher order discretisation we have not done so. Since, we are cautious to impose more regularity on the discrete solution than may exist for the solution to the exact Bingham fluid model. The solution of Bingham fluid flow problems are not twice differentiable and may have yield surfaces that have singular points. Hence, it is not always good to use a smoother approximation than the solution we are trying to compute. A potential disadvantage of our choice of elements is that the inf-sup condition is generally not satisfied by this discretisation. Velocity errors are usually independent of the discrete inf-sup condition; see [10]. The augmented Lagrangian approach for the divergence free condition induces L^2-stability (dependent on the penalty parameter) for the pressure, making the discretisation less sensitive to effects of spurious pressure modes. We have not observed any evidence of spurious modes or numerical instability in any of our computations. These aspects are discussed in more detail in [10, 94].

There are two sources of nonlinearity in the Navier-Stokes equations: the convective terms and the shear stress terms (in the case of the Bingham fluid). Regarding the Bingham fluid, note that the effective viscosity becomes infinite in unyielded regions of the flow, although stress and strain rate tensors remain finite. Two methods are popular for dealing with this. Either one regularises the effective viscosity functional to remove the singular behavior; see e.g. [6, 29, 36, 91]. This system can then be solved iteratively as a flow problem with a nonlinear viscosity. Alternatively, one solves the equations using a relaxation-multiplier approach such as the augmented Lagrangian method; e.g. [36, 37, 38]. The regularisation approach replaces the unyielded region with a region of small strain rate and high viscosity. The augmented Lagrangian method gives zero strain rate in such regions. We implemented both strategies in the code development stage. As regularisation method we have followed [6], replacing (2.6) & (2.7) with

$$\tau_{ij}^{[2]}(\boldsymbol{u}) \;=\; \left[1 + \frac{B}{[\dot{\gamma}^2(\boldsymbol{u}) + \epsilon^2]^{1/2}}\right] \dot{\gamma}_{ij}(\boldsymbol{u}), \tag{2.14}$$

where we take the regularisation parameter $\epsilon = 10^{-4}$, (see below). Except in cases when the unyielded plug is very thin we see only minor differences in our results between methods[2]. For this particular flow it seems that the numerical limit on the unyielded plug thickness is more related to the mesh resolution than to the method used to resolve the stress. The regularisation method gives faster computations than the augmented Lagrangian method, (if one discounts the time spent in establishing an acceptable ϵ), and this has been the main reason for our usage. All results presented in this chapter use regularisation method. However, comparison of viscosity regularisation and augmented Lagrangian method is given in §3.2.1 for VPL flows in channel geometry.

We use a fixed timestep for the Navier-Stokes equations, advancing from

[2]The reader is referred to [29] for more discussion on the use of regularisation method.

timestep N to $N+1$. Regarding the implementation of the nonlinear terms, we use a semi-implicit method. The convective velocity is approximated at time step N while the linear spatial derivatives of the velocity are approximated implicitly at time step $N+1$. The effective viscosity is approximated at time step N^* with the strain rate components at step $N+1$. A Picard iteration is then used within each time step to successively update the variables at step N^*, so that the shear stress discretisation becomes successively closer to being fully implicit. The pressure is approximated at time step $N+1$.

The concentration equation (2.3) is solved via a finite volume method, in which the concentration is approximated at the center of each regular mesh cell. The advective terms are dealt with via a MUSCL scheme (**M**onotone **U**pstream-centred **S**cheme for **C**onservation **L**aws). These are essentially slope-limiter methods for reducing oscillations close to discontinuities; see e.g. [75, 123] for more description. On each (Navier-Stokes) timestep a splitting method is used to advance the concentration equation over a number of smaller sub-timesteps. This time advance is explicit and a CFL condition is implemented for the sub-timesteps to ensure numerical stability.

The numerical algorithm is implemented in C++ as an application of PELICANS.[3] Although the equations could have been implemented in a commercial CFD code, these codes are often over-stabilised and give little access to the detailed implementation. We used 60 elements across the pipe and 40 elements per unit length along the pipe, which is of dimensionless length L. The length is adjusted according to the physical situation we model and for longer geometries we preserve the mesh density. The inflow section of a typical mesh is shown in Fig. 2.1b. Figure 2.3a-c shows the difference between the analytic solution and the computed solution at the exit, for various mesh sizes and

[3]PELICANS is an object oriented platform developed at IRSN, France, to provide a general framework of software components for the implementation of partial differential equation solvers. PELICANS is distributed under the CeCILL license agreement (*http://www.cecill.info/licences/Licence_CeCILL_V2-en.html*). PELICANS can be downloaded from *https://gforge.irsn.fr/gf/project/pelicans/*.

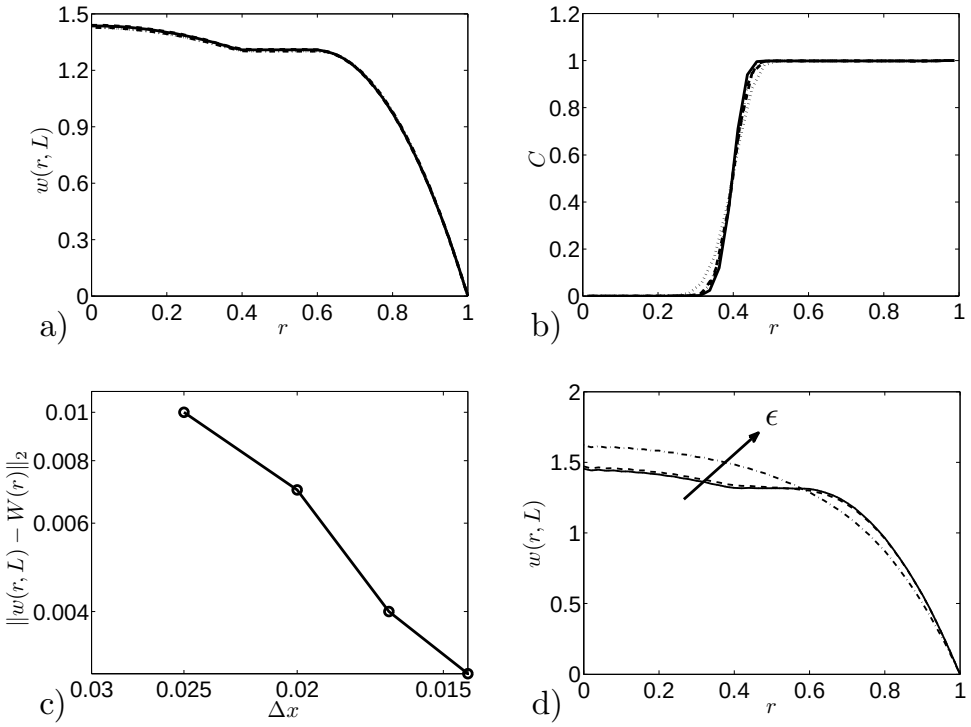

Figure 2.3: Effect of mesh size on: a) exit velocity profile; b) exit concentration profile; c) L^2 norm of difference between exit velocity W and analytic velocity W_a. Flow parameters are: $m = 10$, $Re = 5$, $B = 10$, $r_i = 0.4$ and $R_i = 0.2$. In each figure, line styles (:), (−.), (−−), and (−) correspond to $\Delta r = 0.025$, $\Delta r = 0.02$, $\Delta r = 0.017$ and $\Delta r = 0.014$ respectively; Δr is the radial mesh size. d) Effect of regularisation parameter ϵ on computed exit velocity profile W: $\epsilon = 1,\ 0.1,\ 0.0001$.

fairly typical parameters. It can be seen that the velocity is well represented at this mesh resolution and the concentration field also, except at the interface where the jump in concentration is smeared over a few cells. Refinement does reduce the thickness of the diffuse layer, but this effect of numerical diffusion is always present.

For the same parameters as Fig. 2.3a-c, we show in Fig. 2.3d and in Fig. 2.4 the effects of varying the regularisation parameter ϵ. For $\epsilon = 1$ this is effectively just a shear-thinning fluid, but we observe that even for $\epsilon = 0.1$ the exit velocity

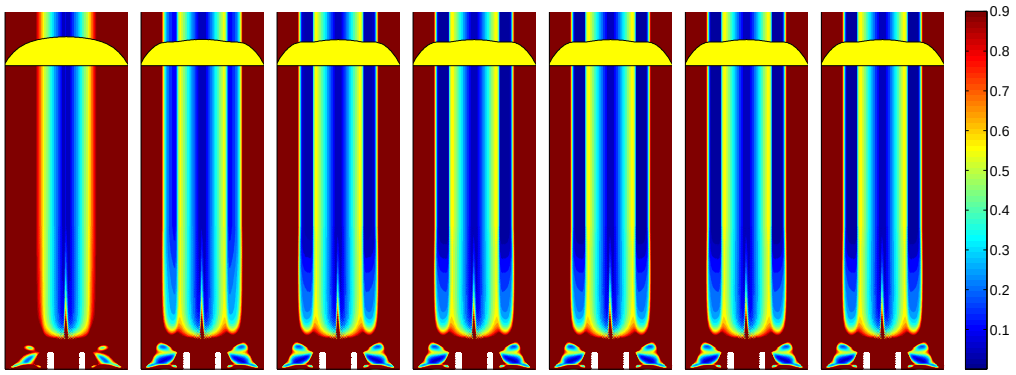

Figure 2.4: Effects of regularization parameter ϵ on computed strain rate: $\epsilon = 1,\ 0.1,\ 0.01,\ 0.001,\ 0.0001,\ 0.00001,\ 0.000001$, (left to right). Flow parameters are: $m = 10$, $Re = 5$, $B = 10$, $r_i = 0.4$ and $R_i = 0.2$.

and strain rate profiles are converging. Our choice of $\epsilon = 0.0001$ is similar to that made by other authors.

It is worth commenting that we have not observed any physically spurious instabilities while using the regularisation method. In hydrodynamic stability studies these instabilities can arise firstly at the interface (which formally is simply *very viscous*), and secondly close to the yield surface where a discontinuity in the second derivative of the velocity is smoothed; see [29]. Although such instabilities are theoretically possible, they occur in parts of the flow that are *very viscous* (of order B/ϵ) and hence grow very slowly. Thus, even if these additional modes were present in our computations they would probably not be observable on the timescale of our computations.

2.1.3 Code validation

In order to validate the code implementation a number of steps have been taken. Firstly, various 1D single fluid benchmark flows were computed, e.g. pipe and plane Poiseuille flow. Secondly, for the start-up/development flow simulations we are able to compute analytically the fully developed base flow (as described in §2.1.1) which can be compared with the velocity profile at the

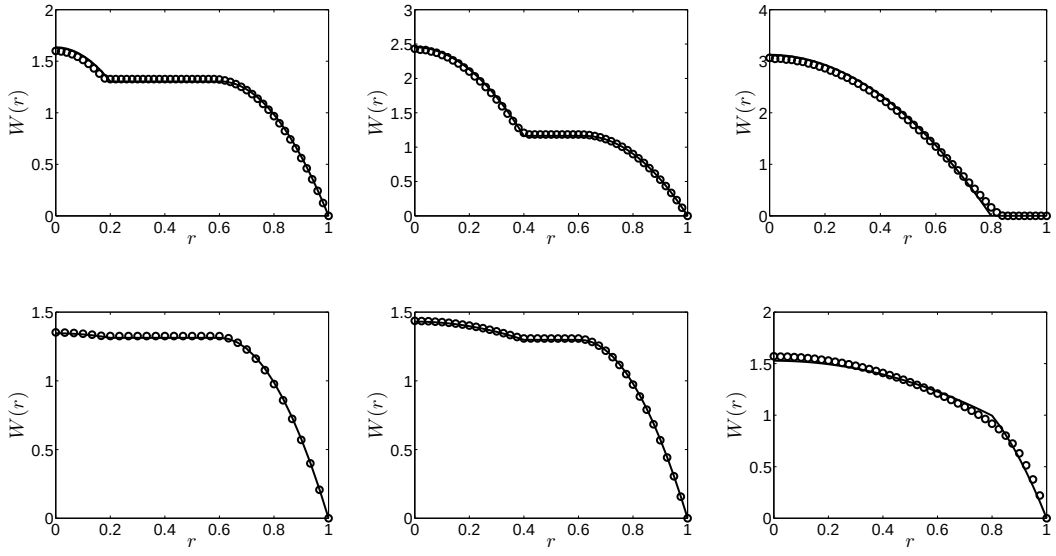

Figure 2.5: Comparison of computed exit axial velocities with the analytic base flow $W(r)$ for $R_i = 0.2$, $Re = 5$, $B = 10$: a) (first row) $m = 1$ and from left to right, $r_i = 0.2,\ 0.4,\ 0.8$; b) (second row) $m = 10$ and from left to right, $r_i = 0.2,\ 0.4,\ 0.8$. In each figure the solid line shows the analytic solution and the circle symbols indicate the computed exit axial velocity.

exit. An example of such a comparison is shown in Fig. 2.5. For the range of r_i selected, some of the base flows are of case 1, whereas others are case 2 and case 3. In general we observe that the comparison between the analytical base flow and computed exit profiles is reasonable. However as we shall see later, there is a small amount of numerical diffusion/dispersion at the interface which leads to some error. For the computations of Fig. 2.5 we have selected $R_i = 0.2$, so that the core fluid expands radially outwards as the developed flow is attained. We shall see later that such flows tend to have the most significant numerical diffusion/dispersion, so effectively we are presenting a worst case scenario. The diffuse interfacial region is also larger when there is strong shear at the interface.

Diffusive effects

In view of the large magnitude of Péclet numbers, we may expect that physical (molecular) diffusion is not significant for the flows we consider. Mixing due to molecular effects only becomes significant on the radial length-scale for long pipes, defined in the dimensionless parameters by $L \sim Pe$, which is the Taylor dispersion regime. Here we are restricted to more practical lengths, $L \lesssim O(10^2)$, and since $L \ll Pe$ we eliminate the diffusive terms from the concentration equation (2.3), by setting $Pe = \infty$ later in this chapter.

Although we may eliminate molecular diffusion easily numerical diffusion still remains. These effects are reduced by method such as a MUSCL scheme, but are not eliminated. As a practical matter, this means that intermediate concentrations $C \in (0, 1)$, are computed during solution of (2.3) in interfacial regions. For such concentrations we interpolate the constitutive laws of the 2 fluids, resulting in:

$$\tau_{ij} = \left([C + m(1 - C)] + \frac{BC}{\dot{\gamma}} \right) \dot{\gamma}_{ij} \quad \Longleftrightarrow \tau > BC, \tag{2.15}$$

$$\dot{\gamma}_{ij} = 0, \quad \Longleftrightarrow \tau \leq BC, \tag{2.16}$$

and use the pure fluid rheologies for concentrations outside of $(0, 1)$.

To quantify the effects of numerical diffusion in our code we have performed a sequence of studies at increasing $Pe = 10^2, 10^3, ..., 10^7$. We fix $R_i = 0.2$, $r_i = 0.4$, $Re = 40$, $B = 10$ and examine the exit velocity and concentration profiles for a channel of length $L = 50$. The results are shown in Fig. 2.6. The base flow for these parameters is a case 1 flow with significant plug region.

The smallest value of Pe ($Pe = 10^2$) is of the same order as L and Re. For this value, molecular and viscous diffusion are equally significant and the length of pipe is sufficient to allow significant diffusive mixing. We observe that over the length of the pipe the two fluids mix completely (see Fig. 2.6b), giving a mean concentration $\bar{C} \approx 0.7$. Note that the mixture has a Bingham number equal to $B\bar{C}$ and therefore an unyielded plug region is found in the

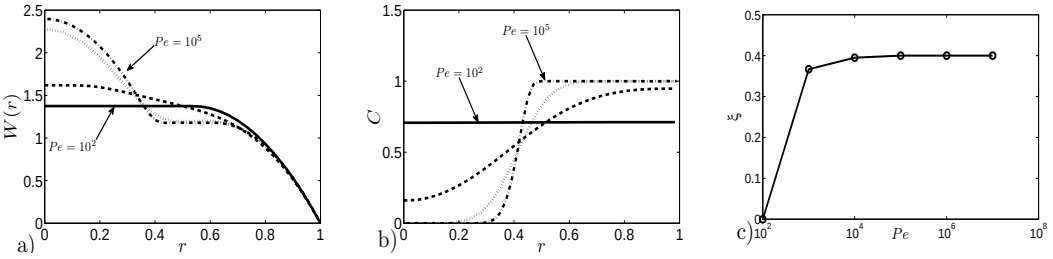

Figure 2.6: Effects of Péclet number on: a) exit velocity profile; b) exit concentration profile; c) numerically defined interface radius ξ. Flow parameters are: $m = 1$, $Re = 40$, $B = 10$, $r_i = 0.4$ and $R_i = 0.2$.

center of the pipe (see Fig. 2.6a).

As Pe is increased the degree of mixing decreases and the interfacial layer becomes progressively less diffuse. For $Pe \geq 10^5$ we find that the profiles are indistinguishable from one another. The diffusion is now dominated by numerical effects and unaffected by Pe. The diffuse region occupies a thickness that is determined by the mesh discretisation, corresponding roughly to 2-3 cells. To give a quantitative measure of the interface radius we define

$$f(C) = \begin{cases} 0 & \text{if} \quad C > \frac{1}{2} \\ 1 & \text{if} \quad C \leq \frac{1}{2} \end{cases}$$

and then integrate to find a numerically defined interface radius, ξ:

$$\xi = \int f(C) dr. \tag{2.17}$$

The final figure in Fig. 2.6 shows the variation of ξ with Pe, converging approximately to $r_i = 0.4$. The numerical interface position is evidently sensitive to the mesh refinement, even as $Pe \to \infty$. Although we could further refine our mesh to reduce numerical effects and perhaps then include physical diffusion via a finite Péclet number, a mesh size of order $Pe^{-1/2}$ would be required

and this quickly becomes prohibitive in terms of computational times required, especially for larger Pe ranges.

Although the interpolation (2.15) & (2.16) is simplistic and imposing $Pe = \infty$ is also partly for simplicity, it is worth noting that providing a more physically realistic model is not easy. In modeling miscible Newtonian flows polynomial splines, exponential and power-law interpolations have all been used as different examples of viscosity closure laws: e.g. [104, 106, 131], but there is evidently no universal closure. All that can be done to establish the robustness of results is to benchmark different closure models over a reasonable range of flows. In preliminary computations we have tested the exponential interpolation of [106] and the power law interpolation of [131], finding little noticeable difference in results. Secondly, if we were to model the molecular diffusivity it would not be constant in the yield stress fluid. Indeed if we accept the idealisation of the Bingham model as a rigid solid when unyielded, then the molecular diffusivity will certainly be drastically reduced in these regions (according to the specifics of the gel structure) so that $Pe = \infty$ may not be a poor approximation.

Pearls and mushrooms

While comparisons such as Fig. 2.5 illustrate that our code is able to simulate the development of stable established base flows, in the second part of this chapter we wish to study evolution of transient imposed perturbations. In order to demonstrate that more complex transient flow structures can also be simulated, we have conducted a number of comparative computations in order to simulate the recent experimental results of [22, 23]. In these experiments two iso-density miscible Newtonian fluids with different viscosities were pumped concentrically into a pipe. The ratio of outer to inner fluid viscosity was 25 and a range of different relative flow rates were tested, producing beautiful "pearl" and "mushroom" shaped patterns.

In the context of our model problem, we have $m = 1/25$, $B = 0$ and a range

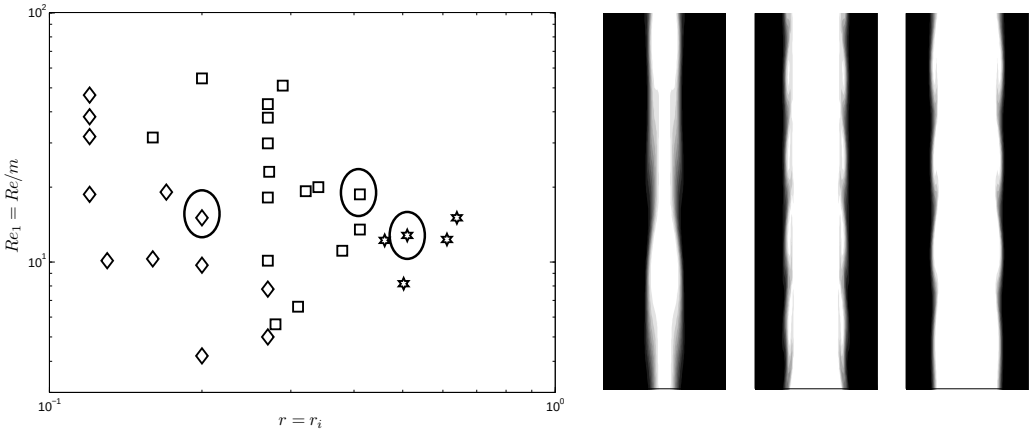

Figure 2.7: Pearl and mushroom patterns computed in $(Re_1, r) = (mRe, r_i)$ space. Left: $\star$ indicates observed mushroom-like flows without any flow perturbation; $\diamond$ and $\square$ indicate pearl-like and mushroom-like flows respectively, observed with a small flow perturbation. The right-hand panels illustrate the flow parameters circled (left to right): (i) pearl-like pattern for $r_i = 0.2, Re_1 = 15$; (ii) mushroom-like pattern for $r_i = 0.411, Re_1 = 18.7$; (iii) mushroom-like pattern for $r_i = 0.51, Re_1 = 12.8$.

of different r_i, according to the different relative flow rates. Since there is no yield stress all base flows are case 3, but equally since there is no unyielded plug, the interface can deform and mix. The experimental regime studied by [22, 23] considers relatively moderate Re and the authors estimate their Péclet number in the range 2×10^4 - 6×10^5, so that although the fluids are miscible, purely diffusive effects are minimal. In Figs. 2.7 and 2.8, we present our numerical simulation results for a wide range of the parameters explored experimentally in [23]. For these figures only, the Reynolds number Re_1 is the fluid 1 Reynolds number, as used by d'Olce and co-investigators (i.e. Re/m in terms of our parameters). The parameter r in [23] is equivalent to r_i used here.

The first observation, by comparison with [23] is that we are able to get qualitatively and quantitatively similar instability patterns using our numerical code. We note that quantitative comparisons beyond comparing the radial

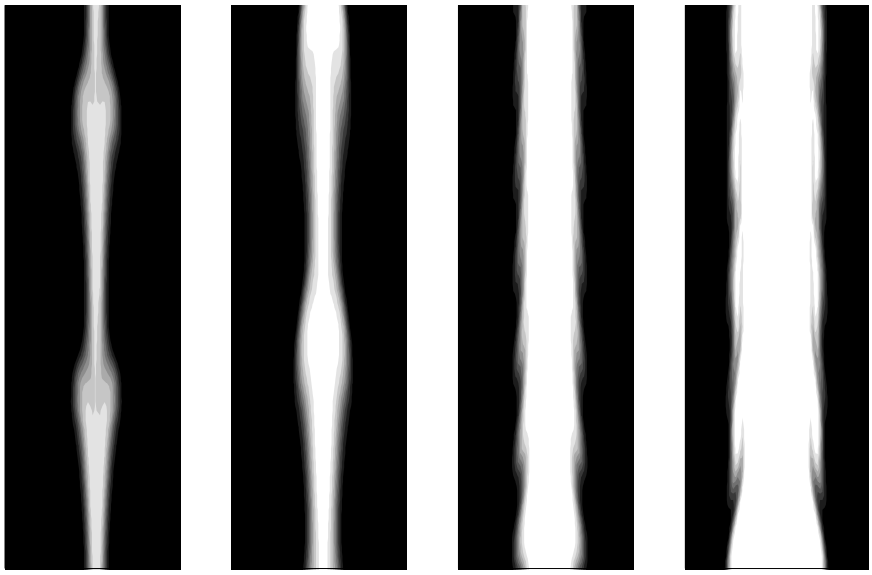

Figure 2.8: Illustration of the pearl to mushroom transition as r_i is increased, for $Re_1 = 19$: a) $r_i = 0.12$; b) $r_i = 0.17$; c) $r_i = 0.27$; d) $r_i = 0.411$.

perturbations of the diffusive interface are difficult: the figures presented in [23] are images (from which a *concentration* might be inferred), whereas the results shown here represent a quantitatively computed concentration, displayed in grayscale for comparison purposes. Nevertheless, it is clear that our numerical simulation can capture the same flow features as those observed experimentally in representative multi-layer flows.

The left panel of Fig. 2.7 illustrates where pearl and mushroom patterns have been computed in (Re_1, r_i) space (compare with Fig. 6 in [23]). Mushroom-like patterns can be found with no flow perturbation for $r_i > 0.45$, but for small $r_i \lesssim 0.45$ we found it necessary to slightly perturb the flow at the inlet, for both pearl-like and mushroom-like patterns. We impose base constant flow rates Q_1 and Q_2, in fluids 1 and 2 respectively, with $Q_1 + Q_2 = 1$. We then

slightly perturb these flow rates as follows:

$$Q_1 \to Q_1 + \delta \sin 2\pi f t, \qquad Q_2 \to Q_2 - \delta \sin 2\pi f t.$$

For the frequency f we choose $f = u_i/\lambda$ where u_i is the interface velocity of the base flow and λ is the wave length of perturbation observed in [23]. Typically we have been able to excite the patterns observed for $r_i \lesssim 0.45$ by using amplitudes $\delta < 5\%$ (and in all cases $\delta < 10\%$).

It is interesting to observe that our simulations are computed with $Pe = \infty$ in (2.3), whereas the study in §2.1.3 indicates that numerical effects dominate for $Pe \gtrsim 10^5$. Although for at least a good part of the computed results our (numerical) diffusive effects are smaller than molecular diffusive effects (as reported in the experimental work), we find in fact quite similar diffuse patterns. This highlights the strong role of dispersive secondary currents in such flows. Although the diffusion we calculate is non-physical the observed dispersive effects are predominantly physical.

2.2 Start-up and entry length effects

Two aspects of the initial part of the core annular flow are of interest. First, is it possible to establish the base multi-layer flows at all, i.e. from a practically realisable initial flow configuration? If realisable, how robust is this initial flow? Secondly, having established a base flow, what factors affect the entry or development length of the flow? Whilst the latter problem could be studied via a steady flow computation, we have in fact studied both questions via a transient flow computation.

As an initial condition the entire pipe is filled with pure fluid 2. For fixed (m, B) the parameter r_i defines the relative flow rates Q_1 and Q_2 in each phase, such that $Q_1 + Q_2 = 1$. The individual flow rates are translated into constant mean inflow velocities, which are applied at the inlets of the inner pipe and annulus for $t > 0$. Also for $t > 0$ we impose $C = 0$ at the inflow of the inner

pipe, with $C = 1$ imposed at the annulus inflow. The computations are run until the inner fluid exits the pipe at $z = L$ and the flow becomes steady. The final steady flow is used for our calculations of entry (or development) length. Estimation of the required development length is a valuable part of process design.

2.2.1 Start-up flows

Typical examples of the start-up phase of the flow are shown in Figs. 2.9 & 2.10. In Fig. 2.9 we show some of the effects of the ratio r_i/R_i. In each row the first 3 panels show C at times $t = 4,\ 8,\ 12$. In each case, we observe that the initial front of fluid 1, penetrating into fluid 2 is destabilised locally, with a recirculating vortex developing at the sides. The extent of this feature varies with r_i/R_i, but does not destabilise the flow behind the front. The recirculation leads to significant dispersive mixing between the fluids in this region. Beyond $t = 12$ this recirculating pattern simply is advected up the pipe and out the exit, leaving behind the smooth multi-layer configuration. Looking between the first three frames we see that the frontal region does grow as it propagates, and hence should be termed convectively unstable, but is not absolutely unstable.

The following 3 panels on each row of Fig. 2.9 show further features of the flow at $t = 12$. From left to right, they show the speed, the absolute value of the shear stress and strain rate, respectively. On the shear stress plot we contour explicitly $\tau = B$, denoting the yield surface when in fluid 2. On the strain rate plot we have superimposed the axial component of velocity at 3 different heights. The plug-like velocity profile is evident in fluid 2, ahead of the front, in both speed and stress plots. The parameters $B = 10$, $r_i = 0.4$, $m = 1$, have a case 1 base solution, see Fig. 2.2a. On the right-hand figure we observe this base flow profile is established in the axial flow region behind the front. Formation of the plug region around the core fluid appears to take longer for the expansion inflow (middle row) and we note that this is also the

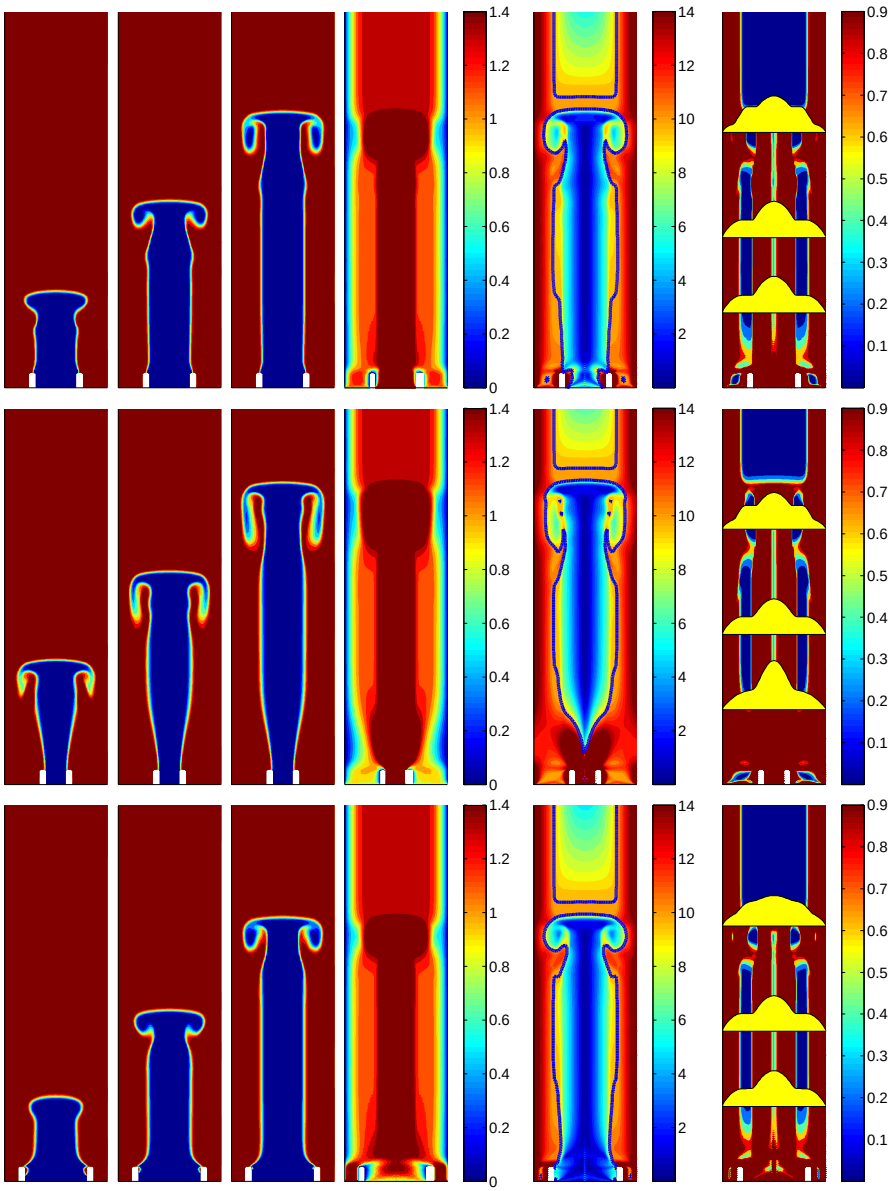

Figure 2.9: Start-up flow for $B = 10$, $r_i = 0.4$, $m = 1$, $Re = 20$, $L = 25$: top row, $R_i = 0.4$; middle row expansion, $R_i = 0.2$; bottom row contraction, $R_i = 0.6$. In each row the first 3 panels show C at times $t = 4$, $t = 8$ and $t = 12$, respectively. The 4th panel is a colourmap of the speed at $t = 12$. The 5th panel shows the shear stress at $t = 12$, with value $\tau = B$ highlighted. The 6th panel shows the strain rate $\dot{\gamma}$ at $t = 12$. On this figure we have superimposed the computed axial velocity profiles at selected distances along the pipe.

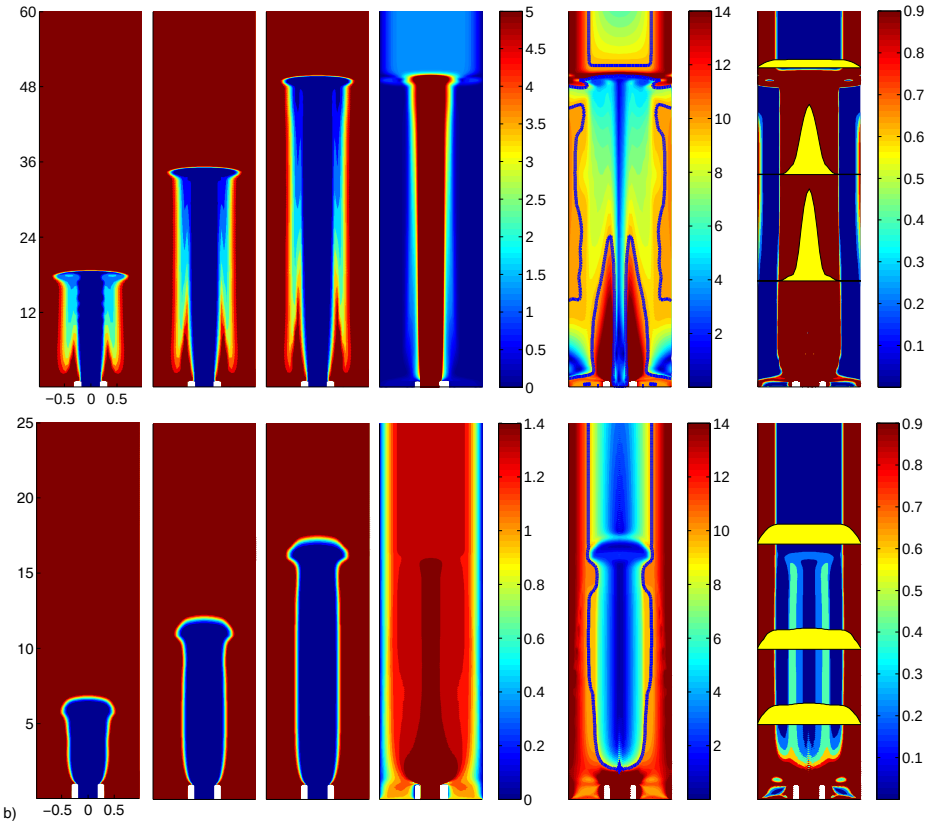

Figure 2.10: Start-up flow for $B = 10$ $r_i = 0.4$, $Re = 20$, $R_i = 0.2$: top row, $m = 0.1$, $L = 60$; bottom row, $m = 10$, $L = 25$. See caption of Fig. 2.9 for description of the different panels.

flow which has the most significant dispersive mixing at the front. Having said this, it is clear that the base flow is established in each case.

Figure 2.10 explores the effects of varying viscosity ratio m with all other parameters fixed. The results for $m = 1$ are shown in the middle row of Fig. 2.9 and can be compared with those for $m = 10$ and $m = 0.1$ in Fig. 2.10. Note that m is the ratio of inner/outer fluid viscosity. For small m the core fluid moves much faster ahead of the outer fluid. This leads to a large change in velocity gradient across the interfacial region. In contrast, for a case 1 solution with large m, across the interface we have a transition from zero strain rate in

the plug to strain rate of $O(1/m)$ in the core fluid. We can see the effects of this change by comparing the top and bottom rows of Fig. 2.10.

Note first that $L = 60$ in the top row ($m = 0.1$), so the aspect ratio in the 2 figures is different. For $m = 0.1$ the large change in shear rate across the interfacial region leads to strong dispersive mixing. Although there is in fact a case 1 base solution for $m = 0.1$, most of the flow rate is focused in the core fluid. Dispersive mixing means that in the mixed region part of the mixture is fluid 2. The result is a very slowly moving plug with narrow yielded layer at the wall. In the near-axial region behind the front there is a smooth transition in C and also in the strain rate, all due to mixing. If we examine the yield surface structure close to the inlet geometry, we can see that fluid 2 is unyielded in a plug attached to the wall, just ahead of where the inlet pipe ends. We can see a relatively high velocity jet-like region, shaped by the yield surface. This jet focuses fluid 2 inwards towards the core and enhances mixing. Further up in the pipe we have recirculatory motion about the displacement front and further mixing. The two effects combine to give the long dispersive "tails" evident in the $t = 12$ concentration plot, extending down towards the inlet. As there are both inlet effects and dispersion backwards from the front, it is unclear how to categorize this flow, except as convectively unstable. At later times the frontal region does advect from the pipe, leaving behind a parallel unyielded interface, but the mixing induced by the jetting in the inlet region does not cease.

The flow for $m = 10$ is quite different. By comparing with $m = 1$ (Fig. 2.9) we observe that the larger viscosity in the core fluid acts to suppress the recirculation and instability at the front, evident in Fig. 2.9. We appear to approach the base flow very quickly and there is minimal dispersive mixing anywhere in the flow.

The results shown are typical in that the frontal dispersive region is eventually advected from the pipe, replaced by the near parallel flow. We have not explored a large variation in B, since at fixed m and r_i as we vary B we

transition from case 2 to case 1 to case 3 base flows, whereas our interest is exclusively the case 1 flows. Similarly, we have some computational restrictions in Re. The development length grows with Re, necessitating increasingly long domains for $R_i \neq r_i$. At the same time we wish to retain the mesh resolution in the axial direction in order to resolve dispersive effects at the front and elsewhere. This results in a very expensive computation that becomes infeasible for pipe aspect ratios $L > 100$. For geometries $R_i = r_i$ entry lengths are markedly reduced and we have been able to compute start-up flows for Re in the range $100 - 500$, but have not studied this regime systematically.

It is worth noting at this stage that we have not found parameters for which a stable steady configuration was not achieved for a case 1 base flow parameter set. This suggests that for $Re < 50$, although the initial frontal displacement is convectively unstable the axisymmetric flow produced is temporally stable and appears to be robust over a range of different inlet/outlet radius ratios. The method of starting the flow is identical with that used experimentally in [55], but is certainly not the only method possible.

2.2.2 Development lengths

Process design requires some estimate of the length of pipe required for the flow to develop, and how this length varies with the principal parameters. We take these estimates from the final computed time of the start-up computations, described above.

An example of the final computed flows is shown in Fig. 2.11. Each row shows results for $r_i = R_i$ as well as for a typical expansion and contraction (at the same fixed r_i, so that the final base flow is identical). From top to bottom the Reynolds number is increased. In each simulation we show C at the final time and also the magnitude of the rate of strain. For all figures shown the final base state is identical.

Two features are evident from Fig. 2.11. Firstly that the flow develops more quickly with the inlet radius closer to the established interface radius

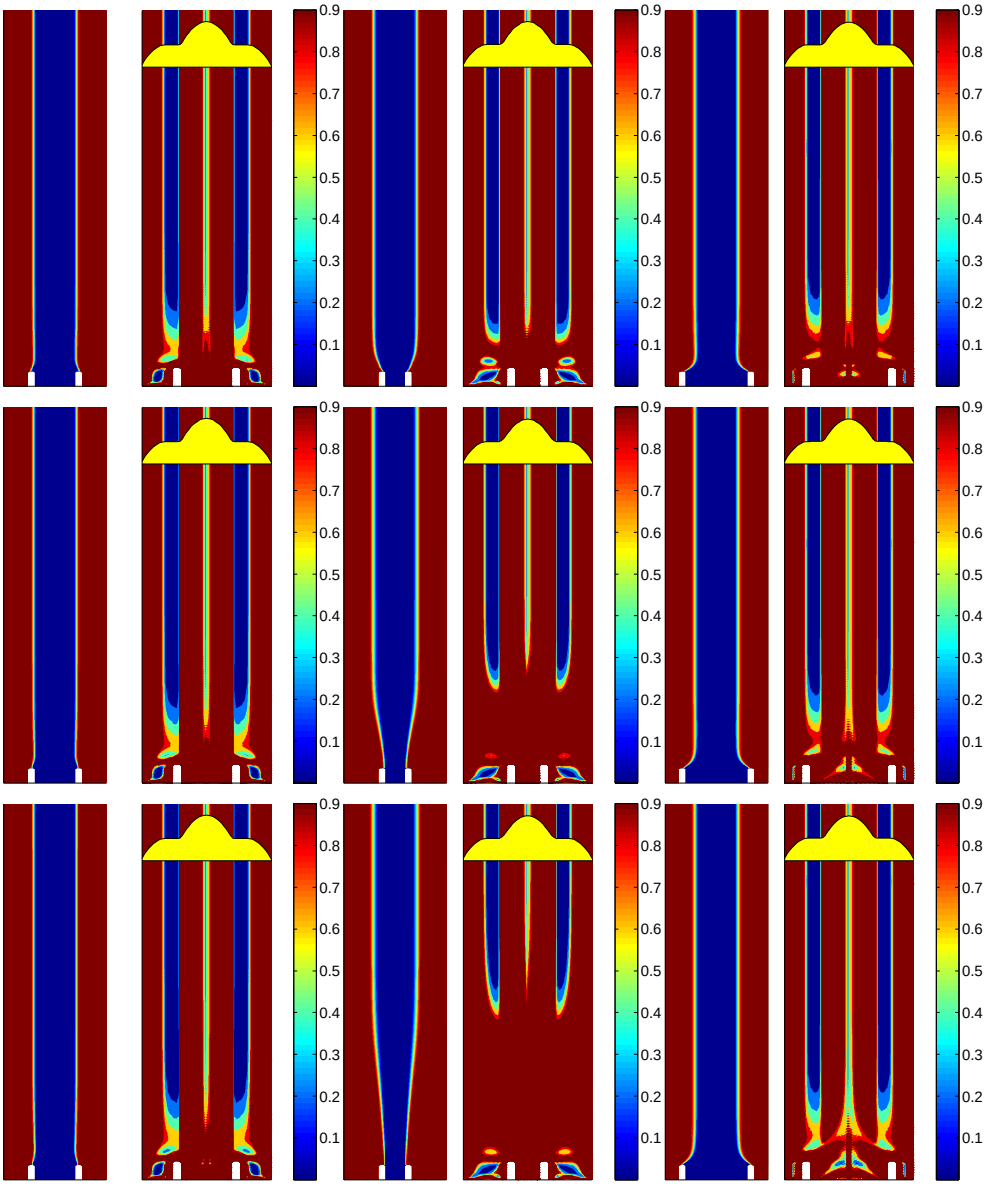

Figure 2.11: Steady developed flow for $m = 1$, $B = 10$: top row $Re = 5$; middle row $Re = 20$; bottom row $Re = 40$. Each row shows (left to right): $R_i = r_i = 0.4$; $0.2 = R_i < r_i = 0.4$; $0.6 = R_i > r_i = 0.4$. For each parameter set we show C and $\dot{\gamma}$, with the computed axial component of velocity superimposed near the outflow.

r_i. Secondly, we can see that increasing Re retards development of the base flow. Less obvious is that the thickness of the diffuse interfacial layer increases slightly with Re and for $R_i \neq r_i$. Essentially, the longer the development length is the more time there is for numerical diffusion and dispersion to occur.

Careful examination of results such as those in Fig. 2.11 reveals that there are in fact different interpretations of the flow development possible. In the first place, as case 1 solutions require an unyielded plug region surrounding the core fluid, it is of interest to know the first point at which this unyielded plug begins to form. We characterise this by L_τ, defined as the distance from the inlet at which the first unyielded fluid is found.

A second entry length consideration in a multi-layer flow is whether the interface becomes parallel and approaches the established radius. As we have seen, a diffuse region emerges around the interface and this makes direct comparison with the analytical r_i problematic as a means of defining flow establishment. For example, the exit flows for contraction and expansion are no less established than those for $r_i = R_i$. It is simply that the thickness of the diffuse interfacial layer is larger. Therefore, we have used the following definition to denote where the concentration field is established. We define L_c as the smallest z that satisfies the following inequality:

$$\frac{L - L_c}{\|C\|_{2r}(L)} \left\| \frac{\partial C}{\partial z} \right\|_{2r} (z) \leq 0.01, \tag{2.18}$$

where for a function $f(r, z)$ we define $\|f\|_{2r}(z)$ by:

$$\|f\|_{2r}(z) = \left[\int_0^1 r |f(r, z)|^2 \, \mathrm{d}r \right]^{1/2}.$$

In addition we verify that the diffuse interfacial layer is centred on $r = r_i$.

Finally, we wish to define an entry length for the velocity, say $z = L_u$. We have similar problems in this definition in comparing against the analytical solution, due to diffusive effects. Therefore, we again define L_U as the smallest

z that satisfies the following inequality:

$$\frac{L - L_u}{\|W\|_{2r}} \left\| \frac{\partial w}{\partial z} \right\|_{2r} (z) \leq 0.01, \tag{2.19}$$

where $W = W(r)$ denotes the analytic velocity profile given by (2.10) and $w(r, z)$ is the computed z-component of velocity.

Fig. 2.12 shows the different development lengths and how they vary as the ratio r_i/R_i is changed along with m, Re and B. In each row we present the different entry lengths L_τ, L_c and L_u, respectively. Each figure consists of data from 2 sets of simulations at fixed R_i: firstly $R_i = 0.6$ with $r_i = 0.2,\ 0.4,\ 0.6$ (contraction flows), and secondly $R_i = 0.2$ with $r_i = 0.2,\ 0.3,\ 0.4,\ 0.5$ (expansion flows). In each row we vary either m, Re or B. In all cases we verify that there exists a case 1 base flow.

The overall trends are as follows. In all cases we have an ascending hierarchy of development lengths: $L_\tau < L_c < L_u$. The minimal entry lengths are found at $r_i = R_i$, although increases in entry length due to contraction are not very significant. It is interesting that for both the contraction and expansion series the entry lengths are comparable at $r_i = R_i$, although these have quite different geometries and relative flow rates for the different series. Flows in which there is a significant expansion have the largest development lengths and also the largest differences between L_c and L_u. the latter is due to increased diffusion/dispersion in expansion flows, as illustrated and discussed earlier; see Fig. 2.11. As the diffuse layer becomes thicker it is not possible for the velocity to become established before the concentration field is developed. For less diffuse interfaces the lengths L_c and L_u are very similar. Variations with m, Re and B follow predictable qualitative trends. Increased m and B (within the range allowable to preserve the case 1 solutions) both increase the viscosity of the flow and decrease the entry lengths. Increasing Re has the effect of increasing entry lengths. Unlike duct flows of Newtonian fluids, the increase in entry length with Re is not linear.

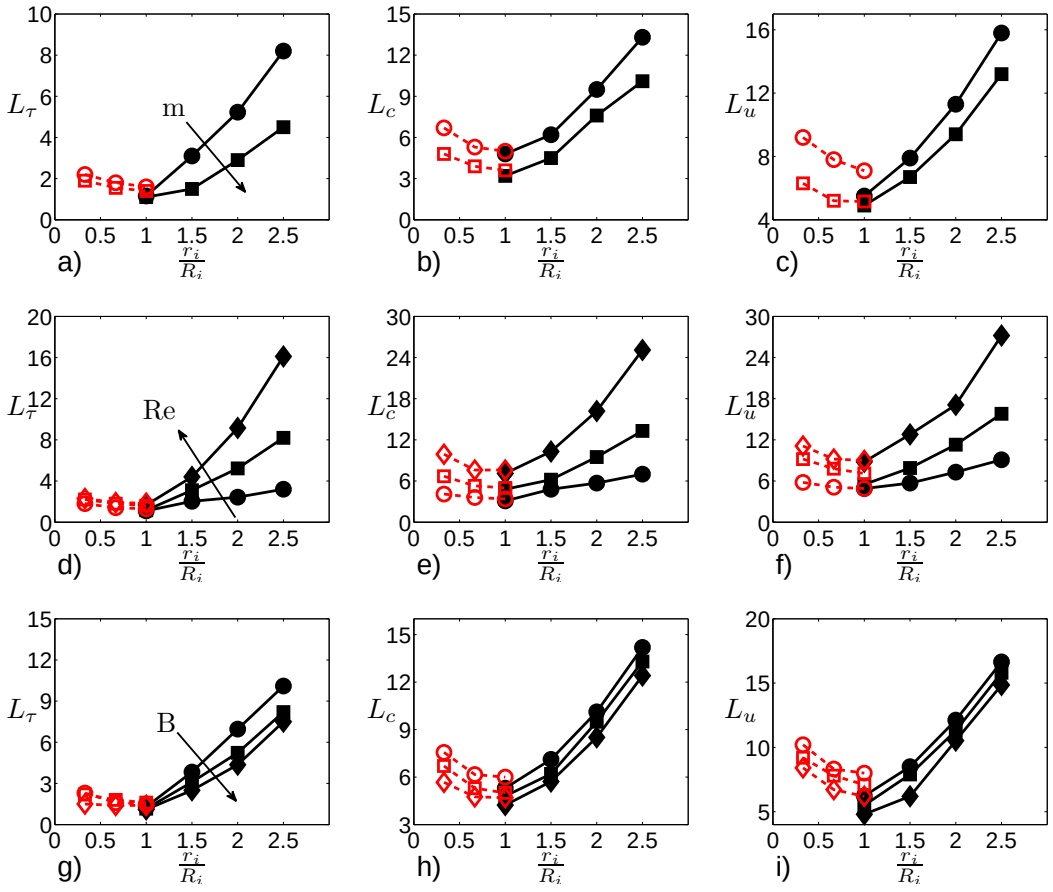

Figure 2.12: Variations in entry lengths with ratio r_i/R_i: top row shows $m = 1$ and $m = 10$ for fixed $Re = 20$, $B = 10$; middle row shows $Re = 5$, $Re = 20$ and $Re = 40$, for fixed $m = 1$, $B = 10$; bottom row shows $B = 5$, $B = 10$ and $B = 20$ for fixed $m = 1$, $Re = 20$. Each row shows the three entry lengths: L_τ, L_c and L_u. Each figure consists of two sequences of simulations: $R_i = 0.6$ with $r_i = 0.2,\ 0.4,\ 0.6$ (contraction flows), and secondly $R_i = 0.2$ with $r_i = 0.2,\ 0.3,\ 0.4,\ 0.5$ (expansion flows).

2.3 Stability of the established flow

The stability of visco-plastically lubricated flows has been studied by [26] and [85]. Although [26] studies linear stability of plane channel flows, as opposed to pipe flows, we expect very similar results. Note that unlike Newtonian fluids, both Hagen Poiseuille and plane Poiseuille flows of a Bingham fluid are linearly stable. In conducting linear stability studies of shear flows of yield stress fluids containing finite plug regions, one makes the (valid) assumption that the plug is not broken by the infinitesimal perturbation. This results in a decoupling of the linear stability into a sequence of reduced single fluid stability problems, each formulated on a purely viscous shear layer. For these reduced problems the length-scales and velocity scales are smaller and we generally find that the linear stability is enhanced.

The linear stability results are of limited practical use unless the stability extends into the nonlinear regime. Here the only nonlinear study is that of [85], who consider a parallel pipe flow similar to that here. For yield stress fluid flows conducting weakly nonlinear stability analysis is problematic, since the topology of the yielded regions when perturbed is unknown, and therefore it is more common to use energy methods. In the flow considered here there is the additional problem of the interface to deal with, which is not ideal for energy methods. However, in [85] they circumvented these difficulties by assuming a finite stress perturbation that is small enough to leave a ring of unyielded fluid around the core. This ring of fluid may translate away from the concentric location, but as it remains unyielded the interface velocity is described as a function of the plug velocity. This enables application of the energy method and derivation of lower bounds on Re, for exponential decay of the velocity perturbation.

This hybrid type of analysis in [85] does give stability for Re in the range $10 - 100$, depending on the other parameters, but has a number of drawbacks. Firstly, the bounds are certainly conservative and also not particularly easy to evaluate numerically. Second, the decay predicted is in fact decay to a base

solution that need not be axisymmetric. The experiments performed by [55] showed that the flows achieved are axisymmetric, but this study did not look at flow stability. Questions of symmetry breaking remain therefore open, but in any case will not be answered here. Thirdly, unlike a weakly nonlinear stability analysis, no information on the flow structure is forthcoming from the energy method. In particular, we have no understanding of how the plug region influences stability of the flow. Lastly, we note that [85] considered the $Pe \to \infty$ limit of the model analytically. However, we have seen earlier in §2.1.3 and 2.2.1 that even with large Pe strong dispersive effects can lead to modified flow structures.

Our stability analysis focuses on developing a finer understanding of the types of flows that occur when perturbing case 1 base flows. This is a temporal stability analysis conducted numerically on a spatially periodic cell. As well as the base flow parameters (m, B, r_i) the flows are characterised by Re and the axial periodicity of the flow. In conducting a numerical study it is necessary to specify initial conditions for the perturbations and in the nonlinear regime the precise solution behavior is influenced by the choice of initial conditions. Thus necessarily, what is presented are examples of flow behavior rather than general results. In this sense the study is complementary to that of [85].

2.3.1 Methodology

Having fixed the base flow parameters (m, B, r_i) and computed the analytic base flow $W(r)$, we select an axial wavelength α, which defines the length of computational domain: $2\pi/\alpha$. Taking $(0, W(r))$ and a unit step in concentration C at r_i as initial conditions, we first run the transient computations until steady state to establish the numerical base flow. This is done imposing periodicity at the ends of the spatial domain.

We then superimpose an initial condition on the numerical base flow and launch the transient computation. Initial conditions are selected to be spatially periodic (wavenumber α), to be divergence free and to satisfy boundary,

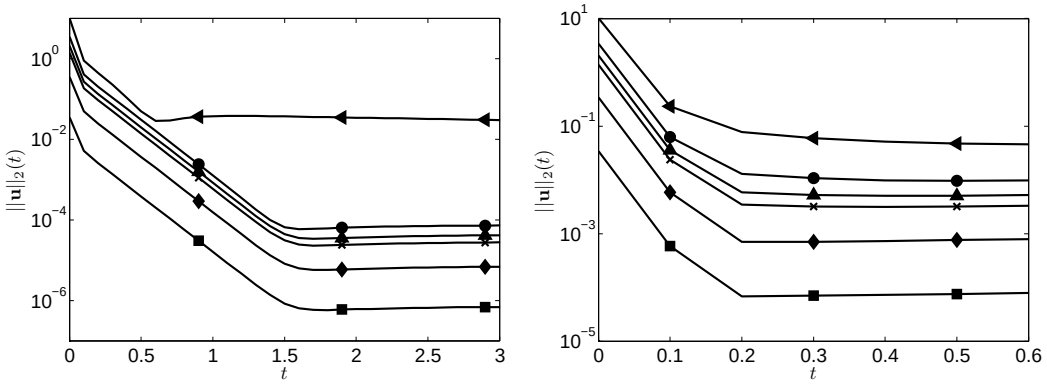

Figure 2.13: Decay of velocity perturbation for $r_i = 0.4$, $m = 10$, $B = 20$, at $Re = 1$: a) case A; b) case B. Different curves denote initial perturbation amplitudes: $A = 0.01$ (■), 0.1 (♦), 0.4 (×), 0.6 (▲), 1 (●), 3 (◀).

interface and symmetry conditions. Within this we construct the radial dependence using polynomials of the lowest order possible. Additionally we consider 2 types of initial perturbation: case A, where the entire domain is perturbed; case B, where only yielded regions of the flow domain are perturbed. These two initial perturbations are given in the form:

$$\mathbf{u}(r, z, 0) = A(v_r(r, z), v_z(r, z)); \qquad \|(v_r(r, z), v_z(r, z))\|_2 = \|W(r)\|_2 ,$$

so that A denotes the size of the L^2 norm of the initial perturbation, relative to that of the base flow, i.e. A^2 represents the relative kinetic energy of the initial perturbation. The spatial structure of these perturbations is described in appendix §A.

2.3.2 Results

For the results presented below we have focused on two specific base flows. For both flows we fix $(m, B) = (10, 20)$ and we consider $r_i = 0.4$ and $r_i = 0.6$. For both interface radii there is a case 1 base solution. With $r_i = 0.4$ the yield surface is at $r_y \approx 0.71$ whereas for $r_i = 0.6$ the yield surface is at $r_y \approx 0.72$, re-

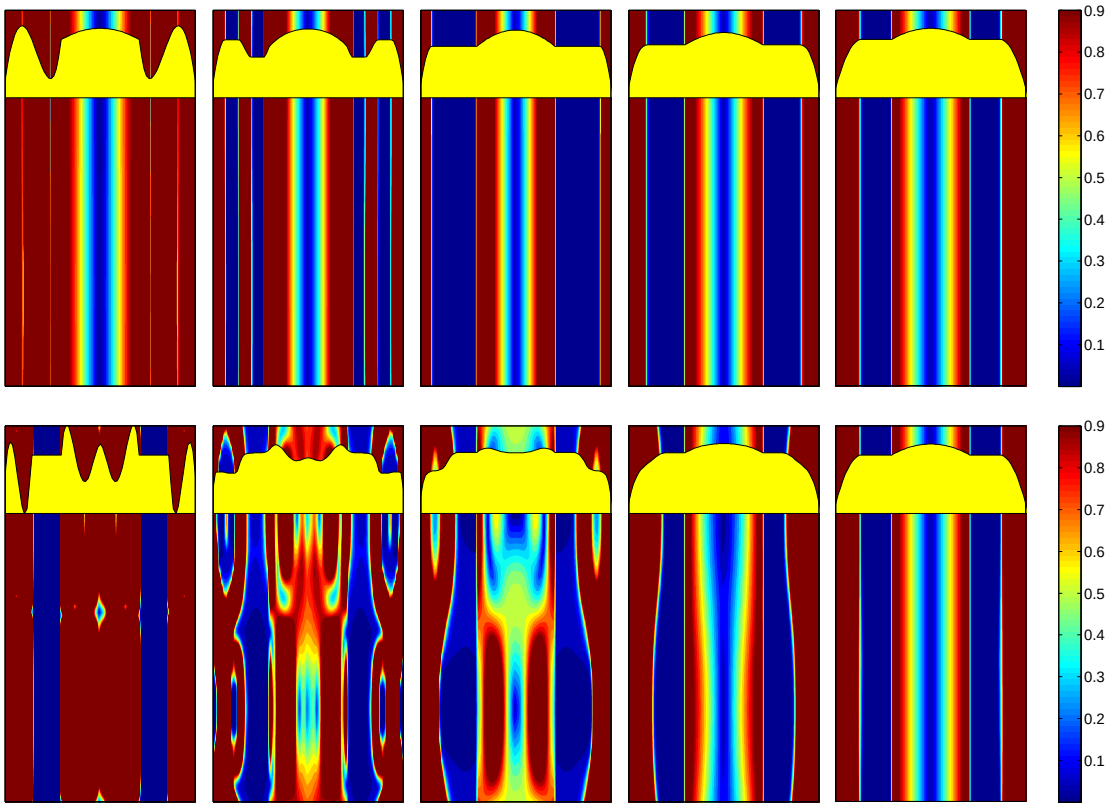

Figure 2.14: Initial stages of decay for amplitude $A = 0.4$ and for $r_i = 0.4$, $m = 10$, $B = 20$, at $Re = 1$. Each figure shows the magnitude of the strain rate at times (left to right) $t = 0$, $t = 0.001$, $t = 0.002$, $t = 0.005$ and $t = 1$, with superimposed axial velocity profile: top row = case A; bottom row = case B.

sulting in a thinner plug. For both base solutions we have performed stability studies for both case A and case B initial conditions, for $Re = 1,\ 10,\ 100,\ 1000$ and for amplitudes $A = 0.01,\ 0.1,\ 0.2,\ 0.4,\ 0.6,\ 0.8,\ 1,\ 2,\ 3$. Various additional computations have also been run to explore specific parameters, so that in total around 200 computations have been performed. For all results shown we have fixed the wavenumber α so that the length of domain is $L = 2\pi/\alpha = 4$.

We start by exploring the decay of $\|\mathbf{u}\|_2(t)$ for different A at low Re and with the thicker plug, $r_i = 0.4$. The results are shown in Fig. 2.13 for cases

A & B. For both cases we see an initial very rapid drop in $\|\mathbf{u}\|_2(t)$, which we shall explore below. The case A perturbation shows a distinct linear profile (exponential decay) until a constant saturation value is obtained. For low amplitudes the saturation values are very small. These values are limited anyway by the tolerance set in the nonlinear iteration for the solution. We see that for $A = 0.01$ we approach this tolerance. At higher A the perturbation decays to a value in the range $\|\mathbf{u}\|_2(t) \sim O(10^{-4})$ for all except the largest A. For this level of error, the final solutions appear to the eye to be very close to the base solution and the error comes principally from diffusive/dispersive effects near the interface.

For the case B initial conditions we see immediately that the decay is rapid, but that the final saturation values are not as small as for the case A initial conditions. There is a linear region of exponential decay, but it is apparently much shorter than for the case A perturbation. To explore this difference we investigate the initial sudden decay of the perturbation. Figure 2.14 shows the strain rate magnitude (and superimposed velocity profile) for the 40% amplitude perturbation with $r_i = 0.4$ at times $t = 0$, $t = 0.001$, $t = 0.002$, $t = 0.005$ and $t = 1$. The top row of figures shows the case A initial condition and the bottom row shows the case B initial condition.

It is interesting to note that for the case A initial condition the plug reforms very quickly. For the case B initial condition since the plug is not initially broken all the energy of the initial perturbation is localised in the core fluid and yielded part of the outer fluid. For $t > 0$ these large gradients dissipate rapidly, but in the process destroy the plug region. Both perturbations in fact decay to the same solution (see last panel at $t = 1$), but we observe that the case A perturbation has a reformed plug and quasi-1D flow structure much more rapidly. The longer time of decay allows for more diffusion and dispersion at the interface, so that the final values of the case B perturbations are larger than those of the case A perturbations.

Similar features are found with the $r_i = 0.6$ base solution, as shown in

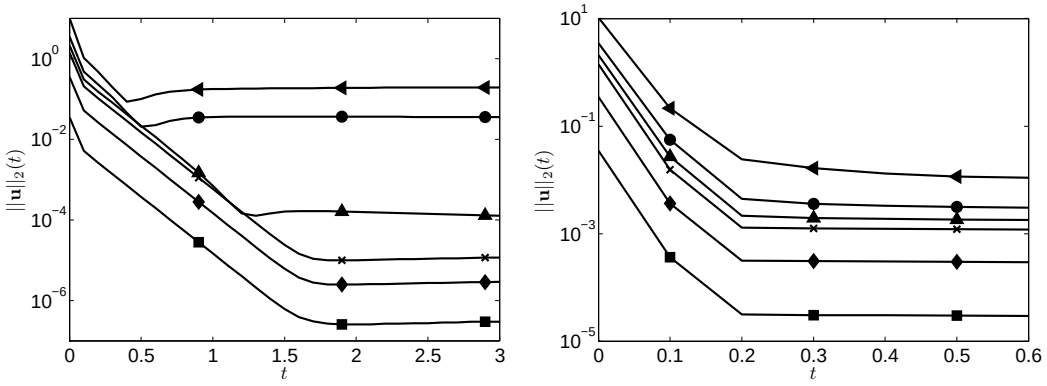

Figure 2.15: Decay of velocity perturbation for $r_i = 0.6$, $m = 10$, $B = 20$, at $Re = 1$: a) case A; b) case B. Different curves denote initial perturbation amplitudes: $A = 0.01$ (■), 0.1 (♦), 0.4 (×), 0.6 (▲), 1 (●), 3 (◀).

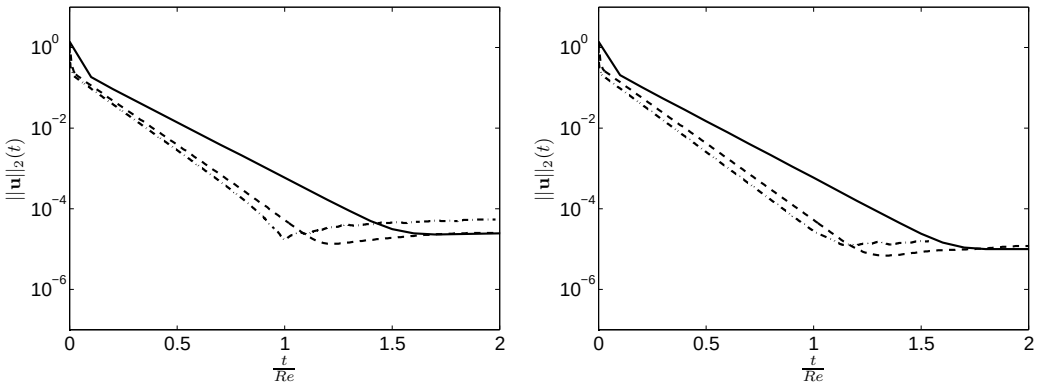

Figure 2.16: Decay of velocity perturbation for case A with $m = 10$, $B = 20$, $A = 0.4$, plotted against t/Re. Line styles $(-)$, $(--)$ and $(-.)$ denote $Re = 1$, $Re = 10$ and $Re = 100$ respectively. a) $r_i = 0.4$; b) $r_i = 0.6$.

Fig. 2.15. This base solution has a thinner plug region and is expected to be less stable. We observe that the decay of $\|\mathbf{u}\|_2(t)$ is qualitatively similar to that at $r_i = 0.4$, but that the final values are larger. For final values greater than around 1% the final solutions are progressively different to the base flow, and we explore some of these secondary flows later.

As Re is increased it is found that the time required for decay of $\|\mathbf{u}\|_2(t)$ to

its saturation value is progressively longer. Figure 2.16 shows this decay as a function of t/Re for 3 different Re values. Although the curves do not collapse to a single curve, the scaling is evident and indicates that this intermediate stage is dominated by pure viscous decay. This makes sense since after the plug has formed (or reformed) and the flow is quasi-1D the dissipation is governed by the viscous terms. Due to the viscosity ratio $m \neq 1$, there are in fact 2 viscous timescales and we should not be surprised that the curves do not collapse fully.

Figures 2.17 & 2.18 present a panorama of our computed results, in the form of colourmaps of $C(r, z, t)$ at $t = 9.9$ for varying A and Re. By this time, even for the larger Re, the flow structure is predictive of the final form. We show only the less stable case B initial perturbation. Figures 2.17 & 2.18 show the case B initial perturbation, for base flows $r_i = 0.4$ and $r_i = 0.6$, respectively. The overall pattern indicated by these figures is that for a wide range of A and Re this flow is temporally stable to axisymmetric perturbations. For $A \lesssim 1$ and $Re \lesssim 100$ we observe that the base flow is essentially recovered, with dispersive effects barely visible. However, as either speed (Re) or amplitude is increased various secondary flow effects become evident. At very large Re and A the flows are unstable and the fluids mix dispersively. We need to be cautious about the interpretation of some of these flows, as the numerical method has limited spatial resolution. Nevertheless, the onset of many of these flows, at lower Re and A are undoubtedly physical, similar to the pearl and mushroom simulations of §2.1.3.

We now look in more detail at some of the basic phenomena that we have seen in the sequence Figs. 2.17 & 2.18. To start with we observe that some of the figures in Figs. 2.17 & 2.18 show a wavy-walled interface at $t = 9.9$. For example, consider a case B initial perturbation with $r_i = 0.4$ for $Re = 100$ and with $A = 1$, (see Fig. 2.17, 3rd row, 6th column). Figure 2.19 shows the magnitude of strain rate and the colourmaps at $t = 0$, $t = 0.2$, $t = 0.5$, $t = 0.8$, $t = 1.1$. We see that, as before, the initial dissipation of energy breaks

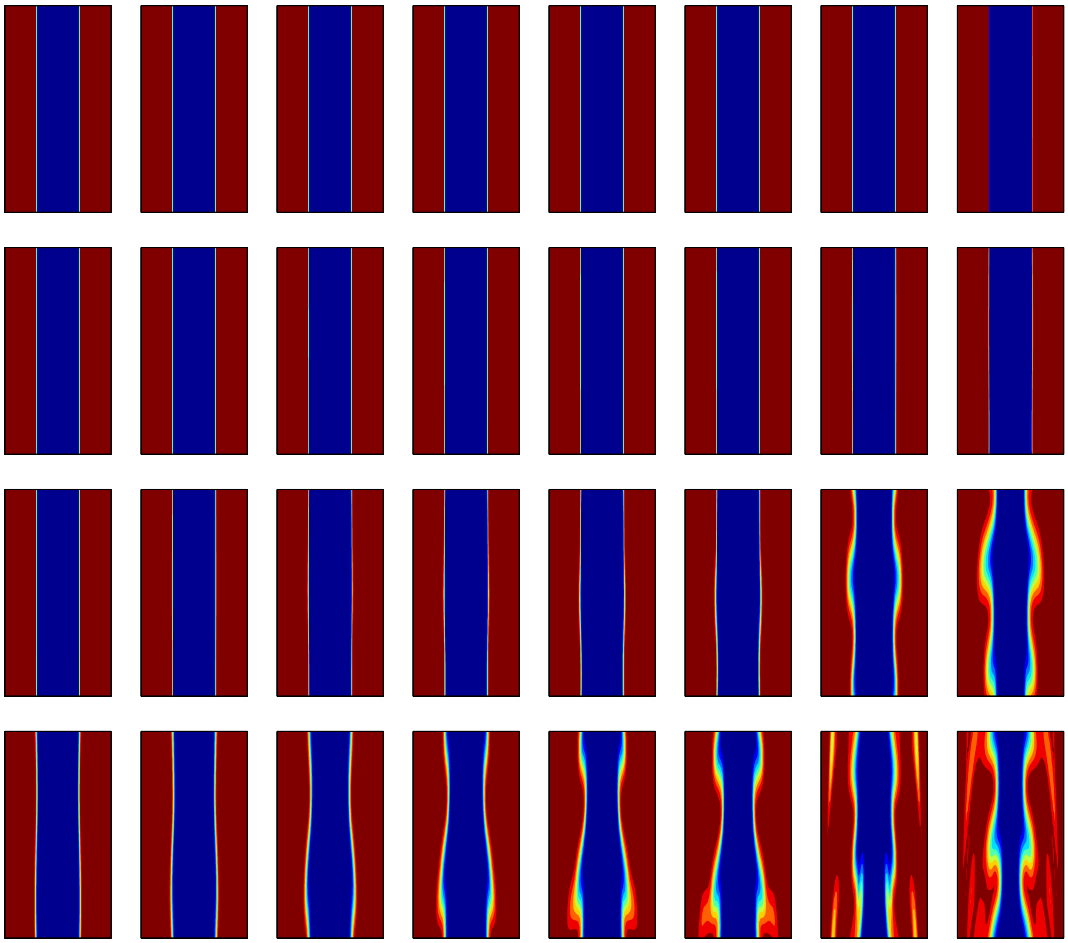

Figure 2.17: Concentration colourmaps for case B initial perturbation for $r_i = 0.4$ and $(m, B) = (10, 20)$, at $t = 9.9$. The rows from top to bottom show $Re = 1$, $Re = 10$, $Re = 100$ and $Re = 1000$. The columns, from left to right show the amplitudes: $A = 0.1,\ 0.2,\ 0.4,\ 0.6,\ 0.8,\ 1\ , 2,\ 3$.

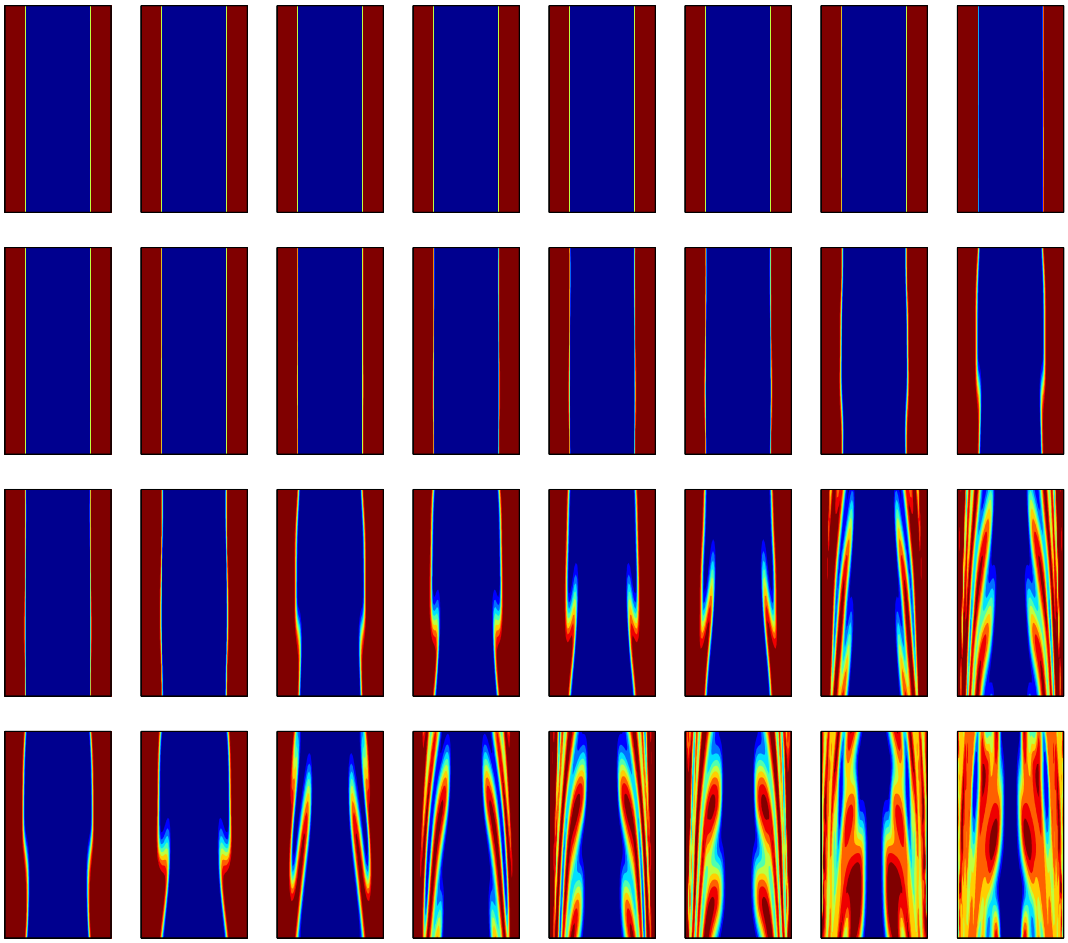

Figure 2.18: Concentration colourmaps for case B initial perturbation for $r_i = 0.6$ and $(m, B) = (10, 20)$, at $t = 9.9$. The rows from top to bottom show $Re = 1$, $Re = 10$, $Re = 100$ and $Re = 1000$. The columns, from left to right show the amplitudes: $A = 0.1,\ 0.2,\ 0.4,\ 0.6,\ 0.8,\ 1\ , 2,\ 3$.

the plug and results in a marked axial variation of the perturbation. The velocity perturbation decays in both the core fluid and in the outer fluid, but we can see that the interface is still deformed at the time which the fluid at the interface becomes unyielded (between $t = 0.5$ and $t = 0.8$). The interface effectively freezes in whatever shape it is in at the point the stress falls below the yield stress. Once frozen in the interface retains its shape. We can see that at $t = 1.1$ the inner fluid velocity field is still perturbed by the shape of the interface, whereas that in the yielded part of the lubricating fluid is essentially axial. This is a first type of secondary flow that can be found.

On increasing the initial perturbation amplitude the wavy nature of the interface is increased and eventually we develop secondary flows that break through the surrounding plug, in places. These flows have partly unyielded plugs and interfacial patterns that are similar to the pearl patterns of [22, 23]. An example is shown in Fig. 2.20. We note that the pearl-like flow structures observed are not permanent when the plug is yielded in parts. The uneven interfacial region means that there are 2D secondary flows present. Over time these disperse the intermediate concentrations and numerical diffusion smooths the concentrations. An example of the long time evolution is shown in the final frame of Fig. 2.20, at $t = 100$.

For larger $r_i = 0.6$ (when the plug region is also narrower), the flows are less stable and the plug breaks at smaller amplitudes. An example is shown in Fig. 2.21. The flow patterns at intermediate times resemble the mushroom patterns of [22, 23]. Again at long times numerical diffusion and physical dispersion dominate to render the flow axial with a significant mixed interfacial region.

2.4 Discussion

This chapter has mostly focused at trying to understand better the stability and robustness of visco-plastically lubricated pipe flows. In the first place we

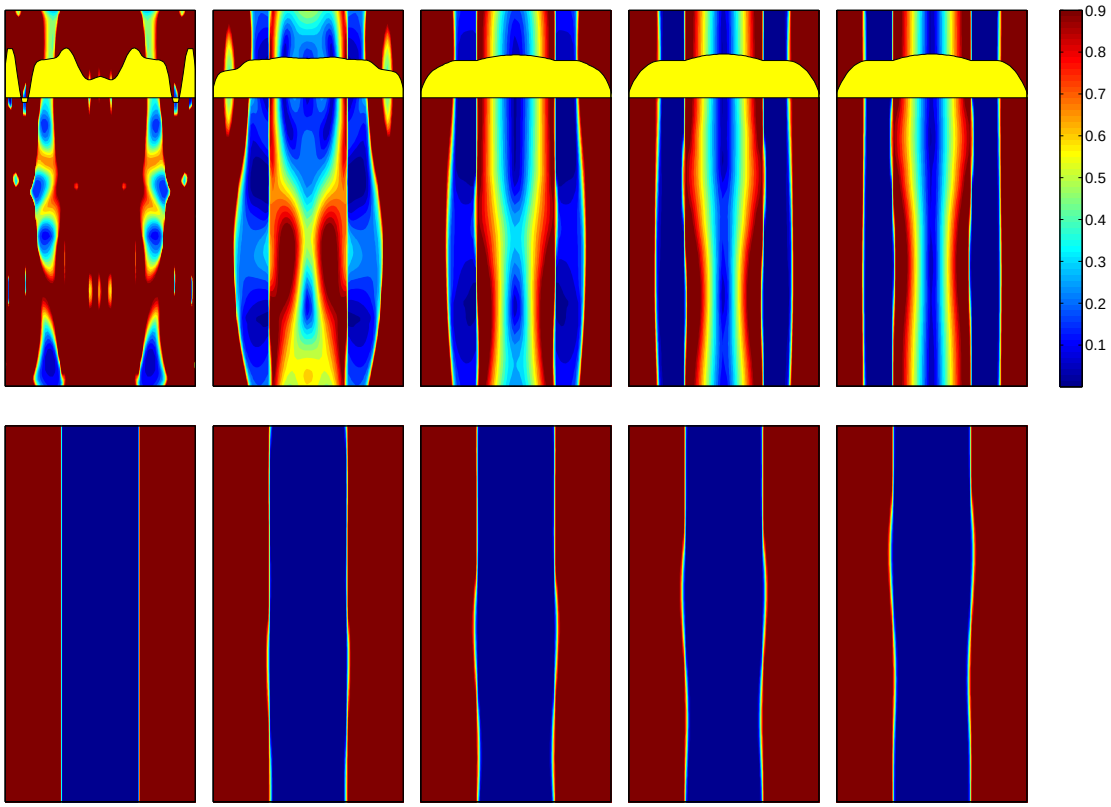

Figure 2.19: Freezing in of wavy-walled interfaces for a case B initial condition at $(m, B) = (10, 20)$ with $r_i = 0.4$, $A = 1$ and $Re = 100$. The figures are shown at $t = 0.2$, $t = 0.5$, $t = 0.8$, $t = 1.1$, $t = 1.4$ (left to right): top row = strain rate magnitude; bottom row = concentration.

have shown that for wide ranges of operating parameters (Re, R_i), as long as the base flow parameters (m, B, r_i) admit a case 1 solution then this base flow can be achieved by a start-up procedure analogous to that used experimentally by [55]. In contrast, for Newtonian multi-layer flows in similar configurations both the experimental work of [22, 23] and our test computations presented in §2.1.3, showed that many of these flows are convectively unstable leading to pearl and mushroom patterns. Even when convectively stable, we have been able to excite these patterns with relatively low amplitude oscillations of the

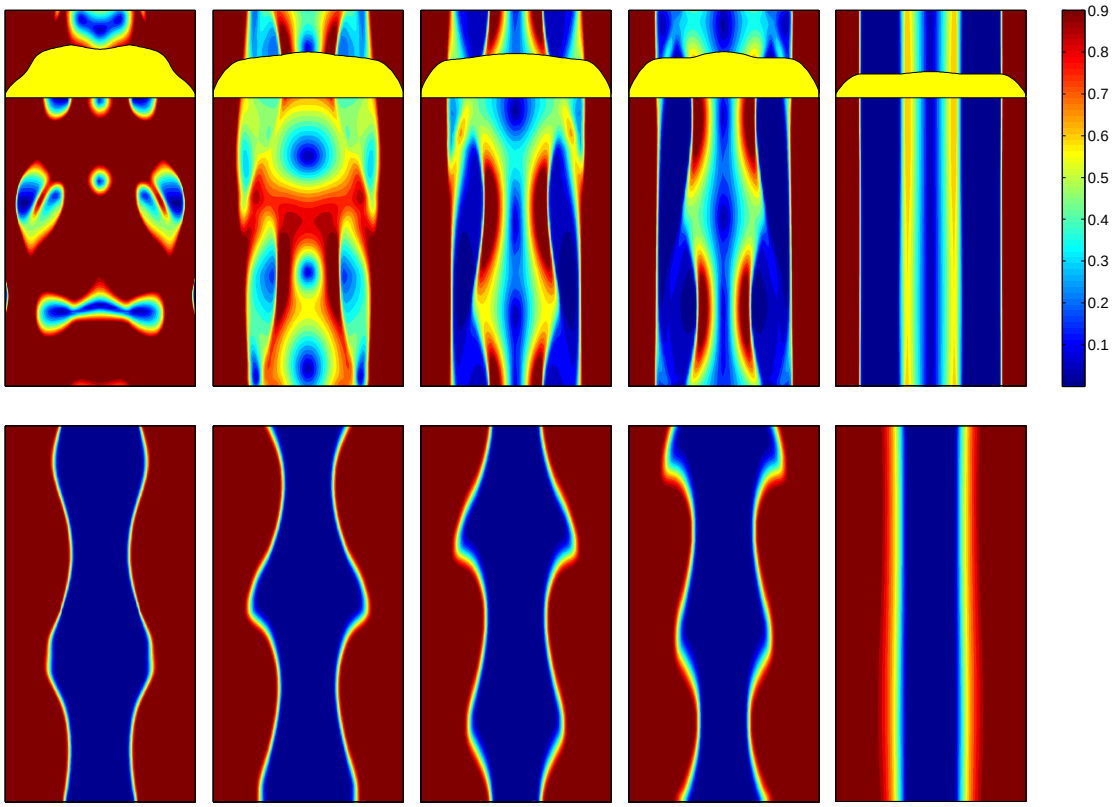

Figure 2.20: Pearl-like instabilities for a case B initial condition at $(m, B) = (10, 20)$ with $r_i = 0.4$, $A = 3$ and $Re = 100$. The figures are shown at $t = 0.7$, $t = 1.2$, $t = 1.7$, $t = 2.3$, $t = 100$ (left to right): top row = strain rate magnitude; bottom row = concentration.

flow rate. In contrast, we have observed no signs of absolute instability in the start-up of our flows, which are established as soon as the convectively unstable frontal region exits the pipe. This is perhaps the first indication of the robustness of the flows we have studied.

Secondly we have carried out a parametric investigation of the entry length for establishment of the base flow. The entry length increases with Re, and decreases with m and B, as is intuitive. Note that the decrease with m is artificial in that we have scaled with the plastic viscosity of the lubricating

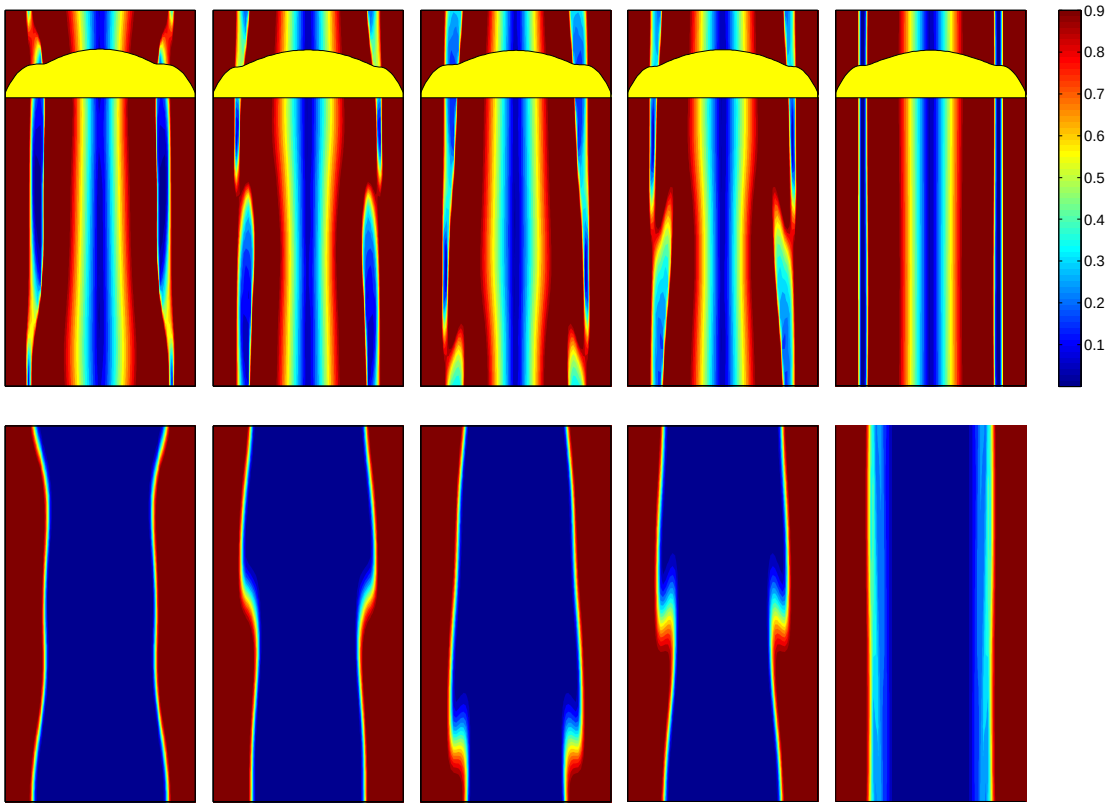

Figure 2.21: Mushroom-like instabilities for a case B initial condition at $(m, B) = (10, 20)$ with $r_i = 0.6$, $A = 0.8$ and $Re = 100$. The figures are shown at $t = 2$, $t = 4$, $t = 6$, $t = 7$, $t = 100$ (left to right): top row = strain rate magnitude; bottom row = concentration.

fluid, as opposed to some average (plastic) viscosity. This means that the average viscosity always increases with m. The behavior with r_i/R_i, being minimal when the inlet radius matches the far-field radius is also intuitive. It is surprising that relatively few radii are needed to establish the flow.

Turning now to the flow stability, we have examined perturbations of 2 different flows with 2 different initial conditions, over a broad range of initial amplitudes A and Re. For $Re < 100$ we have routinely found stable flows for amplitudes $A \lesssim 1$. While this does not establish any theoretical limits, it does

suggest that the analytic results in [85] may be fairly conservative, especially since we have demonstrated that stability may result even when the base flow plug region is perturbed. Retaining an unyielded plug region was an essential part of the analysis in [85].

At larger perturbation amplitudes we have shown that there are interesting flow regimes that may result from perturbation of the base flow. For example, we are able to "freeze in" non-planar interface and form interesting non-Newtonian pearl and mushroom patterns. At still larger perturbations, large scale dispersion occurs and some judgement needs exercising about the validity of the observed results in these regimes. Nevertheless, we have seen that even when significant mixing occurs the perturbations often decay back to stable states.

We have also studied the nature of the energy decay when the flow is stable. There exists a significant and very fast transient in the initial stages, which is responsible for breaking and reforming of the plug. Presumably this process is governed by the yield stress, whereas at later times the decay is exponential and characteristically viscous. It is well known that yield stress fluids can have a finite time decay when stable, e.g. [36, 134]. The typical result is proven by considering the energy decay, and involves a global bound on the decay of $\|\mathbf{u}\|_2$. This bound is exponential when the base flow is non-trivial, but occurs in finite time otherwise. It could be that for complex flows such as this we may have more rapid decay than exponential, but only locally.

Chapter 3

Visco-plastically lubricated channel flows [1]

The computations performed in chapter 2 are axisymmetric. Such flows and perturbations can be significantly more stable than asymmetric perturbations. Having said this, we note that the experimental flows in [55] were also observed to be axisymmetric. We suspect that the study of 3D flows and instabilities would decrease the Reynolds numbers and amplitudes of perturbation required for instability, but that the flow will remain nonlinearly stable for practically significant ranges. This chapter has two motivations.

1. We wished to explore aspects of flow development and start-up in a different geometry to the pipe flow, to assess how general the results of chapter 2 were. The plane channel geometry is a generic geometry for laminated products and eventually also coating applications, so there are some practical benefits.

2. The flows in chapter 2 proved surprisingly stable but were axisymmetric. Fluid mechanics is rife with examples of loss of stability through symmetry breaking and axisymmetric flows can frequently exhibit stability well above stability limits observed in real flows where asymmetry is not controlled. While retaining the economy of 2D computations the plane channel allows for symmetry breaking. We wanted to explore where this effect might become important.

[1] A version of Chapter 3 has been published. [S. Hormozi], K. Wielage-Burchard and I.A. Frigaard. (2011) Multi-layer channel flows with yield stress fluids. Journal of Non-Newtonian Fluid Mechanics. **166**, 262-278, [53].

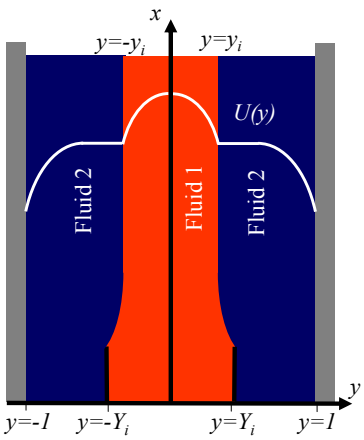

Figure 3.1: Schematic of the dimensionless flow geometry for the start up flow computations.

An outline of this chapter is as follows. Section 3.1 introduces the physical model of the flows that we study. We present the results of our study of start-up flows and development lengths in §3.2 . Section 3.3 includes the results of nonlinear temporal stability. Also, in working with a geometry allowing for asymmetry we look at new types of flow, where interesting and exotic effects can be introduced, but in a controlled manner exploiting still underlying the method of retaining unyielded fluid at the interface. Finally, the chapter ends with summary and discussion in §3.5.

3.1 Multi-layer channel flows

A vertically oriented channel of width $2\hat{R}$ is initially filled with Bingham fluid (fluid 2). For times $\hat{t} > 0$ a Newtonian fluid (fluid 1) is injected upwards through a centrally positioned inner channel of width $2\hat{Y}_i < 2\hat{R}$, while at the same time the Bingham fluid is pumped through the outer part of the channel, (see Fig. 3.1a). The Bingham fluid thus acts as lubricating layer for the Newtonian core fluid. This is the basic geometry studied in this chapter, although later we will consider variations.

The flow parameters are assumed to correspond approximately to those one might have in a typical industrial processing situation. Thus, nominally we suppose that $0.005\text{m} \lesssim \hat{R} \lesssim 0.1\text{m}$, mean velocities $0.001\text{m/s} \lesssim \hat{U}_0 \lesssim 1\text{m/s}$, and we consider fluids that are miscible aqueous solutions of equal density, $\hat{\rho}$. The choice of a Bingham fluid as the lubricant is a simplification of a typical yield stress rheology (which is usually shear-thinning) and the Newtonian core is also selected primarily for simplicity.

Fluid 1 has viscosity $\hat{\mu}^{[1]}$ and fluid 2 is characterised by its yield stress $\hat{\tau}^{[2]}_{yield}$ and plastic viscosity $\hat{\mu}^{[2]}$. The total real flow rate along the channel is $\hat{Q}$, which defines the mean axial velocity: $\hat{U}_0 = \hat{Q}/2\hat{R}$. The pressure is denoted by $\hat{p}(\hat{\boldsymbol{x}}, \hat{t})$, $\hat{\boldsymbol{u}}(\hat{\boldsymbol{x}}, \hat{t})$ is the velocity, $\hat{\tau_{ij}}^{[k]}$ denotes the deviatoric stress tensor in pure fluid k, and $\hat{g}$ is the gravitational acceleration. We model the change between (pure) fluids 1 and 2 via a scalar concentration C, representing the concentration of fluid 2. The Navier-Stokes equations are made dimensionless with the following scaling:

$$\boldsymbol{x} = \frac{\hat{\boldsymbol{x}}}{\hat{R}}, \;\; t = \frac{\hat{t}\hat{U}_0}{\hat{R}}, \;\; \boldsymbol{u} = \frac{\hat{\boldsymbol{u}}}{\hat{U}_0}, \;\; p = \frac{\hat{p} + \hat{\rho}\hat{g}\hat{x}}{\hat{\rho}\hat{U}_0^2}, \;\; \tau_{ij} = \frac{\hat{\tau}_{ij}\hat{R}}{\hat{\mu}^{[2]}\hat{U}_0}. \tag{3.1}$$

The dimensionless model considered is as follows:

$$\frac{\partial u_i}{\partial t} + u_j \frac{\partial u_i}{\partial x_j} = -\frac{\partial p}{\partial x_i} + \frac{1}{Re}\frac{\partial \tau_{ij}}{\partial x_j}, \tag{3.2}$$

$$\frac{\partial C}{\partial t} + u_j \frac{\partial C}{\partial x_j} = \frac{1}{Pe}\frac{\partial^2 C}{\partial x_j^2}, \tag{3.3}$$

$$\frac{\partial u_i}{\partial x_i} = 0. \tag{3.4}$$

Constitutive laws for the two pure fluids are:

$$\tau_{ij}^{[1]} = m\dot{\gamma}_{ij}, \tag{3.5}$$

$$\dot{\gamma}(\boldsymbol{u}) = 0 \iff \tau^{[2]}(\boldsymbol{u}) \leq B, \tag{3.6}$$

$$\tau_{ij}^{[2]}(\boldsymbol{u}) = \left[1 + \frac{B}{\dot{\gamma}(\boldsymbol{u})}\right]\dot{\gamma}_{ij}(\boldsymbol{u}) \iff \tau^{[2]}(\boldsymbol{u}) > B. \tag{3.7}$$

where

$$\dot{\gamma}_{ij} = \frac{\partial u_i}{\partial x_j} + \frac{\partial u_j}{\partial x_i},$$

$$\dot{\gamma}(\boldsymbol{u}) = \left[\frac{1}{2}\sum_{i,j=1}^{2}[\dot{\gamma}_{ij}(\boldsymbol{u})]^2\right]^{1/2} \qquad \tau^{[2]}(\boldsymbol{u}) = \left[\frac{1}{2}\sum_{i,j=1}^{2}[\tau_{ij}^{[2]}(\boldsymbol{u})]^2\right]^{1/2}. \tag{3.8}$$

There are 3 principal dimensionless groups:

$$m = \frac{\hat{\mu}^{[1]}}{\hat{\mu}^{[2]}}, \qquad Re = \frac{\hat{\rho}\hat{R}\hat{U}_0}{\hat{\mu}^{[2]}}, \qquad B = \frac{\hat{\tau}_{yield}^{[2]}\hat{R}}{\hat{U}_0\hat{\mu}^{[2]}}. \tag{3.9}$$

These are the viscosity ratio (m), Reynolds number (Re) and Bingham number (B), respectively. The Bingham number denotes the ratio of the yield stress of the fluid to a typical viscous stress of the flow. The Reynolds number has been based on fluid 2 properties. The relevant Reynolds number for fluid 1 is Re/m, as the fluids are considered iso-density. We also have 2 geometric groups: $Y_i = \hat{Y}_i/\hat{R}$, the inlet width ratio, and y_i which is the position of the interface in a parallel multi-layer flow; see Fig. 3.1. This latter is governed by the relative distribution of the total flow rate between the two fluids, as we discuss below in §3.1.1. A final dimensionless group is the Péclet number, $Pe = \hat{R}\hat{U}_0/\hat{D}_m$, with $\hat{D}_m$ the molecular diffusivity. Typically we have $Pe \sim 10^6 - 10^{10}$, for which values the concentration is effectively advected with the flow. Computations detailed in chapter 2 indicate that the diffusive term in (3.3) can be ignored for Péclet numbers in this range for the size of mesh we typically use. Effectively numerical diffusion is dominant in this range of

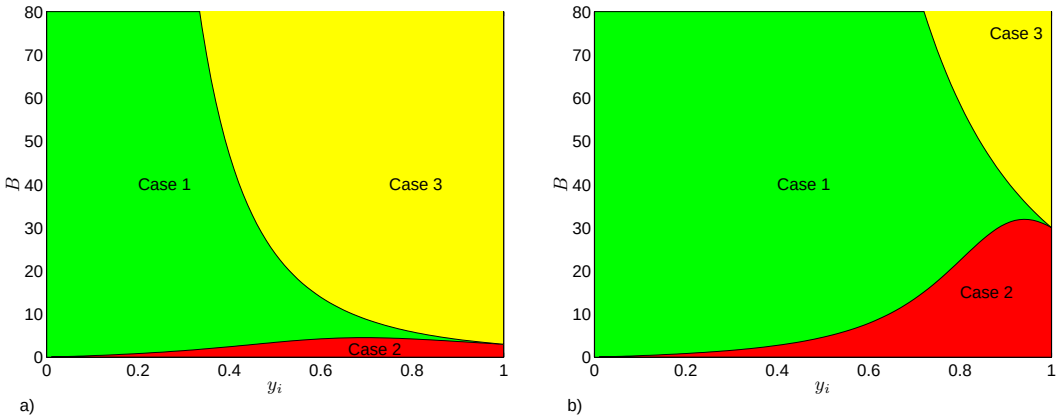

Figure 3.2: Parameter domains where the base solutions are found in (y_i, B, m)-space: a) $m = 1$; b) $m = 10$.

Pe, although physical dispersion due to secondary flows is still present. Thus, throughout this chapter we consider the immiscible limit of 2 miscible fluids ($Pe \to \infty$), or equivalently an immiscible flow at infinite capillary number.

3.1.1 Basic flows, $Pe \to \infty$

Setting $Pe \to \infty$ we recover the ideal *clean interface* limit of the flow, which admits a steady 1D solution. This type of 1D flow has proven useful as a simple model for experimental design; see [55]. In the steady 1D flow, the shear stress varies linearly from the channel centerline to the wall. The type of base flow that one finds depends on whether the shear stress exceeds the yield stress of the lubricating fluid at either the wall or the interface. The flow of principal interest is that in which the yield stress lies between the interfacial stress and the wall shear stress. This ensures that the lubricating layers of Bingham fluid are mobile and that the Bingham fluid remains unyielded at the interface. We call this type of solution, $\mathbf{u} = (U(y), 0)$, a case 1 base solution, defined as

follows for $y \in [-1, 1]$:

$$U(y) = \begin{cases} \dfrac{B}{2y^*}\left[\dfrac{1}{m}(y_i^2 - y^2) + (1-y^*)^2\right] & 0 \le |y| \le y_i, \\ \dfrac{B}{2y^*}(1-y^*)^2 & y_i < |y| \le y^*, \\ \dfrac{B}{2y^*}\left[(1-y^*)^2 - (|y|-y^*)^2\right] & y^* < |y| \le 1. \end{cases} \tag{3.10}$$

Here y^* is defined as the root of

$$0 = (y^*)^3 - 3y^*\left(1 + \frac{2}{B}\right) + 2\left(1 + \frac{y_i^3}{m}\right). \tag{3.11}$$

that lies in $(y_i, 1)$, for $y_i \in [0, 1]$. The two interfaces are at $y = \pm y_i$ and the yield surface positions are at $y = \pm y^*$.

Two other types of solution can be found. If the yield stress is exceeded at the interface we call this a case 2 solution. The boundary between case 2 and case 1 solutions is given by:

$$B < \frac{6y_i}{y_i^3\left(\dfrac{2}{m} + 1\right) - 3y_i + 2}, \tag{3.12}$$

(with case 1 solutions found when this inequality is not satisfied). Finally, if the yield stress is not exceeded at the wall then the entire layer of Bingham fluid is static. The boundary between case 3 and case 1 solutions is given by:

$$B > \frac{3m}{y_i^3}. \tag{3.13}$$

(again case 1 solutions are found when this inequality is not satisfied). Figure 3.2 illustrates the domain in which case 1 solutions are found for 2 different viscosity ratios, m.

3.2 Computational method and development of steady flows

The computational method we use is largely as described in chapter 2, where we have dealt with pipe flows. The model equations (3.2)-(3.8) have been discretised using a mixed finite element/finite volume method. The computations are carried out on a structured rectangular mesh. The Navier-Stokes equations are solved using a semi-implicit Galerkin finite element method, where the divergence-free condition is enforced by an augmented Lagrangian technique. The concentration equation is dealt with via a MUSCL scheme, with on each timestep a splitting method used to advance the concentration equation over a number of smaller sub-timesteps, preserving stability. The numerical algorithm is implemented in C++ as an application of PELICANS.[2] We refer the reader to chapter 2 (see also [124]) for a more detailed description of the numerical method.

In chapter 2 we have validated the code by presenting comparisons between exit velocity profiles and the analytic base solutions. Similar comparisons can be made here and are generally very good, except close to the interface where numerical diffusion can smear the interface over a few cells. This effect can be reduced via mesh refinement, but at computational cost. For computations presented below we use 120 elements across the channel and 40 elements per unit length along the channel, which is of dimensionless length L. The length is adjusted according to the physical situation we model and for longer geometries we preserve the mesh density. Also in chapter 2 we presented studies on the effects of Pe variation and viscosity regularisation, both of which are very similar in the channel geometry. Finally, in chapter 2 we demonstrated that

[2]PELICANS is an object oriented platform developed at IRSN, France, to provide a general framework of software components for the implementation of partial differential equation solvers. PELICANS is distributed under the CeCILL license agreement (http://www.cecill.info/licences/Licence_CeCILL_V2-en.html). PELICANS can be downloaded from https://gforge.irsn.fr/gf/project/pelicans/.

the code was able to reproduce complex convective "pearl and mushroom" type instabilities observed experimentally (see [22, 23]) when Newtonian-Newtonian flows are considered. Similar convective instabilities can be observed in the channel geometry for Newtonian-Newtonian flows that we have simulated, but now we have no experimental study against which to compare.

3.2.1 Comparison of viscosity regularisation and augmented Lagrangian method

We present an additional benchmark for the channel flow. For the Bingham fluid the effective viscosity becomes infinite in unyielded regions of the flow, although the stress and strain rate tensors remain finite. Two methods for dealing with this are either to regularise the effective viscosity functional to remove the singular behavior (see e.g. [6, 29, 36, 91]) or to solve the equations using a relaxation-multiplier approach such as the augmented Lagrangian method (e.g. [36, 37, 38]). We have implemented both strategies, using [6] with regularisation parameter $\epsilon = 10^{-4}$, i.e. (3.6) & (3.7) are replaced with

$$\tau_{ij}^{[2]}(\boldsymbol{u}) \;=\; \left[1 + \frac{B}{[\dot{\gamma}^2(\boldsymbol{u}) + \epsilon^2]^{1/2}}\right] \dot{\gamma}_{ij}(\boldsymbol{u}). \tag{3.14}$$

We show typical comparative results in Figs. 3.3 & 3.4.

The left figure of Fig. 3.3 shows the L^2 norm of the difference in computed axial velocity solutions at different distances x along the channel. We see that there is a discrepancy of the order of 10% close to the inflow that decays with distance as the flows become more one-dimensional. The right figure of Fig. 3.3 shows a comparison of the axial velocity profiles at the exit of the channel, where they are indistinguishable.

Fig. 3.4 shows the colourmaps of the concentration and strain rate at $t = 100$, during the same displacement as in Fig. 3.3. Flows of this complexity are not covered by existing theory, but from the theory available for simpler flows, we might expect that the velocity field of the regularised model should converge

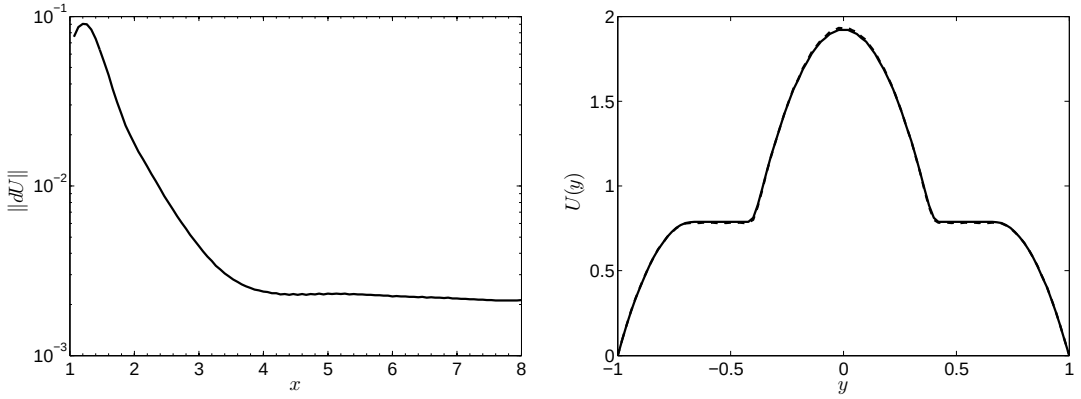

Figure 3.3: Comparison between solutions computed with the augmented Lagrangian and the regularisation (3.14) with $\epsilon = 10^{-4}$. Top figure measures the L^2 norm of the difference in axial velocity solutions at different distances along the channel. Bottom figure presents the exit velocity profiles (solid line = regularized, broken line = augmented Lagrangian). Model parameters: $m = 1,\ B = 10,\ Re = 5,\ y_i = 0.4,\ Y_i = 0.2,\ L = 8$.

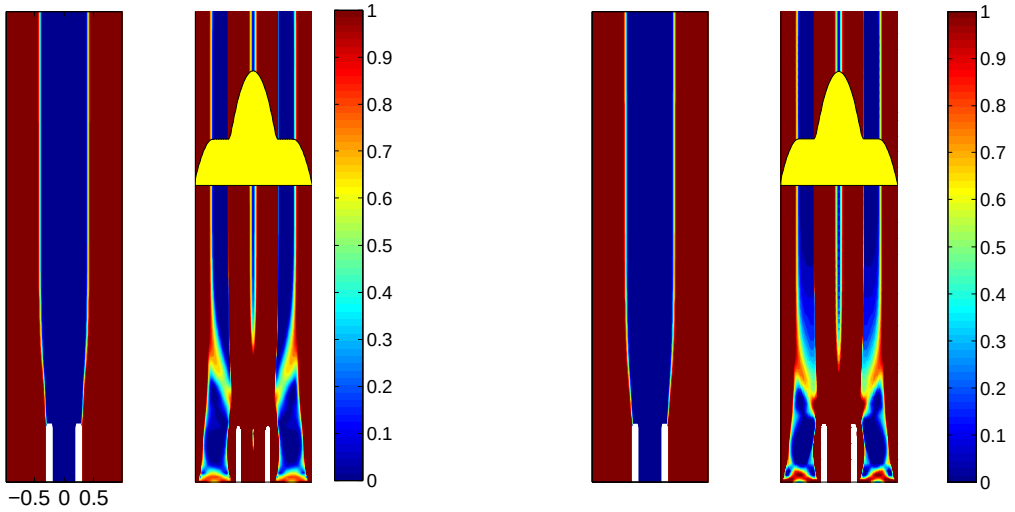

Figure 3.4: Solutions at $t = 100$ for the parameters as Fig. 3.3: left = augmented Lagrangian; right = regularized viscosity model. For each model we see the concentration profile (left) and the strain rate colourmap (right), with a single axial velocity superimposed.

to that of the exact model as the regularisation parameter decreases. The concentration field depends solely on the velocity field and the close comparison between the concentration fields suggests that this is true. On the other hand we can see significant differences in the strain rate distributions in the entry region. The augmented Lagrangian method solution tends to form a plug closer to the inlet than is the case with the regularised solution. However, we have not noticed any significant effect on qualitative results, such as stability of establishment of the flow. The only other discernible difference between solutions comes when the unyielded plug is very thin, e.g. of the order of the mesh. However, in this range numerical diffusion effects also have a significant effect on the results. If these flows need resolving then mesh refinement is more of a concern than choice of solution method for the constitutive law.

3.2.2 Development of steady flows

We move now to the study of developing steady flows, following largely the methodology we have adopted for the pipe flows in chapter 2. In general we have not observed any remarkable qualitative difference between the plane channel development flow and that in the pipe considered in chapter 2. A typical example of the developing flow is shown in Fig. 3.5 (top row). The first 4 frames show the concentration profile at $t = 4,\ 8,\ 12,\ 16$. The initially injected core fluid tends to form a plume and destabilize locally. Although this frontal plume is convectively unstable, as time evolves this initial unstable frontal region is advected further down the channel and eventually exits the channel. Behind the front we observe a stable multi-layer regime developing. The final 3 frames of Fig. 3.5 (top row) show the shear stress, speed and strain rate of the flow, respectively, at $t = 16$. The stress plot also includes the yield stress and the strain rate plot has superimposed on it the axial velocity profile. It can be observed that the flow assumes its characteristic profile, with unyielded plug bounding the viscous core, within a few channel widths of the entry region.

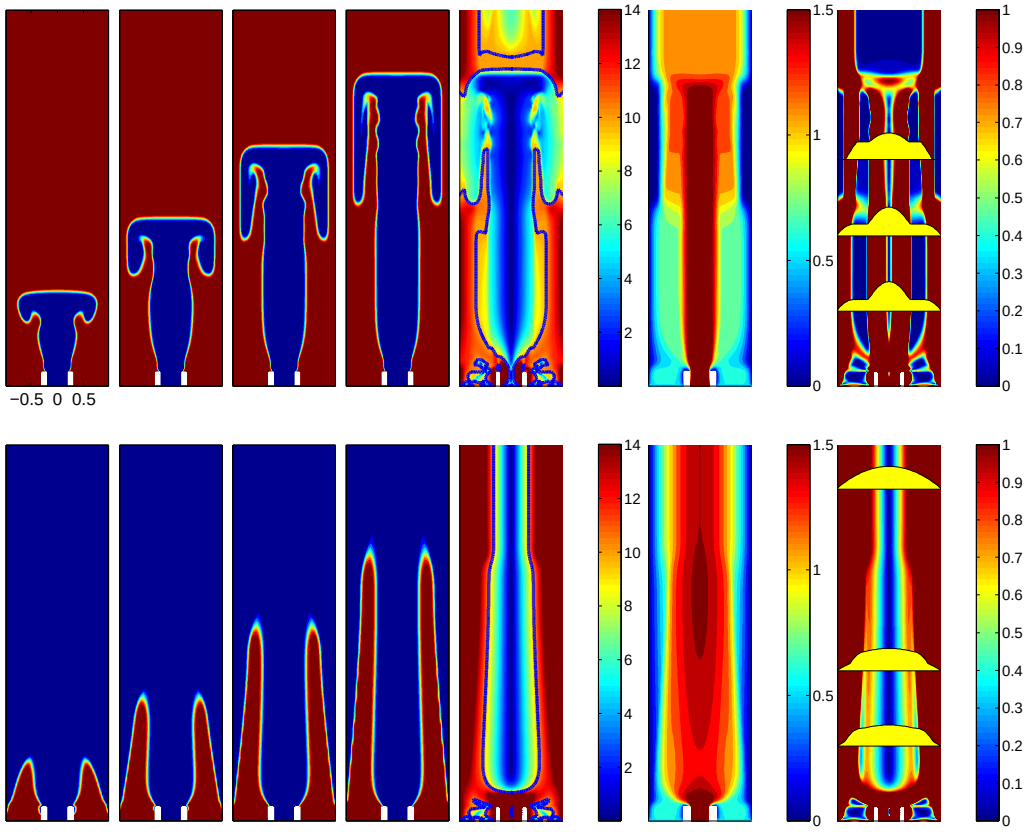

Figure 3.5: Typical start-up flows for $m = 1,\ B = 10,\ Re = 20,\ Y_i = 0.2,\ y_i = 0.4,\ L = 25$. Top row: inner fluid is injected into channel of outer fluid; bottom row: outer fluid is injected into channel of inner fluid. For both rows the first 4 frames show C at $t = 4,\ 8,\ 12,\ 16$. Thereafter we show for $t = 16$ the stress magnitude (with $\tau = B$ marked with the heavy line contour), the speed and the strain rate (with superimposed axial velocity profiles).

The numerical simulation follows that of our experimental practice in [55]. Initially the channel is filled with the Bingham fluid in steady flow. At $t = 0$ the Newtonian fluid is injected in the central inlet while the Bingham fluid is still injected in the outer inlets on either side of the central inlet. The relative balance of flow rates between the inlets is fixed by the far-field downstream velocity profile that one is seeking to establish. This balance is deduced from solution of the 1D base flows described earlier in §3.1.1.

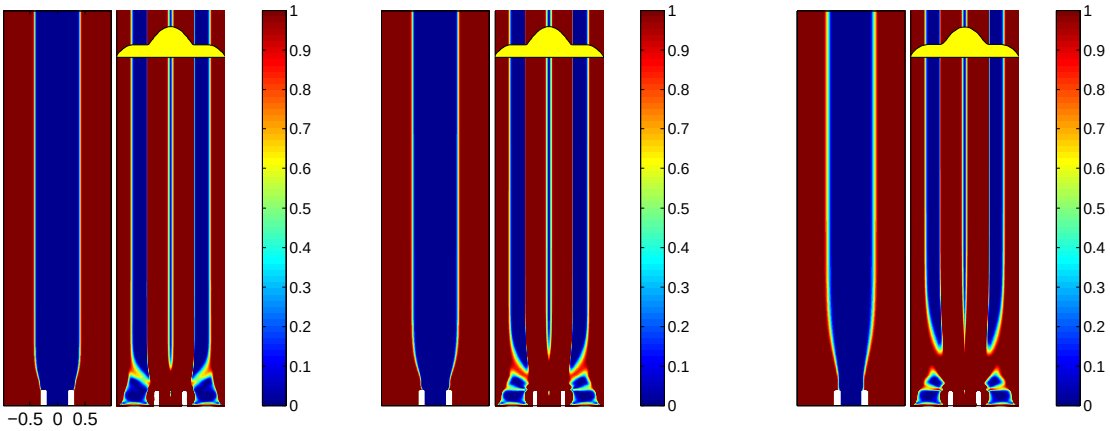

Figure 3.6: Examples of developed flows at $t = 100$ for parameters: $m = 1$, $B = 10$, $y_i = 0.4$, $Y_i = 0.2$, $L = 25$. From left to right: $Re = 5,\ 20,\ 40$. Each figure shows the fluid concentrations C (left) and the magnitude of the strain rate (right), with superimposed axial velocity profiles.

However, this procedure is not the only method of establishing these flows. Fig. 3.5 (bottom row) shows a different strategy, in which we first establish the Newtonian core fluid and then inject the outer lubricating fluid. The displacement front itself appears more stable than the plume formed when injecting the inner fluid, so mixing is reduced. The flow eventually develops into the same parallel flow, but takes longer as it is necessary to displace the Newtonian fluid from near the walls, where long drainage layers form. Depending on the costs of the fluids and other process constraints this method could be more attractive as a means of establishing the flows.

In Fig. 3.6 we show established flows at $t = 100$ for 3 different Re. We can observe that the entry length increases with Re but that the far-field velocity profile near the channel exit is near-identical in each case. From the results of our developing flow computations we can compute development lengths. As discussed in chapter 2 there are (at least) 3 different development lengths: (i) where the first unyielded fluid is found; (ii) where the flow concentration attains its steady profile, say L_c; (iii) where the flow velocity attains its steady

profile, say L_u. More precisely, for the latter two of these we define the development length as where the variation in the (concentration or axial velocity) profile varies by less than 1% in the downstream direction. Although there are slight quantitative differences in these development lengths, the main qualitative trends are the same as for the pipe flow. We present examples in Fig. 3.7, of variations in L_c & L_u with the ratio y_i/Y_i for different Re, m and B. The results are somewhat intuitive. Entry lengths increase with Re but decrease with m and B. The entry lengths are shortest at approximately $y_i/Y_i = 1$, with both expansion and contraction causing the lengths to increase.

The principal difference between the pipe and channel geometries is that asymmetrical instabilities may develop in the plane channel. However, for $Re < 100$ we have rarely observed symmetry breaking. For example for the results shown in Fig. 3.7, all the established flows are symmetrical and stable. Our parameter range is limited since we require that base far field flows are case 1 flows. However, within this restriction we have computed a range of different inlet width ratios and far-field base flow parameters. The base flows are independent of Re but we have a restriction on computational length of our domain, while keeping reasonable mesh resolution and acceptable computational times for a parametric study. As Re increases the development lengths increase and so it becomes increasingly time consuming to study the developing flow. Computing entry flows above $Re = 100$ becomes extremely time consuming.

Within the range of flows computed we have observed symmetry breaking in start-up flows only for base flows that are close to the case 1 - case 3 frontier in the (y_i, B, m) parameter space (see §3.1.1). These flows are characterised by having a large flow of the inner fluid, relative to the outer. An example of the type of symmetry breaking we observe is shown in Fig. 3.8. For $Re = 5$ a symmetric parallel flow develops whereas for $Re = 20$ the flow is unstable and asymmetric. At larger Re the degree of instability and mixing increase, suggesting an inertial origin to this behavior. For the base flow in Fig. 3.8

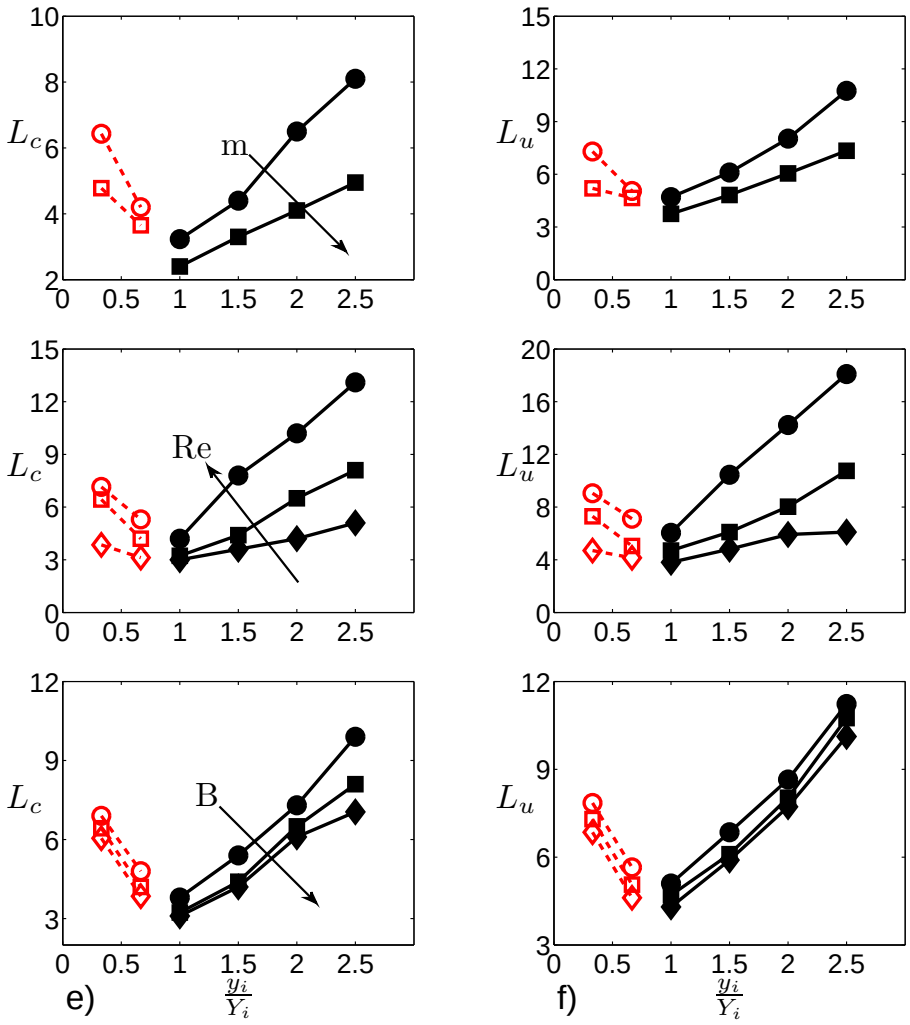

Figure 3.7: Effects of varying the flow parameters on velocity and concentration development lengths for the channel. Effect of viscosity ratio on: a) L_c and b) L_u, at $Re = 20$, $B = 10$ for $m = 1$ and $m = 10$. Effect of Re on c) L_c and d) L_u at $m = 1$, $B = 10$ for $Re = 5$, $Re = 20$ and $Re = 40$. Effect of B on e) L_c and f) L_u at $m = 1$, $Re = 20$ for $B = 5$, $B = 10$ and $B = 20$. The light symbols are computed for an inlet width $Y_i = 0.6$ (contraction flows of the inner fluid) and the dark symbols for $Y_i = 0.2$ (mostly expansion flows of the inner fluid).

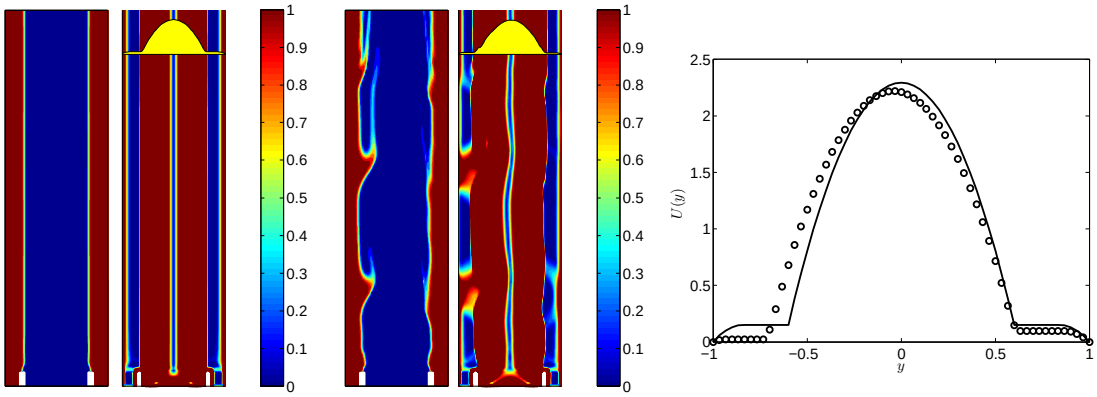

Figure 3.8: Symmetry breaking in developing flows: ($B = 10,\ y_i = 0.6,\ Y_i = 0.6,\ m = 1,\ L = 25$). Left hand images show concentration and strain rate colourmaps for $Re = 5$ at $t = 100$. Right-hand images show concentration and strain rate colourmaps for $Re = 20$ at $t = 100$, with overlay of exit velocity profile (computed vs analytical). Final image shows computed axial velocity at the exit compared with the symmetric base flow.

approximately 95% of the total flow rate takes place in the inner fluid layer. The velocity profile shown in Fig. 3.8 suggests that as symmetry is broken one of the Bingham fluid layers becomes close to stationary while the other layer flows. Since only 5% of the total flow is passing in these 2 outer layers any asymmetry is likely to lead to this type of intermittency. It is interesting to note that in analogous displacement flows (i.e. case 3 flows) the static residual wall layers are very stable; see e.g. [124]. In these case 3 flows the unyielded fluid abuts the wall, which prevents extensional strain rates, whereas here extension can break the plug. The repeating pattern of instability coupled with dispersive mixing is akin to the pearl and mushroom flows observed in [22, 23], but no longer symmetric.

3.3 Temporal stability

The second part of our study considers the stability of the established base flow. Linear stability of visco-plastically lubricated plane channel flows has been studied in [26], wherein the inner fluid was also assumed to be a Bingham fluid. Our flow configuration is therefore included in this analysis. The main result of [26] was to decouple the linear stability problems in the different fluid layers and hence tackle each one individually, with the result that the multi-layer flow is in fact more stable than the corresponding single fluid flow.

Here we are interested in nonlinear stability, where the fluid regions are fully coupled. We study the characteristics of temporal stability numerically by imposing a nonlinear perturbation on a periodic cell of the established base flow. The procedure is as follows. Having fixed a wavenumber α for the perturbation we set the axial distance of the periodic cell: $L = 2\pi/\alpha$. The analytical base solution is set as the initial condition and the numerical solution is integrated forward until convergence. This procedure establishes a numerical steady state, which is the flow which we perturb about, rather than the analytical base solution. After this, we add to the numerical steady flow an initial (periodic and divergence free) perturbation of given amplitude and study evolution of the computed transient flow. The numerical method is that described previously. The only change is the imposition of periodic boundary conditions in the x-direction. The spatial structure of these perturbations is described in appendix §B.

3.3.1 1D perturbations

As a test problem for the numerical method, we also consider the following 1D stability problem: $U(y) \mapsto U(y) + u(y,t)$, for which the 1D momentum balance is satisfied.

$$\frac{\partial u}{\partial t} = -\frac{\partial p}{\partial x}(t) + \frac{1}{Re}\frac{\partial}{\partial y}[\tau_{xy}(U+u) - \tau_{xy}(U)], \tag{3.15}$$

where the 1D constitutive laws are as in §3.1.1. Note that the 1D perturbation only admits a time dependent axial pressure gradient perturbation, which cannot be calculated as part of the solution. We therefore set the axial pressure perturbation to zero and study decay of the velocity $u(y,t)$.

It can be shown that for a 1D the interface is fixed. Hence the classical formulation of our 1D problem is as follows:

$$\frac{\partial u}{\partial t} = \frac{m}{Re}\frac{\partial^2 u}{\partial y^2} \qquad y \in [0, y_i) \tag{3.16}$$

$$\frac{\partial u}{\partial t} = \frac{1}{Re}\frac{\partial}{\partial y}[\tau_{xy}(U+u) - \tau_{xy}(U)] \qquad y \in [y_i, 1] \tag{3.17}$$

together with continuity of the shear stress and velocity at the interface. The perturbation vanishes at the walls.

This is a coupled parabolic system which may be integrated numerically for comparison with the 2D computations. To simplify, we use the Bercovier-Engelmann regularisation for the constitutive law, i.e. equation (3.14). We discretise using a semi-implicit finite difference scheme (approximating only the effective viscosity terms explicitly) and solve the resulting tri-diagonal system on each timestep using the Thomas algorithm. This can be compared with the numerical solution to the 2D problem, using the same 1D initial condition.

In general the comparisons are quite good. Although the 2D solution is fully nonlinear and 2D it does not break symmetry for suitably small Re & initial size of perturbation, $\|u\|_2(0)$. An example of this comparison is given in Fig. 3.9 where we compare the decay rates of the L^2 norm of the perturbation. We observe a small discrepancy between the results, but with identical decay rates. The decay is exponential in time, as would be expected for viscous fluids.

Figure 3.9 also shows comparison against an analytical upper bound for the decay, which we derive as follows. On multiplying (3.16) & (3.17) by $u(y,t)$

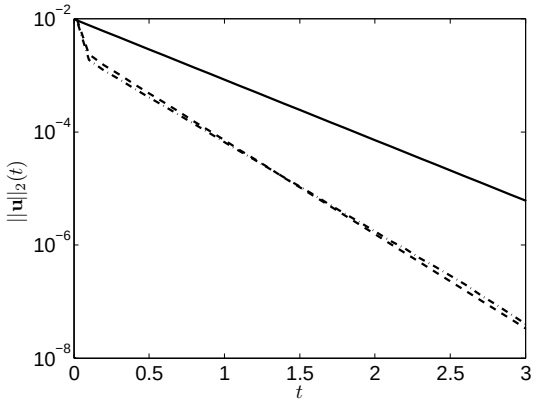

Figure 3.9: Comparisons of the decay of a 1D perturbation for $m = 10,\ y_i = 0.4,\ B = 20,\ Re = 1,\ \|u\|_2(0) = 0.01$: 1D code (–), PELICANS(-.), analytic bound (-)

and integrating over the individual fluid domains and summing we derive:

$$\begin{aligned}\int_0^1 \frac{1}{2}\frac{d}{dt}u^2 \,\mathrm{d}y &= -\frac{m}{Re}\int_0^{y_i} u_y^2 \,\mathrm{d}y \\ &\quad -\frac{1}{Re}\int_{y_i}^1 u_y[\tau_{xy}(U+u) - \tau_{xy}(U)] \,\mathrm{d}y \\ &\leqq -\frac{m}{Re}\int_0^{y_i} u_y^2 \,\mathrm{d}y - \frac{1}{Re}\int_{y_i}^1 u_y^2 \,\mathrm{d}y.\end{aligned} \tag{3.18}$$

Using the Poincaré inequality we have:

$$\frac{1}{2}\frac{d}{dt}\int_0^1 u^2 \,\mathrm{d}y \leqq -\lambda c_p \int_0^1 u^2 \,\mathrm{d}y, \tag{3.19}$$

where

$$\lambda = \min\{\frac{m}{Re}, \frac{1}{Re}\}, \quad c_p = \frac{\pi^2}{4}. \tag{3.20}$$

Finally, this gives the following exponential decay of $\|u\|_2$:

$$\|u\|_2(t) \leqq \|u\|_2(0)\mathrm{e}^{-\lambda c_p t} \tag{3.21}$$

3.3.2 General perturbations

For 2D perturbations we focus on 2 distinct initial conditions (case A & case B) that satisfy stress and velocity continuity conditions at the interface, plus the conditions of periodicity and incompressibility. These functions are normalised with an amplitude A such that for $A = 1$ the L^2 norm of the perturbation is equal to 1, i.e. A^2 gives the initial kinetic energy of the perturbation. The principal qualitative difference between the two initial conditions is that the case B perturbation is selected so that the unyielded plug region is initially undisturbed by the flow, whereas the case A perturbation breaks the plug. The y-dependency of the two initial perturbations is illustrated in Fig. 3.10 at fixed $\alpha x = 3\pi/2$.

3.3.3 Instability and asymmetry

We have carried out a similar range of simulations for the plane channel as for the pipe flow in chapter 2. For 2 different base flows and for $Re =$ 1, 10, 100, 1000 we have carried out sequences of simulations at increasingly large initial perturbation amplitudes A. This has been done for both case A and case B initial conditions. While no computational study can be considered fully comprehensive, the range of computations is wide enough to discern basic trends. A direct comparison with the pipe flow study in chapter 2 is not sensible as for the same base flow parameters the base flows and underlying flow rate ratio in each fluid layer is quite different (due to the radial geometry). However, the overall impression is that we have qualitatively similar results but that the plane channel flows destabilise at lower Re and lower A.

Figure 3.11 illustrates typical decays of the velocity perturbation with time

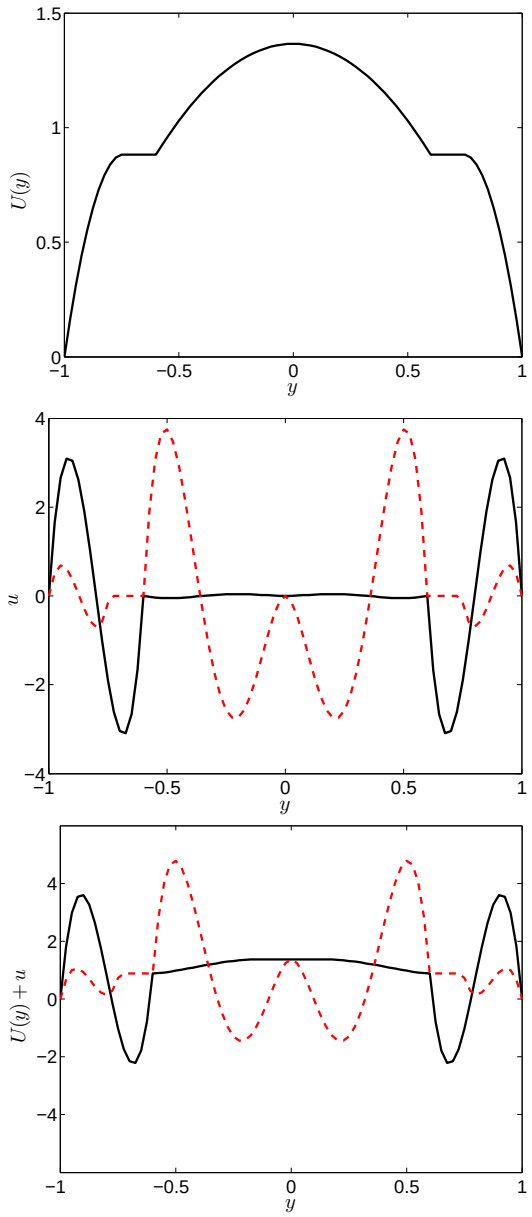

Figure 3.10: Top to bottom: y-dependency of the base flow, initial perturbations, base velocity plus initial perturbation: case A = broken line, case B = solid line. Perturbations are shown at fixed $\alpha x = 3\pi/2$ and for $A = 1$.

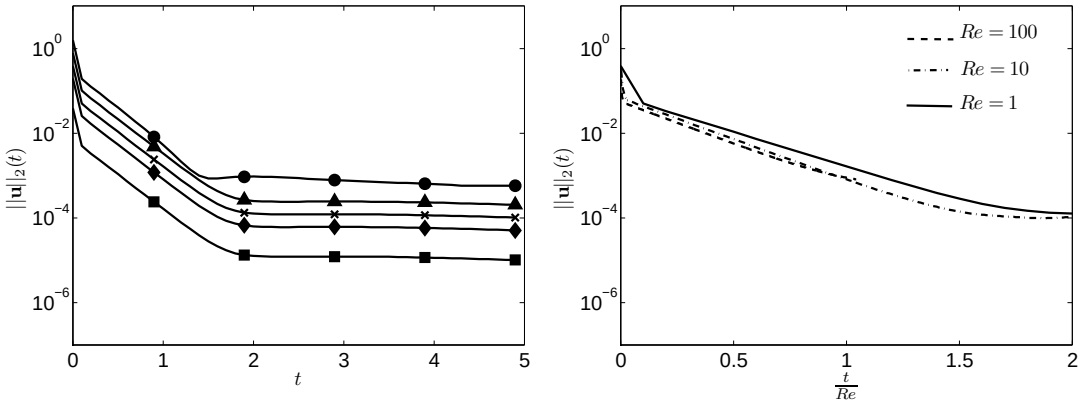

Figure 3.11: Decay of the velocity perturbation for case A initial perturbations ($m = 10$, $B = 20$, $y_i = 0.6$): left panel) $Re = 1$ and $A = 0.01$ (■), 0.05 (⧫), 0.1 (×), 0.2 (▲), 0.4 (•); right panel) $A = 0.1$ and line styles (−), (−−) and (−.) denote $Re = 1,\ 10,\ 100$, respectively.

for the case A initial conditions, showing variations with both amplitude A and Re. We see 3 different regimes. First there is a very short timescale over which we see rapid decay of the kinetic energy. This is followed by a second regime of exponential decay and finally a third regime of near constant perturbation energy. These 3 regimes are similar to those observed in the pipe flow computations of chapter 2. The initial short-time regime is associated with breaking and reforming of the plug region. The second regime is characteristic of viscous decay. The third region, where the kinetic energy plateaus, indicates the decay is over. For low amplitudes the final kinetic energy of the perturbation is close to the numerical residual tolerance in the iteration. However, as A increases the initial transient allows for an increasing amount of dispersion to take place before the kinetic energy decays. Hence the final energy plateau increases with A. For sufficiently low amplitudes A the final flow is indistinguishable from the base flow. The right panel of Fig. 3.11 plots $\|\mathbf{u}\|_2(t)$ for fixed A and various Re against a rescaled time: t/Re. This simply confirms the viscous origin of the second regime.

At larger A or Re we begin to see more interesting phenomena. As with

the pipe flow the case B initial perturbations are the less stable. These perturbations do not initially break the plug but consequently have larger gradients in the initial kinetic energy and the kinetic energy is distributed more in the inner fluid. For brevity we illustrate only the results from the case B perturbation. Figure 3.12 shows the concentration colourmap at $t = 20$ for a range of parameters A and Re. We notice that at moderate A or Re, instabilities that do not decay are frozen into the interface, i.e. when the interfacial shear stress decays below the yield stress before the perturbation in the central fluid has sufficiently decayed. These frozen-in shapes were also observed in the pipe flow study in chapter 2. However, now we also observe the main significant difference to the pipe flow. The observed perturbations no longer evolve symmetrically and even the frozen-in oscillations are generally asymmetric. As A or Re is increased further we observe significant distortion of the interface and plug region, which results in enough dispersive mixing that the flow does not regain its initial profile. It is also interesting to observe that the unstable concentration field evolves into a banded structure.

Figure 3.13 shows the temporal evolution of a case B perturbation that evolves into an asymmetric secondary flow. The top row shows the evolving strain rate and axial velocity profiles. The initial perturbation is of course symmetric. We can observe that in the left-hand side of the channel the perturbation decays faster and that an unyielded interfacial plug appears to partially re-form. In the right-hand side of the channel the flow disturbance is greater and the plug never fully re-forms.

3.4 Asymmetry, flow control and exotic effects

We finally present a range of results that both illustrate the robustness of the flow paradigm that we have studied and stimulate ideas for application.

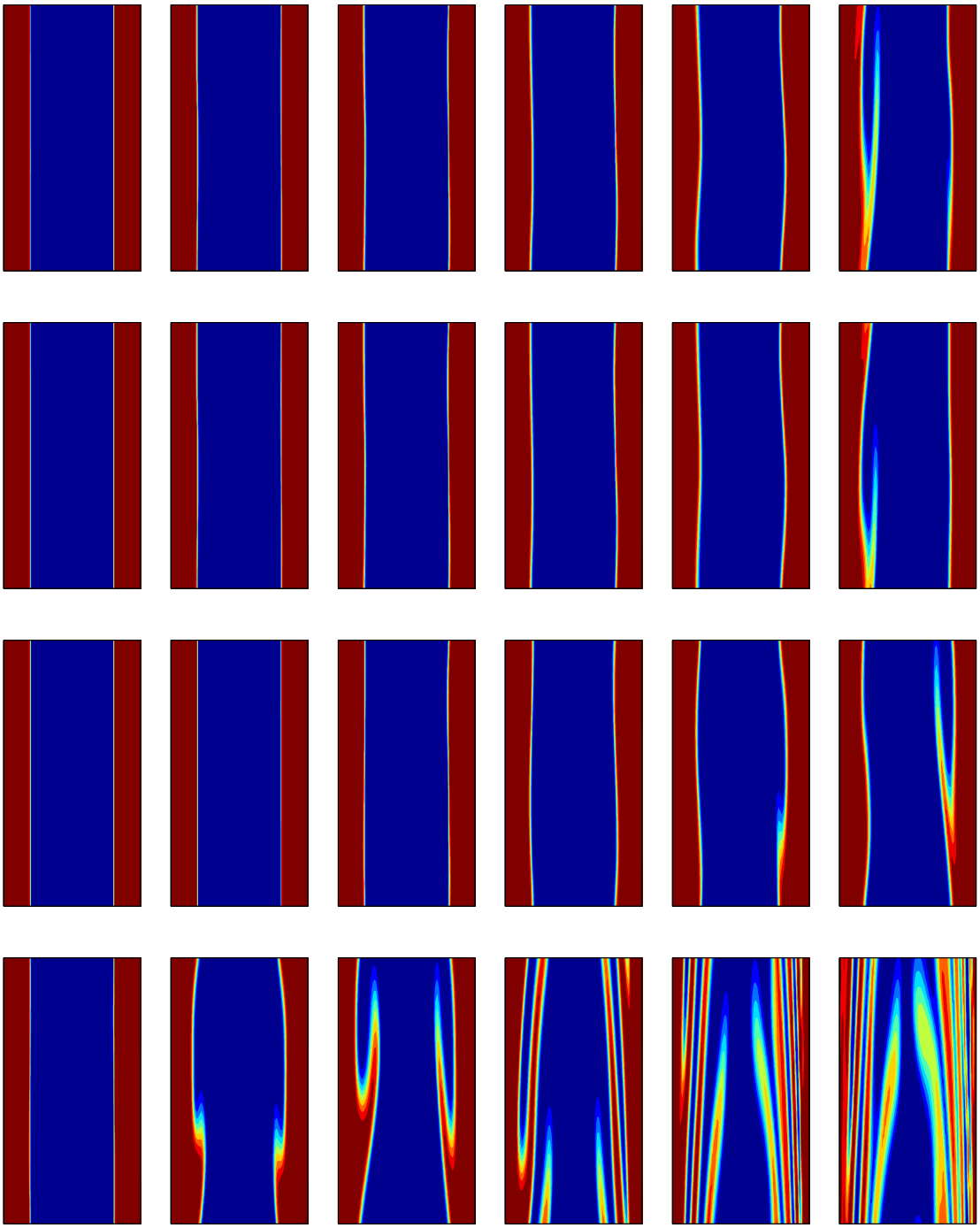

Figure 3.12: Concentration colourmaps for case B initial perturbation for $y_i = 0.6$ and $(m, B) = (10, 20)$, at $t = 20$. The rows from top to bottom show $Re = 1,\ 10,\ 100,\ 1000$. The columns, from left to right show the amplitudes: $A = 0.01,\ 0.05,\ 0.1,\ 0.2,\ 0.4,\ .6$.

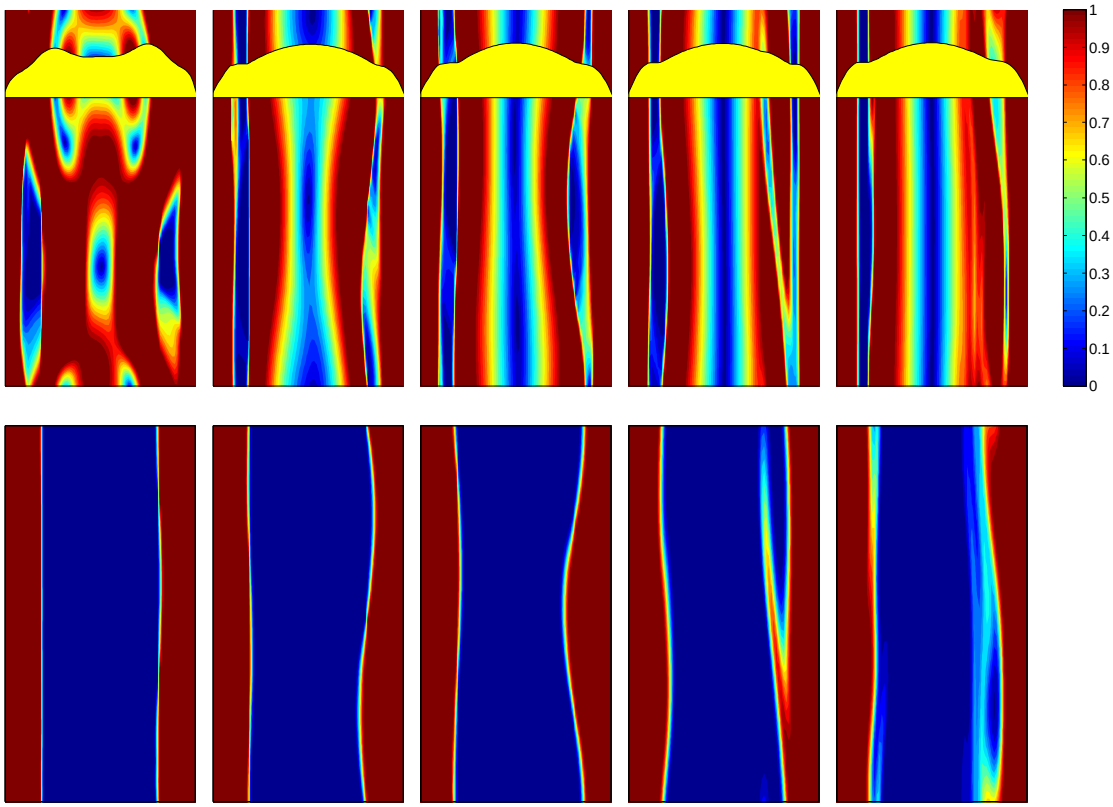

Figure 3.13: Asymmetric instabilities for a case B initial condition at $(m, B) = (10, 20)$ with $r_i = 0.6$, $A = 0.6$ and $Re = 100$. The figures are shown at $t = 0.3$, $t = 1$, $t = 2$, $t = 20$, $t = 50$ (left to right): top row = strain rate magnitude; bottom row = concentration.

3.4.1 Asymmetry and control

The first observation that we wish to emphasize is the importance of the base flow in flow design and control. Until now we have considered symmetric 3-layer base flows. These are the easiest to conceptualize and also to calculate. More generally, if we decide on a distribution of the flow rates between the 3 layers that is not symmetric we can compute an asymmetric velocity profile and interface positions. Alternatively, we can specify the interface positions and compute the unique velocity profile and hence the flow rate distribution

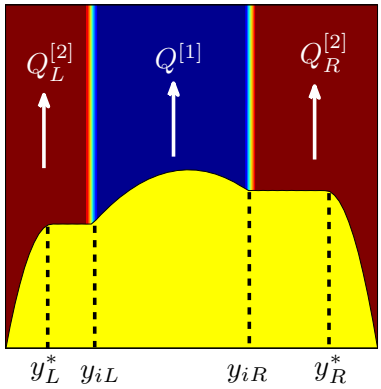

Figure 3.14: Schematic of an asymmetric base flow illustrating interface positions and flow rates.

between the layers.

Suppose for example that the base flow interfaces are at $y = y_{iL}$ and $y = y_{iR}$; see Fig. 3.14. Integrating the 1D momentum balance (3.2) we have

$$\tau_{xy}^{[1]} = \tau_{xy}^{[2]_L} = \tau_{xy}^{[2]_R} = -Gy + c,$$

in the respective layers (the superscript denotes the fluid and "L" and "R" the left and right layers, respectively). Here $G = -Re\frac{\partial p}{\partial x}$ and c is constant of integration. The velocity profiles for the base flow are found inverting the 1D constitutive laws and integrating the velocity gradient, assuming continuity of velocity at the interfaces ($y_{iL}\&y_{iR}$). The no slip condition at the walls determine c.

Having found $U(y)$ we integrate across each layer to give the respective flow rates in left-hand, central and right-hand layers: $Q_L^{[2]}$, $Q^{[1]}$ and $Q_R^{[2]}$, respectively. The constraint on the flow rate, due to scaling with the mean velocity is as follows:

$$Q_L^{[2]} + Q^{[1]} + Q_R^{[2]} = 2.$$

It may be shown that each of the flow rates increases monotonically with G and hence this constraint is used to determine G. The above procedure is

identical for any 1D multi-layer flow and is fairly straightforward. For at least some of these asymmetric base velocity profiles we will maintain an unyielded plug at both interfaces and these flows should also be suitable as stable visco-plastically lubricated flows.

What we have found surprising is how easy these asymmetric flows are to establish and control via the flow rates. To demonstrate this fact we have computed a number of start up flows for the same base parameters ($B = 10$, $Re = 5$, $m = 10$), but with differing asymmetries. The width of the inner fluid inlet is always $2Y_i$ (where here $Y_i = 0.2$) and the base flow is designed so that the width of the inner fluid layer is also $2Y_i$. The start up flow follows the usual pattern whereby the frontal region displaces up the channel and is eventually advected from the channel, leaving behind a steady flow. Four different 2D simulations have been computed, as detailed below. The start up and final steady flows are illustrated in Fig. 3.15 and the parameters (flow rates and interface positions) are tabulated in Table 1 for convenience.

- Simulation 1 is the standard symmetric simulation: the inlets are symmetrically located and the flow rates are symmetrically distributed (Fig. 3.15a).

- Simulation 2 distributes the flow rates symmetrically, but the core fluid inlet is asymmetrically positioned: $y \in [0, 2Y_i]$ (Fig. 3.15b).

- Simulation 3 has the asymmetric core fluid inlet, $y \in [0, 2Y_i]$, and also the asymmetric distribution of flow rates corresponding to the asymmetric base flow (Fig. 3.15c).

- Simulation 4 has symmetric inlets, $y \in [-Y_i, Y_i]$, but with asymmetric distribution of flow rates corresponding to the asymmetric base flow (Fig. 3.15d).

We observe that in the first two simulations the exit velocity profile is symmetric, while in the last two simulations the exit velocity profile is asymmetric.

Fig	Y_{IL}	Y_{IR}	y_{iL}	y_{iR}	$Q^{[1]}$	$Q^{[2]_L}$	$Q^{[2]_R}$
(3.15.a)	-0.2	0.2	-0.2	0.2	0.4684	0.7658	0.7658
(3.15.b)	0.0	0.4	-0.2	0.2	0.4684	0.7658	0.7658
(3.15.c)	0.0	0.4	0.0	0.4	0.46	1.0213	0.5187
(3.15.d)	-0.2	0.2	0.0	0.4	0.46	1.0213	0.5187

Table 1: Flow data for fig 3.15.

Looking at the comparison of exit velocity profiles we see that in each case the numerical axial velocity is very close to the predicted analytical solution. Note that in each of the 4 simulations it is the desired base flow (and consequent distribution of flow) that determines the far-field flow. Secondly, note that the flow development appears robust with respect to these (quite significant) changes in the inlet conditions.

To demonstrate that these flows can be achieved at higher Re, Fig. 3.16 show results at $Re = 20$ and $Re = 40$ for the same simulation as in the bottom row of Fig. 3.15. Again the flow develops stably from the initial channel full of Bingham fluid and the same final asymmetric 3-layer flow is achieved. The larger Re results in a slightly longer development length, but otherwise there is little difference.

It is natural to question whether this robustness can be exploited in controlling the flow position in a transient setting. Either one could move the inlet nozzle and/or one could simply control the flow rates into the different layers upstream. To test this we alternate between two asymmetric flows by switching instantaneously from a left-handed inlet to right-handed inlet, while at the same time adjusting the flow rates appropriately so that the far-field base flow should converge. The spatial distributions of imposed flow rate and inlet concentration are shown in Fig. 3.17. The results of the simulation are shown in Fig. 3.18. The initial flow development is asymmetric, with he central core to the left of the channel, at $t = 20$ we switch the central layer to the right hand side of the channel by changing both inflow rates and inlet position. It can be

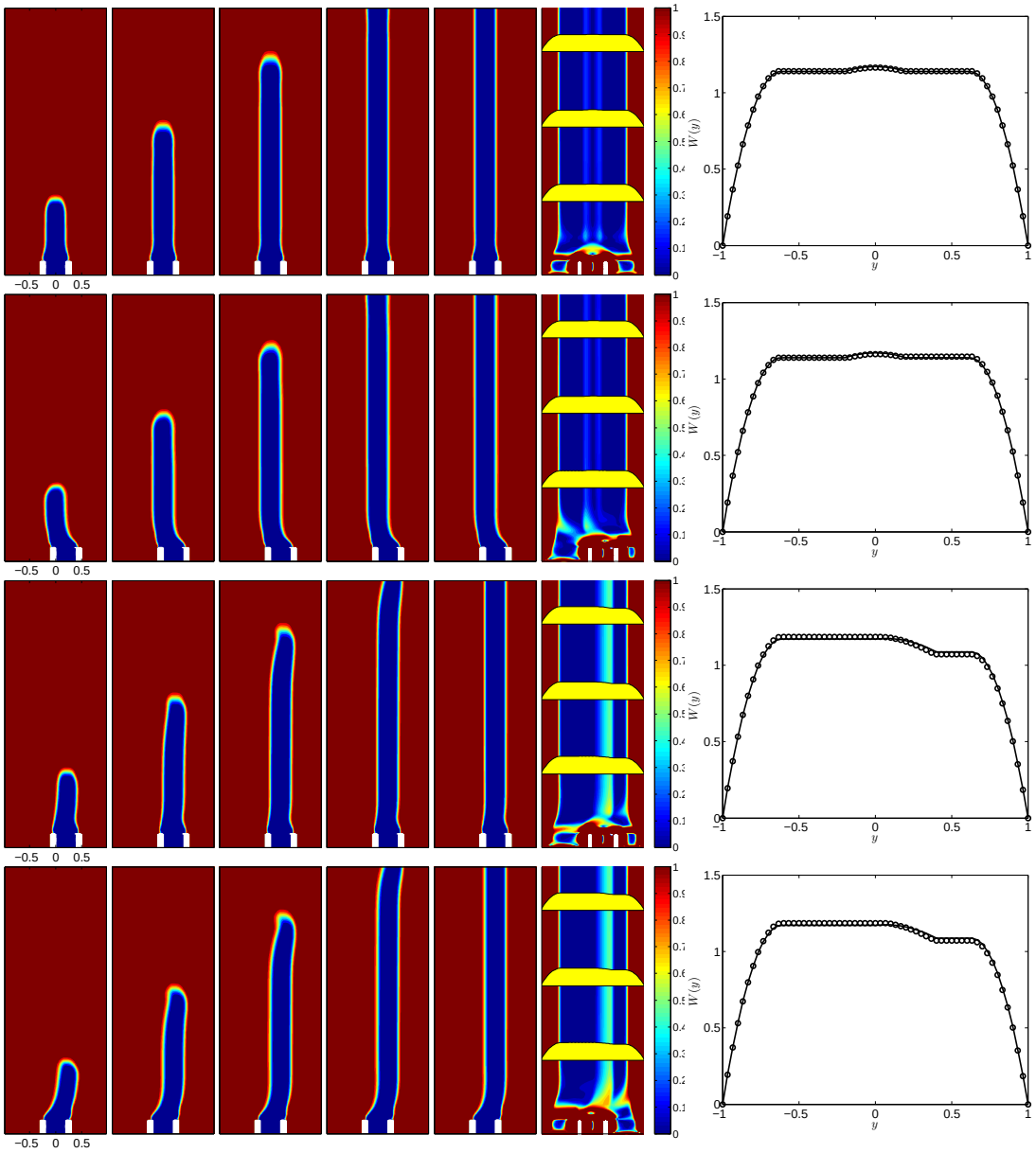

Figure 3.15: Illustration of asymmetrical start-up flows and steady flows: $B = 10$, $Re = 5$, $m = 10$, $L = 18$. In each row we present concentration fields for $t = 4,\ 8,\ 12,\ 16,\ 100$. The next colourmap plots the magnitude of the strain rate, with axial velocity profiles superimposed, at $t = 100$. The final image shows the exit velocity profile for the established flow, compared to the analytical solution (solid line), at $t = 100$.

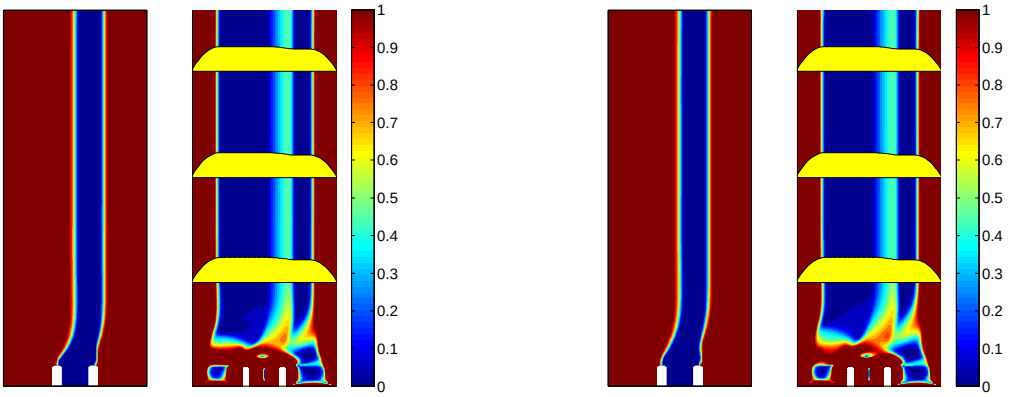

Figure 3.16: The simulation of Fig. 3.15 (bottom row) for $Re = 20$ (left) and $Re = 40$ (right) at $t = 100$.

seen that there is a small region where the abrupt step change ruptures the interface, but then the stable flow re-establishes. At $t = 30$ we again switch the central layer back to the left-hand side of the channel. Again the small region of rupture is observed. The rupture might be reduced by imposing a more gradual change in flow rates and inlet position. Note also that the change in inlet position is not strictly necessary in order to control the downstream flow asymmetry (see our earlier Fig. 3.15), but doing so does tend to reduce the development length required for establishing the new parallel flow.

3.4.2 More complex multi-layer flows

Next we look at the possibility of introducing more fluid layers into these flows. Note that purely in terms of the final axial base flow there is no essential difficulty in having additional layers. This is simply an exercise in mathematics to compute flows of increasing algebraic complexity. However, establishing such multi-layer flows will induce additional stresses at the inlet while also reducing the thickness of stabilizing unyielded fluid layers. Therefore, there are questions about how easy it will be to establish multi-layer flows of increasing complexity. Numerically there are also additional potential costs in simulation.

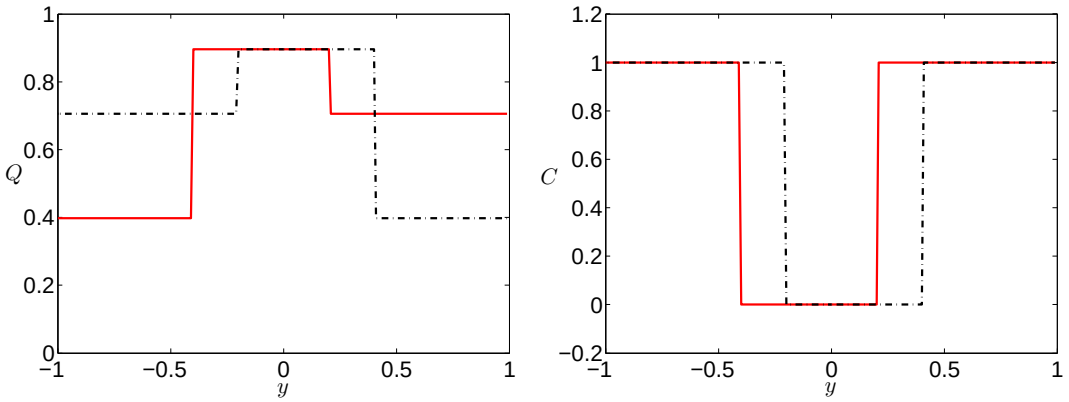

Figure 3.17: Spatial distributions of inflow rates (left) and fluid concentration (right) for the moving inlet example in Fig. 3.18. Solid line indicates initial left-handed configuration with broken line illustrating the right-handed asymmetry.

First, one would want to refine the mesh sufficiently to capture the layers and particularly the unyielded layers. Second, as the layers thin computations should be performed with the augmented Lagrangian method to ensure that unyielded layers do not deform.

To demonstrate that more complex layering patterns are possible we demonstrate a 7-layer flow. We first select parameters such that the symmetric 3-layer base flow has a suitably wide plug. The simulation starts by establishing the 3-layer symmetric flow. Having done this, two layers are injected in the interior of the two plug regions. This inlet configuration is maintained for a finite time and then we switch back to the 3-layer inlet control. The distributions of inlet flow rates and fluid concentrations are illustrated in Fig. 3.19. The results of the simulation are shown in Fig. 3.20. We observe that apart from dispersive spreading at the initial injection of the additional layers, the 7-layer flow is stably and uniformly established, and returns to the 3-layer flow in a controlled manner.

Note that in our case for simplicity we have used the same Newtonian fluid injected in the additional layers. Of course different fluids could be used to

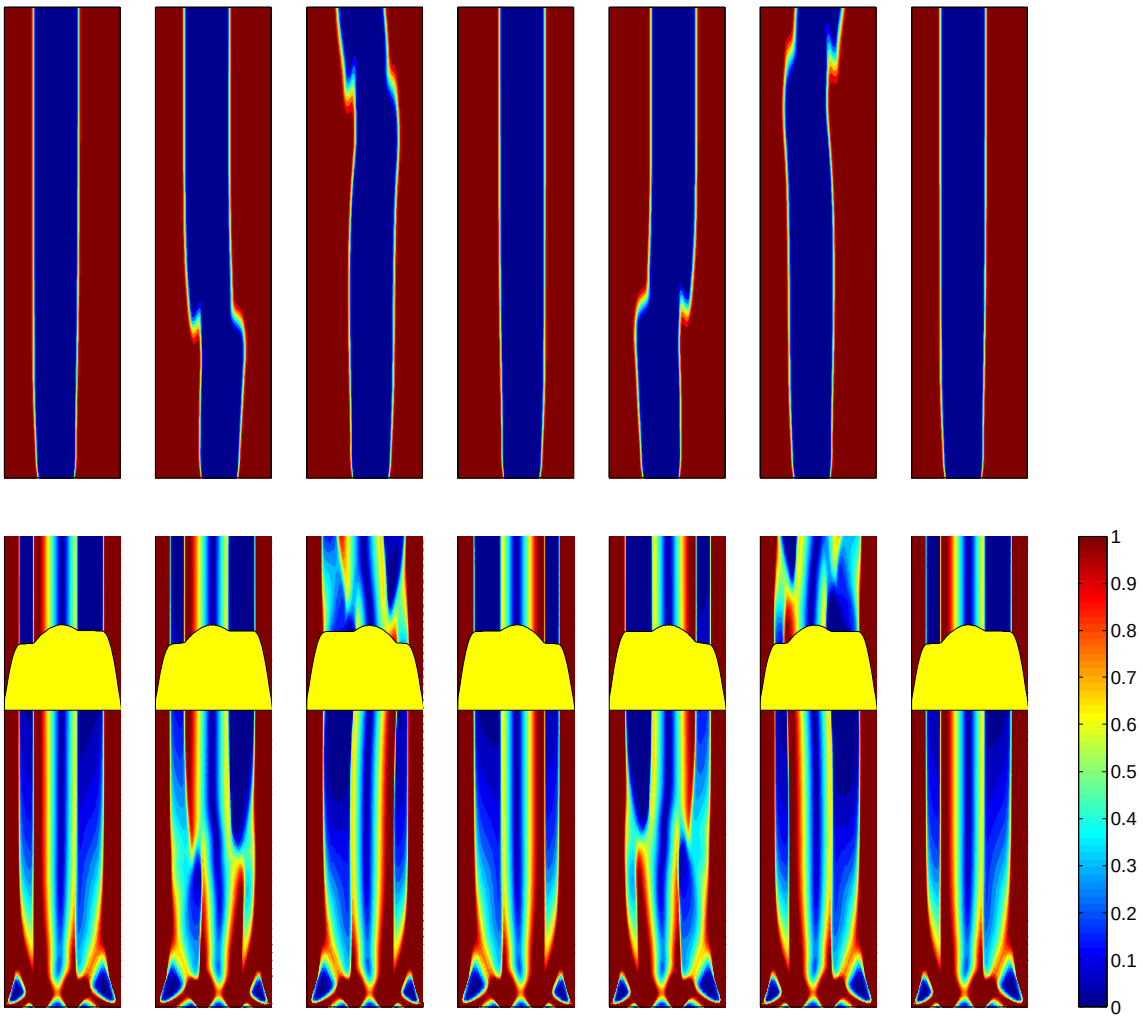

Figure 3.18: The effects of step changes in inlet flow rates and position for parameters $m = 1$, $B = 20$, $Re = 40$, $L = 8$. Top row illustrates the fluid concentration. Bottom row illustrates the magnitude of the rate of strain, with an axial velocity profile superimposed. Times shown are $t = 20,\ 22,\ 26,\ 30,\ 32,\ 36,\ 40$.

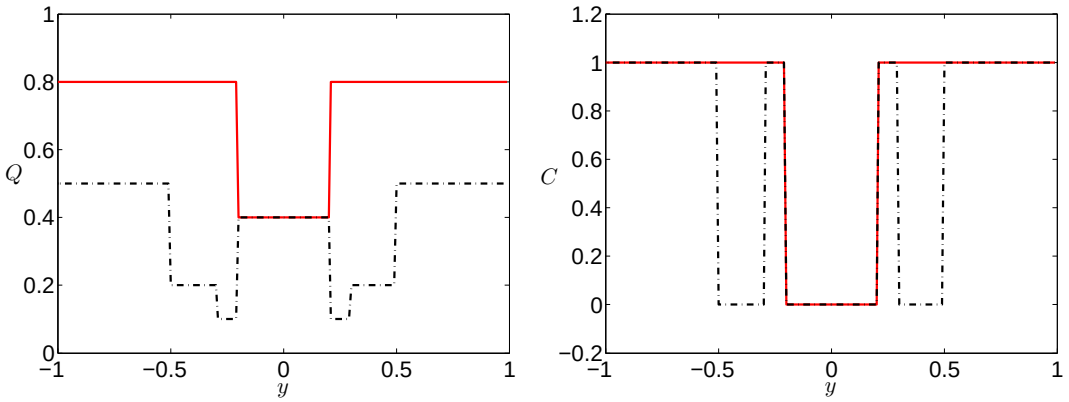

Figure 3.19: Spatial distributions of inflow rates (left) and fluid concentration (right) for the 7-layer flow example in Fig. 3.20. Solid line indicates the initial and final 3-layer flow controls; the broken line illustrates the inlet control for the 7 layer flow, at intermediate times.

construct laminated flows of very different properties. It is also possible to embed an unyielded yield stress fluid in the channel center (ensuring that it is unyielded at the interface), lubricated by thin Newtonian wall layers, and then add additional layers of fluid within the plug.

3.4.3 More exotic flow effects

As a final example we combine many of the techniques of the previous examples: moving multiple inlets, varying the flow rates, turning on and off new inlets. By judicious control of these variable we are able to "write" within the inner unyielded core, and have these letters advect along the channel. As an example we show in Fig. 3.21 the loci of the center of 3 inlet channels which inject Newtonian fluid at constant rate over a fixed time interval, with Bingham fluid injected elsewhere along the channel inlet. The resulting flow is shown at different time intervals Fig. 3.22. by generalising this methodology we are able to produce the flow in Fig. 3.23. Whilst such effects are mostly decorative, it is still impressive that stability is largely preserved as these flows are established.

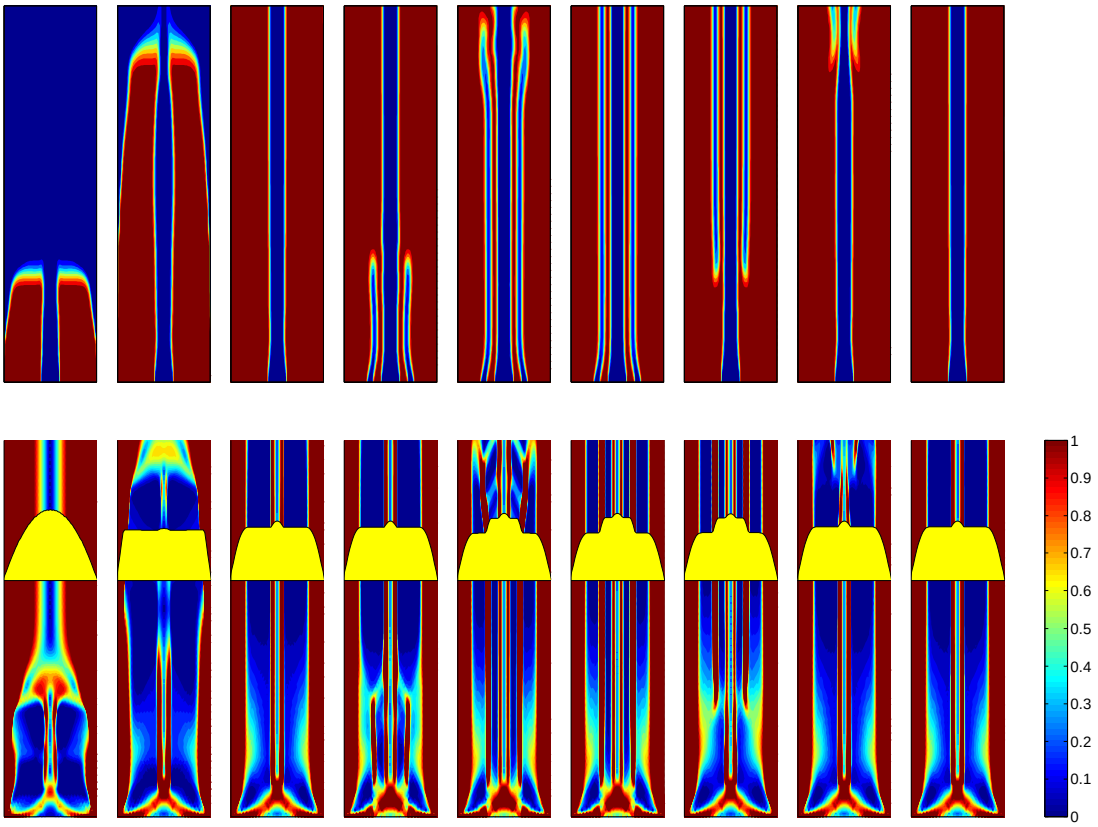

Figure 3.20: Example of a 7-layer flow for $m = 10,\ B = 10,\ Re = 5,\ L = 8$ for the flow control of Fig. 3.19. Top row shows fluid concentration distribution and the bottom row shows the magnitude of the strain rate, with superimposed axial velocity profiles. Times shown: $t = 2,\ 6,\ 45,\ 52,\ 56,\ 100,\ 102,\ 106,\ 150,$ from left to right.

Some dispersion is observed, but note that we have not paid special attention to control of acceleration/deceleration of the inlets and/or gradually varying the flow rates - these are produced using crude on/off controls.

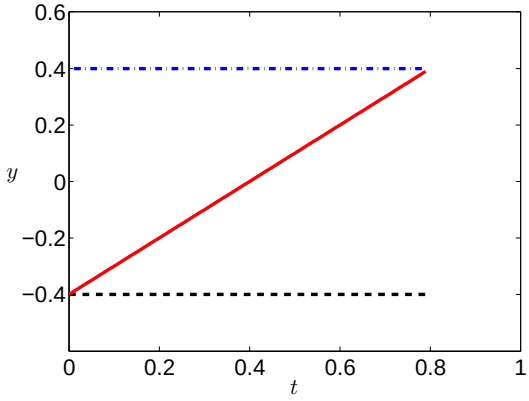

Figure 3.21: Loci of the center of the 3 inlet channels used to inject the letter "N".

3.5 Summary and discussion

The first part of this chapter was focused at start-up flows and establishment of multi-layer configurations. We have shown that multi-layer flows can be established by injecting either fluid into a channel full of the other fluid, in steady motion. This indicates an inherent robustness to the flows. We have tested various flow configurations admitting case 1 base solutions (with a plug at the interface) and in most cases have been able to establish the multi-layer flow, for $Re \leq 100$ (limited by computational cost). The development lengths decrease with either B or m, both of which tend to increase viscosity of the fluids, and increase with Re. For different ratios of inlet width ($2Y_i$) to width of the core fluid in the established flow ($2y_i$) we observe that the development lengths are smallest when $y_i \approx Y_i$.

We have also considered nonlinear temporal stability via computation. After benchmarking against a simpler 1D stability problem, we have run a range of simulations using 2 different initial conditions, selected to be divergence free and to either break the plug initially or to leave it intact (cases A and B, respectively). For low enough Re or amplitude A^2 of the initial kinetic energy, we observe stable flows with decay of the energy norm of the perturbation.

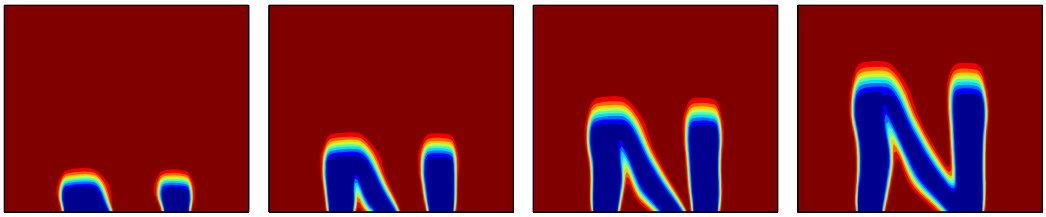

Figure 3.22: Flow resulting from the 3 moving inlet channels of Fig. 3.21.

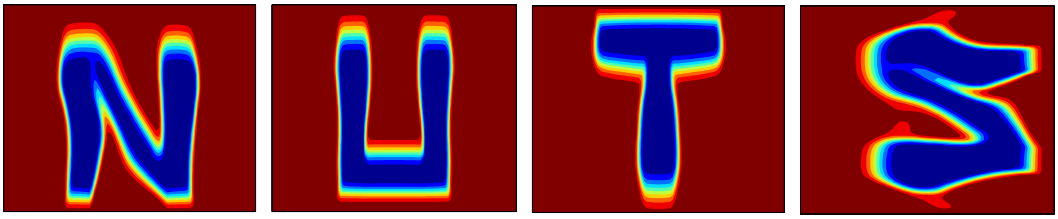

Figure 3.23: NUTS.

All the features discussed above are qualitatively very similar to the core annular pipe flows considered in chapter 2. This suggests that these features may be more general for other duct flows where we keep an unyielded plug at the interface. Having said this we do note a number of differences. Firstly, we have observed instability coupled to symmetry breaking of the flow. This arises in the start-up flows, apparently in situations where the flow rate passes mostly through the inner fluid layer, and is inertial in origin. It also arises in the temporal stability calculations. In these results, observed instabilities are nearly always asymmetric and arise via increases in either Re or A.

The second difference with the pipe flow is that instability arises at lower Re and A. In chapter 2 we did not observe any instability at all for start-up flows (for $Re \leq 100$), but here we have. In temporal stability calculations, the axisymmetric flows of chapter 2 remained stable for $A \geq 1$ and $Re \geq 100$ in

some cases. Of course the base flows are different in the two geometries and in making computational studies of instability we are vulnerable to the choice of initial conditions and any particular susceptibility of the flow to specific perturbations (which is unknown in general). Nevertheless, the evidence is that the channel flows are less stable.

Apart form the symmetry breaking, the main novelty of our results comes in the last section of this chapter, where we have purposefully explored the flexibility of these flows in producing specific controlled effects. The main point to emphasize in all these flows is that control (or design) of the flow is entirely via an understanding of the established parallel flows. Mathematically these flows are easy to compute: algebraically there is of course complexity increasing with the number of layers, fluids etc., but in principle all such problems are calculable.

We have presented a number of examples. The asymmetric base flows indicate how asymmetric multi-layer products could be stably produced. The 7-layer flows are an extreme example of this. Our transient variation of flow asymmetry shows that online control could be applied and the final example of writing in the core fluid shows an admittedly extreme example. In each of the transient flows we must emphasize that our control strategies are simplistic in the extreme: step or ramp changes in position and flow rate only, in each of the flow inlets. We do see dispersive effects at the corners/edges of some of the structures produced, but suspect that much of this could be reduced via smoother flow control and possibly with immiscible fluids.

Chapter 4

Visco-plastically lubricated flows of viscoelastic fluids: Experiment [1]

The present chapter serves to extend the breadth of experimental observations of VPL (Visco-Plastically Lubricated) flows by considering viscoelastic core fluids. Many industrial multi-layer flows involve fluids with viscoelastic properties. Therefore, the feasibility of establishing VPL flows with viscoelastic core fluids is inherently of interest. Although viscoelastic fluids have been studied within the context of linear stability in [86], this is a completely different flow configuration. We are unaware of any experimental, analytical or computational study of the core-annular VPL flow using a viscoelastic core. Our study has 2 principal objectives. Firstly, we seek to definitively demonstrate the experimental feasibility of this type of flow in a laboratory environment. Secondly, we should like to understand how viscoelasticity might affect design of the inlet geometry, e.g. the effects of downstream contraction and expansion.

An outline of this chapter is as follows. Below, in §4.1 we give a brief outline of the base flow we are trying to achieve, showing that for steady 1D shear flows this is not affected by the fluid elasticity. This helps to distinguish the 3 base types of flow possible in the core-annular configuration and delineate

[1] A version of Chapter 4 has been submitted for publication (under review). [S. Hormozi], D.M. Martinez and I.A. Frigaard. Stable core-annular flows of viscoelastic fluids using the visco-plastic lubrication technique [51].

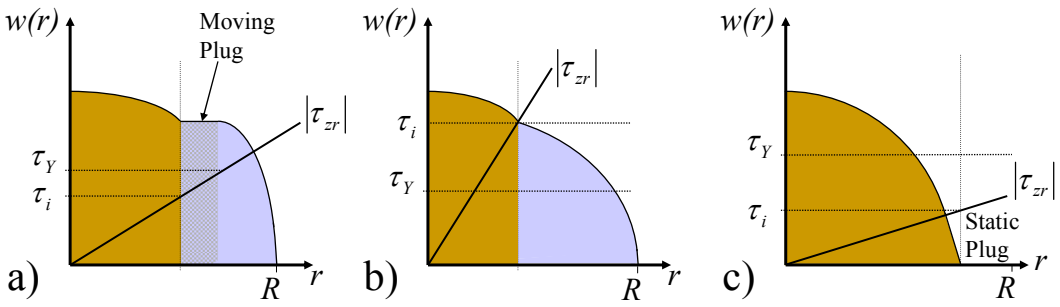

Figure 4.1: Schematic of the 3 base flow types for an iso-density core-annular VPL flow: a) *Stable* (the desired VPL flow configuration, with an unyielded plug at the interface); b) *Unstable* (meaning yielded at the interface); c) *Static* (meaning an unyielded plug is attached to the wall).

those that may be stable VPL flows. This is followed in §4.2 by an overview of the experimental setup and scope of the study. Results are presented in §4.3. These are divided into calibration studies, those that demonstrate stable/unstable VPL flows with a visco-elastic core, and those that consider the effects of inlet geometry. The chapter finishes with concluding remarks in §4.4.

4.1 Multi-layer flows with a visco-elastic core

We consider a fully developed axisymmetric core-annular pipe flows of 2 fluids. We do this under the assumption that the same constant pressure gradient ($P = -Gz$) acts in both fluid layers. This simplifying assumption can be relaxed to allow for different constant axial pressure gradients in each fluid, but this does not affect the type of base flow velocity that we derive. As our main purpose is to highlight the relation between shear stress and velocity, we do not consider the more general case.

We either assume that the fluids are immiscible with zero surface tension (infinite capillary number) or are miscible but at infinite Péclet number. We denote the velocity components in radial, azimuthal and axial directions

respectively, by (u, v, w). From symmetry arguments the stress tensor components $\sigma_{ij}^{[k]}$ are:

$$\begin{bmatrix} -P+\tau_{rr}^{[k]} & 0 & \tau_{rz}^{[k]} \\ 0 & -P+\tau_{\theta\theta}^{[k]} & 0 \\ \tau_{zr}^{[k]} & 0 & -P+\tau_{zz}^{[k]} \end{bmatrix} = \sigma_{ij}^{[k]}. \tag{4.1}$$

In a viscoelastic fluid (fluid 1) $\tau^{[1]}$ is non-deviatoric and contains both viscous and elastic contributions. In an inelastic fluid (fluid 2) $\tau^{[2]}$ is the deviatoric stress tensor. Since the flow is fully developed and axisymmetric the stress components ($\tau_{ij}^{[k]}$) vary only in the radial direction and the velocity reduces to $(0, 0, w(r))$. Hence, the momentum equations reduce to

$$\frac{\partial P}{\partial r} = \frac{1}{r}\frac{\partial}{\partial r}[r\tau_{rr}^{[k]}] - \frac{\tau_{\theta\theta}^{[k]}}{r}, \qquad k = 1, 2 \tag{4.2}$$

$$\frac{1}{r}\frac{\partial P}{\partial \theta} = 0, \tag{4.3}$$

$$\frac{\partial P}{\partial z} = \frac{1}{r}\frac{\partial}{\partial r}[r\tau_{rz}^{[k]}] - \rho_k g, \qquad k = 1, 2 \tag{4.4}$$

where ρ_k is the density of fluid k. Differentiating (4.2) with respect to z confirms that the axial pressure gradient must be independent of r. The shear stress τ_{rz} is obtained from the axial momentum equation (4.4), which integrates to:

$$\tau_{zr}^{[1]} = \frac{r}{2}\left[\frac{\partial P}{\partial z} + \rho_1 g\right], \quad 0 \le r \le r_i, \tag{4.5}$$

$$\tau_{zr}^{[2]} = \frac{r}{2}\left[\frac{\partial P}{\partial z} + \rho_2 g\right] + \frac{(\rho_1 - \rho_2) g r_i^2}{2r}, \quad r_i \le r \le R, \tag{4.6}$$

In all the flows we consider the outer fluid is a visco-plastic fluid, with a yield stress τ_Y and no elasticity. The inner fluids have no yield stress, but could be visco-elastic. In the outer fluid, in those parts where the shear stress exceeds the yield stress, the fluid is nonlinearly viscous and from the form of

the velocity we have that

$$\tau_{rr}^{[2]} = \tau_{\theta\theta}^{[2]} = \tau_{zz}^{[2]} = 0.$$

The shear stresses are continuous through the yield surface but are indeterminate within a plug region. Thus, non-zero normal stresses are not generated at the yield surface but are possible within any unyielded plug region. However for the established flows we consider, the normal stresses within the plug could vary only with r, would need to satisfy the momentum equations and jump conditions at the interface, and the magnitude of the deviatoric stress must lie below the yield stress.

If the inner fluid is inelastic we also have

$$\tau_{rr}^{[1]} = \tau_{\theta\theta}^{[1]} = \tau_{zz}^{[1]} = 0.$$

If the inner fluid is viscoelastic the viscous part of the normal stresses is zero, but there can exist non-zero elastic components. Assuming an established parallel flow, the elastic part of $\tau_{rr}^{[1]}$ contributes to the interfacial stress but the elastic part of $\tau_{zz}^{[1]}$ does not, and so can be discontinuous across the interface. The separation of the deviatoric stress into elastic and viscous components depends upon the constitutive relation that describes the rheological behaviour. However, for the moment suppose that we measure the steady shear rheology of the inner fluid, i.e. in fully relaxed elastic state. This steady shear flow curve gives a viscometric relationship of form

$$\tau_{zr}^{[1]} = \mu_1 \left(\left| \frac{\partial w}{\partial r} \right| \right) \frac{\partial w}{\partial r},$$

where μ_1 may have components stemming from polymer and solvent constituents.

For a given pressure gradient and desired interface radius r_i in the established base flow it is straightforward to substitute the shear rheometry data

into (4.5) and (4.6) integrate to find the velocity field in each fluid, and eventually the required flow rates in inner and outer fluids, which we denote by Q_1 and Q_2, respectively. Provided that the flow curves for the shear rheology of the 2 fluids exhibit a monotonically increasing relationship, the mapping

$$(\frac{\partial P}{\partial z}, r_i) \mapsto (Q_1, Q_2)$$

will be one-to-one and invertible. The integration of (4.5) and (4.6) can either use a numerical approximation of the flow curve or could be based on a closed-form constitutive model (fitted to the flow curve data). Both approaches have been adopted before in [55] and the only difference here is that density difference can potentially be incorporated.

Assuming $\rho_1 = \rho_2$, (following [55]), there are three distinct types of base velocity profile, $\mathbf{u} = (0, 0, w(r))$, that may arise, according to the values of interfacial shear stress, wall shear stress and yield stress. These are illustrated schematically in Fig. 4.1. The type of velocity that is of primary interest here is that for which the inner core fluid is surrounded by a ring of unyielded/plug fluid, denoted here as *stable*. The other types of base velocity profile are denoted *unstable* and *static*. The former refers to the case for which the outer fluid is yielded at the interface and the latter refers to the case in which the outer fluid is completely unyielded and remains fully static.

This simple multi-layer flow model, based on the shear rheology, forms the basis for our experimental design. If one specifies the flow rates of the individual fluid phases, the pressure drop and the radial interface position are uniquely determined. Conversely (and perhaps more obviously) specifying the pressure drop and radial interface position uniquely determine the flow rates in the individual fluid phases. Later, we indicate the flow maps in both (Q_1, Q_2) and $(|P_z|, r_i)$ spaces. In our experiments we fix the two pump flow rates (Q_1, Q_2) and the simple model predicts the expected radial position of the interface. The predicted pressure gradient is of less direct interest but does dictate the flow type (see Fig. 4.1) and hence gives a prediction of where the

transition from stable to unstable base flows is, according to the values of the interfacial stress and yield stress of the outer fluid.

We see that from the perspective of the base flow velocity profile, the shear rheology is sufficient to determine the profile. This does not require a specification of the elastic and viscous parts of the stress tensor. The normal stresses may be ignored in this calculation. We consider elastic effects further in interpreting our results.

4.2 Experimental description

A schematic of the experimental multi-layer flow loop is shown Fig. 4.2. A 4 m long plexiglass pipe of radius 25.4 mm is attached to a C-Channel which is bolted to the ground. Approximately 60 L of both the inner and outer fluids are stored in separate reservoirs. A progressive cavity pump was used to pump the outer fluid directly from the reservoir to the manifold inlet, which is located at the bottom of the plexiglass pipe. The manifold consists of 8 inlet ports of 6.35 mm inner diameter (ID), equally distributed along the circumference of the pipe. The total flow rate of the outer fluid is measured with a magnetic flow meter (FMG-400 series from http://www.omega.com) which is connected to a computer for data logging purposes. The flow rate of the inner fluid is measured with a paddle wheel flow meter (model DRG-1105N1F300, from http://www.kobold.com) which is also connected to a computer. The inner fluid is injected on the central axis of the pipe, in the direction of the main flow, using a 300 mm length tube. Five different ID tubes were used in this study: 3.17, 7.67, 10.74, 13.86 and 18.84 mm. Details of the apparatus as well as the methodology of preparing the outer fluid are described fully in [54].

To begin each experiment, the outer fluid is pumped through the channel at the designated flowrate Q_2. When the entire channel is filled, the inner fluid is then introduced at flowrate Q_1. The inner fluid is colored black using a commercially available food dye to increase the contrast between the two

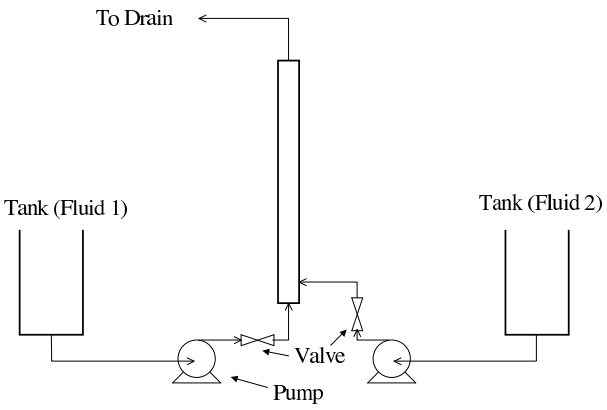

Figure 4.2: Flowloop schematic. Fluids 1 and 2 are inner and outer fluids respectively.

fluids. For each combination of fluids we performed experiments at different flow rates (Q_1, Q_2), in order to observe changes in the interface radius, r_i. The range of flow rates feasible, for both the inner and outer fluids, is approximately $5 - 60\ mL/s$ and is restricted by the operating range of our pumps.

In total 120 experiments were conducted using either glycerin (Fisher Scientific Canada), water, or Polyethylene Oxide (PEO, MW 7×10^6) (Sigma Aldrich) as the inner fluid and Carbopol-940 (Noveon Inc) as the outer fluid. Details of the experimental series conducted are given in Table 4.1. We shall discuss the results in detail later, but briefly, series 1 and 2 tested effects of a Newtonian fluid as inner fluid with a visco-plastic outer fluid. Principally these series were intended as control cases. In series 3-5, we have studied visco-elastic core fluids with visco-plastic lubricating fluid, in different scenarios with fixed inlet geometry. In series 6, we have studied the effect of varying the size of the diameter of the core fluid inlet pipe to test the effect of inlet geometry on elasticity.

Our visualization system consisted of two CCD cameras with 720×480 and 2590×3870 pixel spatial resolution, mounted $0.5\ m$ and $1.5\ m$ above the inlet

Series	Fluid		Flowrate		Inner Pipe
	Inner (wt/wt)	Outer (wt/wt)	Inner (mL/s)	Outer (mL/s)	ID (mm)
1	0.95% Gly.	0.15% Carb.	5-40	8	3.17
2	Water	0.15% Carb.	5-40	10	3.17
3	0.5% PEO	0.15% Carb.	5-40	5-60	3.17
4	0.75% PEO	0.15% Carb.	5-40	5-60	3.17
5	1.0% PEO	0.10% Carb.	5-40	5-25	3.17
6	0.75%PEO	0.15% Carb.	5-40	30	3.17-18.84

Table 4.1: Concentrations of the solutions, range of flow rate and size of inner pipe in each experimental series. Abbreviations: Gly. = Glycerin (Fisher Scientific Canada); PEO = Polyethylene Oxide (MW 7×10^6) (Sigma Aldrich); Carb. = Carbopol-940 (Noveon Inc).

manifold. With this set-up, the maximum resolution of the cameras is about 0.14 $mm/pixel$ and the cameras are able to capture 20 cm and 60 cm lengths of the tube. The recorded images are post-processed in 2 different ways: (i) to create spatiotemporal plots of the interface evolution, as described e.g. in [31]; and (ii) to measure the width of the inner core fluid. Spatiotemporal plots (i) are obtained by averaging the pixel intensity across the pipe at each time. The averaged intensity value is indicative of the inner fluid radius. To measure (ii), the width of the inner core fluid, we locate the edges of the inner fluid using a second derivative test on the pixel intensity (from Matlab). Corrections are made for concavity of the pipe and the measurements are calibrated against a sequence of 5 metal cylinders of representative known diameters, placed inside a section of plexiglass pipe filled with Carbopol solution. We average the measured r_i values to compare against predictions from the multi-layer model (described in §4.1). To do this we first select a range of $10-15$ s over which the flow is visually stable, then average both spatially and temporally. For each second we have about 30 frames and from each frame we can make about 700 axial measurements of r_i. Therefore in total we have ≈300,000 measurements

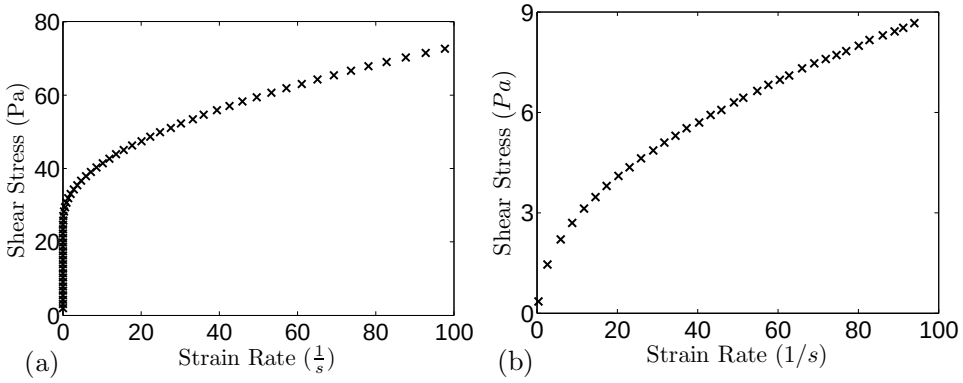

Figure 4.3: Example flowcurve data: (a) 0.15% Carbopol 940 solution at pH 5.8 and $22°C$; (b) 0.75% Polyethylene Oxide solution at $22°C$.

for each comparison point.

A number of different test procedures were used to characterize the fluid rheology, using both a Bohlin C-VOR rotational rheometer (www.malvern.com) and a HAAKE CaBER 1 Extensional Rheometer (www.rheowin.com/caber.htm). For all inner fluids, the shear rheometry was performed using a Cone and Plate $4°/40\ mm$ geometry and the rheological parameters were determined through regression to a power-law fluid model, see Table 4.2. For the Newtonian fluids tested, our results are similar to those reported in the literature. For the PEO, shear thinning behavior was the most evident feature. Examples of the shear stress plotted as a function of strain rate are shown in Fig. 4.3.

Turning now to the elastic properties of the PEO, the longest relaxation time was determined by performing oscillatory shear tests using a Bohlin C-VOR digital rotational rheometer and extensional rheometry tests using a HAAKE CaBER 1 extensional rheometer. The characteristic relaxation time, λ_s, can be obtained from the inverse of the frequency where elastic modulus G' and viscous modulus G'' cross over, [19]. The break up time of the fluid sample in extensional rheometry is denoted by t_b. Note that t_b is not a material property; however, it quantifies the stringiness of the material. Measured values of λ_s and t_c with their uncertainties are shown in Table 4.2.

Fluid	Shear rate, $\dot{\gamma}$	Yield Stress, τ_Y	Consistency, κ	Power-law index, n	Relaxation time, λ_s	Extensional break up time, t_b
(wt/wt)	$(1/s)$	(Pa)	$(Pa^{1/n})$		(s)	(s)
95% Gly.	1-100	-	0.525	1	-	-
Water	1-100	-	0.0013	1	-	-
0.10% Carb.	1-80	$3.4(\pm 1)$	4.54	0.34	-	-
0.15% Carb.	1-80	$11(\pm 1)$	18.66	0.27	-	-
0.50% PEO	1-200	-	0.27	0.6	-	0.71 (± 0.1)
0.75% PEO	1-200	-	1.02	0.49	3.0 (± 0.5)	1.96 (± 0.25)
1.0% PEO	1-200	-	2.47	0.43	3.0 (± 0.5)	4.9 (± 0.45)

Table 4.2: Rheological properties of the fluids tested. Abbreviations: Gly. = Glycerin (Fisher Scientific Canada); PEO = Polyethylene Oxide (MW 7×10^6) (Sigma Aldrich); Carb. = Carbopol-940 solution at pH 5.8 (Noveon Inc). This pH is used for all experiments.

The shear rheometry of the Carbopol solutions was determined using a 40 mm serrated parallel plate geometry (see Fig. 4.3). The yield stress was evaluated using the maximal instantaneous viscosity technique [76]. This test has been performed 8 times for each sample, with a high degree of repeatability. Nevertheless, precisely measuring a *yield stress* that agrees with the theoretical notion is not straightforward. We expect that there is some uncertainty (around $\pm 1\ Pa$) in considering our measured yield stress as equivalent to a theoretical yield stress. It is partly due to this difficulty that we have used the same concentration of Carbopol solution for all but one of our series of experiments. Having fixed τ_Y, we fit the consistency κ and power law index n, from the plot of $(\tau - \tau_Y)$ vs $\dot{\gamma}$, using regression.

4.3 Experimental results

Our experimental series follow 3 main directions. First, we have carried out a number of calibration studies using Newtonian core fluids (series 1 and 2; see §4.3.1). Secondly, we establish whether or not viscoelastic core fluids can be used in the VPL technique, by using different concentrations of PEO in the core region (series 3-5; see §4.3.2). This is the main objective of this chapter. Thirdly, we explore the effects of inlet radius on these flows (series 6; see §4.3.3).

4.3.1 Calibration experiments

In §4.1, we introduced a simple laminar multi-layer flow model and defined 3 different types of flow, namely *stable*, *unstable* and *static*, classified according to the value of shear stress at the interface. This model suggests that the transition between different flow types is determined by the shear rheology of the fluids. Evidently, when elasticity is introduced this may be incorrect. Thus, our initial experiments considered Newtonian core fluids in order to

establish that at least for inelastic fluid flows this type of idealised description is valid.

The procedure used for the multi-layer flow model is the same as [55]. We compute the relation

$$(r_i, |\frac{\mathrm{d}p}{\mathrm{d}z}|) \mapsto (Q_1, Q_2)$$

directly from the rheological measurements of the shear rheology. For given $(r_i, |\frac{\mathrm{d}p}{\mathrm{d}z}|)$, equations (4.5) and (4.6) define the shear stress in each fluid layer. We interpolate linearly from the flowcurve data to define $\dot{\gamma}(\tau)$ in each fluid layer. We integrate once from the pipe wall to give the velocity profile and then integrate again to give the flow rates (Q_1, Q_2). We carry out all numerical integrations using the fourth order Simpson's rule. These computations are generally very quick. We then invert the mapping $(r_i, |\frac{\mathrm{d}p}{\mathrm{d}z}|) \mapsto (Q_1, Q_2)$ numerically to give a mapping $(Q_1, Q_2) \mapsto (r_i, |\frac{\mathrm{d}p}{\mathrm{d}z}|)$. This mapping is more natural for experimental design as we have a limited range of flow rates attainable with our pumps.

Although we have given values for τ_Y, κ and n in Table 4.2, note that these fitted values are not used in the above design procedure. We have used directly the measured shear rheology in order to eliminate errors that would otherwise result from curve-fitting of the rheological data to a Herschel-Bulkley fluid model, and subsequently using algebraic expressions for the flow rates. The only fitted rheological parameter that is used in experimental design is the yield stress. This is used only to distinguish between stable, static and unstable parameter regimes. The actual value of the yield stress does not affect the computation of the two flow rates, nor the inversion of this mapping. Uncertainty in τ_Y is not uncommon and anyway does not translate into significant uncertainty in computed velocity and flow rates, since the strain rate is close to zero when the shear stress is close to the yield stress of the fluid.

In the first series of experiment a 95% glycerin solution and 0.15% Carbopol 940 solution are pumped through the inner pipe and the annular space respectively. The viscosity of 95% Glycerin solution is comparable to the vis-

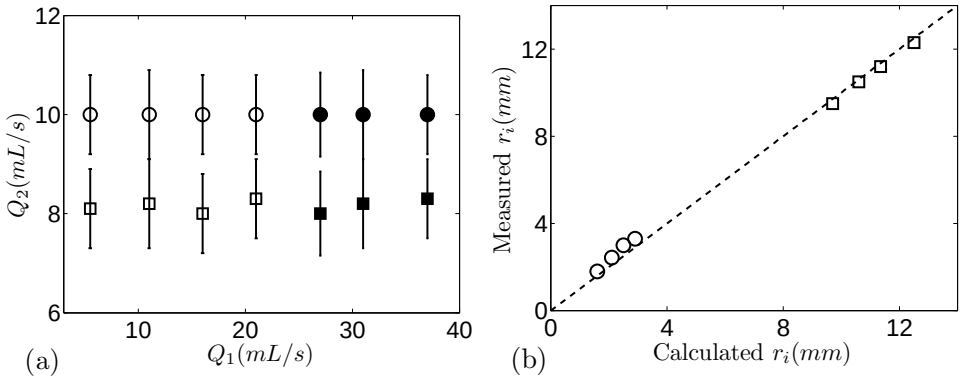

Figure 4.4: Experimental data from series 1 and 2. Inner core fluids are 95% glycerin solution and water at $22°C$. Outer fluid is 0.15% Carbopol 940 solution at pH 5.8 and $22°C$. (a) Experimentally measured flow rates and classification: series 1 (95% glycerin solution), stable (□) and unstable (■); series 2 (water) stable (∘) and unstable (•). (b) Measured r_i vs. predicted r_i for stable data of 95% glycerin solution (□) and water (∘).

cosity of the 0.75% PEO solutions at average shear rate of core fluid for a moderate range of Q_1 and Q_2. Seven experiments have been performed at constant flow rate of outer fluid $Q_2 = 8\ mL/s$ and different flow rate of inner fluid ($5 \leq Q_1 \leq 37\ mL/s$). The multi-layer flow model gives the radius of the core fluid (95% Glycerin solution) in the established flow, which is compared with the experimentally measured radius. The multi-layer model also gives us a predicted flow rate for the transition from stable to unstable flows, which can be compared with experimental observations.

The (□) and (■) symbols in Fig. 4.4a show the stable and unstable experiments from series 1, plotted in the (Q_1, Q_2) plane. The uncertainty for Q_1 is small and is not shown here. In the stable visco-plastic lubrication regime the flow is stable and is observed to have a sharp interface. Outside this regime (when the outer fluid is yielded at the interface, $\tau_i > \tau_Y$) the flow becomes unstable and mixing occurs. The multi-layer flow model predicts the transition between stable and unstable for experimental series 1 to be at $Q_1 \approx 30\ mL/s$. Experimentally, the transition is observed at slightly lower Q_1. We have some

uncertainty in the yield stress measurement. Also note that the unyielded plug around the interface thins as Q_1 is increased and this transition is approached, and can become vulnerable to small finite flow perturbations. Given these factors we feel that the comparison is relatively good. For the stable experiments the measured interfacial radii are in good agreement with those predicted from the multi-layer model; see Fig. 4.4b.

A second series of experiments is performed using water as the Newtonian core fluid, at different Q_1 while keeping constant flowrate for the outer fluid ($Q_2 = 10\ mL/s$). The ($\circ$) and ($\bullet$) symbols in Fig. 4.4a show the observed stable and unstable experiments of this second series in the (Q_1, Q_2) plane. The transition from stable to unstable flows for experimental series 2 (as predicted by the multi-layer model) occurs at a high flow rate, well above the range of our pumps. However, Fig. 4.4a shows that for $Q_1 \gtrsim 25\ mL/s$ the flow is observed to be unstable. This flow rate is well below the transition value at which the interface would become yielded. If the laminar multi-layer model were valid in this range, the interface should be surrounded by a plug of unyielded lubricating fluid. However, in these unstable experiments a considerable amount of mixing occurs and it is clear that the assumptions behind the laminar multi-layer model are no longer valid in this range. The inner fluid Reynolds number is around 1750 at $Q_1 = 25\ mL/s$. The high Re suggests that the inner fluid stream is perhaps close to the limit for shear flow transition when $Q_1 \gtrsim 25\ mL/s$. This is only a rough estimate as the transitional Re for this type of flow is not known. Instabilities observed at these flow rates are localized, suggestive of the initial turbulent puffs in a shear flow transition. It appears that these localized disturbances have sufficient momentum to break the unyielded layer of the lubricating fluid, allowing mixing. Compared with series 1, note that the Reynolds numbers of the inner fluid in series 1 are significantly lower due to the higher viscosity of the glycerin.

Figure 4.4b also shows the measured radii for the stable experiments in series 2. We see that the measured radii are in good agreement with the pre-

dicted ones when the flow is stable. In conclusion, series 1 and 2 establish that in cases where the flow is stable and laminar the multi-layer model provides a good prediction of the interfacial radius of the established flow. Provided that the inner fluid is in a laminar regime (series 1) stable flows are found for flow rates that approach the theoretical stability limit of the multi-layer model. However, highly inertial flows of the inner fluid (series 2) can render the multi-layer model invalid far below the theoretical stability limit. This theoretical stability limit is anyway only defined by the existence of an unyielded ring around the interface and does not address decay of the perturbation energy. Finally, although intended only for calibration, we comment that in series 1 there is a significant difference in density between the two fluids $\rho_1/\rho_2 = 1.24$. This has not been studied previously: experimentally, computationally or theoretically.

4.3.2 Viscoelastic core fluids

We now turn to the main objective of our study: establishing the feasibility of the VPL technique with visco-elastic core fluids. Firstly, a series of experiments has been performed with 0.5% Polyethylene Oxide solution in the core and 0.15% Carbopol 940 solution at pH 5.8 in the outer region (Experimental series 3). The shear rheometry of 0.5% Polyethylene Oxide solution is comparable to 0.3% Xanthan NF-C solution which [55] used for the core fluid. However, 0.3% Xanthan NF-C solution is largely inelastic. Hence, we expect to detect novel qualitative effects of elasticity in our experiment, by comparison with the previous work [55]. As a second step, we increase the elasticity of the core fluid by using 0.75% Polyethylene Oxide solution, but keep the yield stress constant by again using 0.15% Carbopol 940 solution in the outer region (Experimental series 4).

Figure 4.5a and b show contours of Q_1 and Q_2, as functions of $(r_i, \left|\frac{\mathrm{d}p}{\mathrm{d}z}\right|)$, for the pair of fluids used in experimental series 3 and 4. Regions of stable, unstable and static base flows are indicated in the $(r_i, \left|\frac{\mathrm{d}p}{\mathrm{d}z}\right|)$-planes. We have

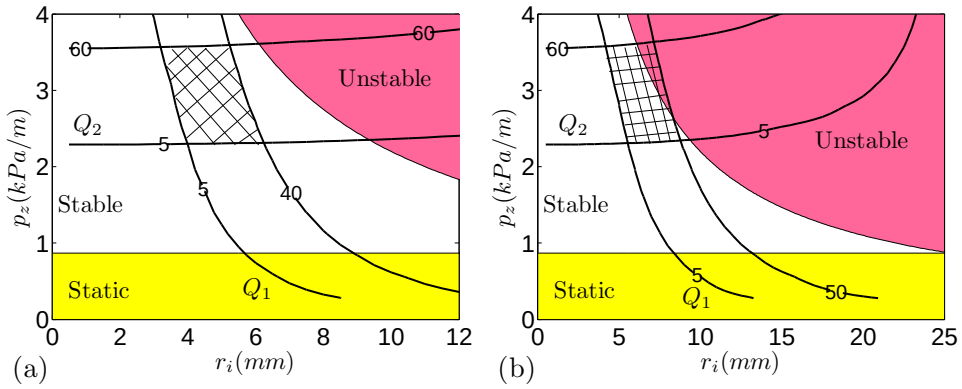

Figure 4.5: Stable, unstable and static regions for experimental series 3 and 4, with the range of our experimental matrix (cross-hatched region) illustrated in terms of Q_1 and Q_2 (mL/s).

also crosshatched the region occupied by our experimental matrix of flow rates. This shows that for the range of flowrates studied in series 3 (see Table 4.1), the multi-layer model predicts stability for all the experimental points. By increasing the concentration of PEO (see Fig. 4.5b) the experimental matrix of flow rates includes flows that are unstable as well as stable.

Figures 4.6a and b identify stable (□) and unstable (⊞, ■) experiments for series 3 and 4. The dashed line shows the theoretical boundary of transition between stable and unstable regions. We first note that instability is observed before passing the theoretical transition. Secondly, we note that increasing the elasticity of the core fluid (increasing the concentration of PEO) appears to destabilize the flow, i.e. instability appears at smaller flow rates of the core fluid.

Before describing the unstable flows we illustrate a typical stable experiment in Fig. 4.7. A series of snapshots illustrate the time evolution of the interfaces in the first 0.3 m after the exit of the inner pipe. We observe that the initial front of core fluid, penetrating into outer fluid is destabilised locally but does not destabilise the flow behind the front. The front region is advected up the pipe and out the exit, leaving behind the smooth multi-layer config-

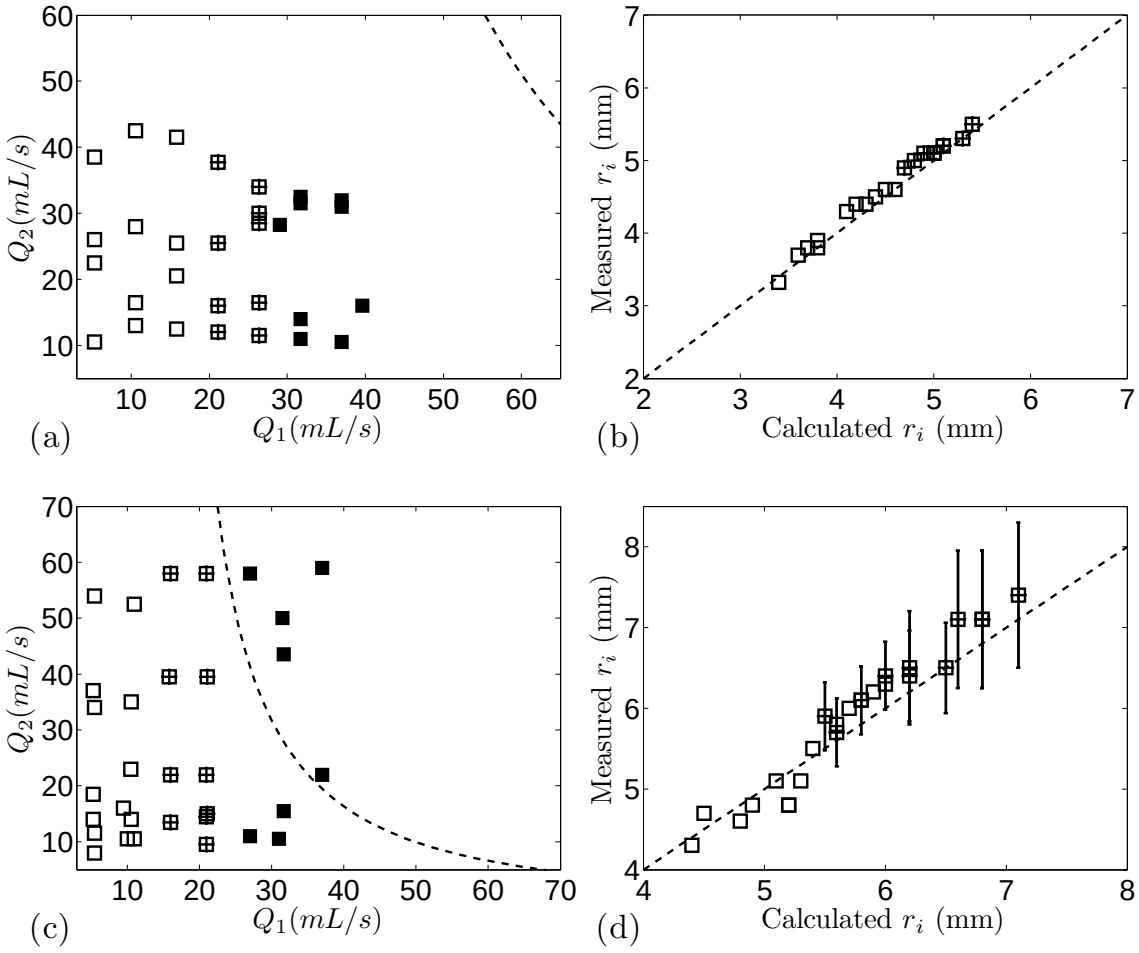

Figure 4.6: (a) Series 3 and (c) Series 4: experimental classifications plotted with respect to flow rates of two fluids, compared against model predictions. Stable (□); frozen (⊞); mixing (■). Broken line indicates the predicted transition between stable and unstable. (b) Series 3 and (d) Series 4: measured r_i vs. predicted r_i.

uration. The interface is generally sharp and clear with no new mixing nor localised instability observed along the total length of the pipe. Visually there is no difference in Fig. 4.7 between the snapshots at $t = 300\ s$ and $t = 600\ s$. This particular experiment carries on for at least 15 *min*. When no instability of the interface is observed, the flow is classified as stable by visual inspection. We also construct a spatiotemporal plot of the mean intensity at each height in the pipe, which can be used for more quantitative analysis if the visual inspection is ambiguous. The right panel in Fig. 4.7 shows an example of this. The steep dark wedge indicates the convectively unstable initial front. There is a light region at the bottom of the spatiotemporal plot which diffuses upwards into a uniform grey. This lighter region is the expanding development length of core fluid exiting from the nozzle. In our experiments only the frontal view is recorded by our video system, but by visual inspection of numerous flows from different angles, those flows that are stable certainly appear to be axisymmetric. For the stable cases our results are largely similar to those reported in [55] with xanthan-Carbopol combinations. However, the interface appears sharper here (with the viscoelastic core fluid) and the degree of mixing at the front appears to be reduced. We have not attempted to quantify either effect.

We have observed two different instability patterns in Series 3 and 4. We designate these as either frozen (⊞) or mixed (■). By increasing the flowrate of the core fluid (Q_1) gentle waves with small amplitudes begin to appear at the interface. These waves are *frozen* at the interface by the unyielded plug region of the lubricating fluid and are convected along the pipe with the same velocity as the interface. Figure 4.8 shows snapshots at 1 s time intervals from a typical experiment with a frozen interfacial wave. Note that these images are scaled with an aspect ratio of $\approx 15:1$ to show more of the wave pattern. The right panel of Fig. 4.8 shows the spatiotemporal plot of the same experiment, focusing on a region above the exit nozzle expansion. The constant slope lines of dark and white regions confirm the constant advective velocity of the frozen interfacial waves. Note that the wavelengths are not

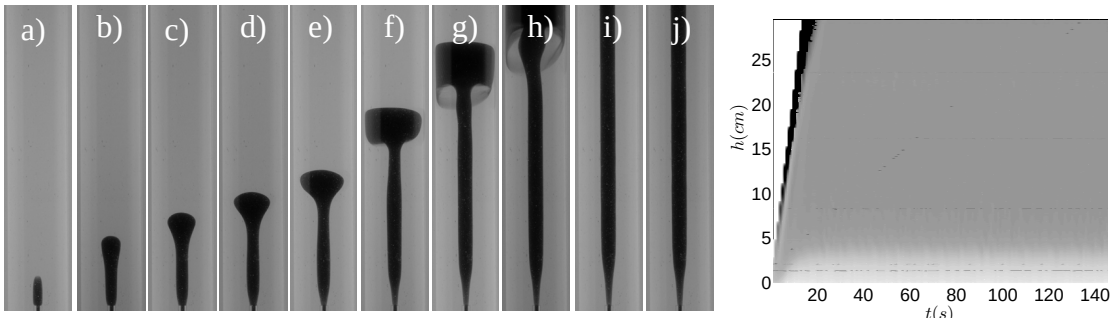

Figure 4.7: Snapshots of a typical stable experiment from Series 4 at $(Q_1, Q_2) = (11, 30)$ mL/s. Inner core and lubricated fluids are Polyethylene Oxide solution 0.75% and Carbopol 940 solution at pH 5.8, respectively. Images taken at $t = 2,\ 4,\ 5,\ 6,\ 7,\ 10,\ 13,\ 16,\ 300,\ 600$ s, for (a)-(j). The camera captures the first 0.3 m after the exit of the inner pipe. The right panel shows a spatiotemporal plot constructed from the same experiment

constant, which leads to the rather exotic patterning of the spatiotemporal plot. This kind of instability is not observed with Newtonian core fluids (see §4.3.1) nor with inelastic shear thinning core fluids (see [55]), at the same range of flowrates or Reynolds numbers of core fluid. In either of these cases with inelastic core fluids, interfacial disturbances lead to mixing of the two fluids. PEO has a larger extensional viscosity than the fluids of series 1 and 2, and the extensional viscosity is a measure of the resistance of the fluid to the stretching motions that would occur during mixing.

Figures 4.6b and d plot the measured r_i vs. predicted r_i for Series 3 and 4, respectively. Both stable and frozen experimental data is used. The stable experiments have radii that are predicted well by the multi-layer model (i.e. from the shear rheology). For Series 3 the frozen interface oscillations are small, of the order of the camera resolution, and no error bars are shown. For Series 4 the error bars indicate the range of radii observed in the frozen experiments. It is worth noting that the multi-layer model still predicts reasonably well the mean radii of these flows. The viscoelastic core fluid exits the inner pipe and

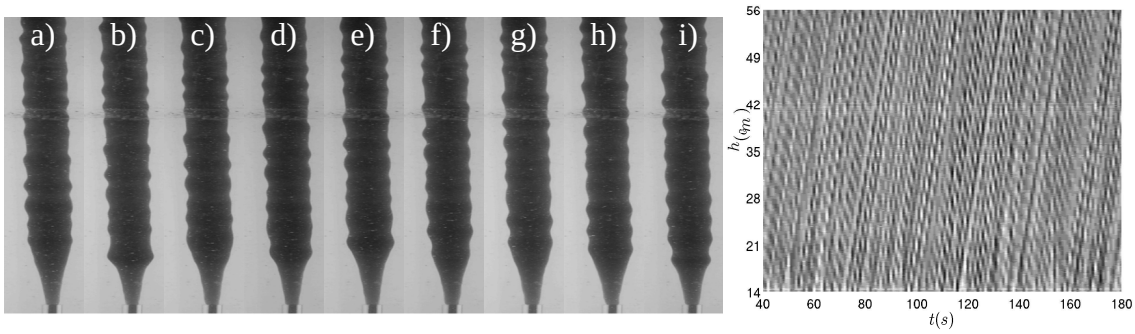

Figure 4.8: Snapshots of a typical experiment with frozen interfacial wave from Series 4 at $(Q_1, Q_2) = (21, 30)\ mL/s$. The interfacial wave has mean amplitude $\simeq 0.7\ mm$ and mean wave length $\simeq 48\ mm$. Snapshots (a)-(k) show t varying from $80s$ to $88s$ with time interval of $1s$. The camera captures the first $0.65\ m$ of the pipe from the exit of the inner pipe. The right panel shows the spatiotemporal plot of the same experiment.

expands to an average radius (predicted by multi-layer model; §4.1) and then waves appear as the fluid relaxes. Roughly speaking, the amplitudes are of order 1 mm and the wavelengths are of order 50 mm.

At higher flowrates of core fluid the interfacial waves do not remain convectively stable, propagating downstream as frozen interfacial perturbations. The disturbances are strong enough to yield the plug region along the flow and hence mixing occurs. The ■ symbols in Fig. 4.6 correspond to this type of observation. An example is shown in the snapshots of Fig. 4.9. Dynamic waves appear directly after the inlet region and expand while traveling downstream, penetrating into the outer fluid. In the spatiotemporal plot we note constant slope in the grey-scale variations after a short distance ($\approx 20cm$) from the entrance region. The expanding darker regions and non-constant slope further downstream indicate that the interfacial non-uniformities propagate at speeds different to the interfacial speed.

Looking at Figs. 4.6a and c we note that unstable flows are found further below the multi-layer model stability threshold in Series 3 than in Series 4.

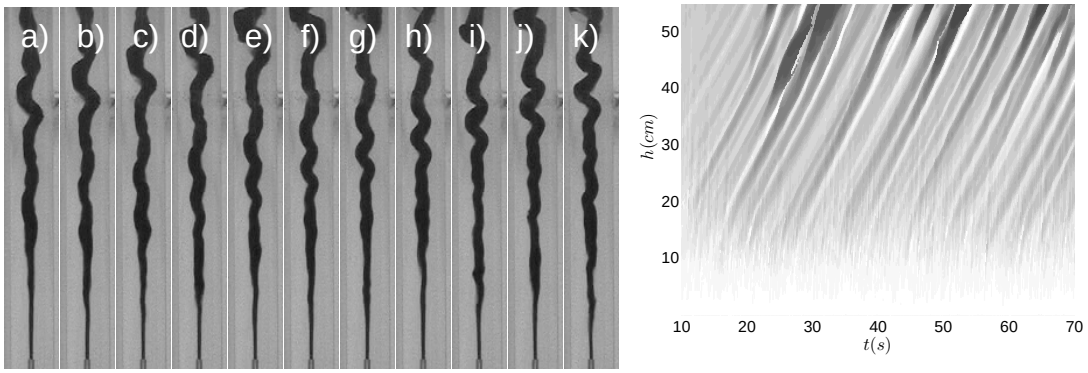

Figure 4.9: A typical unstable experiment from Series 3 at $(Q_1, Q_2) = (37, 32.5)$ mL/s. The snapshots (a)-(k) show t between 41 s and 51 s with time interval of 1 s. The camera captures the first 60 cm of the pipe from the exit of the inner pipe. The right panel shows the spatiotemporal plot of the same experiment.

This further suggests that the instabilities observed are due to the elasticity of the inner fluid. Further, it is evident the instability occurs after passing a threshold in flowrate of the inner fluid (approximately $Q_1 > 21$ mL/s for Series 3 and $Q_1 > 10$ mL/s for Series 4). These both suggest that the instabilities initiate before the flow has fully developed, after the exit from the inner pipe, and depend to some extent on the state of stress of the core fluid transported to the exit of the inner pipe.

Purely elastic effects on interfacial instability

So far, our experimental results appear mostly to show that the elasticity of the core fluid has a destabilizing effect and that interfacial instabilities appear before passing the theoretical transition line. However, we have also noticed that the degree of mixing appears retarded by the PEO. This leads us to question if we can stabilize the flows using primarily elasticity. Series 5 has therefore been performed with 1% Polyethylene Oxide solution as the core

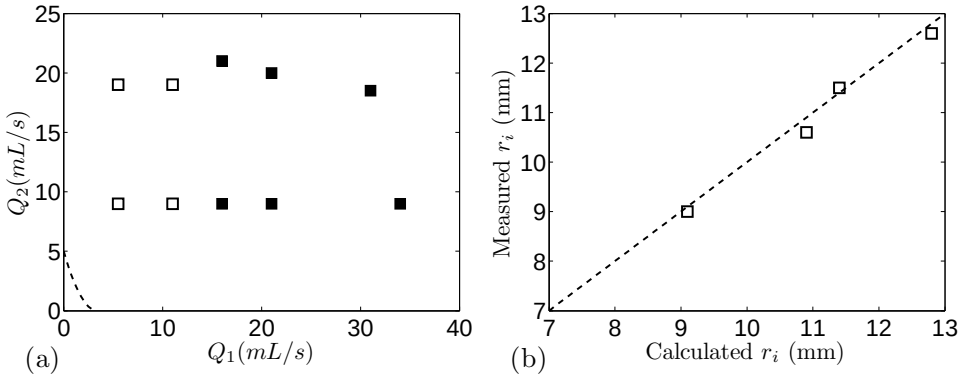

Figure 4.10: (a) Experimental observations plotted with respect to flow rates of two fluids, compared against model predictions. Stable (□); unstable (■). predicted transition line is shown. (b) Measured r_i vs. predicted r_i.

fluid and 0.1% Carbopol 940 solution as the lubricating fluid. The core fluid has increased elasticity [2] over that in Series 3 and 4, but this also increases the shear viscosity. The lubricating fluid has a reduced yield stress ($\tau_Y \approx 3.4$). In consequence, for all of the experiments in Series 5, the visco-plastic fluid is yielded at the interface (e.g. as in Fig. 4.1b). The simple multi-layer model classifies all these flows as unstable.

The experimental points are marked in Fig. 4.10a, It is interesting to see that these flows are observed to be stable at small enough flow rates and become unstable when $Q_1 > 11\ mL/s$. In the absence of an unyielded plug around the core fluid, frozen interfacial waves are not observed in this set of experiment. Instead it appears that at sufficiently low flow rates the elasticity is sufficient to damp out oscillations due to the stress relaxation as the flow expands. For these stable flows we show in Fig. 4.10b a good comparison between predicted and observed interfacial radii.

Figure 4.11a-h shows snapshots of the interfacial waves in the entrance region as a result of relaxation for an unstable flow. Compared to Series 3 and 4, the development length is shorter and the amplitudes of the waves are

[2] 1% Polyethylene Oxide solution has increased both normal stress and relaxation time.

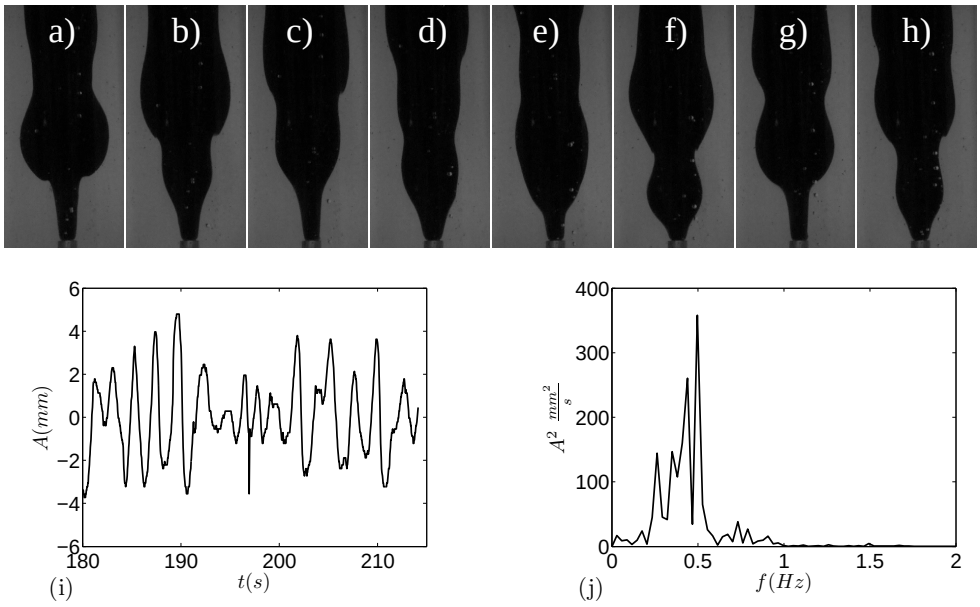

Figure 4.11: (a)-(h) Snapshots of a typical unstable experiment from Series 5 at $(Q_1, Q_2) = (16, 21)\ mL/s$: t varies from 180 s to 187 s from left to right. The camera captures 11 cm of the pipe from above the exit of the inner pipe. (i) Variation of the amplitude of the interface oscillation (A) vs time. (j) Power spectrum (A^2) vs frequency ($f(Hz)$), for a point located at 5 cm above the exit of the inner pipe on the left edge of the observed interface.

larger. These images show 11 cm of the plexiglass pipe from above the inner pipe exit. We have selected a point on the *left* interface of the core fluid, located 5 cm above the inner pipe exit, and have measured the amplitude A of the oscillation about the predicted radial position (see Fig.4.11i). Taking the Fourier transform, we find the dominant frequency of the oscillation which is in the range of 0.25 to 0.5 Hz (see Fig.4.11j). Table 4.2 shows the relaxation time and break-up time of the 1.0% PEO solution, which are in the ranges $1 < \lambda_s < 5$ s and 4.9 s respectively. We note simply that these timescales correspond approximately with the range of dominant frequencies observed in the interface oscillations.

Size of pipe	Inner Diameter ID (mm)	Outer Diameter OD (mm)
1	3.17	6.35
2	7.67	13.71
3	10.74	17.14
4	13.86	21.33
5	18.84	26.67

Table 4.3: Sizes of inner pipes used in Series 6.

4.3.3 Inlet geometry effects

In §4.3.2 the radius of the inner pipe used is significantly smaller than the established radius of the developed flow, as predicted by multi-layer model of §4.1. Thus, the inner fluid experiences high stress in the inner pipe followed by flow expansion and a net relaxation of the elastic stresses. We have seen that this relaxation can lead to interfacial instability even when a ring of unyielded fluid exists around the core fluid stream. This suggest that selection of R_i could have a dominant effect on the transition, over the range of our experiments.

Therefore, in this final set of experiments we study the effect of inner pipe geometry on the flow by increasing the inlet diameter ($2R_i$). We have used 5 different diameters of inner pipe (including that used in the previous experiments) and for each pipe diameter we conducted 7 experiments at constant outer fluid flow rate ($Q_2 \approx 30\ mL/s$) for increasing core fluid flow rate ($5 < Q_1 < 40\ mL/s$). The dimensions of the pipes are given in Table 4.3. Note that the same length of inner pipe is used in each geometry and no other changes are made to the inlet manifold. The inner and outer fluids are 0.75% Polyethylene Oxide solution and 0.15% Carbopol 940 solution at pH 5.8, respectively.

Figure 4.12a marks the stable and unstable experimental points for different sizes of inner fluid pipe at different core fluid flow rate. We observe that the unstable region is reduced by increasing the diameter of the inner pipe,

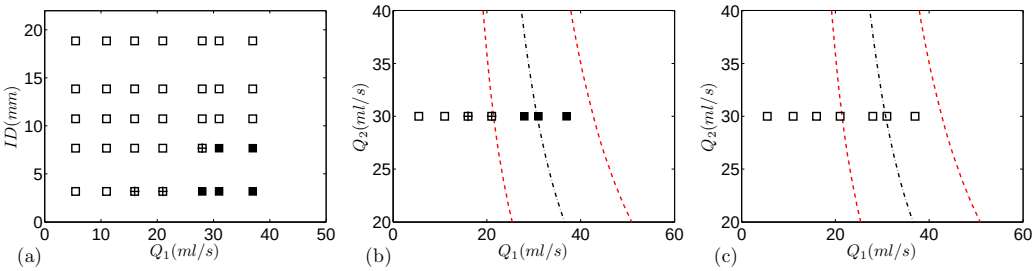

Figure 4.12: (a) Series 6 experimental observations plotted with respect to inner diameter of the pipes and flow rates of inner fluids: stable (□); frozen (⊞); mixed (■). Experimental observations plotted in the (Q_1, Q_2)-plane for: (b) the smallest inner pipe; (c) the largest inner pipe. The predicted transition from the multi-layer model is plotted. To account for uncertainty in the value of τ_Y we plot additional transition curves that would be predicted if $\tau_Y = 11 \pm 1\ Pa$.

which has the effect of reducing the elastic stresses of the core fluid inside the inner pipe. In Fig. 4.12b and c we have plotted the experimental points in the (Q_1, Q_2)-plane, for the smallest and largest diameter inner pipes, respectively. We have indicated in these figures the transition between stable and unstable regions predicted by the multi-layer model, and also additional transition boundaries representing uncertainty in the yield stress, i.e. corresponding to $\tau_Y = 11 \pm 1\ Pa$. It can be seen that as the inner pipe diameter is increased the flow remains stable up to larger flow rates, possibly also exceeding the theoretical bounds for transition. Figures 4.13a and b, show images of the established flows for the smallest and largest inner pipe diameters (i.e. corresponding to Fig. 4.12b and c). These results confirm that elastic effects are primarily due to the stress history at the exit of the inner pipe, before the flow becomes established.

We now try to quantify the total normal stress in the entry region of our flow. Figure 4.14a shows an example of the extensional viscosity $\eta_E(\varepsilon)$ for the 0.75% Polyethylene Oxide solution used in these experimental series. From the images of the experiments we can measure the developing radial position

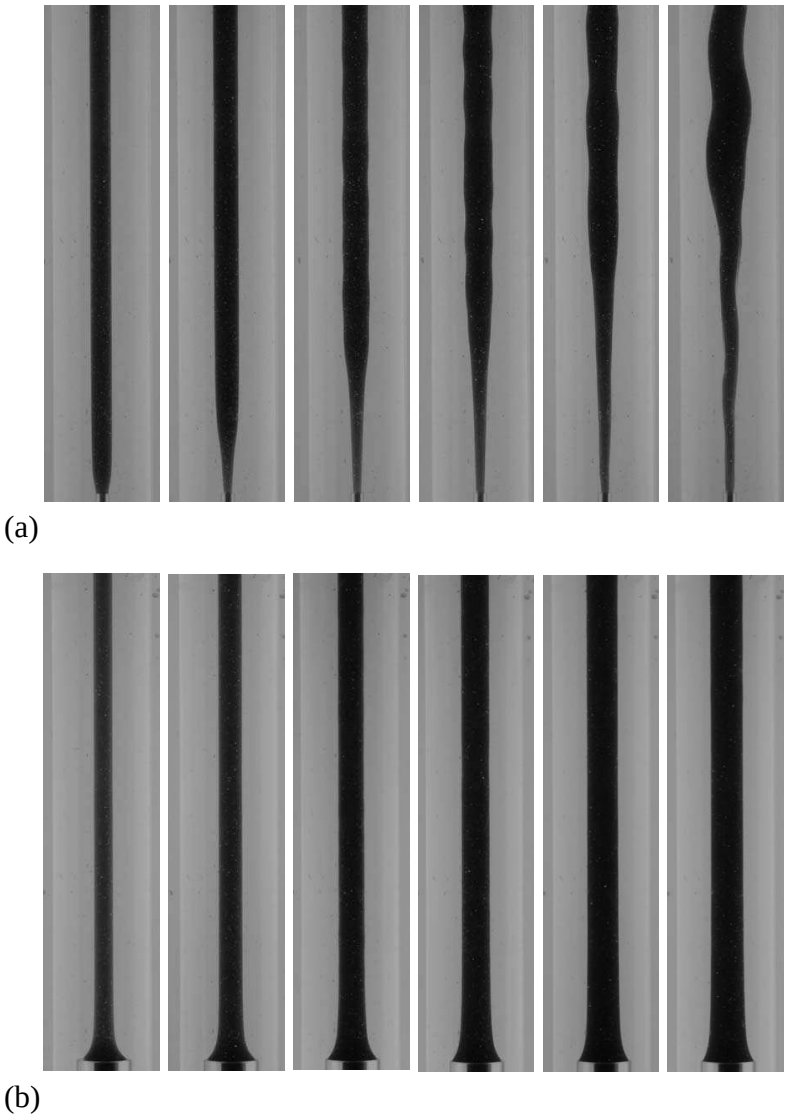

Figure 4.13: Snapshots of the established flows in Series 6 for (a) inner pipe of size 1 (b) inner pipe of size 5. From left to right $Q_1 = 5.5,\ 11,\ 16,\ 21,\ 28,\ 37\ mL/s$ respectively. The camera captures 30 cm of the pipe from above the exit of the inner pipe.

r_d of the interface as it evolves along the development region. For the smallest diameter inner pipe (size 1), Fig. 4.14b plots r_d against the distance z from the nozzle exit, at different flow rates. The vertical broken lines in this figure show the fully developed radius, as predicted from the multi-layer model. From the flow rate and interface position we are able to estimate the mean extensional strain (ε) and strain rate ($\dot{\varepsilon}$), as the flow develops in the entry region. We then evaluate the mean total normal stress difference σ_t^e from

$$\sigma_t^e = \eta_E(\dot{\varepsilon}, t)\dot{\varepsilon}. \tag{4.7}$$

Equation (4.7) gives a reasonable estimate of the normal stress difference in the development region. How much of σ_t^e remains at the end of the development region is estimated using a characteristic time (t_c = development length/mean velocity) and on assuming an exponential decay. The residual normal stress difference σ_t^r is therefore estimated by:

$$\sigma_t^r = \sigma_t^e \exp(-\frac{t_c}{\lambda}), \tag{4.8}$$

where λ comes from fitting an upper convected Maxwell model to our extensional rheometry data. Here we have taken $\lambda = 0.08$s, but in practice for such fluids, a spectrum of relaxation times can occur. Figure 4.14c shows the characteristic time for the smallest and largest inner pipes at different flow rates. Note that at fixed flow rate the larger inner pipe diameter has a much slower mean velocity. Therefore, although the development lengths are typically shorter when the interface contracts rather than expands, the characteristic time may be longer. The other main influence is from the flow rate: the development length tends to increase with Reynolds number.

The total and residual normal stress differences are shown in Fig. 4.15 for the different flow rate and for inner pipes of size 1 and 5. For the large pipe diameter we see that the residual normal stress difference has decayed to the yield stress value or below, whereas for the smaller inlet diameter the residual

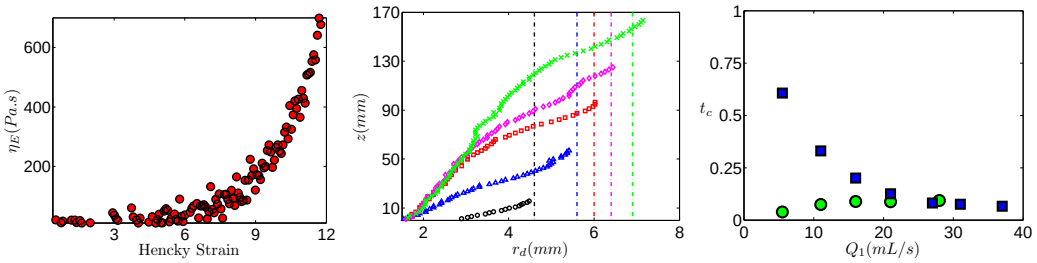

Figure 4.14: a) Example of the extensional viscosity for 0.75% Polyethylene Oxide solution at $\dot{\varepsilon}_0 = 9\ s^{-1}$. b) Developing radius of inner fluid (r_d) against axial distance z, measured from the inner pipe exit for size 1 pipe at: $(Q_1, Q_2) = (5.5, 30)\ mL/s$, $\circ$; $(Q_1, Q_2) = (11, 30)\ mL/s$, $\triangle$; $(Q_1, Q_2) = (16, 30)\ mL/s$, $\square$; $(Q_1, Q_2) = (21, 30)\ mL/s$, $\diamond$;$(Q_1, Q_2) = (28, 30)\ mL/s$, $\times$. Broken vertical lines show the value of r_i predicted from the multi-layer model. c) Characteristic times t_c for inner pipe of size 1, $\bullet$, and size 5, $\blacksquare$.

stresses far exceed the yield stress. Although we may estimate σ_t^e and σ_t^r in this way, interpretation of the values is quite hard. First of all, let us note that even with inelastic fluids there is an entry/development region in which the outer fluid is yielded at the interface. Thus, trying to make quantitative estimates for the normal stresses that are transmitted to the Carbopol in the entry/development region has no purpose.

Secondly, the residual stress estimates do not tell us the distribution of the normal stresses between radial and axial components. If we consider the residual normal stress differences in Fig. 4.15b for the smaller pipe size, we see that even at low flow rates these far exceed the yield stress. However, for these flows there is no evidence of instability. We can infer that the interface is unyielded at these stable low flow rates since at slightly higher flow rates we have observed the frozen interfacial wave pattern, advected at constant speed. Since the radial component of the normal stress would transmit across the interface and be sufficient to yield the Carbopol at low flow rates, it seems that the majority of σ_t^r comes from the axial component. Even when we have the frozen wavy interface, note that the axial stress component is multiplied by the

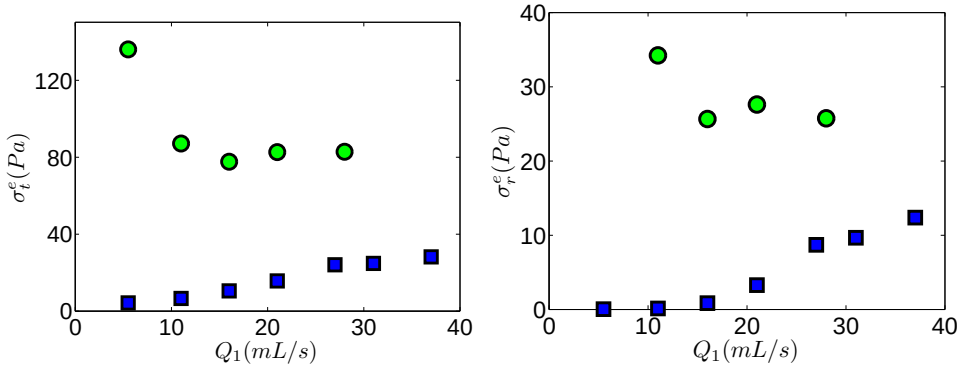

Figure 4.15: a) Total normal stress difference; b) residual normal stress difference. Pipe of size 1, •; size 5, ■.

slope of the interface before contributing to the normal stress transmitted at the interface. This slope may be approximated by twice the ratio of amplitude to wavelength of the oscillations, i.e. $\approx 1/25$, meaning that the contribution from the axial stresses is of the order of $1-2\ Pa$ for our smallest size inner diameter, for the observed frozen wavy interfaces. As we already have significant shear stresses, the size of this additional contribution is consistent with the observed eventual yielding of the plug as Q_1 is further increased. However, this falls short of a quantitative prediction.

4.4 Conclusions

This chapter has mostly focused on establishing the practicality of using the visco-plastic lubrication technique with a viscoelastic core fluid. A simple one-dimensional multi-layer model has been outlined for experimental design and control purposes. This model relies exclusively on the shear rheology of the two fluids. We have performed two series of test experiments with Newtonian core fluids (water and Glycerin 95%) to verify the multi-layer model. These initial results indicate that the stable flow is robust and persists over lengths of $\sim 1000 r_i$, for the duration of our experiments. Moreover the presence of

the plug around the core fluid guaranties the stability of the multi-layer flow provided the inner core fluid is itself stable and lies in laminar flow regime. These conclusions largely confirm those of [55]. A new finding of relevance to the design of robust multi-layer transport processes is that the series of experiments performed with Glycerin 95% exhibited a significant density difference between the fluids but was still found to be stable where predicted. The pipe inclination is vertical here, so this may be affected by other inclinations, but at least the methodology does not break down with density differences. This is an area that merits further investigation.

Turning now to the main focus of this chapter, viscoelastic core fluids, the first conclusion is that we have been able to observe stable multi-layer flows when lubricated by a visco-plastic fluid, i.e. the methodology does extend to this important class of flows. The more difficult question to answer is whether the elasticity of the core fluid has a positive or negative effect on the stability.

Our second set of experiments (Series 3-5) used a small inlet pipe diameter, so that the core fluid always has to expand to attain the radius r_i of the established base flow. This expansion entails a relaxation of the normal stresses, which we have seen is destabilizing. The flows in Series 3 and 4 do destabilize before the transition predicted by the multi-layer shear flow model. Indeed the transition occurs at a threshold in flow rate Q_1, which largely corresponds to a threshold in normal stresses. At small Q_1 the flow is stable with a sharp interface along the length of the pipe, but on increasing Q_1 interfacial instabilities appear.

When the unyielded plug exists around the core fluid we see an interesting transitional regime in which the wavy elastic instability is frozen into the unyielded plug and then translates along the pipe. This effect is amplified with the inner fluid elasticity. The frozen interface flows are a fascinating combination of both elastic and yield stress effects. The yield stress does the freezing but the viscoelasticity combined with the flow expansion (= stress relaxation) combine to instigate the interfacial waves in the flow development

region, before the parallel flow is established and the plug forms at the interface. Our recent computational work (albeit for Newtonian core fluids and Bingham outer fluids) indicates that the plug can begin to form within a few diameters of the core fluid inlet pipe exit, [52, 53]. Therefore, the balance of elastic instability and freezing is evidently delicate.

At still larger flow rates Q_1 (but still below the shear flow threshold) the plug is broken. However, even in the unstable regime the degree of mixing is much less than in the case of a Newtonian core fluid. One phenomenon associated with viscoelasticity is the resistance to stretching of fluid elements due to the large extensional viscosity. This evidently retards local mixing mechanisms and can be viewed as a stabilizing effect.

In Series 5 we reduced the yield stress in the outer fluid and amplified the elasticity of the core fluid, so that all our base flows had a yielded interface. This series highlighted the importance of the elasticity in both stabilizing and destabilizing the flow. At low flow rates we found stable axisymmetric flows with a sharp interface at the predicted radial position: the elasticity is stabilizing with the larger extensional viscosity resisting interfacial deformation that is instigated by normal stress relaxation due to the flow expansion. As Q_1 increases, the normal stress relaxation dominates and interfacial waves appear. Analysis of typical instabilities indicate that the range of dominant frequency of the viscoelastic oscillation overlaps with the range of relaxation frequencies obtained from extensional and shear rheometry measurements.

Finally we have shown (Series 6) that elastic instabilities depend to a large extent on the state of stress of the core fluid transported to the exit of the inner pipe and thereafter to the established flow. Hence the inlet geometry has significant effect on stability of the flow. Our experiments have shown that for large inlet pipe diameters the appearance of interfacial instabilities is retarded. This leads to the interesting question of whether or not a flow contraction could be used to stabilize an otherwise unstable flow?

Chapter 5

Nonlinear stability of a visco-plastically lubricated viscoelastic fluid flow[1]

In this chapter, we study theoretically a core-annular pipe flow configuration, with a viscoelastic core fluid lubricated by a yield stress fluid (see Figs. 5.1a-c). As many industrial multi-layer flows involve fluids with viscoelastic properties it is of interest to establish the feasibility of VPL (Visco-Plastically Lubricated) flows with viscoelastic core fluids. In Chapter 4, we have addressed this question from an experimental perspective and here we consider analysis of the flow stability for the established flow.

In the context of the existing literature (see chapter 1) our study is somewhat unique in that we consider fully nonlinear stability of two complex fluids via an energy stability method, i.e. this is not a weakly nonlinear extension of linear stability. Energy stability methods are rarely used for multi-fluid problems since in general the deforming interface makes it hard to track the domains of perturbed and unperturbed fluids. However, in VPL flows an interfacial region in the yield stress fluid remains unyielded which means that the set of interfacial motions is restricted to rigid body motions. Here we adapt the method of [85] for dealing with this aspect of the flow stability.

One particular feature of the study of stability in shear flows of yield stress

[1] A version of Chapter 5 has been submitted for publication (under review). [S. Hormozi], and I.A. Frigaard. Nonlinear stability of a visco-plastically lubricated viscoelastic fluid flow [50].

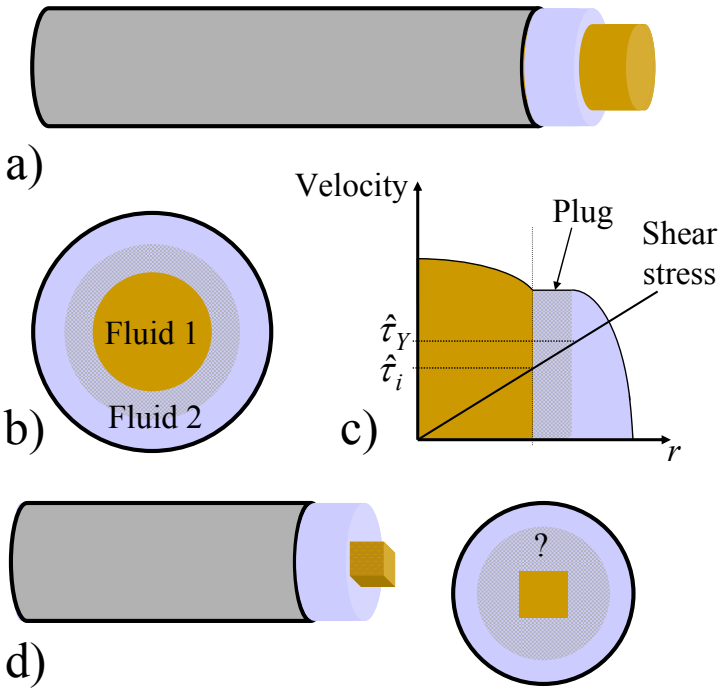

Figure 5.1: a) A visco-plastically lubricated pipe flow; b) Cross-section of the flow in the axisymmetric case, with Ω_1 (Newtonian fluid) lubricated by Ω_2 (Bingham fluid); c) Schematic of the type of basic velocity profiles considered, with reduced rate of strain in the Newtonian fluid and an unyielded plug zone adjacent to the interface in the lubricating fluid; d) A visco-plastically lubricated flow with a square cross-section.

fluids is the implicit assumption of boundedness of the shear stress perturbations, i.e. in both linear stability and nonlinear stability, smallness of the perturbations is measured with respect to the stress perturbations and not the velocity perturbations. Although we use the energy method, our results are conditional on the size of perturbations. In the yield stress context this translates into conditions on the L^∞ norm of shear stress perturbations. Here we also assume a similar condition on the maximal perturbation of the elastic stresses. This enables us to derive decay bounds for the two-fluid system, via control of both Weissenberg and Reynolds numbers. The energy used is a

linear combination of the L^2 norms of the velocity and elastic stress perturbation. Since assumptions were made on the L^∞ norm of the elastic stress perturbation our results are not self-consistent, i.e. this assumption cannot be verified by the results. However, this self-consistency is anyway lacking in VPL flows without elasticity due to the necessity to bound the shear stress perturbations. In this sense the introduction of viscoelasticity does not compromise the stability results.

The chapter proceeds as follows. Below in §5.1 we introduce the model equations and class of flows that we consider. Section 5.2 introduces the analysis for the case where the interface does not move. For clarity, we start with the case in which even the outer fluid layer is static in order to expose the treatment of individual terms in the viscoelastic region. We focus on the core annular case with a circular interface (Figs. 5.1a-c) but also state more general bounds that could be applied to non-circular interfaces (e.g. Fig. 5.1d), which are feasible as steady flows in the VPL context. We allow the outer layer to move in §5.2.2 and then finally in §5.3 allow the fluid domains to translate within the pipe. The chapter closes with a discussion.

5.1 Model equations

Two Non-Newtonian fluids flow along an infinite circular pipe. We focus on the case where the pipe cross section is separated into two distinct fluid domains, with fluid 2 providing a lubricating layer for fluid 1, i.e. the cross-sectional domain occupied by fluid 1 is completely surrounded by fluid 2, which abuts the wall of the pipe, see Fig. 5.1. It will be assumed throughout that fluid 1 is a visco-elastic fluid and fluid 2 is a visco-plastic fluid with yield stress. The aim of this chapter is to show that the type of (conditional) energy stability that was established in [85] for the above configuration with an inelastic core fluid also holds for visco-elastic fluids, under the same physical assumptions on the stress perturbations as made in [85].

We fix an arbitrary finite length $\hat{L}$ of the pipe and will consider nonlinear stability of the basic flows to perturbations that are $\hat{L}$-periodic with respect to the axial direction. We denote the total fluid domain by Ω and the 2 individual fluid domains by Ω_1 and Ω_2, respectively. The pipe and coordinates are aligned such that the $\hat{z}$-axis corresponds to the pipe axis. Fluid 1 has total viscosity $\hat{\mu}^{[1]}$ and solvent viscosity $\hat{\eta}$. Fluid 2 is characterised rheologically by its yield stress $\hat{\tau}^{[2]}_{yield}$ and plastic viscosity $\hat{\mu}^{[2]}$. It is assumed that both fluids have the same density $\hat{\rho}$ and surface tension is neglected. The total flow rate along the pipe is $\hat{Q}$ and the pipe radius is $\hat{R}$, thus defining the mean axial velocity: $\hat{U}_0 = \hat{Q}/\pi\hat{R}^2$. The pressure is denoted $\hat{p}(\hat{\boldsymbol{x}}, \hat{t})$, $\hat{\boldsymbol{u}}(\hat{\boldsymbol{x}}, \hat{t})$ is the velocity, $\hat{\tau_{ij}}^{[k]}$ denotes the deviatoric stress tensor in fluid k, and $\hat{g}_i$ is the gravitational acceleration in direction i.

The Navier-Stokes equations are made dimensionless with the following scaling:

$$\boldsymbol{x} = \frac{\hat{\boldsymbol{x}}}{\hat{R}}, \quad t = \frac{\hat{t}\hat{U}_0}{\hat{R}}, \quad \boldsymbol{u} = \frac{\hat{\boldsymbol{u}}}{\hat{U}_0}, \quad p = \frac{\hat{p}}{\hat{\rho}\hat{U}_0^2}, \quad \tau_{ij} = \frac{\hat{\tau}_{ij}\hat{R}}{\hat{\mu}^{[2]}\hat{U}_0}, \quad f_i = \frac{\hat{g}_i\hat{R}}{\hat{U}_0^2}, \tag{5.1}$$

leading to:

$$\frac{\partial u_i}{\partial t} + u_j\frac{\partial u_i}{\partial x_j} = -\frac{\partial p}{\partial x_i} + \frac{1}{Re^{[2]}}\frac{\partial \tau_{ij}{}^{[l]}}{\partial x_j} + f_i, \qquad l = 1, 2 \tag{5.2}$$

$$0 = \frac{\partial u_i}{\partial x_i}, \tag{5.3}$$

in each fluid domain. Constitutive laws for the two fluids are:

$$\tau_{ij}^{[1]} = \beta m\dot{\gamma}_{ij} + \tau_{ij}^e \tag{5.4}$$

$$\frac{1}{We}\tau_{ij}^e + \frac{\partial \tau_{ij}^e}{\partial t} + u_k\frac{\partial \tau_{ij}^e}{\partial x_k} - \frac{\partial u_i}{\partial x_k}\tau_{kj}^e - \tau_{ik}^e\frac{\partial u_j}{\partial x_k} = \frac{m}{We}(1-\beta)\dot{\gamma}_{ij}, \tag{5.5}$$

$$\dot{\gamma}(\boldsymbol{u}) = 0 \iff \tau^{[2]}(\boldsymbol{u}) \leq B, \tag{5.6}$$

$$\tau_{ij}^{[2]}(\boldsymbol{u}) = \left[1 + \frac{B}{\dot{\gamma}(\boldsymbol{u})}\right] \dot{\gamma}_{ij}(\boldsymbol{u}) \iff \tau^{[2]}(\boldsymbol{u}) > B. \tag{5.7}$$

where

$$\dot{\gamma}_{ij} = \frac{\partial u_i}{\partial x_j} + \frac{\partial u_j}{\partial x_i},$$

$$\dot{\gamma}(\boldsymbol{u}) = \left[\frac{1}{2}\sum_{i,j=1}^{3}[\dot{\gamma}_{ij}(\boldsymbol{u})]^2\right]^{1/2} \qquad \tau^{[2]}(\boldsymbol{u}) = \left[\frac{1}{2}\sum_{i,j=1}^{3}[\tau_{ij}^{[2]}(\boldsymbol{u})]^2\right]^{1/2}. \tag{5.8}$$

Thus, we have assumed that the outer fluid is a Bingham fluid and the inner fluid is an Oldroyd-B fluid.

The 5 dimensionless parameters appearing above are defined by:

$$m = \frac{\hat{\mu}^{[1]}}{\hat{\mu}^{[2]}}, \quad \beta = \frac{\hat{\eta}}{\hat{\mu^{[1]}}}, \quad We = \frac{\hat{\lambda}\hat{U}_0}{\hat{R}}, \quad Re^{[2]} = \frac{\hat{\rho}\hat{R}\hat{U}_0}{\hat{\mu}^{[2]}}, \quad B = \frac{\hat{\tau}_{yield}^{[2]}\hat{R}}{\hat{U}_0\hat{\mu}^{[2]}}. \tag{5.9}$$

These are the viscosity ratio m (total viscosity of inner to plastic viscosity of outer fluid), the solvent to total viscosity ratio of fluid 1 (β), the Weissenberg number of fluid 1 (We, where $\hat{\lambda}$ is characteristic relaxation time for viscoelastic fluid), the fluid 2 Reynolds number and the Bingham number, respectively. A fluid 1 Reynolds number $Re^{[1]}$ may also be defined as: $Re^{[2]} = m\beta Re^{[1]}$, and will be used for convenience later.

Boundary conditions are:

$$\boldsymbol{u} = 0, \qquad x^2 + y^2 = 1, \tag{5.10}$$

$$\boldsymbol{u}(x, y, z, t) = \boldsymbol{u}(x, y, z + L, t), \tag{5.11}$$

Across the interface, (denoted Γ_i with unit normal $\boldsymbol{n}$), velocity and stress are

continuous:

$$\boldsymbol{u} \qquad \text{continuous on } \Gamma_i, \tag{5.12}$$

$$(-p\delta_{ij} + \frac{1}{Re^{[2]}}\tau_{ij}^{[k]})n_j \qquad \text{continuous on } \Gamma_i, \tag{5.13}$$

where δ_{ij} is the Kronecker delta.

5.1.1 Axisymmetric base flows

In what follows we shall consider nonlinear perturbations of the base flow. Following [85] the base flows of interest will include those that are asymmetric. However, to gain some insight into the problem we start by considering axisymmetric base flows, in which a circular region of fluid 1 is surrounded concentrically by an annulus of fluid 2. The base flows are parallel shear flows with a single velocity component W in the z-direction. We adopt cylindrical coordinates (r, θ, z), and denote the axisymmetric base solution $\boldsymbol{u} = (0, 0, W(r))$. The interface between the fluids is at $r = r_i$.

For fluid 1, the elastic stress of the base flow has the following form:

$$\tau_{ij}^{[e]} = \begin{bmatrix} 0 & 0 & m(1-\beta)W' \\ 0 & 0 & 0 \\ m(1-\beta)W' & 0 & 2\,We\,m(1-\beta)W'^2 \end{bmatrix}$$

We note that in a fully developed flow the component $\tau_{zz}^{[e]}$ plays no role in determining the base velocity, which is essentially Newtonian and determined from $\tau_{rz} = \beta m\dot{\gamma}_{rz} + \tau_{rz}^{[e]}$. Instead, this expression defines $\tau_{zz}^{[e]}$ in terms of the base velocity gradient.

To find the base flow we include the body force terms f_i into a modified pressure field, $P(z)$, which decreases linearly with z, and define

$$G = -Re^{[2]}\frac{\partial P}{\partial z} > 0.$$

In the Bingham fluid the only non-zero components of the stress tensor are:

$$\tau_{rz}^{[2]} = \tau_{zr}^{[2]} = -\frac{Gr}{2}, \tag{5.14}$$

and we observe that the Bingham fluid is yielded for $r > r_y$, where $r_y = 2B/G$. If the Bingham fluid is yielded, then we have:

$$\tau_{rz}^{[2]} = \tau_{zr}^{[2]} = -\frac{Gr}{2} = W'(r) - B,$$

and otherwise $W'(r) = 0$. Three different types of base flow can be found according to whether or not the Bingham fluid moves at all, and whether or not the Bingham fluid is yielded at the interface, i.e. $r_y \geq 1$, $1 > r_y > r_i$ or $r_y \leq r_i$. We illustrate these solution types in Fig. 5.2 and describe the different cases as follows.

Case 1: $r_y \in (r_i, 1)$, in which case there exists an unyielded plug surrounding the Newtonian region. The solution is given by:

$$W(r) = \begin{cases} \dfrac{G}{4m}[(r_i^2 - r^2)] + W_p & 0 \leq r \leq r_i, \\ W_p & r_i < r \leq r_y, \\ W_p - \dfrac{B}{2r_y}[(r - r_y)^2] & r_y < r \leq 1. \end{cases} \tag{5.15}$$

where the flow rate constraint now leads to finding G from the root of the following quartic:

$$0 = G^4(3 + \frac{3r_i^4}{m}) - 8G^3(3 + B) + 16B^4. \tag{5.16}$$

This can be recast into an implicit equation for r_y:

$$0 = 3 + \frac{3r_i^4}{m} - 4r_y\left(\frac{3}{B} + 1\right) + r_y^4. \tag{5.17}$$

The plug velocity W_p and yield surface radius are given by:

$$W_p = \frac{B}{2r_y}(1 - r_y)^2, \qquad r_y = \frac{2B}{G} \tag{5.18}$$

Case 2: $r_y \in [0, r_i)$, in which case the Bingham fluid region is entirely yielded. The solution is given by:

$$W(r) = \begin{cases} \dfrac{G}{4m}(r_i^2 - r^2) + \dfrac{G}{4}(1 - r_i^2) + B(r_i - 1) & 0 \le r \le r_i, \\ \dfrac{G}{4}(1 - r)^2 + B(r - 1) & r_i < r \le 1. \end{cases} \tag{5.19}$$

with G determined from:

$$0 = 8B(r_i^3 - 1 - \frac{3}{B}) + 3G(1 + \frac{r_i^4}{m} - r_i^4). \tag{5.20}$$

Note that in cases 2 & 3 the nonlinear equations for the pressure gradient G can be recast in the form of equations for $r_y < 1$. The solutions to these equations depend exclusively on (r_i, B, m). The parameter domains where each solution type is found are displayed in Fig. 5.2.

Case 3: $r_y \in [1, \infty)$, in which case the Bingham fluid is wholly unyielded and does not flow. The solution is:

$$W(r) = \begin{cases} \dfrac{G}{4m}[(r_i^2 - r^2)] & 0 \le r \le r_i, \\ 0 & r_i < r \le 1. \end{cases} \tag{5.21}$$

Where, G, which is determined from:

$$0 = 8m - Gr_i^4. \tag{5.22}$$

This latter equation is simply the constraint on the flow rate which follows from scaling with the mean velocity, i.e. the mean velocity must equal 1.

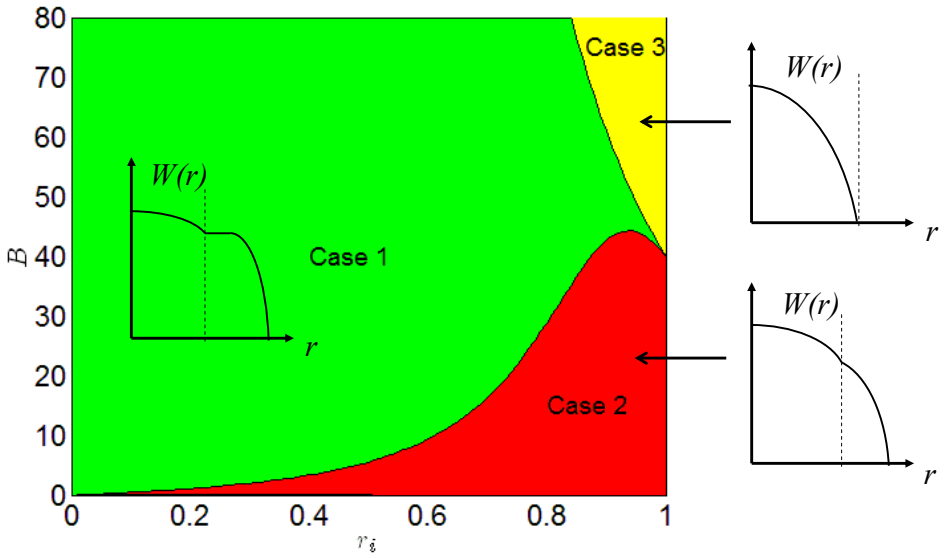

Figure 5.2: Parameter domains where the base solutions are found in (r_i, B, m)-space for $m = 10$, with schematic velocity profiles.

5.2 Conditional stability for a stationary domain Ω_1

Compared to previous studies the main physical difference we consider is that the inner core fluid 1 is now viscoelastic. Our treatment of the Bingham fluid will be largely as in [85], so we structure this chapter to expose the analysis of the viscoelastic core. For this reason we start (§5.2.1) with the simplest situation, namely that in which the outer Bingham fluid is static (i.e. case 3, above) which has only the viscoelastic fluid to deal with. We then move to the visco-plastic lubrication scenario (case 2, above), but still keeping the interface between domains fixed (§5.2.2). In the following section (§5.3) we allow the interface and plug to move. As we develop our analysis we consider primarily the concentric circular interface, but also outline how the various bounds are changed for a more general shape of Ω_1.

5.2.1 Conditional stability of the case 3 axisymmetric base flow

Although we start with a case 3 axisymmetric base flow, which apparently requires only analysis of fluid 1, it is important to realize at the outset that the validity of the analysis is still conditional on the size of shear stress perturbation. The base stress in the outer fluid is given by (5.14) and the non-zero components have maximal value $G/2 < B$ at the outer wall. If the outer fluid is to remain unyielded we require:

$$|{\tau_{ij}}^{[2]}(\boldsymbol{U}+\boldsymbol{u}) - {\tau_{ij}}^{[2]}(\boldsymbol{U})| < \mathcal{A}, \quad i,j = 1,2,3, \tag{5.23}$$

for some $\mathcal{A} > 0$ such that

$$\tau^{[2]}(\boldsymbol{U}+\boldsymbol{u}) \leq |\mathcal{A} + \tau_{ij}(\boldsymbol{U})| = \left[(\mathcal{A}+G/2)^2 + \frac{7}{2}\mathcal{A}^2\right]^{1/2} < B.$$

Thus, assuming bounds on the L^∞ norm of the perturbed shear stress components is a natural part of any analysis of stability of yield stress fluid flows.

Below we shall also assume a similar bound on the size (L^∞ norm) of the perturbed elastic stresses. This is necessary, but evidently weakens the self-consistency of the energy method. We acknowledge this weakness and can offer no analytical remedy, but simply point out that this type of assumption is anyway necessary in dealing later with the yield stress fluid.

We consider nonlinear stability of (5.21) via the classical energy stability approach. The perturbed velocity and pressure fields are assumed periodic in the axial direction, and are denoted:

$$\boldsymbol{U}+\boldsymbol{u} = (0,0,W) + (u,v,w), \quad \boldsymbol{P}+\boldsymbol{p} = P + p,$$

where $W = W(r)$ is given by (5.21) and $P = P(z)$ is linear in z. The pertur-

bation of the elastic stresses is denoted

$$\delta\tau_{ij}^e = \tau_{ij}^e(\boldsymbol{U}+\boldsymbol{u}) - \tau_{ij}^e(\boldsymbol{U}).$$

The equations of motion and constitutive equation for the base flow are:

$$0 = -\frac{\partial P}{\partial x_i} + \frac{1}{Re^{[2]}}\frac{\partial}{\partial x_j}\tau_{ij}{}^{[1]}(\boldsymbol{U}), \tag{5.24}$$

$$0 = \frac{\partial U_i}{\partial x_i} \tag{5.25}$$

$$0 = \frac{1}{We}\tau_{ij}^e(\boldsymbol{U}) - \frac{\partial U_i}{\partial x_k}\tau_{kj}^e(\boldsymbol{U}) - \tau_{ik}^e(\boldsymbol{U})\frac{\partial U_j}{\partial x_k} - \frac{m}{We}(1-\beta)\dot{\gamma}_{ij}(U) \tag{5.26}$$

and for the perturbed flow:

$$\begin{aligned} 0 = {} & \left[\frac{\partial}{\partial t} + (U_j+u_j)\frac{\partial}{\partial x_j}\right](U_i+u_i) + \frac{\partial}{\partial x_i}(P+p) \\ & -\frac{1}{Re^{[2]}}\frac{\partial}{\partial x_j}\tau_{ij}{}^{[1]}(\boldsymbol{U}+\boldsymbol{u}). \end{aligned} \tag{5.27}$$

$$0 = \frac{\partial}{\partial x_i}(U_i+u_i) \tag{5.28}$$

$$\begin{aligned} 0 = {} & \frac{1}{We}\tau_{ij}^e(\boldsymbol{U}+\boldsymbol{u}) + \frac{\partial\tau_{ij}^e(\boldsymbol{U}+\boldsymbol{u})}{\partial t} + (U_k+u_k)\frac{\partial\tau_{ij}^e(\boldsymbol{U}+\boldsymbol{u})}{\partial x_k} \\ & -\frac{\partial(U_i+u_i)}{\partial x_k}\tau_{kj}^e(\boldsymbol{U}+\boldsymbol{u}) - \tau_{ik}^e(\boldsymbol{U}+\boldsymbol{u})\frac{\partial(U_j+u_j)}{\partial x_k} \\ & -\frac{m}{We}(1-\beta)\dot{\gamma}_{ij}(U+u) \end{aligned} \tag{5.29}$$

For the kinetic energy we subtract (5.24) from (5.27), multiply by u_i, and

integrate over Ω_1 to give

$$\begin{aligned}\int_{\Omega_1} \frac{1}{2}\frac{D}{Dt}{u_i}^2 \,\mathrm{d}\boldsymbol{x} &= -\int_{\Omega_1} u_j \frac{\partial U_i}{\partial x_j} u_i \,\mathrm{d}\boldsymbol{x} \\ &\quad -\frac{1}{Re^{[2]}}\int_{\Omega_1} \frac{\partial u_i}{\partial x_j}[{\tau_{ij}}^{[1]}(\boldsymbol{U}+\boldsymbol{u}) - {\tau_{ij}}^{[1]}(\boldsymbol{U})] \,\mathrm{d}\boldsymbol{x} \\ &\quad +\int_{\partial\Omega_1} u_i[-p + \frac{1}{Re^{[2]}}[\tau_{ij}^{[1]}(\boldsymbol{U}+\boldsymbol{u}) - \tau_{ij}^{[1]}(\boldsymbol{U}))]n_j^{[1]} \,\mathrm{d}s,\end{aligned} \tag{5.30}$$

where we have used the divergence theorem to derive the last term, $\boldsymbol{n}$ denoting the outward normal to the boundary $\partial\Omega_1$ of Ω_1. All the boundary integrals vanish, through a combination of: (i) periodicity at the ends of the domain considered, (ii) zero perturbed velocity $\boldsymbol{u} = 0$ in the outer fluid and consequently (by continuity), $\boldsymbol{u} = 0$ at the interface. This leads to:

$$\frac{1}{2}\frac{D}{Dt}\langle u_i u_i\rangle = -\langle u_j \frac{\partial U_i}{\partial x_j} u_i\rangle - \frac{m\beta}{Re^{[2]}}\langle \frac{\partial u_i}{\partial x_j}\frac{\partial u_i}{\partial x_j}\rangle - \frac{1}{Re^{[2]}}\langle \frac{\partial u_i}{\partial x_j}\delta\tau_{ij}^e\rangle \tag{5.31}$$

where, we have denoted by $\langle . \rangle$ the operation of integration over Ω_1.

For the elastic perturbation we consider (a linear multiple of) the polymer's elastic potential energy. We subtract (5.26) from (5.29), multiply by $\delta\tau_{ij}^e$, and integrate over domain Ω_1 to give:

$$\begin{aligned}&\frac{1}{2}\frac{D}{Dt}\langle \delta\tau_{ij}^e \delta\tau_{ij}^e\rangle + \frac{1}{We}\langle \delta\tau_{ij}^e \delta\tau_{ij}^e\rangle = \frac{2m(1-\beta)}{We}\langle \frac{\partial u_i}{\partial x_j}\delta\tau_{ij}^e\rangle \qquad (5.32)\\ &+\langle \frac{\partial(U_i+u_i)}{\partial x_k}\delta\tau_{kj}^e\delta\tau_{ij}^e\rangle + \langle \delta\tau_{ik}^e \frac{\partial(U_j+u_j)}{\partial x_k}\delta\tau_{ij}^e\rangle \qquad \text{(Term A)}\\ &+\langle \frac{\partial u_i}{\partial x_k}\tau_{kj}^e(\boldsymbol{U})\delta\tau_{ij}\rangle + \langle \tau_{ik}^e(\boldsymbol{U})\frac{\partial u_j}{\partial x_k}\delta\tau_{ij}\rangle \qquad \text{(Term B)}\\ &-\langle u_k \frac{\partial \tau_{ij}^e(\boldsymbol{U})}{\partial x_k}\delta\tau_{ij}^e\rangle \qquad \text{(Term C)}\end{aligned}$$

As total energy functional $E^{[1]}$ for the perturbed flow of fluid 1, we select

$$E^{[1]} = \frac{1}{2}\left[\langle u_i u_i\rangle + \frac{We}{2m(1-\beta)Re^{[2]}}\langle \delta\tau^e_{ij}\delta\tau^e_{ij}\rangle\right] =$$

$$\frac{1}{2}\left[||\boldsymbol{u}||_2^2 + \frac{We}{2m^2\beta(1-\beta)Re^{[1]}}||\delta\boldsymbol{\tau}^e||_2^2\right];$$

recall $Re^{[2]} = m\beta Re^{[1]}$. Note that we use $||\cdot||_p$ to denote the L^p norm. This choice of a specific linear combination of kinetic and elastic perturbation energies serves to balance the last term in (5.31) with the first term on the right-hand side of (5.32). Combining (5.31) with (5.32) leads to:

$$\begin{aligned}\frac{D}{Dt}E^{[1]} &= -\langle u_j\frac{\partial U_i}{\partial x_j}u_i\rangle - \frac{1}{Re^{[1]}}\langle\frac{\partial u_i}{\partial x_j}\frac{\partial u_i}{\partial x_j}\rangle - \frac{1}{2m^2\beta(1-\beta)Re^{[1]}}\langle\delta\tau^e_{ij}\delta\tau^e_{ij}\rangle \\ &+\frac{We}{2m^2\beta(1-\beta)Re^{[1]}}\left[(\text{Term A}) + (\text{Term B}) + (\text{Term C})\right] \quad (5.33)\end{aligned}$$

The first term in (5.33) is bounded as follows

$$-\langle u_j\frac{\partial U_i}{\partial x_j}u_i\rangle = \frac{G}{2m}\langle ruw\rangle \leq \frac{G\Lambda_N}{2m}\langle\frac{\partial u_i}{\partial x_j}\frac{\partial u_i}{\partial x_j}\rangle, \quad (5.34)$$

and following [85] we have the upper bound $\Lambda_N \leq r_i^3/R_J$, with $R_J = 81.49$ from Joseph & Carmi (see e.g. [58, 60]). We now consider bounds for (Term A) - (Term C).

Term A

General Ω_1: From the symmetry of $\delta\tau^e_{ij}$ and linearity of $\dot{\gamma}_{ij}$, we can rewrite:

$$(\text{Term A}) = \langle\delta\tau^e_{ij}\dot{\gamma}_{ik}(\boldsymbol{U})\delta\tau^e_{kj}\rangle + \langle\delta\tau^e_{ij}\dot{\gamma}_{ik}(\boldsymbol{u})\delta\tau^e_{kj}\rangle.$$

Using the generalized Holder inequality and modified Young's inequality (see [3]) we can bound the first term above as follows (making the summations

explicit):

$$\begin{aligned}\langle \delta\tau^e_{ij}\dot{\gamma}_{ik}(\boldsymbol{U})\delta\tau^e_{kj}\rangle &= \langle \sum_{i,k=1}^{3}\dot{\gamma}_{ik}(\boldsymbol{U})\sum_{j=1}^{3}\delta\tau^e_{kj}\delta\tau^e_{ij}\rangle \\ &\leq \sum_{i,j,k=1}^{3}||\dot{\gamma}_{ik}(\boldsymbol{U})||_\infty\ ||\delta\tau^e_{kj}||_2\ ||\delta\tau^e_{ij}||_2 \\ &\leq C_{A,1}\sum_{i,j,k=1}^{3}\frac{\langle\delta\tau^e_{kj}\delta\tau^e_{kj}\rangle^2}{2}+\frac{\langle\delta\tau^e_{ij}\delta\tau^e_{ij}\rangle^2}{2} = 3C_{A,1}\langle\delta\tau^e_{ij}\delta\tau^e_{ij}\rangle,\end{aligned}$$

where

$$C_{A,1}\equiv\max_{ik}\{||\dot{\gamma}_{ik}(\boldsymbol{U})||_\infty\}.$$

For the second part of (Term A) we note that the expressions are cubic in the perturbation. As discussed earlier, we shall assume a bound of the form (5.23) on the elastic stress perturbations. For simplicity we adopt the same upper bound, i.e. we assume

$$||\delta\boldsymbol{\tau}^e||_\infty < \mathcal{A}. \tag{5.35}$$

Applying the same inequalities as for the first part of (Term A) we may write :

$$\begin{aligned}\langle\sum_{i,j,k=1}^{3}\dot{\gamma}_{ik}(\boldsymbol{u})\delta\tau^e_{kj}\delta\tau^e_{ij}\rangle &\leq ||\delta\boldsymbol{\tau}^e||_\infty\sum_{i,j,k=1}^{3}\frac{\langle\dot{\gamma}_{ik}(\boldsymbol{u})\dot{\gamma}_{ik}(\boldsymbol{u})\rangle}{2}+\frac{\langle\delta\tau^e_{ij}\delta\tau^e_{ij}\rangle}{2} \\ &\leqq \frac{3}{2}\mathcal{A}\{\langle\dot{\gamma}_{ij}(\boldsymbol{u})\dot{\gamma}_{ij}(\boldsymbol{u})\rangle+\langle\delta\tau^e_{ij}\delta\tau^e_{ij}\rangle\}.\end{aligned}$$

Circular Ω_1: For the circular cylindrical domain we have only one non-zero rate of strain for the base flow, so that $C_{A,1} = Gr_i/2m$ and:

$$\langle\delta\tau^e_{ij}\dot{\gamma}_{ik}(\boldsymbol{U})\delta\tau^e_{kj}\rangle \leq C_{A,1}\langle\delta\tau^e_{ij}\delta\tau^e_{ij}\rangle = \frac{Gr_i}{2m}||\delta\boldsymbol{\tau}^e||_2^2. \tag{5.36}$$

Consequently for (Term A) we have:

$$(\text{Term A}) \leqq \left(\frac{Gr_i}{2m} + \frac{3\mathcal{A}}{2}\right) ||\delta\boldsymbol{\tau}^e||_2^2 + 3\mathcal{A}\langle\frac{\partial u_i}{\partial x_j}\frac{\partial u_i}{\partial x_j}\rangle. \tag{5.37}$$

Note we have used that:

$$\langle\dot{\gamma}_{ij}(\boldsymbol{u})\dot{\gamma}_{ij}(\boldsymbol{u})\rangle = 2\langle\frac{\partial u_i}{\partial x_j}\frac{\partial u_i}{\partial x_j}\rangle.$$

Term B

General Ω_1: For (Term B) we use symmetry of the elastic stress tensor, then apply the generalized Holder inequality and modified Young's inequality:

$$\begin{aligned}
(\text{Term B}) &= \langle\sum_{i,k=1}^{3}\dot{\gamma}_{ik}(\boldsymbol{u})\sum_{j=1}^{3}\tau_{ji}^e(\boldsymbol{U})\delta\tau_{jk}^e\rangle \\
&\leq \sum_{i,j,k=1}^{3}||\dot{\gamma}_{ik}(\boldsymbol{u}))||_2||\tau_{ji}^e(\boldsymbol{U})||_\infty||\delta\tau_{jk}^e(\boldsymbol{U})||_2 \\
&\leq C_{B,1}\sum_{i,j,k=1}^{3}\frac{\langle\dot{\gamma}_{ik}(\boldsymbol{u})\dot{\gamma}_{ik}(\boldsymbol{u})\rangle}{2} + \frac{\langle\delta\tau_{jk}^e\delta\tau_{jk}^e\rangle}{2} \\
&= 3C_{B,1}\left(\frac{||\delta\boldsymbol{\tau}^e||_2^2}{2} + \langle\frac{\partial u_i}{\partial x_j}\frac{\partial u_i}{\partial x_j}\rangle\right),
\end{aligned}$$

where $C_{B,1} \equiv \sup_{ij}\{||\tau_{ij}^e(\boldsymbol{U})||_\infty$.

Circular Ω_1: In this case there are only 2 non-zero elastic stress components:

$$\tau_{rz}^e(\boldsymbol{U}) = \tau_{zr}^e(\boldsymbol{U}) = (1-\beta)\frac{Gr}{2}, \quad \tau_{zz}^e(\boldsymbol{U}) = We(1-\beta)\frac{G^2r^2}{2m}, \tag{5.38}$$

so that

$$C_{B,1} = (1-\beta)\frac{Gr_i}{2}\max\left\{1, \frac{WeGr_i}{m}\right\},$$

and the bound can be improved to:

$$\text{(Term B)} \quad \leq \quad C_{B,1}\left(||\delta\boldsymbol{\tau}^e||_2^2 + 2\langle\frac{\partial u_i}{\partial x_j}\frac{\partial u_i}{\partial x_j}\rangle\right). \tag{5.39}$$

Term C

General Ω_1: We apply the generalized Holder inequality on (Term C) in the following way:

$$\text{(Term C)} \leq \sum_{i,j,k=1}^{3}\left\|\frac{\partial\tau_{ij}^e(\boldsymbol{U})}{\partial x_k}\right\|_3 ||u_k||_6||\delta\tau_{ij}^e||_2 \tag{5.40}$$

For this choice of spaces, using the Sobolev embedding theorem, we have:

$$||\boldsymbol{u}||_{L^6} \leq C_{C,0}||\boldsymbol{u}||_{W^{1,2}}$$

for some positive constant $C_{C,0}$. Thus, we can proceed in the usual fashion to derive an energy bound. The main point here is that we can use the norm

$$\left\|\frac{\partial\tau_{ij}^e(\boldsymbol{U})}{\partial x_k}\right\|_3$$

for the base flow elastic stress field. This may allow us to treat less regular base flow elastic stress fields within the same framework. Such stress fields are likely to arise from less regular domains Ω_1.

Circular Ω_1: For this case the base flow elastic stresses are C^∞, have only 3 non-zero components (depending only on r) and we can use a simpler choice

of spaces:

$$\begin{aligned}(\text{Term C}) &\leq \sum_{i,j=1}^{3} \left\| \frac{\partial \tau_{ij}^e(\boldsymbol{U})}{\partial x_k} \right\|_\infty ||u||_2 ||\delta\tau_{ij}^e||_2 \\ &\leq C_{C,1} \sum_{i,j=1}^{3} ||\boldsymbol{u}||_2 ||\delta\tau_{ij}^e||_2 \leq \frac{3C_{C,1}}{2}||\boldsymbol{u}||_2^2 + \frac{C_{C,1}}{2}||\delta\boldsymbol{\tau}^e||_2^2\end{aligned}$$

where, from (5.38) we have:

$$C_{C,1} \equiv \sup_{ij}\left\{ \left\| \frac{\partial \tau_{ij}^e(\boldsymbol{U})}{\partial x_k} \right\|_\infty \right\} = (1-\beta)\frac{G}{2}\max\left\{1, \frac{2WeGr_i}{m}\right\}.$$

Energy decay bound

Combining our bounds for the above terms we have the following energy inequality:

$$\begin{aligned}\frac{D}{Dt}E^{[1]} &\leq \frac{1}{2m^2\beta(1-\beta)Re^{[1]}}\left[\mathcal{F}_{\mathcal{I}}-1\right]||\delta\boldsymbol{\tau}^e||_2^2 \\ &\quad + \left[\mathcal{F}_{\mathcal{II}}^* - \frac{1}{Re^{[1]}}\right]\langle \frac{\partial u_i}{\partial x_j}\frac{\partial u_i}{\partial x_j}\rangle + \mathcal{F}_{\mathcal{III}}^*||\boldsymbol{u}||_2^2 \qquad (5.41)\end{aligned}$$

where the constants are:

$$\mathcal{F}_{\mathcal{I}} = We\left[\frac{3\mathcal{A}}{2} + \frac{Gr_i}{2m} + C_{B,1} + \frac{C_{C,1}}{2}\right] \qquad (5.42)$$

$$\mathcal{F}_{\mathcal{II}}^* = \frac{G\Lambda_N}{2m} + \frac{We}{2m^2\beta(1-\beta)Re^{[1]}}\left[3\mathcal{A} + 2C_{B,1}\right] \qquad (5.43)$$

$$\mathcal{F}_{\mathcal{III}}^* = \frac{We}{2m^2\beta(1-\beta)Re^{[1]}}\frac{3C_{C,1}}{2} \qquad (5.44)$$

For energy decay we shall assume that $\mathcal{F}_{\mathcal{II}}^* < 1/Re^{[1]}$, after which we can

apply the Poincaré inequality, combining the last two terms in (5.41):

$$-\left[\frac{1}{Re^{[1]}}-\mathcal{F}^*_{\mathcal{II}}\right]\langle\frac{\partial u_i}{\partial x_j}\frac{\partial u_i}{\partial x_j}\rangle+\mathcal{F}^*_{\mathcal{III}}||\boldsymbol{u}||_2^2 \;\leq\; -\frac{1}{Re^{[1]}C_P}[1-\mathcal{F}_{\mathcal{II}}]||\boldsymbol{u}||_2^2$$

where

$$\mathcal{F}_{\mathcal{II}}=\frac{G\Lambda_N Re^{[1]}}{2m}+\frac{We}{2m^2\beta(1-\beta)}\left[3\mathcal{A}+2C_{B,1}+\frac{3C_PC_{C,1}}{2}\right]$$

and C_P is the coefficient in the Poincaré-inequality for circular Ω_1 of radius r_i:

$$C_P=\frac{r_i^2}{R_M},$$

where $R_M=5.78319$; see [85].

We can see that $\mathcal{F}^*_{\mathcal{II}}<1/Re^{[1]}$ is satisfied if $\mathcal{F}_{\mathcal{II}}<1$. Assuming the two conditions: $\mathcal{F}_{\mathcal{I}}<1$ and $\mathcal{F}_{\mathcal{II}}<1$ we have:

$$\begin{aligned}\frac{D}{Dt}E^{[1]}(t) &= \frac{D}{Dt}\left[\frac{We}{2m^2\beta(1-\beta)Re^{[1]}}\frac{||\delta\boldsymbol{\tau}^e||_2^2}{2}+\frac{||\boldsymbol{u}||_2^2}{2}\right]\\ &\leq -\left[\frac{(1-\mathcal{F}_{\mathcal{I}})}{2m^2\beta(1-\beta)Re^{[1]}}||\delta\boldsymbol{\tau}^e||_2^2+\frac{(1-\mathcal{F}_{\mathcal{II}})}{Re^{[1]}C_P}||\boldsymbol{u}||_2^2\right],\\ &\leq -2\min\left\{\frac{(1-\mathcal{F}_{\mathcal{I}})}{We},\frac{(1-\mathcal{F}_{\mathcal{II}})}{Re^{[1]}C_P}\right\}E^{[1]}(t). \qquad (5.45)\end{aligned}$$

and consequently:

$$E^{[1]}(t)\leq E^{[1]}(0)\exp\left(-2\min\left\{\frac{(1-\mathcal{F}_{\mathcal{I}})}{We},\frac{(1-\mathcal{F}_{\mathcal{II}})}{Re^{[1]}C_P}\right\}t\right),$$

showing the role of both We and $Re^{[1]}$ in the decay of the energy.

Let's now examine the two conditions $\mathcal{F}_{\mathcal{I}}<1$ and $\mathcal{F}_{\mathcal{II}}<1$, with the aim of extracting simpler expressions that can be interpreted physically. If $\mathcal{F}_{\mathcal{I}}<1$ we see that $WeGr_i/m<2$ and this allows us to bound the constants $C_{B,1}$ and

$C_{C,1}$. Substituting also for the expression for $G = 8m/r_i^4$, we have:

$$\mathcal{F}_{\mathcal{I}} \leq We \left[\frac{3\mathcal{A}}{2} + \frac{8}{r_i^4}(r_i[0.5 + m(1-\beta)] + m(1-\beta)) \right] \leq 1.$$

$$\mathcal{F}_{\mathcal{II}} \leq \frac{4Re^{[1]}}{81.49 r_i} + \frac{We}{m^2\beta(1-\beta)} \left[\frac{3\mathcal{A}}{2} + \frac{m(1-\beta)}{r_i^3}(8 + \frac{12 r_i}{5.783..}) \right] \leq 1.$$

Starting with $\mathcal{F}_{\mathcal{II}} < 1$, we see that it is first necessary to satisfy a bound on $Re^{[1]}$. Suppose we satisfy the constraint on $Re^{[1]}$ by setting

$$\frac{4Re^{[1]}}{81.49 r_i} = \alpha < 1, \tag{5.46}$$

for some chosen α. We now select We to satisfy:

$$We \leq \min \left\{ \frac{1}{\left[\frac{3\mathcal{A}}{2} + \frac{8}{r_i^4}(r_i[0.5 + m(1-\beta)] + m(1-\beta)) \right]}, \frac{(1-\alpha)m^2\beta(1-\beta)}{\left[\frac{3\mathcal{A}}{2} + \frac{m(1-\beta)}{r_i^3}(8 + \frac{12 r_i}{5.783..}) \right]} \right\} \tag{5.47}$$

Both the above bounds depend on r_i. In the bound for We this dependency is strong. Note however that for a case 3 base flow all the fluid passes through the central core: the mean velocity scales like $1/r_i^2$ and the diameter like r_i. Consequently, we may consider that an appropriate Reynolds number for the inner fluid in a case 3 flow is:

$$\tilde{Re}^{[1]} = \frac{Re^{[1]}}{r_i},$$

and similarly, an appropriate Weissenberg number is

$$\tilde{We} = \frac{We}{r_i^3}.$$

Consequently, the bounds become

$$\begin{aligned}
\tilde{Re}^{[1]} &= \frac{81.49\alpha}{4}: \quad \alpha < 1, && (5.48)\\
\tilde{We} &\leq \min\{\Xi_1\Xi_2\} && (5.49)\\
\Xi_1 &= \frac{1}{\left[\frac{3\mathcal{A}r_i^3}{2} + 8([0.5 + m(1-\beta)] + m(1-\beta)/r_i)\right]},\\
\Xi_2 &= \frac{(1-\alpha)m^2\beta(1-\beta)}{\left[\frac{3\mathcal{A}r_i^3}{2} + m(1-\beta)(8 + \frac{12r_i}{5.783..})\right]}.
\end{aligned}$$

Neither bound is particularly severe when expressed in terms of the modified Reynolds and Weissenberg numbers, $\tilde{Re}^{[1]}$ and $\tilde{We}$.

If we were to consider a non-circular Ω_1, the more general bounds on terms A-C need to be applied, which rely on some regularity of Ω_1. However, we can see that the basic structure of the inequalities and the conditions for energy stability, are not qualitatively affected.

5.2.2 Conditional stability for the case 1 axisymmetric base solution: stationary Ω_1

We now look at the situation in which the base solution is the case 1 axisymmetric solution, so that the outer Bingham fluid is mobile. In the next section (§5.3) we allow for the possibility that the interface and surrounding plug region are mobile, but here we consider a more restricted problem.

(i) The domain Ω_1 remains stationary, i.e. the interface does not move and the perturbed velocity is zero at the interface.

(ii) The shear stress of the nonlinear perturbation satisfies a stress bound of form (5.23), such that we retain a layer of unyielded fluid around the interface. We also assume again a bound on the elastic stress perturbation of the same form, as in the previous section.

This last condition amounts to choosing a sufficiently small (but finite) bound $\mathcal{A}$ in (5.23). Note that the unperturbed stress varies linearly with r:

$$\tau^{[2]}(\boldsymbol{U})(r) = |\tau_{rz}{}^{[2]}(\boldsymbol{U})|(r) = \frac{r}{r_y}B.$$

From (5.23) we see that

$$\tau^{[2]}(\boldsymbol{U}+\boldsymbol{u}) \leq \left[\left(\mathcal{A}+\frac{r}{r_y}B\right)^2 + \frac{7}{2}\mathcal{A}^2\right]^{1/2},$$

and setting $r^* \in (r_i, r_y)$ the perturbed flow will be unyielded for $r \in (r_i, r^*)$ provided that

$$\mathcal{A} < \frac{2B}{9}\left(\left[\frac{9}{2} - \frac{7}{2}(\frac{r^*}{r_y})^2\right]^{1/2} - \frac{r^*}{r_y}\right), \tag{5.50}$$

i.e. with $\mathcal{A}$ satisfying (5.50) we have an unyielded fluid ring of width $h = r^* - r_i$ surrounding the interface.

This restricted problem might be (falsely) interpreted as being irrelevant, but in fact is a natural extension of a linear stability analysis. In linear stability of visco-plastic fluids, the asymptotically small size of perturbation is imposed on the shear stress rather than on the strain rate (or velocity); see the discussion in [28]. Essentially we take $\mathcal{A} \ll 1$, which implies only a linear perturbation in the yield surface. Under the normal mode approach, for temporal stability, the linearly perturbed stresses are periodic in z, which has the consequence that the net force of the perturbation on the unyielded plug integrates to zero. Thus, linear perturbation problems for yield stress fluids leave any finite plug regions unperturbed. Our assumptions above can be viewed as relaxing $\mathcal{A} \ll 1$ into the nonlinear domain, but retaining the (linear) condition that the plug region is not perturbed. Even in nonlinear stability studies of yield stress fluid flows it is common to make assumptions of boundedness of the shear stress perturbation, e.g. [87].

The kinetic energy equation in each domain Ω_k is:

$$\begin{aligned}\int_{\Omega_k} \frac{1}{2}\frac{D}{Dt}{u_i}^2 \,\mathrm{d}\boldsymbol{x} &= -\int_{\Omega_k} u_j \frac{\partial U_i}{\partial x_j} u_i \,\mathrm{d}\boldsymbol{x} \\ &\quad -\frac{1}{Re^{[2]}}\int_{\Omega_k} \frac{\partial u_i}{\partial x_j}[{\tau_{ij}}^{[k]}(\boldsymbol{U}+\boldsymbol{u}) - {\tau_{ij}}^{[k]}(\boldsymbol{U})] \,\mathrm{d}\boldsymbol{x} \\ &\quad +\int_{\partial\Omega_k} u_i[-p + \frac{1}{Re^{[2]}}[\tau_{ij}^{[k]}(\boldsymbol{U}+\boldsymbol{u}) - \tau_{ij}^{[k]}(\boldsymbol{U}))]n_j^{[k]} \,\mathrm{d}s,\end{aligned} \tag{5.51}$$

On summing the kinetic energy equations for the two domains the interfacial terms above cancel, via continuity. The rest of the boundary integrals cancel out due to either periodicity in z or to the boundary conditions at the wall. We now add the perturbation kinetic energy of the Bingham fluid region to the energy $E^{[1]}(t)$ of the viscoelastic region, to give:

$$E(t) = \frac{1}{2}[\langle u_i u_i\rangle_{\Omega_1} + \langle u_i u_i\rangle_{\Omega_2} + \frac{We}{2m^2\beta(1-\beta)Re^{[1]}}\langle \delta\tau_{ij}^e \delta\tau_{ij}^e\rangle_{\Omega_1}].$$

We have appended a subscript to the $\langle . \rangle$ operator, to indicate which domain the integration is over. Adding in (5.32) as before, to the total kinetic energy we arrive at:

$$\begin{aligned}\frac{D}{Dt}E &= -\langle u_j\frac{\partial U_i}{\partial x_j}u_i\rangle_{\Omega_1} - \frac{1}{Re^{[1]}}\langle\frac{\partial u_i}{\partial x_j}\frac{\partial u_i}{\partial x_j}\rangle_{\Omega_1} - \frac{\langle\delta\tau_{ij}^e\delta\tau_{ij}^e\rangle_{\Omega_1}}{2m^2\beta(1-\beta)Re^{[1]}} \\ &\quad +We\frac{[(\text{Term A})+(\text{Term B})+(\text{Term C})]}{2m^2\beta(1-\beta)Re^{[1]}} \\ &\quad -\langle u_j\frac{\partial U_i}{\partial x_j}u_i\rangle_{\Omega_2} - \frac{1}{Re^{[2]}}\langle\frac{\partial u_i}{\partial x_j}[\tau_{ij}^{[2]}(\boldsymbol{U}+\boldsymbol{u}) - \tau_{ij}^{[2]}(\boldsymbol{U})]\rangle_{\Omega_2}\end{aligned} \tag{5.52}$$

Note that (Term A) - (Term C) are exactly as in (5.32).

The Viscoelastic fluid region, Ω_1

The base flow velocity is still an axisymmetric function, depending only on r. The velocity gradients, strain rate components and elastic stresses of the inner fluid are the same as for the case 3 base solution, given by identical expressions except that now the modified pressure gradient G is found from (5.16). Since we consider the case where the interface and plug region are not perturbed, it follows that $\boldsymbol{u} = 0$ at the interface $r = r_i$.

It follows that the stability analysis for the viscoelastic region is the same as §5.2.1. We may write

$$\begin{aligned}\frac{D}{Dt}E \;\leq\; & \frac{[\mathcal{F}_{\mathcal{I}}-1]}{2m^2\beta(1-\beta)Re^{[1]}}||\delta\boldsymbol{\tau}^e||^2_{\Omega_1} + \left[\mathcal{F}^*_{\mathcal{II}} - \frac{1}{Re^{[1]}}\right]\langle\frac{\partial u_i}{\partial x_j}\frac{\partial u_i}{\partial x_j}\rangle_{\Omega_1} + \mathcal{F}^*_{\mathcal{III}}||\boldsymbol{u}||^2_{\Omega_1} \\ & -\langle u_j\frac{\partial U_i}{\partial x_j}u_i\rangle_{\Omega_2} - \frac{1}{Re^{[2]}}\langle\frac{\partial u_i}{\partial x_j}[\tau^{[2]}_{ij}(\boldsymbol{U}+\boldsymbol{u}) - \tau^{[2]}_{ij}(\boldsymbol{U})]\rangle_{\Omega_2} \qquad (5.53)\end{aligned}$$

where $||\cdot||_{\Omega_k}$ denotes the L^2 norm on Ω_k. The constants $\mathcal{F}_{\mathcal{I}}$, $\mathcal{F}^*_{\mathcal{II}}$ and $\mathcal{F}^*_{\mathcal{III}}$ are as defined in (5.42)-(5.44), except that now G is found from (5.16). The only terms left to treat in (5.53) come from the Bingham fluid region.

The Bingham fluid region, Ω_2

We follow precisely the analysis in [85] for the inertial and dissipative terms in (5.53):

$$-\langle u_j\frac{\partial U_i}{\partial x_j}u_i\rangle_{\Omega_2} \leq \frac{G}{2}[\Lambda_B + (r_y - r_i - h)\Lambda_C]\langle\frac{\partial u_i}{\partial x_j}\frac{\partial u_i}{\partial x_j}\rangle_{\Omega_2} \qquad (5.54)$$

$$-\frac{1}{Re^{[2]}}\langle\frac{\partial u_i}{\partial x_j}[\tau^{[2]}_{ij}(\boldsymbol{U}+\boldsymbol{u}) - \tau^{[2]}_{ij}(\boldsymbol{U})]\rangle_{\Omega_2} \leq -\frac{1}{Re^{[2]}}\langle\frac{\partial u_i}{\partial x_j}\frac{\partial u_i}{\partial x_j}\rangle_{\Omega_2} \qquad (5.55)$$

where

$$\Lambda_B \leq \frac{[1-(r_i+h)]^3}{R_J}, \qquad \Lambda_C \leq \frac{[1-(r_i+h)]^2}{R_M}. \qquad (5.56)$$

Energy stability and decay

Combining the bounds of §5.2.2 and §5.2.2, we have straightforwardly:

$$\begin{aligned}\frac{D}{Dt}E &\leq \frac{1}{2m^2\beta(1-\beta)Re^{[1]}}\left[\mathcal{F}_{\mathcal{I}}-1\right]||\delta\boldsymbol{\tau}^e||^2_{\Omega_1}+\left[\mathcal{F}^*_{\mathcal{II}}-\frac{1}{Re^{[1]}}\right]\langle\frac{\partial u_i}{\partial x_j}\frac{\partial u_i}{\partial x_j}\rangle_{\Omega_1}\\ &\quad+\mathcal{F}^*_{\mathcal{III}}||\boldsymbol{u}||^2_{\Omega_1}+\frac{1}{Re^{[2]}}\left[\mathcal{F}_{\mathcal{III}}-1\right]\langle\frac{\partial u_i}{\partial x_j}\frac{\partial u_i}{\partial x_j}\rangle_{\Omega_2} \qquad (5.57)\end{aligned}$$

with

$$\mathcal{F}_{\mathcal{III}}=\frac{Re^{[2]}G}{2}[\Lambda_B+(r_y-r_i-h)\Lambda_C]. \qquad (5.58)$$

We make the assumptions that $\mathcal{F}_{\mathcal{I}}<1$, $\mathcal{F}^*_{\mathcal{II}}<1/Re^{[1]}$ (or $\mathcal{F}_{\mathcal{II}}<1$) and that $\mathcal{F}_{\mathcal{III}}<1$. This allows us to use the Poincaré inequality in both domains, leading to:

$$\begin{aligned}\frac{D}{Dt}E(t) &\leq -\left[\frac{(1-\mathcal{F}_{\mathcal{I}})}{2m^2\beta(1-\beta)Re^{[1]}}||\delta\boldsymbol{\tau}^e||^2_2+\frac{(1-\mathcal{F}_{\mathcal{II}})}{Re^{[1]}C_P}||\boldsymbol{u}||^2_{\Omega_1}+\frac{(1-\mathcal{F}_{\mathcal{III}})}{Re^{[2]}C_{P,2}}||\boldsymbol{u}||^2_{\Omega_2}\right],\\ &\leq -2\min\left\{\frac{(1-\mathcal{F}_{\mathcal{I}})}{We},\frac{(1-\mathcal{F}_{\mathcal{II}})}{Re^{[1]}C_P},\frac{(1-\mathcal{F}_{\mathcal{III}})}{Re^{[2]}C_{P,2}}\right\}E(t). \qquad (5.59)\end{aligned}$$

Here $C_{P,2}$ is the Poincaré constant for Ω_2, which we do not evaluate as it affects the decay rate rather than the condition for stability. Under these conditions we have:

$$E(t)\leq E(0)\exp\left(-2\min\left\{\frac{(1-\mathcal{F}_{\mathcal{I}})}{We},\frac{(1-\mathcal{F}_{\mathcal{II}})}{Re^{[1]}C_P},\frac{(1-\mathcal{F}_{\mathcal{III}})}{Re^{[2]}C_{P,2}}\right\}t\right).$$

Exploration of the stability bounds

As before, we can analyse the bounds $\mathcal{F}_{\mathcal{I}}<1$, $\mathcal{F}_{\mathcal{II}}<1$ and $\mathcal{F}_{\mathcal{III}}<1$, but this is made simpler by some simplification. First, $\mathcal{F}_{\mathcal{I}}<1$ implies that $WeGr_i/m<2$ which allows simple upper bounds on $C_{B,1}$ and $C_{C,1}$:

$$C_{B,1}\leq(1-\beta)Gr_i,\qquad C_{C,1}\leq 2(1-\beta)G,$$

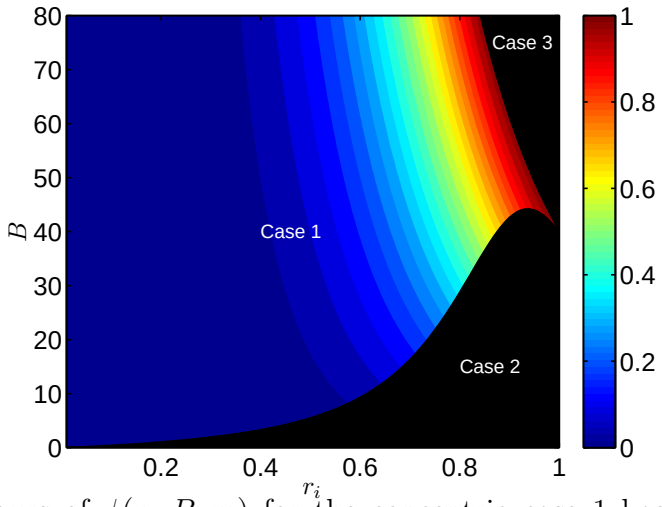

Figure 5.3: Contours of $\phi(r_i, B, m)$ for the concentric case 1 base solution, plotted for $m = 10$. The black shaded regions indicate the regimes for yielded interface (case 2) and static wall layer (case 3) base solutions.

We now write for the case 1 solutions

$$G = \frac{8m}{r_i^4}\phi, \tag{5.60}$$

(essentially scaling with the value of G for the case 3 solutions). Figure 5.3 plots contours of ϕ. This leads to the following bounds:

$$\mathcal{F}_{\mathcal{I}} \leq \frac{We}{r_i^3}\left[\frac{3\mathcal{A}r_i^3}{2} + 8\phi(0.5 + m(1-\beta) + m(1-\beta)/r_i)\right] \leq 1.$$

$$\mathcal{F}_{\mathcal{II}} \leq \frac{4\phi}{81.49}\frac{Re^{[1]}}{r_i} + \frac{We}{r_i^3}\frac{1}{m^2\beta(1-\beta)}\left[\frac{3\mathcal{A}r_i^3}{2} + \phi m(1-\beta)(8 + \frac{12r_i}{5.783..})\right] \leq 1.$$

and

$$\mathcal{F}_{\mathcal{III}} = \frac{4m\phi Re^{[2]}}{r_i^4}\left[\frac{[1-(r_i+h)]^3}{R_J} + \frac{(r_y - r_i - h)[1-(r_i+h)]^2}{R_M}\right] \leq 1.$$

Suppose we now consider for simplicity a weak nonlinear perturbation, i.e. taking $\mathcal{A}$ small. The terms involving $\mathcal{A}$ in the bounds for $\mathcal{F}_{\mathcal{I}}$ & $\mathcal{F}_{\mathcal{II}}$ are

multiplied by r_i^3 so can be ignored in comparison to the others. Also note that as $\mathcal{A} \to 0$ we have that $r_i + h \to r_y$. Let us fix $\mathcal{A}$ so that

$$r_y - r_i - h = (1 - r_i - h)\frac{R_M}{R_J} < 1.$$

This leads to the following approximate bounds for weak nonlinear stability:

$$\frac{We}{r_i^3}\left[8\phi(0.5 + m(1-\beta) + m(1-\beta)/r_i)\right] \leq 1, \tag{5.61}$$

$$\frac{4\phi}{81.49}\frac{Re^{[1]}}{r_i} + \frac{We}{r_i^3}\left[\frac{\phi\left(8 + \frac{12r_i}{5.783..}\right)}{m\beta}\right] \leq 1, \tag{5.62}$$

$$\frac{8m^2\beta\phi Re^{[1]}(1-r_y)^3}{81.49 r_i^4} \leq 1. \tag{5.63}$$

Again (5.62) involves both We and Re. If we choose $0 < \alpha < 1$ and select $Re^{[1]}$ and We such that

$$Re^{[1]} < \frac{81.49 r_i}{4\phi}\min\left\{\alpha, \frac{r_i^3}{2m^2\beta(1-r_y)^3}\right\} \tag{5.64}$$

$$We < \frac{r_i^3}{\phi}\min\left\{\frac{1}{8(1 + m(1-\beta) + m(1-\beta)/r_i)}, \frac{(1-\alpha)m\beta}{\left(8 + \frac{12r_i}{5.783..}\right)}\right\} \tag{5.65}$$

the flow is stable. In Fig. 5.4 we plot contours of the maximal Reynolds number for stability, according to the simplified bounds (5.64) & (5.65). We plot these contours in the $(B, \tilde{We})$-plane (recall that $\tilde{We} = We/r_i^3$ is the Weissenberg number appropriate to the inner core fluid region). We present contours of $Re^{[2]} = m\beta Re^{[1]}$. We see that for modest $\tilde{We}$ we can achieve stability for moderately large $Re^{[2]}$. There is an apparent non-monotonicity as B is increased. Note however that for the large values of B, $r_y \sim 1$ and it would be unlikely to operate in this regime for a lubricated transport process. Thus, practically speaking one is more likely to observe the increase in critical $Re^{[2]}$ with B.

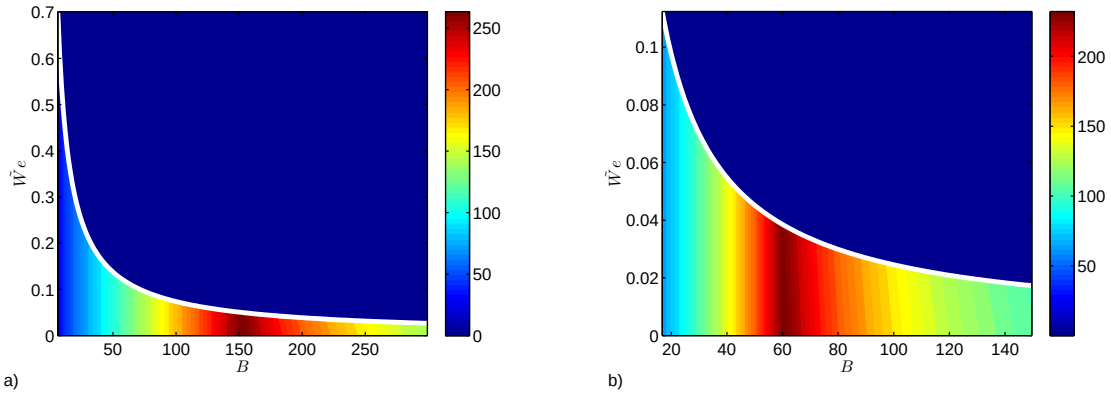

Figure 5.4: Contours of maximal $Re^{[2]}$ for stability, computed from the simplified bounds (5.64) & (5.65) for $m = 10$, $\beta = 0.7$, plotted in the $(B, \tilde{We})$-plane: a) $r_i = 0.5$; b) $r_i = 0.7$

5.3 Conditional stability for a moving Ω_1

We now turn to the general problem in which the viscoelastic region may move. Our results will be derived under the assumption that for small finite perturbations away from the axisymmetric flow and for a bounded stress perturbation satisfying (5.23), for small finite $\mathcal{A}$ an annular region of thickness at least h will remain about Ω_1. Since there is no deformation within the plug, the shape of the interface Γ_i remains circular of radius r_i, but Ω_1 may move. Thus, $\Omega_1(t)$ is a cylinder of radius r_i, which at time t has axis centered at $\boldsymbol{x}_c(t) = (x_c(t), y_c(t), 0)$. We show later that the departure from axisymmetry:

$$r_c(t) \equiv |(x_c(t), y_c(t))|, \tag{5.66}$$

is bounded when the flow is energy stable. Similar to [85], we consider the evolution of a perturbation from the base that is defined by $\boldsymbol{x}_c(t)$. We shall write the solution at time t as follows:

$$\boldsymbol{U} + \boldsymbol{u} = (0, 0, W(x, y; x_c(t), y_c(t)) + (u, v, w), \qquad P(z; x_c(t), y_c(t)) + p,$$

where the base flow is parameterised by (x_c, y_c). Since we consider an infinitely long pipe, rotational movements of the plug region are only possible about axes that are parallel to the z-axis. Thus, at time t, the plug motion can be described as combination of a linear motion, say $(u_c, v_c, w_c + W_p)$, and a rigid body rotation about an axis through $(x_c(t), y_c(t), 0)$, parallel to the z-axis, with angular velocity $\tilde{\omega}_c(t)$.

Before proceeding, we consider further the form of the base solution within the viscoelastic region. Firstly, note that since the inner region is surrounded by a rigid plug region with constant axial velocity W_p the difference $W - W_p$ will only depend on the shear viscosity of fluid 1, the shape of Ω_1 and the modified pressure gradient $G = G(\boldsymbol{x}_c)$. Indeed this part of the base solution is effectively Newtonian, it scales linearly with G/m and could be described in terms of coordinates $(x', y') = (x - x_c, y - y_c)$. For the specific case in which at any time t the interface retains its circular shape we may deduce that $W - W_p$ depends only on the radial distance from $\boldsymbol{x}_c(t)$ and furthermore that $G = G(\boldsymbol{x}_c) = G(r_c)$, i.e. it does not matter in which direction the interface translates. The axial velocity within the viscoelastic region is given by:

$$W(r', r_c) = \frac{G}{4m}[(r_i^2 - (r')^2)] + W_p, \qquad 0 \leq r' \leq r_i, \tag{5.67}$$

where r' measures radial distance from $\boldsymbol{x}_c$ and both G and W_p depend only on r_c (and the shear rheology of both fluids). The symmetry of Ω_1 and reduced dependence of the base solution on $\boldsymbol{x}_c$ only through r_c does help to produce more specific bounds below. However, nothing is changed qualitatively if the interface is non-circular, (except see the earlier comments on bounding Term C).

5.3.1 Perturbation equations and energy equation

The main advantage of perturbing around the base flow parameterized by $\boldsymbol{x}_c(t)$ is that the fluid domains of base flow and perturbation coincide at all

times. The cost however is that time-dependency has entered the base flow, via the dependence on $\boldsymbol{x}_c(t)$. This results in additional terms in the momentum balance and viscoelastic stress equation. The perturbed momentum equation in Ω_k is:

$$\begin{aligned} 0 &= \left[\frac{\partial}{\partial t} + (U_j + u_j)\frac{\partial}{\partial x_j}\right](U_i + u_i) + \frac{\partial}{\partial x_i}(P + p) \\ &\quad -\frac{1}{Re^{[2]}}\frac{\partial}{\partial x_j}{\tau_{ij}}^{[k]}(\boldsymbol{U} + \boldsymbol{u}) + \delta_{iz}(u_c, v_c)\cdot\nabla_c W. \end{aligned} \tag{5.68}$$

and the perturbed constitutive equation is:

$$\begin{aligned} \frac{m}{We}(1-\beta)\dot{\gamma}_{ij}(U+u) &= \frac{1}{We}\tau^e_{ij}(\boldsymbol{U}+\boldsymbol{u}) + \frac{\partial}{\partial t}[\tau^e_{ij}(\boldsymbol{U}) + \delta\tau^e_{ij}] \\ &\quad +(U_k+u_k)\frac{\partial\tau^e_{ij}(\boldsymbol{U}+\boldsymbol{u})}{\partial x_k} - \frac{\partial(U_i+u_i)}{\partial x_k}\tau^e_{kj}(\boldsymbol{U}+\boldsymbol{u}) \\ &\quad -\tau^e_{ik}(\boldsymbol{U}+\boldsymbol{u})\frac{\partial(U_j+u_j)}{\partial x_k} + (u_c, v_c)\cdot\nabla_c\tau^e_{ij}(\boldsymbol{U}) \end{aligned} \tag{5.69}$$

Here $\nabla_c = (\frac{\partial}{\partial x_c}, \frac{\partial}{\partial y_c})$.

We formulate the energy equation in the same way as before, using again the total energy:

$$E(t) = \frac{1}{2}[\langle u_i u_i\rangle_{\Omega_1} + \langle u_i u_i\rangle_{\Omega_2} + \frac{We}{2m^2\beta(1-\beta)Re^{[1]}}\langle\delta\tau^e_{ij}\delta\tau^e_{ij}\rangle_{\Omega_1}].$$

The following equation is straightforwardly derived:

$$\begin{aligned} \frac{D}{Dt}E &= -\langle u_j\frac{\partial U_i}{\partial x_j}u_i\rangle_{\Omega_2} - \langle[\boldsymbol{u}_c\cdot\nabla_c W]w\rangle_{\Omega_2} - \frac{1}{Re^{[2]}}\langle\frac{\partial u_i}{\partial x_j}[\tau^{[2]}_{ij}(\boldsymbol{U}+\boldsymbol{u}) - \tau^{[2]}_{ij}(\boldsymbol{U})]\rangle_{\Omega_2} \\ &\quad -\langle u_j\frac{\partial U_i}{\partial x_j}u_i\rangle_{\Omega_1} - \langle[\boldsymbol{u}_c\cdot\nabla_c W]w\rangle_{\Omega_1} - \frac{1}{Re^{[1]}}\langle\frac{\partial u_i}{\partial x_j}\dot{\gamma}_{ij}(\boldsymbol{u})\rangle_{\Omega_1} \\ &\quad -\frac{\langle\delta\tau^e_{ij}\delta\tau^e_{ij}\rangle_{\Omega_1}}{2m^2\beta(1-\beta)Re^{[1]}} \\ &\quad +We\frac{\big[(\text{Term A}) + (\text{Term B}) + (\text{Term C}) + \langle\boldsymbol{u}_c\cdot\nabla_c\tau^e_{ij}(\boldsymbol{U})\delta\tau^e_{ij}\rangle_{\Omega_1}\big]}{2m^2\beta(1-\beta)Re^{[1]}} \end{aligned} \tag{5.70}$$

The first two lines of this equation are the same as for the Newtonian-Bingham flow studied in [85]. These terms may be bounded in an identical fashion and we simply summarise in §5.3.1 the bounds from [85]. The last line of (5.70) contains the elastic stress terms, which we will treat in §5.3.1 below (borrowing from the analysis of the stationary Ω_1 cases studied earlier).

Inelastic terms

For the purposes of analysis, we introduce the velocity field $\boldsymbol{u}^*$:

$$\boldsymbol{u}^* = (u^*, v^*, w^*) \equiv (u_c, v_c, w_c) + (-(y - y_c)\tilde{\omega}_c, (x - x_c)\tilde{\omega}_c, 0). \tag{5.71}$$

Note that (u_c, v_c) is the velocity of $(x_c(t), y_c(t))$. If $\Omega_{2,p}(t)$ denotes the unyielded part of the outer domain Ω_2, we observe that for any $\boldsymbol{x} \in \Omega_{2,p}(t)$, $\boldsymbol{u}^* + \boldsymbol{U}$, gives exactly the perturbed velocity of the fluid in the rigid plug and $\boldsymbol{u}^* = \boldsymbol{u}$. In what follows we often consider the velocity field $\boldsymbol{u}' = \boldsymbol{u} - \boldsymbol{u}^*$, which subtracts off the rigid plug perturbation from the perturbation velocity. We note that $\boldsymbol{u}' = 0$ at the interface and that $\dot{\gamma}_{ij}(\boldsymbol{u}) = \dot{\gamma}_{ij}(\boldsymbol{u}')$, since $\dot{\gamma}_{ij}(\boldsymbol{u}^*) = 0$.

The first line of (5.70) involves the irregular domain and is bounded exactly as in equation 4.26 of [85], see :

$$-\langle u_j \frac{\partial U_i}{\partial x_j} u_i \rangle_{\Omega_2} - \langle [\boldsymbol{u}_c \cdot \nabla_c W] w \rangle_{\Omega_2} - \frac{1}{Re^{[2]}} \langle \frac{\partial u_i}{\partial x_j} [\tau_{ij}^{[2]}(\boldsymbol{U} + \boldsymbol{u}) - \tau_{ij}^{[2]}(\boldsymbol{U})] \rangle_{\Omega_2} \leq \left[A_B - \frac{1}{Re^{[2]}} \right] \langle \frac{\partial u_i}{\partial x_j} \frac{\partial u_i}{\partial x_j} \rangle_{\Omega_2} - \frac{2\pi L (r_i \tilde{\omega}_c)^2}{Re^{[2]}} \tag{5.72}$$

The first two terms of the next line can be slightly simplified, on noting that the derivatives of the base flow are only in the radial direction(s). We use a similar approach to [85], splitting into components involving $\boldsymbol{u}'$ and $\boldsymbol{u}_c$ and adopting the bounds on the components of $\boldsymbol{u}_c$; see equations (4.23), (4.24) and

(4.33) in [85]. This leads to:

$$-\langle u_j \frac{\partial U_i}{\partial x_j} u_i \rangle_{\Omega_1} - \langle [\boldsymbol{u}_c \cdot \nabla_c W] w \rangle_{\Omega_1} \leq A_N \langle \frac{\partial u_i}{\partial x_j} \frac{\partial u_i}{\partial x_j} \rangle_{\Omega_2 | \Omega_{2,p}}$$
$$+2B_N \left[\langle \frac{\partial u_i}{\partial x_j} \frac{\partial u_i}{\partial x_j} \rangle_{\Omega_2 | \Omega_{2,p}} \langle \frac{\partial u_i'}{\partial x_j} \frac{\partial u_i'}{\partial x_j} \rangle_{\Omega_1} \right]^{1/2} + C_N \langle \frac{\partial u_i'}{\partial x_j} \frac{\partial u_i'}{\partial x_j} \rangle_{\Omega_1} \tag{5.73}$$

where the constants are

$$A_N = \frac{\pi r_i^2 [1 - (r_i + h)^2]}{4(r_i + h)^2} \left[\frac{G r_i}{3\pi m} + \frac{r_i^2}{8m} \left| \frac{\partial G}{\partial r_c} \right| + \left| \frac{\partial W_p}{\partial r_c} \right| \right] \tag{5.74}$$

$$B_N = \frac{\pi r_i^2 [1 - (r_i + h)^2]^{1/2}}{4(r_i + h)} \times$$
$$\left[\frac{G r_i}{2m} \left(\tilde{\Lambda}_{N,2}^{1/2} + \frac{\tilde{\Lambda}_{N,4}^{1/2}}{\pi} \right) + \tilde{\Lambda}_{N,3}^{1/2} \left(\frac{r_i^2}{4m} \left| \frac{\partial G}{\partial r_c} \right| + \left| \frac{\partial W_p}{\partial r_c} \right| \right) \right] \tag{5.75}$$

$$C_N = \frac{G r_i^3 \tilde{\Lambda}_{N,1}}{2m}. \tag{5.76}$$

The constants $\tilde{\Lambda}_{N,k}$ are scaled versions of the $\Lambda_{N,k}$ in [85] and have the following numerical upper bounds; see equations (4.58) & (4.60) in [85].

$$\tilde{\Lambda}_{N,1} \leq \frac{1}{R_J}, \qquad \tilde{\Lambda}_{N,2},\ \tilde{\Lambda}_{N,4} \leq \frac{1}{23.13275}, \qquad \tilde{\Lambda}_{N,3} \leq \frac{1}{R_M}. \tag{5.77}$$

For the third term we note the identities:

$$-\frac{1}{Re^{[1]}} \langle \frac{\partial u_i}{\partial x_j} \dot{\gamma}_{ij}(\boldsymbol{u}) \rangle_{\Omega_1} = -\frac{1}{2Re^{[1]}} \langle \dot{\gamma}_{ij}(\boldsymbol{u}) \dot{\gamma}_{ij}(\boldsymbol{u}) \rangle_{\Omega_1}$$

$$= -\frac{1}{2Re^{[1]}} \langle \dot{\gamma}_{ij}(\boldsymbol{u}') \dot{\gamma}_{ij}(\boldsymbol{u}') \rangle_{\Omega_1} = -\frac{1}{Re^{[1]}} \langle \frac{\partial u_i'}{\partial x_j} \frac{\partial u_i'}{\partial x_j} \rangle_{\Omega_1}.$$

Putting all this together:

$$-\langle u_j \frac{\partial U_i}{\partial x_j} u_i \rangle_{\Omega_1} - \langle [\boldsymbol{u}_c \cdot \nabla_c W] w \rangle_{\Omega_1} - \frac{1}{Re^{[1]}} \langle \frac{\partial u_i}{\partial x_j} \dot{\gamma}_{ij}(\boldsymbol{u}) \rangle_{\Omega_1} \leq$$
$$(A_N + B_N) \langle \frac{\partial u_i}{\partial x_j} \frac{\partial u_i}{\partial x_j} \rangle_{\Omega_2} \left[B_N + C_N - \frac{1}{Re^{[1]}} \right] \langle \frac{\partial u_i'}{\partial x_j} \frac{\partial u_i'}{\partial x_j} \rangle_{\Omega_1}. \tag{5.78}$$

Visco-elastic terms

For the visco-elastic terms in (5.70) we mostly proceed as before. Terms A-C are as defined in (5.32). The only difference in our treatment of (Term A) and (Term B) is that we establish bounds in terms of $\dot{\gamma}_{ij}(\boldsymbol{u}')$. Straightforwardly these are

$$\text{(Term A)} \leq \left(\frac{Gr_i}{2m} + \frac{3\mathcal{A}}{2} \right) ||\delta \boldsymbol{\tau}^e||^2_{\Omega_1} + \frac{3\mathcal{A}}{2} \langle \dot{\gamma}_{ij}(\boldsymbol{u}') \dot{\gamma}_{ij}(\boldsymbol{u}') \rangle_{\Omega_1}. \tag{5.79}$$

$$\text{(Term B)} \quad \leq \quad C_{B,1} \left(||\delta \boldsymbol{\tau}^e||^2_{\Omega_1} + \langle \dot{\gamma}_{ij}(\boldsymbol{u}') \dot{\gamma}_{ij}(\boldsymbol{u}') \rangle_{\Omega_1} \right). \tag{5.80}$$

For (Term C) we split $\boldsymbol{u}$ into $\boldsymbol{u}' + \boldsymbol{u}^*$, note that the base elastic stresses depend only on r' and that the radial component of $\boldsymbol{u}^*$ is simply $u_{c,r}$ (the radial component of (u_c, v_c)).

$$-\langle u_k \frac{\partial \tau^e_{ij}(\boldsymbol{U})}{\partial x_k} \delta \tau^e_{ij} \rangle_{\Omega_1} = -\langle (u_r' + u_{c,r}) \frac{\partial \tau^e_{ij}(\boldsymbol{U})}{\partial r'} \delta \tau^e_{ij} \rangle_{\Omega_1}.$$

We consider separately the terms involving u_r' and $u_{c,r}$, apply the generalised Holder inequality to each term, and after a little algebra:

$$\text{(Term C)} \quad \leq \quad C_{C,1} ||\delta \boldsymbol{\tau}^e||^2_{\Omega_1} + \frac{3C_{C,1}}{2} ||\boldsymbol{u}'||^2_2 +$$
$$\frac{3C_{C,1}\pi^2 r_i^2 [1 - (r_i + h)^2]}{8(r_i + h)^2} \langle \frac{\partial u_i}{\partial x_j} \frac{\partial u_i}{\partial x_j} \rangle_{\Omega_2 | \Omega_{2,p}} \tag{5.81}$$

The constant $C_{C,1}$ is as before and the final term above comes from bounding $|u_{c,r}|$, (see equations (4.23) & (4.24) in [85]).

Finally, we bound the last term in (5.70) as follows:

$$\begin{aligned}\langle \boldsymbol{u}_c \cdot \nabla_c \tau^e_{ij}(\boldsymbol{U}) \delta\tau^e_{ij} \rangle_{\Omega_1} \;\leq\; & \frac{(1-\beta)}{4}\left|\frac{\partial G}{\partial r_c}\right| \max\left\{1, \frac{2WeG}{m}\right\} ||\delta\boldsymbol{\tau}^e||^2_{\Omega_1} \\ & + \frac{(1-\beta)\pi^2 r_i^2[1-(r_i+h)^2]}{16(r_i+h)^2}\left|\frac{\partial G}{\partial r_c}\right| \\ & \times \left(1 + \frac{2WeGr_i^4}{3m}\right) \langle \frac{\partial u_i}{\partial x_j}\frac{\partial u_i}{\partial x_j}\rangle_{\Omega_{2|\Omega_{2,p}}}. \end{aligned} \tag{5.82}$$

5.3.2 Energy decay

Putting together the different inequalities and bounds leads to the energy decay inequality:

$$\begin{aligned}\frac{D}{Dt}E \;\leq\; & -\frac{[1-\mathcal{K}_{\mathcal{I}}]}{Re^{[1]}}\langle \frac{\partial u_i'}{\partial x_j}\frac{\partial u_i'}{\partial x_j}\rangle_{\Omega_1} - \frac{[1-\mathcal{K}_{\mathcal{II}}]}{Re^{[2]}}\langle \frac{\partial u_i}{\partial x_j}\frac{\partial u_i}{\partial x_j}\rangle_{\Omega_2} \\ & - \frac{[1-\mathcal{K}_{\mathcal{III}}]}{2m^2\beta(1-\beta)Re^{[1]}}||\delta\boldsymbol{\tau}^e||^2_{\Omega_1}. \end{aligned} \tag{5.83}$$

The constants $\mathcal{K}_{\mathcal{I}} - \mathcal{K}_{\mathcal{III}}$ are defined as follows:

$$\mathcal{K}_{\mathcal{I}} = Re^{[1]}[B_N + C_N] + WeB_E \tag{5.84}$$

$$\mathcal{K}_{\mathcal{II}} = Re^{[2]}[A_B + A_N + B_N] + WeC_E \tag{5.85}$$

$$\mathcal{K}_{\mathcal{III}} = WeA_E. \tag{5.86}$$

The subscript B indicates that the constant comes from bounding inertial terms in the Bingham fluid region. The subscript N indicates that the constant comes from bounding inertial terms in the core region, and these terms are essentially Newtonian. The subscript E indicates that the constant comes from bounding terms involving the elastic stress perturbation. It is worth noting that the structure of (5.83) is similar to those bounds considered before for

the case of stationary Ω_1. However, due to movement of the fluid domains it is necessary to use the dissipation of the outer region to bound part of both the inertial contributions from the core fluid ($A_N + B_N$) and an elastic stress contribution (C_E). The various constants are defined more precisely below in §5.3.2. The decay bound proceeds as follows. First we assume that

$$\mathcal{K}_{\mathcal{I}} < 1, \quad \mathcal{K}_{\mathcal{II}} < 1, \quad \mathcal{K}_{\mathcal{III}} < 1, \tag{5.87}$$

(essentially by making We, $Re^{[1]}$ and $Re^{[2]}$ sufficiently small). This ensures energy decay, but to get the actual bound we use:

$$\langle \frac{\partial u_i'}{\partial x_j} \frac{\partial u_i'}{\partial x_j} \rangle_{\Omega_1} = \frac{1}{2} \langle \dot{\gamma}_{ij}(\boldsymbol{u}') \dot{\gamma}_{ij}(\boldsymbol{u}') \rangle_{\Omega_1},$$

$$\langle \dot{\gamma}_{ij}(\boldsymbol{u}) \dot{\gamma}_{ij}(\boldsymbol{u}) \rangle_{\Omega_2} \leq 2 \langle \frac{\partial u_i}{\partial x_j} \frac{\partial u_i}{\partial x_j} \rangle_{\Omega_2},$$

so that when (5.87) is satisfied

$$\begin{aligned}
\frac{D}{Dt}E \;\leq\; & -\frac{[1-\mathcal{K}_{\mathcal{I}}]}{2Re^{[1]}} \langle \dot{\gamma}_{ij}(\boldsymbol{u}') \dot{\gamma}_{ij}(\boldsymbol{u}') \rangle_{\Omega_1} - \frac{[1-\mathcal{K}_{\mathcal{II}}]}{2Re^{[2]}} \langle \dot{\gamma}_{ij}(\boldsymbol{u}) \dot{\gamma}_{ij}(\boldsymbol{u}) \rangle_{\Omega_2} \\
& - \frac{[1-\mathcal{K}_{\mathcal{III}}]}{2m^2\beta(1-\beta)Re^{[1]}} ||\delta\boldsymbol{\tau}^e||^2_{\Omega_1} \leq -\min\left\{ \frac{[1-\mathcal{K}_{\mathcal{I}}]}{Re^{[1]}}, \frac{[1-\mathcal{K}_{\mathcal{II}}]}{Re^{[2]}} \right\} \\
& \times \frac{1}{2} \langle \dot{\gamma}_{ij}(\boldsymbol{u}) \dot{\gamma}_{ij}(\boldsymbol{u}) \rangle_{\Omega} - \frac{[1-\mathcal{K}_{\mathcal{III}}]}{2m^2\beta(1-\beta)Re^{[1]}} ||\delta\boldsymbol{\tau}^e||^2_{\Omega_1} \leq \\
& - \frac{C_K}{2C_{P,0}} \min\left\{ \frac{[1-\mathcal{K}_{\mathcal{I}}]}{Re^{[1]}}, \frac{[1-\mathcal{K}_{\mathcal{II}}]}{Re^{[2]}} \right\} ||\boldsymbol{u}||^2_{\Omega} \\
& - \frac{[1-\mathcal{K}_{\mathcal{III}}]}{2m^2\beta(1-\beta)Re^{[1]}} ||\delta\boldsymbol{\tau}^e||^2_{\Omega_1} \leq \\
& - 2\min\left\{ \frac{C_K}{2C_{P,0}} \frac{[1-\mathcal{K}_{\mathcal{I}}]}{Re^{[1]}}, \frac{C_K}{2C_{P,0}} \frac{[1-\mathcal{K}_{\mathcal{II}}]}{Re^{[2]}}, \frac{[1-\mathcal{K}_{\mathcal{III}}]}{We} \right\} E(t)
\end{aligned} \tag{5.88}$$

where C_K is the constant in Korn's inequality and $C_{P,0}$ is the constant from the Poincaré inequality, (both applied over the entire domain Ω); see e.g. [3].

Therefore, when (5.87) is satisfied the perturbation energy decays exponentially over timescale, $t \sim \lambda^{-1}$:

$$\lambda = 2 \min \left\{ \frac{C_K}{2C_{P,0}} \frac{[1-\mathcal{K}_{\mathcal{I}}]}{Re^{[1]}}, \frac{C_K}{2C_{P,0}} \frac{[1-\mathcal{K}_{\mathcal{II}}]}{Re^{[2]}}, \frac{[1-\mathcal{K}_{\mathcal{III}}]}{We} \right\}.$$

Note that, as in [85], decay of the energy $E(t)$ implies that the perturbation from the base solution at $\boldsymbol{x}_c(t)$ decays to zero. To complete the analysis, we may show that decay of $E(t)$ implies decay of $||\boldsymbol{u}||^2_\Omega$, which implies decay of (u_c, v_c), all on the same exponential timescale. Integrating the bound on (u_c, v_c) over time guarantees that $\boldsymbol{x}_c(t)$ is bounded for all time, and the bound on $\boldsymbol{x}_c(t)$ is made small by making λ large. This procedure is explained in more detail in [85]. To summarise, the perturbation decays exponentially to zero and we are left with a base solution that is *close* to the concentric axisymmetric base flow.

Discussion of the terms in (5.87)

We start with $\mathcal{K}_{\mathcal{III}} = WeA_E$ which is defined by:

$$A_E = \frac{3\mathcal{A}}{2} + \frac{Gr_i}{2m} + C_{B,1} + C_{C,1} + \frac{1-\beta}{4} \left| \frac{\partial G}{\partial r_c} \right| \max \left\{ 1, \frac{2WeG}{m} \right\}. \tag{5.89}$$

Note that the first terms in this expression are very similar to those in $\mathcal{F}_{\mathcal{I}}$, considered earlier, except that now we compute G from the asymmetric flow. When $\mathcal{K}_{\mathcal{III}} < 1$ we can bound $WeGr_i < 2m$ and this allows simplification of the various constants, as earlier:

$$\mathcal{K}_{\mathcal{III}} = WeA_E \leq \frac{We}{r_i^3} \left[\frac{3\mathcal{A}r_i^3}{2} + 4\phi + \frac{8m(r_i+2)(1-\beta)\phi}{r_i} + \frac{(1-\beta)}{r_i} \left| \frac{\partial \phi}{\partial r_c} \right| \right].$$

recall that $\phi = Gr_i^4/8m$.

The main difference from earlier bounds is the term $\left|\frac{\partial \phi}{\partial r_c}\right|$. Typically, the pressure gradient for the concentric interface configuration is maximal, which

implies that $\frac{\partial \phi}{\partial r_c} = 0$, for the concentric case. As we bound the motion of the inner region, r_c, we can assume that this value is close to zero, i.e.

$$\left| \frac{\partial \phi}{\partial r_c} \right| \sim O(r_c) \text{ as } r_c \to 0.$$

This suggests that the bound $\mathcal{K}_{\mathcal{III}} < 1$ is not much more severe than the bounds on $\mathcal{F}_{\mathcal{I}}$ for stationary Ω_1.

The bound on $\mathcal{K}_{\mathcal{I}}$ has contributions from B_N and C_N, multiplying $Re^{[1]}$. If we re-express G in terms of ϕ we can see that the $Re^{[1]}$ bounds do not vary strongly with r_i. They also contain a term proportional to $\left| \frac{\partial \phi}{\partial r_c} \right|$. The elastic terms are captured in the term WeB_E:

$$B_E = \frac{3\mathcal{A} + 2C_{B,1} + 1.5C_{C,1}C_P}{2m^2\beta(1-\beta)}, \tag{5.90}$$

which has similar dependency on r_i as the term A_E.

Finally the terms in $\mathcal{K}_{\mathcal{II}}$ contain the constants A_B, A_N and C_N which multiply $Re^{[2]}$. These terms are discussed in [85]. In particular, due to the irregular domain, the estimates made for A_B are quite conservative. We note that the term $\left| \frac{\partial W_p}{\partial r_c} \right|$ enters A_N and this is also zero for the symmetric concentric flow. The elastic terms are bounded by

$$C_E \leq \pi r_i^2 [1 - (r_i + h)^2] \frac{6C_{B,1} + \frac{7}{3}(1-\beta)\left| \frac{\partial G}{\partial r_c} \right|}{32m(1-\beta)(r_i+h)^2}, \tag{5.91}$$

which is again similar to the previous stationary Ω_1 case.

5.4 Discussion and conclusions

In this chapter we have shown that, provided the maximal shear stress and elastic stress perturbations are bounded (i.e. sufficiently small but finite bounds) a suitable energy functional will decay exponentially for sufficiently small

Reynolds and Weissenberg numbers. In the case where the domains do not move, which may be thought of a weakly linear assumption, this implies stability of the concentric core-annular base state. In the case that the fluid domains may change in time, the perturbation is measured relative to an arbitrary nearby base solution. Thus, energy decay implies only stability of the concentric core-annular base state, but asymptotic stability of a nearby state. This situation is analogous to that in [85] and in this sense the introduction of viscoelasticity changes neither the assumptions required for the analysis nor the results. Given the complexity of the flow we feel that our results are reasonable.

A weakness in our results comes in the fact that the assumption of bounds on the L^∞ norm of the elastic stress perturbation cannot be verified as a consequence of the energy decay of the L^2 norm, i.e. we cannot make the analysis self-consistent. Thus, the validity of the analysis really rests on whether such an assumption is physically reasonable. As we consider established flows with smooth domains there is no obvious source of singular behavior. On the other hand, mathematical degeneracy is relatively common amongst viscoelastic constitutive models. As we have developed our analysis we have also derived bounds for the various elastic terms that are valid for more general cross-sectional domains, e.g. polygonal domains as in Fig. 5.1d. Provided that we can reasonably bound the L^∞ norm of the elastic stress perturbation, the same analysis developed here would apply equally to such flows. Similarly, although we have focused on the Oldroyd-B model for simplicity, some other models could be treated in a similar way with similar assumptions, e.g. FENE-CR. However, this treatment is algebraically more complex and it is hard to motivate the additional complexity.

In chapter 4, we demonstrated this type of flow experimentally, using Polyethylene Oxide (PEO) as the core fluid and Carbopol as the lubricating fluid. There is a significant disconnect between the experimental study and the analysis here: the experimental fluids are strongly shear-thinning, the

experimental study shows strong entry/development effects, etc. Nevertheless both studies point in the same direction in establishing the feasibility of these flows with viscoelastic core fluids. Closing the gap between these two approaches requires computational study, which is underway.

Throughout the study we have ignored surface tension effects. This is partly to be faithful to our experimental study where the fluids were miscible, although in practice the elasticity tends to retard interfacial mixing. If we were to consider immiscible fluids note that in static situations it is hard to cleanly measure the surface tension of yield stress fluids. Secondly, for the scale of experiments we performed surface tension forces would generally be much smaller that the yield stress. Therefore, it is unlikely that surface tension could become important unless the interface was able to deform. Preventing such deformation is at the heart of the VPL technique.

Chapter 6

Summary and future research directions

6.1 Summary

The work carried out in this thesis considers one strategy for eliminating interfacial instabilities in multi-layer shear flows, by using a visco-plastic fluid with unyielded plug at the interface. This strategy is investigated from computational, experimental and theoretical perspectives.

The computational study is addressed in chapter 2 and 3. We have investigated the initiation, development lengths and temporal stability of VPL (Visco-Plastically Lubricated) flows in the setting of a Newtonian core fluid surrounded by a Bingham lubricated fluid, within a pipe and channel configuration. The study of multi-layer shear flows in channel geometry allows for symmetry breaking as a result of relaxing axisymmetric condition existing in pipe flow. Flow initiation is affected by starting the flow with a domain full of stationary Bingham fluid and injecting both inner and outer fluids simultaneously. Initial instability and dispersive mixing at the front remains localised and is advected from the domain leaving behind a stable multi-layer configuration, found for moderate Reynolds numbers (Re), for a broad range of interface radii (r_i) and for different inlet diameters (R_i), whenever the base flow parameters admit a multi-layer flow with unyielded interface. We have found 3 distinct entry lengths for the established flows. These relate to: (a) establishment of the first unyielded plug close to the interface (shortest); (b)

establishment of the interface radius; (c) establishment of the velocity profile (longest). The 3 entry lengths increase with Re and decrease with both the Bingham number (B) and the viscosity ratio (m).

Nonlinear temporal stability to axisymmetric perturbations has been studied numerically, considering initial perturbations that are either localised in yielded parts of the flow, or that initially break the unyielded plug regions. The aim is to understand structural aspects of the flow stability that are not easily extracted from the energy stability results of [85]. The initial stages of a stable perturbed flow are characterised by a very rapid decay of the perturbation kinetic energy during which time the unyielded plug reforms (or breaks and reforms). This is followed by slower exponential decay on a viscous timescale ($t \sim Re$). For smaller Re and moderate initial amplitudes A the perturbations decay to the numerical tolerance. As either Re or A is increased sufficiently a number of interesting phenomena arise. The amount of dispersion increases, making the interfacial region increasingly diffuse and limiting the final decay. At larger Re or A we have found secondary flow structures that persist. A first example of these is when the shear stress decays below the yield stress before the velocity perturbation has decayed, leading to *freezing in* of the interface shape. This can lead to flows with a rigid wavy interface. Secondly, depending on the core fluid radius and thickness of the surrounding plug region, we observed a range of dispersive structures similar to the pearls and mushrooms of [23].

In the case of channel geometry, we have also demonstrated the establishment of symmetric 3-layer flows for wide ranges of viscosity ratio (m), Bingham number (B) and interface position (y_i), for Reynolds numbers $Re \leq 100$. Where an inner Newtonian layer was sandwiched between 2 layers of Bingham fluid. However, unlike the pipe geometry, for the situations where the inner fluid flow rate is dominant we observed inertial symmetry breaking in the symmetric start-up flows as Re was increased. Asymmetry was also observed in studying temporal nonlinear stability of these flows, which appear stable up

to moderate Re and significant amplitudes. In general the flows destabilize at lower Re and perturbation amplitudes than do the analogous core-annular pipe flows, but 1-1 comparison is hard. Because, the base flows do not really correspond to each other at the same m, B and r_i.

Multi-layer channel flows allow us to explore more exotic flow effects. We showed how flow control could be used to position layers asymmetrically within the flow, and how this effect might be varied transiently. We demonstrated that more complex layered flows can be stably achieved, e.g. a 7-layered flow is established. We also showed how a varying inlet position can be used to "write" in the yield stress fluid: complex structures that are advected with the flow and encapsulated within the unyielded fluid.

We extended our study to VPL flow of different flow scenario by using the visco-elastic core fluids in place of inelastic fluids within a pipe. In chapter 4, we gave an experimental demonstration that stable core-annular flows can be achieved when lubricating a viscoelastic core fluid with a yield stress fluid. We have used Carbopol as the lubricating yield stress fluid and Polyethylene Oxide (PEO) as the core fluid. The yield stress in the lubricating fluid preserves a ring of unyielded material around the interface, restricting the growth of instabilities. When the inlet radius is smaller than that of the established flow the core fluid stream expands, resulting in a net relaxation of the elastic normal stresses as the flow becomes fully developed. At low flow rates (Q_1) of the core fluid this relaxation does not break the surrounding plug. At larger Q_1 secondary flows and then instabilities are observed. The secondary flows are interesting in that the elastic instability is frozen into the yield stress fluid at the interface, as the stresses drop below the yield stress in the developing flow. At still larger Q_1 the surrounding plug is broken and the interface may deform. In this case elasticity appears to retard the degree of interfacial mixing, in comparison to Newtonian core fluids. When the inlet radius is larger than that of the established flow a stabilizing effect is observed.

Finally in chapter 5, we have investigated theoretically VPL flows with

visco-elastic core fluids. We extended the nonlinear stability analysis of [85] to the situation where the core fluid is viscoelastic. A core-annular flow of an Oldroyd-B fluid surrounded by a lubricating Bingham fluid was studied using energy stability methods. For small finite restrictions on the size of shear stress and elastic stress perturbations we have demonstrated the exponential decay of a suitable energy functional, for sufficiently small Reynolds number and Weissenberg number.

6.2 Limitations of the study

Although we have made a number of advances, as listed above, we must also acknowledge some limitations of our computational and experimental studies.

In terms of computational study, one restriction is on not exploring wavelength dependency of the nonlinear perturbations, instead keeping $\alpha = O(1)$ and fixed. In the Newtonian context the long and short wavelength limits are often studied because of analytical simplifications of the linear stability problem, but here the linear stability problem is anyway stable to high Re, so that there is little benefit here. Another interest is in considering capillary effects, particularly at short wavelengths, but here these are absent due to the miscibility of the fluids. Even if we were to consider immiscible fluids, for typical experimental geometries and fluid properties ($\hat{R}$ in the range $0.01 - 0.1$m and yield stresses $\hat{\tau}_Y \gtrsim 1$Pa) capillary effects are only significant by comparison to the yield stress at extremely small wavelengths and in initial perturbations that break the plug. Thus, we feel that $\alpha = O(1)$ is the most practically relevant range, although we acknowledge that a further study could be interesting.

In chapter 2, much of our study has been targeted at verifying analytical stability results and exploring these flow features. An alternative approach would have been to use the computational solutions to compare against the experimental results in [55]. This comparison is hard to make at a quanti-

tative level for a number of reasons. First the fluids used in [55], (Carbopol and Xanthan solutions) are not well represented by Bingham and Newtonian constitutive models, due to shear-thinning, so that the present computational model would need extending. Secondly, the experiments in [55] were not particularly detailed, with only bulk quantities being measured. Principally this was the interface radius, which did compare favourably with the 1D (base flow) design model used by [55]. If we were to extend this experimental study to compare directly against numerical solutions we would certainly improve the visualisation aspects of [55] to allow more detailed comparisons to be made.

Moreover, we have not considered convective stability explicitly (except in the sense that the frontal region of the start-up flows are convectively unstable). Partly the reason for this is that we focus on case 1 flows for which the objective is to establish a stable multi-layer configuration. Once established, in all the usual multi-layer applications one would be avoiding introduction of entry perturbations as far as is possible.

In terms of the broader interest of our experimental results in the context of interfacial instability of multi-layer flow of viscoelastic fluids, there is little direct relevance. Only experimental series 5 (see chapter 4) studied flows for which the base flow was yielded at the interface and even here it is hard to isolate the purely viscoelastic effects. Our experiments have been focused at establishing the feasibility of stable flows, rather than studying hydrodynamic instability. Although we have data for unstable regimes that could be analysed further to extract the statistics of experimental wavelengths and growth rates, our experiments have not systematically explored any such instability. This could be also a future direction.

6.3 Summary of contributions

The novel significant contribution of this thesis can be summarized in two main categories: VPL flow of inelastic fluids and VPL flow with elastic core fluid.

6.3.1 VPL flow of inelastic fluids

- The possibility of visco-plastic lubrication flows has been established by a systematic computational study over a wide range of flow parameters in pipe and channel configurations.
- Entry/development lengths of the established flow have been obtained for governing parameters in both pipe and channel geometries. Estimation of the required development length is a valuable part of process design.
- The physical mechanism of energy decay for finite perturbation to VPL flow has been studied computationaly. The results provide more detailed understanding, which can not be obtained from theoretical nonlinear stability analysis [85]. Two examples of these results are
  - The initial short time scale on which the perturbation kinetic energy decays rapidly and the unyielded plug reforms (or breaks and reforms).
  - Flows with rigid wavy interface which occur when the shear stress decays below the yield stress before the velocity perturbation has decayed.
- In practical situations the multi-layer flow might lose its symmetry. Hence, the symmetry breaking has been allowed by performing the simulation in channel geometry and we have seen that these flows are less stable than the axisymmetric pipe flows.

- Asymmetry has been used to establish exotic effects such as
  - Establishing and controling of the asymmetric base flows via the flow rates.
  - Establishing complex layering patterns such as 7-layer flow.
  - Controlling the flow position in a transient setting by either moving the inlet nozzle or controlling the flow rates into the different layers upstream.
  - "Writing" within the unyielded fluid by combining many techniques such as moving multiple inlets, varying the flow rates, turning on and off new inlets.
- Stable VPL flow of fluids with different densities has been obtained experimentally.

6.3.2 VPL flow of elastic core fluids

- VPL flows with visco-elastic core fluid have been established experimentally. The results are new practical achievment since many industrial multi-layer flows involve fluids with visco-elastic properties.
- A fascinating combination of both elastic instability and stabilizing yield stress effects results in a frozen wavy interface. This is a novel flow effect that was not predicted.
- The energy stability method has been applied to demonstrate nonlinearly stable VPL flows with visco-elastic core fluid. The exponential decay of the energy of perturbation has been obtained when both Reynolds and Weissenberg numbers are controlled. To obtain the nonliear stability bound, we considered bounds on the L^∞ norm of elastic stress perturbation. However, assumption of boundedness of the L^∞ norm of the

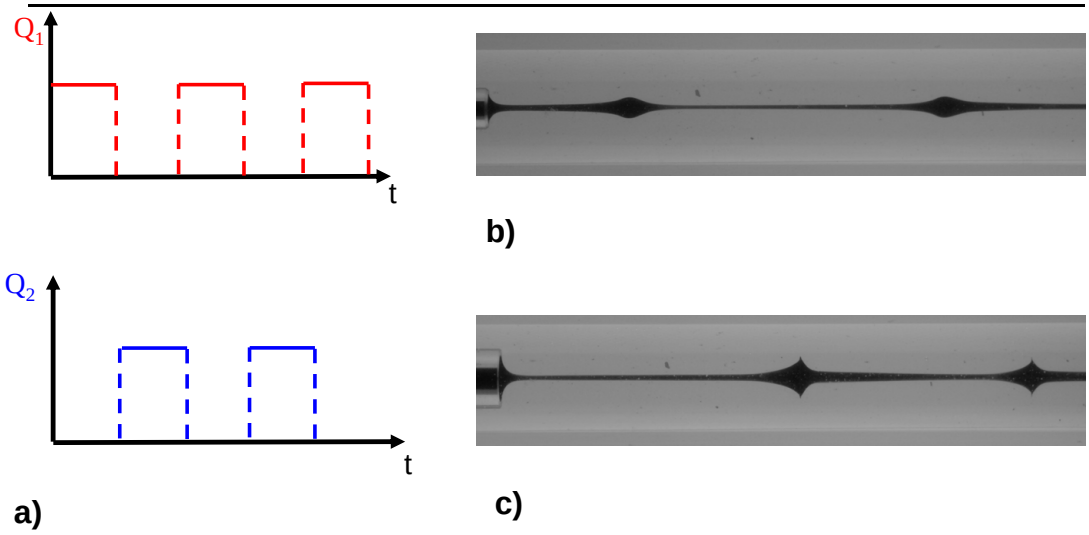

Figure 6.1: Examples of visco-elastic necklaces in visco-plastic fluid a) Pulsating flow rate of inner Q_1 and outer Q_2 fluid b) Pearl necklace c) Diamond necklace

perturbed shear stress components is a natural part of any analysis of stability of yield stress fluid flows.

6.4 Future research directions

Probing deeper, the results in this thesis also provide a strong foundation for future work. This section discusses several lines of research arising from this work which can be pursued.

- Our computational studies have shown that interesting convective effects may be frozen into the interface. This opens up interesting areas for application such as possibilities for drop encapsulation, multi-layer products with axial variations, near net shape product (see Fig. 6.1). This is an area we are exploring in a more systematic fashion.

- There is a significant disconnect between the experimental study of VPL

Figure 6.2: The art of confectionery

flows with visco-elastic core fluid (chapter 4) and the analysis in chapter 5: the experimental fluids are strongly shear-thinning, the experimental study shows strong entry/development effects, etc. Nevertheless both studies point in the same direction in establishing the feasibility of these flows with viscoelastic core fluids. The gap between these two approaches requires computational study, which is underway.

- It could be practically of interest to explore hydrodynamic instability of VPL flows of visco-elastic fluid when the base flow is yielded at the interface.

- We have performed a small number of test case experiments to establish stable VPL flows with significant density difference between two fluids. A systematic, computational and experimental study is of practical interest.

- Confectionery is a good example of an engineered food item with non-Newtonian behavior that is produced industrially. The food industry

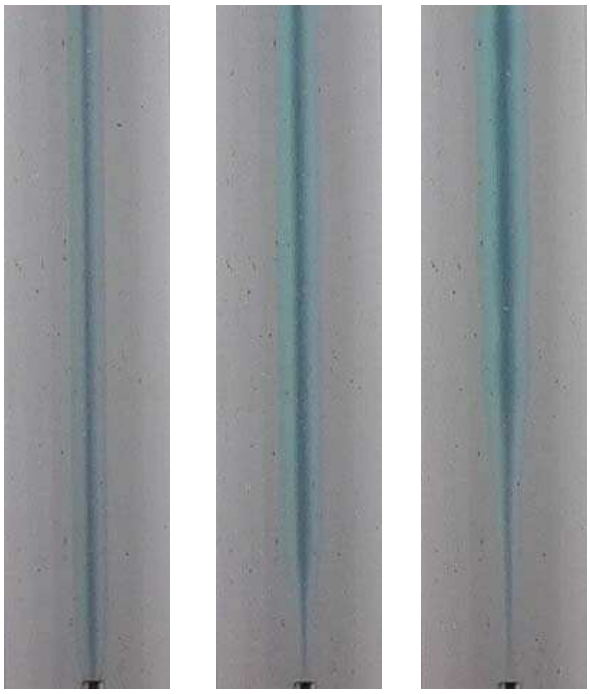

Figure 6.3: Snapshots of the established flows for separation process, inner fluid: 0.75%PEO dyed with particulate paint, Outer fluid: Carbopol Solution 0.15% (a) $(Q_1, Q_2) = (5.5, 20)mL/s$ (b) $(Q_1, Q_2) = (11, 20)mL/s$ (c)$(Q_1, Q_2) = (16, 20)mL/s$.The camera captures 30 cm of the pipe from above the exit of the inner pipe.

has to produce products that people want to eat at a price they can afford. An example of a complex confectionaery item is shown in Fig. 6.2. These items are currently produced laboriously by rolling and stretching individual strands. The VPL method could provide a viable alternative for continuous production of such items. A first step would be to consider VPL flows with more exotic cross-sections than the core-annular configuration.

- A small number of experiments have been performed to establish VPL flows with particulate visco-elastic core fluid. Elasticity enforces particles to migrate to the axis of the flow while yield stress prevents interfacial mixing. This flow might have potential in separation process (see Fig. 6.3).

Bibliography

[1] M. Allouche, I. Frigaard, and G. Sona. Static wall layers in the displacement of two visco-plastic fluids in a plane channel. *Journal of Fluids Mechanics*, 424:243–277, 2000.

[2] K. Atalik and R. Keunings. Non-linear temporal stability analysis of viscoelastic plane channel flows using a fully-spectral method. *Journal of Non-Newtonian Fluid Mechanics*, 102:299–319, 2002.

[3] K. Atkinson and W. Han. *Theoretical numerical analysis; a functional analysis framework.* Springer-Verlag., 2001.

[4] S. Bakhtiyarov and D. Siginer. Fluid displacement in a horizontal tube. *Journal of Non-Newtonian Fluid Mechanics*, 65:1–15, 1996.

[5] R. Balasubramaniam, N. Rashidnia, T. Maxworthy, and J. Kuang. Instability of miscible interfaces in a cylindrical tube. *Physics of Fluids*, 17, 2005.

[6] M. Bercovier and M. Engleman. A finite element method for incompressible non-newtonian flows. *Journal of Computational Physics*, 36:313–326, 1980.

[7] R. Bird, R. Armstrong, and O.Hassager. *Dynamics of polymeric liquids.*, volume 2. Wiley-Interscience., 1987.

[8] A. Bogaerds, A. Grillet, G. Peters, and F. Baaijens. Stability analysis of constituitve equations for polymer melts in viscometric flows. *Journal of Non-Newtonian Fluid Mechanics*, 103:221–250, 2002.

[9] A. Bogaerds, A. Grillet, G. Peters, and F. Baaijens. Stability analysis of polymer shear flows using the extended pom-pom constitutive equations. *Journal of Non-Newtonian Fluid Mechanics*, 108:187–208, 2002.

[10] F. Brezzi and M. Fortin. *Mixed and Hybrid Finite Element Method.* Springer, 1991.

[11] T. Burghelea, K. Wielage-Burchard, I. Frigaard, D. Martinez, and J. Feng. A novel low inertia shear flow instability triggered by a chemical reaction. *Physics of Fluids*, 19:083102, 2007.

[12] F. Charru. "phase diagram" of interfacial instabilities in two-layer shear flows. *Proceedings of the Third International Conference on Multiphase Flow, ICMF'98. Held at Lyon, France June 8-12.*

[13] F. Charru and E. Hinch. "Phase diagram" of interfacial instabilities in a two-layer Couette flow and mechanism of the long wave instability. *Journal of Fluids Mechanics*, 414:195–223, 2000.

[14] C. Y. Chen and E. Meiburg. Miscible displacements in capillary tubes. part 2. numerical simulations. *Journal of Fluids Mechanics*, 326:57–90, 1996.

[15] K. Chen and D. Joseph. Elastic short wave instability in extrusion flows of viscoelastic liquids. *Journal of Non-Newtonian Fluid Mechanics*, 42:189–211, 1992.

[16] B. Cox. On driving a viscous fluid out of a tube. *Journal of Fluids Mechanics*, 14:81–96, 1962.

[17] R. Darby. *Viscoelastic fluids, An introduction to their properties and behavior*, volume 9. New York: M. Dekker, 1976.

[18] P. de Souza Mendes, E. Dutra, J. Siffert, and M. Naccache. Gas displacement of viscoplastic liquids in capillary tubes. *Journal of Non-Newtonian Fluid Mechanics*, 145:30–40, 2007.

[19] J. Dealy and R. Larson. *Structure and Rheology of Molten Polymers - From Structure to Flow Behavior and Back Again.* Hanser Publishers, 2006.

[20] Y. Dimakopoulos and J. Tsamopoulos. Transient displacement of Newtonian and viscoplastic liquids by air in complex tubes. *Journal of Non-Newtonian Fluid Mechanics*, 142:162–182, 2007.

[21] C. Doering, B. Echardt, and J.Schumacher. Failure of energy stability in Oldroyd-B fluids at arbitrarily low reynolds numbers. *Journal of Non-Newtonian Fluid Mechanics*, 135:92–96, 2006.

[22] M. d'Olce. *Instabilite's de cisaillement dans l'e'coulement concentrique de deux fluides miscibles*. These de l'Universite' Pierre et Marie Curie (PhD thesis), Paris, France, 2008.

[23] M. d'Olce, J. Martin, N. Rakotomalala, and D. Salin. Pearl and mushroom instability patterns in two miscible fluids core annular flows. *Physics of Fluids*, 20:024104, 2008.

[24] M. d'Olce, J. Martin, N. Rakotomalala, D. Salin, and L.Talon. Convective/absolute instability in miscible core-annular flow. part 1. experiments. *Journal of Fluid Mechanics*, 618:305–322, 2009.

[25] P. Ern, F. Charru, and P. Luchini. Stability analysis of a shear flow with strongly stratified viscosity. *Journal of Fluids Mechanics*, 496:295–312, 2003.

[26] I. Frigaard. Super-stable parallel flows of multiple visco-plastic fluids. *Journal of Non-Newtonian Fluid Mechanics*, 100:49–76, 2001.

[27] I. Frigaard, S. Howison, and I. Sobey. On the stability of Poiseuille flow of a Bingham fluid. *Journal of Fluids Mechanics*, 263:133–150, 1994.

[28] I. Frigaard and C. Nouar. On three-dimensional linear stability of Poiseuille flow of Bingham fluids. *Physics of Fluid.*, 15(10):2843–2851, 2003.

[29] I. Frigaard and C. Nouar. On the usage of viscosity regularisation methods for visco-plastic fluid flow computation. *Journal of Non-Newtonian Fluid Mechanics*, 127:1–26, 2005.

[30] I. Frigaard, O. Scherzer, and G. Sona. Uniqueness and non-uniqueness in the steady displacement of two viscoplastic fluids. *ZAMM*, 81:99–118, 2001.

[31] C. Gabard. *Etude de la stabilité de films liquides sur les parois d'une conduite verticale lors de l'ecoulement de fluides miscibles non-newtoniens.* These de l'Universite Pierre et Marie Curie (PhD thesis), Orsay, France., 2001.

[32] C. Gabard and J. Hulin. Miscible displacements of non-newtonian fluids in a vertical tube. *European Physical Journal E*, 11:231–241, 2003.

[33] H. Ganpule and B. Khomami. A theoretical investigation of interfacial instabilities in the three layer superposed channel flow of viscoelastic fluids. *Journal of Non-Newtonian Fluid Mechanics*, 81:315–360, 1998.

[34] H. Ganpule and B. Khomami. The effect of transient viscoelastic properties on interfacial instabilities in superposed pressure driven channel flows. *Journal of Non-Newtonian Fluid Mechanics*, 80:217–249, 1999.

[35] H. Ganpule and B. Khomami. An investigation of interfacial instabilities in the superposed channel flow of viscoelastic fluids. *Journal of Non-Newtonian Fluid Mechanics*, 81:27–69, 1999.

[36] R. Glowinski. *Numerical Methods for Nonlinear Variational Problems*. Springer-Verlag, 1983.

[37] R. Glowinski, J. Lions, and R.Tremolieres. *Analyse Numérique des inéquations variationelles*, volume 2. North-Holland, Amsterdam, 1981.

[38] R. Glowinski and P. L. Tallec. *Augmented Lagrangian and operator-splitting methods in nonlinear mechanics.* SIAM, 1989.

[39] N. Goyal and E. Meiburg. Miscible displacements in Hele-Shaw cells: two-dimensional base states and their linear stability. *Journal of Fluid Mechanics*, 558:329–355, 2006.

[40] N. Goyal, H. Pichler, and E. Meiburg. Variable density, miscible displacements in a vertical Hele-Shaw cell: linear stability. *Journal of Fluid Mechanics*, 584:357–372, 2007.

[41] C. Han. Studies on multilayer film extrusion ii. interfacial instability in flat film coextrusion. *Polymer Engineering and Science*, 18:180–186, 1978.

[42] C. Han, Y. Kim, and H. Chin. Rheological investigation of interfacial instabilities in two-layer flat film coextrusion. *Polymer Engineering Review*, 4:3–13, 1984.

[43] C. Hickox. Instability due to viscosity and density stratification in axisymmetric pipe flow. *Physics of Fluids*, 14:251–262, 1971.

[44] E. Hinch, , O. Harris, and J. Rallison. The instability mechanism for two elastic elastic liquids being co-extruded. *Journal of Non-Newtonian Fluid Mechanics*, 43:311–324, 1992.

[45] E. Hinch. A note on the mechanism of the instability at the interface between two shearing fluids. *Journal of Fluid Mechanics*, 114:463–465, 1984.

[46] T. Ho and M. Denn. Stability of plane Poiseuille flow of a highly elastic liquid. *Journal of Non-Newtonian Fluid Mechanics*, 3:179–195, 1977.

[47] N. Hoda, M. Jovanovi, and S. Kumar. Energy amplification in channel flows of viscoelastic fluids. *Journal of Fluid Mechanics*, 601:407–424, 2008.

[48] N. Hoda, M. Jovanovi, and S. Kumar. Frequency responses of streamwise-constant perturbations in channel flows of Oldroyd-B fluids. *Journal of Fluid Mechanics*, 625:411–434, 2009.

[49] A. Hooper and W. Boyd. Shear flow instability due to a wall and a viscosity discontinuity at the interface. *Journal of Fluid Mechanics*, 179:201–225, 1987.

[50] S. Hormozi and I. Frigaard. Nonlinear stability of a visco-plastically lubricated viscoelastic fluid flow. *Journal of Non-Newtonian Fluid Mechanics, under review*, 2011.

[51] S. Hormozi, D. Martinez, and I. Frigaard. Stable core-annular flows of viscoelastic fluids using the visco-plastic lubrication technique. *Journal of Non-Newtonian Fluid Mechanics, under review*, 2011.

[52] S. Hormozi, K. Wielage-Burchard, and I. Frigaard. Entry, start up and stability effects in visco-plastically lubricated pipe flows. *Journal of Fluid Mechanics*, 673:432–467, 2011.

[53] S. Hormozi, K. Wielage-Burchard, and I. Frigaard. Multi-layer channel flows with yield stress fluids. *Journal of Non-Newtonian Fluid Mechanics, in press*, 166:262–278, 2011.

[54] C. Huen. *Experimental studies of visco-plastic lubrication.* M.A.Sc. thesis, University of British Columbia, 2005.

[55] C. Huen, I. Frigaard, and D.M.Martinez. Experimental studies of multi-layer flows using a visco-plastic lubricant. *Journal of Non-Newtonian Fluid Mechanics*, 142:150–161, 2007.

[56] R. Huilgol and N. P. Thien. *Fluid Mechanics of viscoelasticity.* Elsevier Science., 1997.

[57] Y. Joo and E. Shaqfeh. A purely elastic instability in Dean and Taylor-Dean flow.

[58] D. Joseph. *Stability of Fluid Motions I.* Springer-Verlag., 1976.

[59] D. Joseph, R. Bai, K. Chen, and Y. Renardy. Core-annular flows. *Annual Review of Fluid Mechanics*, 29:65–90, 1997.

[60] D. Joseph and S. Carmi. Stability of Poiseuille flow in pipes, annuli, and channels. *Quarterly of Applied Mathematics.*, 26:575–599, 1969.

[61] D. Joseph and Y. Renardy. *Fundamentals of Two-Fluid Dynamics.* Interdisciplinary Applied Mathematics,Springer., 1993.

[62] M. Jovanovic' and S. Kumar. Transient growth without inertia. *Physics of Fluids*, 22:023101, 2010.

[63] B. Khomami. Interfacial stability and deformation of two stratified power law fluids in plane Poiseuille flow, part 1. stability analysis. *Journal of Non-Newtonian Fluid Mechanics*, 36:289–303, 1990.

[64] B. Khomami and M. Ranjbaran. Experimental studies of interfacial instabilities in multilayer pressure-driven flow of polymeric melts. *Rheologica Acta.*, 36:345–366, 1997.

[65] B. Khomami and K. Su. An experimental/theoretical investigation of interfacial instabilities in superposed pressure-driven channel flow of newtonian and well characterized viscoelastic fluids part I: linear stability and encapsulation effects. *Journal of Non-Newtonian Fluid Mechanics*, 91:59–84, 2000.

[66] J. Kuang, T.Maxworthy, and P. Petitjeans. Miscible displacements between silicone oils in capillary tubes. *European Journal of Mechanics - B*, 22:271–277, 2003.

[67] R. Kupferman. On the linear stability of plane Couette flow for an Oldroyd-B fluid and its numerical approximation. *Journal of Non-Newtonian Fluid Mechanics*, 127:169–190, 2005.

[68] W. Lai, D. Rubin, and E. Krempl. *Introduction to Continuum Mechanics.* Elsevier Science., 1994.

[69] E. Lajeunesse. *Déplacement et instabilités de fluides miscibles et immiscibles en cellules de Hele-Shaw.* These de l'Universite Pierre et Marie Curie (PhD thesis), Orsay, France.

[70] E. Lajeunesse, J. Martin, N. Rakotomalala, and D. Salin. 3d instability of miscible displacements in a Hele-Shaw cell. *Physical Review Letter*, 79:5254–5257, 1997.

[71] E. Lajeunesse, J. Martin, N. Rakotomalala, and D. Salin. The threshold of the instability in miscible displacements in a Hele-Shaw cell at high rates. *Physics of Fluids*, 13:799–801, 2001.

[72] E. Lajeunesse, J. Martin, N. Rakotomalala, D. Salin, and Y. Yortsos. Miscible displacement in a Hele-Shaw cell at high rates. *Journal of Fluid Mechanics*, 398:299–319, 1999.

[73] B. Lee and J. White. An experimental study of rheological properties of polymer melts in laminar shear flow. *Journal of Rheology*, 18:467–492, 1974.

[74] K. Lee and B. Finlayson. Stability of plane Poiseuille and Couette flow of a Maxwell fluid. *Journal of Non-Newtonian Fluid Mechanics*, 21:65–78, 1986.

[75] R. LeVeque. *Finite Volume Methods for Hyperbolic Problems.* Cambridge Texts in Apllied Mathematics, Cambridge University Press., 2002.

[76] P. S. Mendes and E. Dutra. Viscosity function for yield-stress liquids. *Applied Rheology*, 14:296–302, 2004.

[77] C. Metivier, C. Nouar, and J. Brancher. Linear stability involving the Bingham model when the yield stress approaches zero. *Physics of Fluids*, 17:104106, 2005.

[78] C. Metivier, C. Nouar, and J. Brancher. Weakly nonlinear dynamics of thermoconvective instability involving viscoplastic fluids. *Journal of Fluid Mechanics*, 660:316–353, 2010.

[79] B. Meulenbroek, C. Storm, V. Bertola, C. Wagner, D. Bonn, and W. Saarloos. Intrinsic route to melt fracture in polymer extrusion: a weakly nonlinear subcritical instability of viscoelastic Poiseuille flow. *Physical Review Letter*, 90(2):024502:1–4, 2003.

[80] B. Meulenbroek, C. Storm, C. Morozov, and W. Saarloos. Weakly nonlinear subcritical instability of visco-elastic Poiseuille flow. *Journal of Non-Newtonian Fluid Mechanics*, 116:235–268, 2004.

[81] J. Miller and J. Rallison. Instability of coextruded elastic liquids at high Weissenberg number. *Journal of Non-Newtonian Fluid Mechanics*, 143:88–106, 2007.

[82] J. Miller and J. Rallison. Interfacial instability between sheared elastic liquids in a channel. *Journal of Non-Newtonian Fluid Mechanics*, 143:71–87, 2007.

[83] A. Morozov and W. Saarloos. Intrinsic route to melt fracture in polymer extrusion: a weakly nonlinear subcritical instability of viscoelastic Poiseuille flow. *Physical Review Letter*, 95(2):024501:1–4, 2005.

[84] M. Moyers-Gonzalez. *Nonlinearly stable multilayer viscoplastic flows.* M.A.Sc. thesis, University of British Columbia, 2002.

[85] M. Moyers-Gonzalez, I. Frigaard, and C.Nouar. Nonlinear stability of a visco-plastically lubricated viscous shear flow. *Journal of Fluid Mechanics*, 577:211–239, 2007.

[86] M. Moyers-Gonzalez, I. Frigaard, and C. Nouar. Stable two-layer flows at all Re; visco-plastic lubrication of shear-thinning and viscoelastic fluids. *Journal of Non-Newtonian Fluid Mechanics*, 165:1578–1587, 2010.

[87] C. Nouar and I. Frigaard. Nonlinear stability of Poiseuille flow of a Bingham fluid: theoretical results and comparison with phenomenological criteria. *Journal of Non-Newtonian Fluid Mechanics*, 100:127–149, 2001.

[88] C. Nouar and I. Frigaard. On three-dimensional linear stability of Poiseuille flow of Bingham fluids . *Physics of Fluids*, 15:28432851, 2003.

[89] C. Nouar, N. Kabouya, J. Dusek, and M. Mamou. Modal and non-modal linear stability of the plane BinghamPoiseuille flow. *Journal of Fluid Mechanics*, 506:117–146, 2004.

[90] A. L. R. Owens. An energy estimate for the Oldroyd-B model: theory and applications. *Journal of Non-Newtonian Fluid Mechanics*, 112:161–176, 2003.

[91] T. Papanastasiou. Flows of materials with yield. *Journal of Rheology*, 31:385–404, 1987.

[92] P. Petitjeans and T. Maxworthy. Miscible displacements in capillary tubes. part 1. experiments. *Journal of Fluid Mechanics*, 326:37–56, 1996.

[93] A. Pinarbasi and A. Liakopoulos. Stability of two-layer Poiseuille flow of Carreau-Yasuda and Bingham-like fluids. *Journal of Non-Newtonian Fluid Mechanics*, 57:227–241, 1995.

[94] A. Quarteroni and A. Valli. *Numerical Approximation of Partial Differential Equations*. Springer Series in Computational Mathematics, **23** Springer, 2008.

[95] N. Rakotomalala, D. Salin, and P. Watzky. Miscible displacement between two parallel plates: BGK lattice gas simulations. *Journal of Fluid Mechanics*, 338:277–297, 1997.

[96] T. Ranganathan and R. Govindarajan. Stabilization and destabilization of channel flow by location of viscosity-stratified fluid layer. *Physics of Fluids*, 13:1–3, 2001.

[97] D. Reinelt and P. Saffman. The penetration of a finger into a viscous fluid in a channel and tube. *SIAM Journal on Scientific Computing*, 6:542–561, 1985.

[98] M. Renardy. *Mathematical analysis of viscoelastic flows.*, volume 73. SIAM., 2000.

[99] M. Renardy. Stress modes in linear stability of viscoelastic flows. *Journal of Non-Newtonian Fluid Mechanics*, 159:137–140, 2009.

[100] M. Renardy and Y.Renardy. Linear stability of plane Couette flow of an upper convected Maxwell fluid. *Journal of Non-Newtonian Fluid Mechanics*, 22:23–33, 1986.

[101] Y. Renardy. Stability of the interface in two-layer Couette flow of upper convected Maxwell liquids. *Journal of Non-Newtonian Fluid Mechanics*, 28:99–115, 1988.

[102] R.Govindarajan. Effect of miscibility on the linear instability of two-fluid channel flow. *International Journal of Multiphase Flow*, 30:1177–1192, 2004.

[103] P. Saffman and G. Taylor. The penetration of a fluid into a porous medium or Hele-Shaw cell containing a more viscous liquid. *Proceedings of the Royal Society of London, Series A*, 245:312–329, 1958.

[104] K. Sahu, H. Ding, P. Valluri, and O. Matar. Pressure-driven miscible two-fluid channel flow with density gradients. *Physics of Fluids*, 21:043603, 2009.

[105] J. Scoffoni, E. Lajeunesse, and G. Homsy. Interfacial instabilities during displaceemnts of two miscible fluids in a vertical pipe. *Physics of Fluids*, 13:553–556, 2001.

[106] B. Selvam, S. Merk, R. Govindarajan, and E. Meiburg. Stability of miscible core-annular flow with viscosity stratification. *Journal of Fluid Mechanics*, 592:23–49, 2007.

[107] B. Selvam, L. Talon, L. Leshafft, and E. Meiburg. Convective/absolute instability in miscible core-annular flow. part 2. numerical simulations and nonlinear global modes. *Journal of Fluid Mechanics*, 618:323–348, 2009.

[108] M. Shariati, L. Talon, J. Martin, N. Rakotomala, D. Salin, and Y. Yortsos. Fluid displacement between two parallel plates: a

non-empirical model displaying change of type from hyperbolic to elliptic equations. *Journal of Fluid Mechanics*, 519:105–132, 2004.

[109] E. Soares, M. Carvalho, and P. S. Mendes. Immiscible liquid-liquid displacement in capillary tubes. *Journal of Fluids Engineering*, 127:24–31, 2005.

[110] D. Sousa, E. Soares, R. Queiroz, and R. Thompson. Numerical investigation on gas-displacement of a shear-thinning liquid and a visco-plastic material in capillary tubes. *Journal of Non-Newtonian Fluid Mechanics*, 144:149–159, 2007.

[111] Y. Su and B. Khomami. Stability of multi-layer power law and second order fluids in plane Poiseuille flow. *Chemical Engineering Communications*, 109:209–223, 1991.

[112] R. Sureshkumar, M. Smith, R. Armstrong, and R. Brown. Linear stability and dynamics of viscoelastic flows using time-dependent numerical simulations. *Journal of Non-Newtonian Fluid Mechanics*, 82:57–104, 1999.

[113] S. Taghavi, T. Seon, D. Martinez, and I. Frigaard. Buoyancy-dominated displacement flows in near-horizontal channels: the viscous limit. *Journal of Fluid Mechanics*, 639:1–35, 2009.

[114] L. Talon, J. Martin, N. Rakotomala, D. Salin, and Y. Yortsos. Crossing the elliptic region in a hyperbolic system with change-of-type behavior arising in flow between two parallel plates. *Phys. Review E*, 69:066318, 2004.

[115] G. Taylor. Deposition of a viscous fluid on the wall of a tube. *Journal of Fluid Mechanics*, 10:161–165, 1960.

[116] R. Thompson, E. Soares, and R. Bacchi. Further remarks on numerical investigation on gas-displacement of a shear-thinning liquid and a visco-plastic material in capillary tubes. *Journal of Non-Newtonian Fluid Mechanics*, 168:448–452, 2010.

[117] C. Truesdell and W. Noll. *The non-linear field theories of mechanics*. Springer, Heidelberg., 3 edition, 1965.

[118] C. Truesdell and R. Toupin. *The classical field theories.* Springer, Heidelberg., 2 edition, 1960.

[119] R. Valette, P. Laure, Y. Demay, and J. Agassant. Convective linear stability analysis of two-layer coextrusion flow for molten polymers. *Journal of Non-Newtonian Fluid Mechanics*, 121:41–53, 2004.

[120] R. Valette, P. Laure, Y. Demay, and J. Agassant. Convective linear stability analysis of two-layer coextrusion flow for molten polymers. *international Polymer Processing.*, 19(2):118–128, 2004.

[121] N. Waters. The stability of two stratified power law fluids in Couette flow. *Journal of Non-Newtonian Fluid Mechanics*, 12:85–94, 1983.

[122] N. Waters and A. Keeley. The stability of two stratified non-newtonian liquids in Couette flow. *Journal of Non-Newtonian Fluid Mechanics*, 24:161–181, 1987.

[123] P. Wesseling. *Principles of Computational Fluid Dynamics.*, volume 29. Springer Series in Computational Mathematics, 2001.

[124] K. Wielage-Burchard and I. Frigaard. Static wall layers in plane channel displacement flows. *Journal of Non-Newtonian Fluid Mechanics*, 166:245–261, 2011.

[125] G. Wilson and B. Khomami. An experimental investigation of interfacial instabilities in the multilayer flow of viscoelastic fluids: Part I incompatible polymer systems. *Journal of Non-Newtonian Fluid Mechanics*, 41:355–384, 1992.

[126] G. Wilson and B. Khomami. An experimental investigation of interfacial instabilities in the multilayer flow of viscoelastic fluids: Part II elastic and nonlinear effects in incompatible polymer systems. *Journal of Rheology*, 37:315–339, 1993.

[127] G. Wilson and B. Khomami. An experimental investigation of interfacial instabilities in the multilayer flow of viscoelastic fluids: Part III compatible polymer systems. *Journal of Rheology*, 37:341–354, 1993.

[128] G. Wilson and B. Khomami. An experimental investigation of interfacial instabilities in the superposed flow of viscoelastic fluids in

converging/diverging channel geometries. *Journal of Non-Newtonian Fluid Mechanics*, 58:47–65, 1995.

[129] H. Wilson. *Shear Flow Instabilities in Viscoelastic Fluids.* PhD thesis, Cambridge University, Cambridge, United Kingdom., 1998.

[130] H. Wilson and J. Rallison. Instability of channel flow of a shear-thinning White-Metzner fluid. *Journal of Non-Newtonian Fluid Mechanics*, 87:75–96, 1999.

[131] Z. Yang and Y. Yortsos. Asymptotic solutions of miscible displacements in geometries of large aspect ratio. *Physics of Fluids*, 9:286–298, 1997.

[132] S. Yiantsos and B. Higgins. Linear stability of plane Poiseuille flow of two superposed fluids. *Physics of Fluids*, 31:3225–3238, 1988.

[133] C. Yih. Instability due to viscosity stratification. *Journal of Fluid Mechanics*, 27:337–352, 1967.

[134] J. Zhang, D.Vola, and I. Frigaard. Yield stress effects on Rayleigh-Benard convection. *Journal of Fluid Mechanics*, 566:389–419, 2006.

Appendix A

Initial perturbations for pipe flows

We outline here the initial perturbations used in chapter 2, section 2.3, for the study of temporal stability.

Initial conditions for the velocity perturbation $\mathbf{u}$ are constructed so as to satisfy the continuity equation and the various boundary and interface conditions. We consider two different cases A & B. In case A initially the whole domain is perturbed. In case B the plug region is left intact by the initial perturbation. In both cases we denote the initial velocity perturbation by $\mathbf{u}(r, z, 0) = A(v_r(r, z), v_z(r, z))$, where v_r and v_z are shape functions for the radial and axial components of the perturbed velocity, respectively, and A is the amplitude of the perturbation. The components v_r and v_z can be defined in terms of a stream function ψ:

$$v_r = \frac{1}{r}\frac{\partial \psi}{\partial z}, \quad v_z = -\frac{1}{r}\frac{\partial \psi}{\partial r} \tag{A.1}$$

We assume that ψ has the following form

$$\psi = \zeta \left\{ \phi(r) \sin(\alpha z) + f(r) \right\}. \tag{A.2}$$

where the length of the pipe section is $\frac{2\pi}{\alpha}$ and ζ is defined so as to normalise the perturbation with the base flow:

$$\zeta = \frac{\|W(r)\|_2}{\|(v_r(r, z), v_z(r, z))\|_2}. \tag{A.3}$$

A.1 Case A

We satisfy the following boundary conditions and continuity of stress and velocity at interface

1. at $r = 0$, $v_r = 0$, $\frac{\partial v_z}{\partial r} = 0$, $\psi = 0$
2. at $r = r_i$, $\psi = 0$
3. at $r = 1$, $v_r = 0$, v_z, $\psi = 0$

Note that to simplify the imposition of stress continuity at interface, we consider

$$\dot{\gamma}_{rr} = 0, \dot{\gamma}_{zz} = 0, \dot{\gamma}_{\theta\theta} = 0.$$

For $r \leq r_i$ we have:

$$v_r = -\zeta r^3 (r - r_i)^3 \alpha \cos \alpha z. \tag{A.4}$$

$$v_z = \zeta \left[r^2 (r - r_i)^2 (7r - 4r_i) \sin \alpha z + 4r^2 (r - r_i)^2 + 2r^3 (r - r_i) \right]. \tag{A.5}$$

and for $r > r_i$:

$$v_r = -\zeta \frac{(r - r_i)^3 (r - 1)^2 \alpha \cos \alpha z}{r}. \tag{A.6}$$

$$v_z = \zeta \left(\frac{(r-1)(r-r_i)^2(5r - 2r_i - 3)}{r} \sin \alpha z + \frac{2(r-1)(r-r_i)(2r - r_i - 1)}{r} \frac{2mr_i^4 - Br_i^2/r_y - Br_i}{2(r_i - 1)^2} \right). \tag{A.7}$$

A.2 Case B

To keep the plug intact, we apply the following conditions

1. at $r = 0$, $v_r = 0$, $\frac{\partial v_z}{\partial r} = 0$, $\psi = 0$
2. $r \in [r_i, r_y]$, $v_r = v_z = 0$, $\psi = 0$

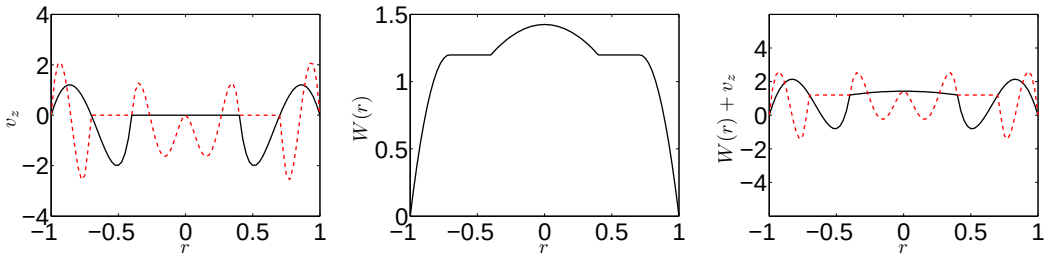

Figure A.1: Example of the axial component of the initial velocity perturbations for $(m, B) = (10, 20)$ with $r_i = 0.4$, $A = 1$, plotted where $\sin \alpha z = 1$. From left to right: a) axial component of initial velocity perturbations (solid line = case A, broken line = case B); b) base flow; c) superposition of perturbation and base flow.

3. at $r = 1$, $v_r = v_z = 0$, $\psi = 0$

For $r \leq r_i$ we have:

$$v_r = -\zeta r^3 (r - r_i)^2 \alpha \cos \alpha z. \tag{A.8}$$

$$v_z = \zeta r^2 (r - r_i)(6r - 4r_i) \sin \alpha z. \tag{A.9}$$

For $r > r_i$:

$$v_r = -\zeta \frac{(r - r_y)^2 (r - 1)^2 \alpha \cos \alpha z}{r}. \tag{A.10}$$

$$v_z = \zeta \frac{2(r - 1)(r - r_y)(2r - r_y - 1) \sin \alpha z}{r}. \tag{A.11}$$

Figure A.1 shows an illustrative example of axial components of the two initial velocity perturbations (case A and case B) and their superposition with the base flow velocity profile.

Appendix B

Initial perturbations for channel flows

We outline here the initial perturbations used in chapter 3, section 3.3, for the study of temporal stability.

Initial conditions for the velocity perturbation $\mathbf{u}$ are constructed so as to satisfy the continuity equation and the various boundary and interface conditions. We consider two different cases, A & B. In case A initially the whole domain is perturbed. In case B the plug region is left intact by the initial perturbation. In both cases we denote the initial velocity perturbation by $\mathbf{u}(x, y, 0) = A(v_x(y, z), v_y(x, y))$, where v_x and v_y are shape functions for the radial and axial components of the perturbed velocity, respectively, and A is the amplitude of the perturbation. The components v_x and v_y can be defined in terms of a stream function ψ:

$$v_x = \frac{\partial \psi}{\partial y}, \quad v_y = -\frac{\partial \psi}{\partial x} \tag{B.1}$$

We assume that ψ has the following form

$$\psi = \zeta \left\{ \phi(y) \sin(\alpha x) + f(y) \right\}. \tag{B.2}$$

where the length of the periodic cell considered is $\frac{2\pi}{\alpha}$ and ζ is defined so as to normalise the perturbation with the base flow:

$$\zeta = \frac{\|W(y)\|_2}{\|(v_x(y, z), v_y(x, y))\|_2}. \tag{B.3}$$

B.1 Case A

We satisfy the following boundary conditions

1. at $y = 0$, $\frac{\partial v_x}{\partial y} = 0$, $v_y = 0$, $\psi = 0$
2. at $y = 1$, v_x, $v_y = 0$, $\psi = 0$

and continuity of stress and velocity at the interface. For $y \leq y_i$ we have:

$$\begin{aligned} v_x &= \zeta \left[y^2(y-y_i)^2(6y-3y_i)\sin\alpha x + 3y^2(y-y_i)^2 \right. \\ &\qquad \left. +2y^3(y-y_i) \right]. \qquad \text{(B.4)} \\ v_y &= -\zeta y^3(y-y_i)^3\alpha\cos\alpha x. \qquad \text{(B.5)} \end{aligned}$$

and for $y > y_i$:

$$\begin{aligned} v_x &= \zeta \left((y-1)(y-y_i)^2(5y-2y_i-3)\sin\alpha x + \right. \\ &\qquad \left. 2(y-1)(y-y_i)(2y-y_i-1)\frac{2my_i^3 - By_i/y^* - B}{2(y_i-1)^2} \right). \qquad \text{(B.6)} \\ v_y &= -\zeta(y-y_i)^3(y-1)^2\alpha\cos\alpha x. \qquad \text{(B.7)} \end{aligned}$$

B.2 Case B

To keep the plug intact, we apply the following conditions

1. at $y = 0$, $\frac{\partial v_x}{\partial y} = 0$, $v_y = 0$, $\psi = 0$
2. $y \in [y_i, y^*]$, $v_x = v_y = 0$, $\psi = 0$
3. at $y = 1$, $v_x = v_y = 0$, $\psi = 0$

For $y \leq y_i$ we have:

$$\begin{aligned} v_x &= \zeta y^2(y-y_i)(5y-3y_i)\sin\alpha x. \qquad \text{(B.8)} \\ v_y &= -\zeta y^3(y-y_i)^2\alpha\cos\alpha x. \qquad \text{(B.9)} \end{aligned}$$

For $y > y^*$:

$$v_x = \zeta 2(y-1)(y-y^*)(2y-y^*-1)\sin\alpha x. \quad \text{(B.10)}$$

$$v_y = -\zeta(y-y^*)^2(y-1)^2\alpha\cos\alpha x. \quad \text{(B.11)}$$

B.3 Stream function conditions

The stream function conditions at the interface ($\psi = 0$) may appear unnecessary at first reading. However, here we consider finite perturbations and to impose a non-zero ψ at the interface would essentially shift the balance of flow rates between the layers, i.e. we would expect the perturbations to decay to a different base flow in this case.